AMCTURKEY

ADDITIVE MANUFACTURING CONFERENCE

17-18 OCTOBER 2019,GREEN PARK HOTEL PENDİK - İSTANBUL

PROCEEDINGS BOOK

SUPPORTING INSTITUTIONS

ALUTEAM · EKTAM · MARC · İTÜ EKAM · SU IMC

SPONSORS

GOLD SPONSORS

ERMAKSAN YENİLİKÇİ TEKNOLOJİLER · TEI · EOS

SILVER SPONSORS

COŞKUNÖZ HOLDİNG · aselsan

BRONZE SPONSORS

TÜRKHAVACILIK UZAYSANAYİİ · MT · Fronius · FNSS · SENTESBİR · BEAM · RENISHAW apply innovation

EDUCATION SPONSORS

roketsan · AUTODESK · FORM MAKİNA · INTECRO · ZEISS · İNCEKARALAR · TRON

Dear Participants,

Manufacturing concepts are rapidly changing and manufacturing processes are completely being redefined in the last decade. Industry 4.0, digitalization and IoT are at the core of next-generation manufacturing technologies. Additive Manufacturing, considered to be one of the cornerstones of next- generation digital manufacturing, is replacing/will replace some of the traditional manufacturing methods in several industries not only in our country but also globally.

For digital transformation of manufacturing industries, it is critical that scientific research and R&D studies on Additive Manufacturing technologies need to be shared on a common platform where scientific community and researchers from industry come together. The first "Additive Manufacturing Conference" in Turkey (AMCTURKEY) will be held in İstanbul Green Park Hotel (Pendik/İstanbul/TURKEY), on October 17-18, 2019 for this purpose.

AMCTURKEY brings local and international scientists, researchers, and representatives both from academia and industry, where they can present and share their recent scientific discoveries, research activities and emerging applications in Additive Manufacturing and related technologies. The conference covers all the areas of Additive Manufacturing and will include internationally-renowned invited speakers as well as panel discussions and industrial presentations.

One of the objectives of the AMCTURKEY is to play a bridge between academia and industry in Additive Manufacturing Technologies. Thus, special attention is given to our companies/firms who are interested in and intending an investment in Additive Manufacturing Technologies and also would like to follow the developments in this field. The AMCTURKEY will provide a better understanding of Additive Manufacturing Technologies and industrial applications and to increase the awareness about this new technology. This cooperation between academia and industry will further extend the knowledge and the possible applications of additive manufacturing and ultimately benefit both. In this context, this conference will be one of the most important common platforms of the Additive Manufacturing for academicians and researchers working in this field.

It is our pleasure to invite all of the scientists, academicians, business delegates, sector representatives, students and policy-makers from all over the world to attend the 2019 AMCTURKEY.

Organizing Committee

AMCTURKEY2019 ORGANIZATION COMMITTEE

Oğuzhan YILMAZ, *Gazi University*	*Co-Chair*
Bahattin KOÇ, *Sabancı University*	*Co-Chair*
Yusuf KAYNAK, *Marmara University*	*Co-Chair*
Ebubekir KOÇ, *Fatih Sultan Mehmet Vakif University*	*Co-Chair*

Conference Secretary

Mustafa Safa YILMAZ, *Fatih Sultan Mehmet Vakif University*

AMCTURKEY2019 STEERING COMMITTEE

Evren Y. BAL	*Eskisehir Osmangazi University*
Eralp DEMİR	*Sabanci University*
Tevfik DEMİR	*TOBB University*
M. Cengiz KAYACAN	*Suleyman Demirel University*
Yusuf KAYNAK	*Marmara University*
Bahattin KOÇ	*Sabanci University*
Ebubekir KOÇ	*Fatih Sultan Mehmet Vakif University*
İsmail LAZOĞLU	*Koc University*
İ. Ethem SAKLAKOGLU	*Ege University*
Metin U. SALAMCI	*Gazi University*
Emrecan SÖYLEMEZ	*Marmara University*
Rahmi ÜNAL	*Gazi University*
Ulaş YAMAN	*Orta Dogu Technical University*
Mehmet YILDIZ	*Sabanci University*
Oğuzhan YILMAZ	*Gazi University*

Conference Topics

- Hybrid Processes
- Design for Additive Manufacturing
- Process Planning for Additive Manufacturing
- Lattices and Cellular Structures
- Post-Processing Operations
- Microstructural Characterization of Components Fabricated by Additive Manufacturing
- Additive Manufacturing Process Modeling and Simulation
- Data Analytics in Additive Manufacturing
- Applications of Additive Manufacturing
- Novel Materials for Additive Manufacturing
- Functionally Graded Materials in Additive Manufacturing
- Process Monitoring and Control in Additive Manufacturing
- Topology Optimisation Applications in Additive Manufacturing

INDEX

ID NO	PAPER TITLE	PAGE
04	MACHINE LEARNING-BASED INTELLIGENT PATH ANALYZER TECHNOLOGY TO ACHIEVE MAXIMUM YIELD IN METAL ADDITIVE MANUFACTURING	7
05	A FEASIBILITY STUDY ON CMT ADDITIVE MANUFACTURING TECHNIQUE	10
06	WEIBULL DISTRIBUTION OF SELECTIVE LASER MELTED ALSI10MG PARTS FOR COMPRESSION TESTING	14
10	ADDITIVE MANUFACTURING OF CONTINOUSLY ALIGNED CARBON FIBRE STRUCTURES	19
12	SELECTIVE LASER MELTING PROCESS DEVELOPMENT FOR ENHANCED PRODUCTIVITY WITH PH17-4 STAINLESS STEEL	21
13	INFLUENCE OF PROCESSING PARAMETERS ON SURFACE PROPERTIES OF SELECTIVE LASER MELTED TI-6AL-4V PARTS	24
15	IMPROVEMENT MECHANICAL AND BIOLOGICAL PROPERTIES OF COCR SCAFFOLDS FABRICATED BY SELECTIVE LASER MELTING	26
18	FAILURE ANALYSIS OF CARBON FIBER REINFORCED PA11 PRODUCED BY SLS	28
19	CHARACTERIZATION AND COMPRESSION TESTING OF DOUBLE GYROID LATTICE STRUCTURES PRODUCED BY DIRECT METAL LASER MELTING	33
23	IN SITU ELEMENTAL ANALYSIS AND FAILURES DETECTION DURING ADDITIVE MANUFACTURING PROCESS UTILIZING LASER INDUCED BREAKDOWN SPECTROSCOPY	35
25	INVESTIGATION OF ENERGY ABSORPTION BEHAVIOR OF STIFFNESS OPTIMIZED LATTICE STRUCTURES	37
26	THE EFFECT OF PROCESSING PARAMETERS ON THE MICROSTRUCTURE AND MECHANICAL PROPERTIES OF SLS PEKK	43
27	ON THE OPTIMIZATION OF METAL SPATTER SWEEPING IN SELECTIVE LASER MELTING	47
30	PROCESSING OF NDFEB BY SELECTIVE LASER MELTING	50
32	LASER INDUCED BREAKDOWN SPECTROMETRY FOR ONLINE ANALYSIS OF METAL PARTICLES FEEDSTOCK DURING LASER METAL DEPOSITION PROCESS	52

39	INFLUENCE OF BUILD ORIENTATION ON RESIDUAL STRESSES IN 3D PRINTED PARTS	**54**
42	EVALUATION OF ALTERNATIVE PARAMETERS TO DESCRIBE THE QUALITY OF ADDITIVELY MANUFACTURED ALUMINIUM ALLOY SURFACES	**56**
46	DESIGN AND VALIDATION OF GRADED POROUS STRUCTURES PRODUCED BY POWDER BED FUSION PROCESS	**60**
47	EVALUATION OF TANTALUM ALLOY WITH TITANIUM IN UNIVERSAL POWDER BED SYSTEM (UPB) FOR ELECTRON BEAM MELTING PROCESS	**65**
49	A METALLURGICAL PHASE TRANSFORMATION MODEL APPLIED TO DIRECTED ENERGY DEPOSITION ADDITIVE MANUFACTURING OF Ti-6Al-4V	**71**
51	PRODUCTION OF PRIMECAST® POLYSTYRENE BY SELECTIVE LASER SINTERING (SLS) METHOD AND DEVELOPMENT OF SURFACE ROUGHNESS OF SINTERED PARTS	**75**
54	INFLUENCE OF HOT ISOSTATIC PRESSING AND SUBSEQUENT HEAT TREATMENT ON MECHANICAL PROPERTIES OF DIRECT METAL LASER SINTERED ALSI10MG ALLOY	**78**
55	TRANSIENT MELT POOL MODELING FOR THE ABRUPT PROCESS PARAMETER CHANGE IN SELECTIVE LASER MELTING PROCESS	**80**
56	CERAMIC COMPOSITE COATING AND LASER SURFACE MELTING OF COCR ALLOY, AND ITS CHARACTERIZATION	**83**
59	A NEW DESIGN APPROACH FOR ADDITIVE MANUFACTURING OF SATELLITE COMPONENTS	**86**
60	VALIDATION OF DYNAMIC MODELS OF ADDITIVE MANUFACTURED PARTS USING SELECTIVE LASER MELTING METHOD	**89**
63	THERMAL PROCESS SIMULATION FOR DIRECT ENERGY DEPOSITION ADDITIVE MANUFACTURING PROCESS	**93**
64	TOPOLOGY OPTIMIZATION AND FINITE ELEMENTAL ANALYSIS FOR AN INCONEL 718 ENGINE MOUNTING BRACKET MANUFACTURED VIA ELECTRON BEAM MELTING	**97**
65	MICROSTRUCTURE AND EFFECT OF HOLE ON MECHANICAL PROPERTIES OF INCONEL 718 BUILT VIA DIRECT METAL LASER SINTERING	**100**
66	PRINTABLE DENSITY LIMITS OF ADDITIVELY-MANUFACTURED STRUCTURED FOAMS	**103**

68	GENERATIVE TOPOLOGY OPTIMIZATION FOR METAL ADDITIVE MANUFACTURING	**108**
70	THE EFFECT OF POST PROCESSING ON SURFACE PROPERTIES OF AS-PRINTED AND HEAT TREATED Ti-6Al-4V ALLOY PRODUCED BY ELECTRON BEAM MELTING	**110**
71	HEAT TREATMENT TEMPERATURE-INDUCED MICROSTRUCTURE, MICROHARDNESS AND WEAR RESISTANCE OF INCONEL 718 PRODUCED BY SELECTIVE LASER MELTING	**113**
76	ON THE EFFECT OF UNFIXED PROCESS VARIABLES ON MECHANICAL PROPERTIES IN SELECTIVE LASER MELTING	**116**
77	A PROCESS PLANNING STUDY IN WIRE ARC ADDITIVE MANUFACTURING	**121**
78	MEASURING HAZE, TRANSMITTANCE AND COLOUR OF CLEAR 3D PRINTED STEREOLITHOGRAPHY RESINS	**122**
79	MECHANICAL PROPERTIES OF 3D PRINTED PARTS MADE OF RECYCLED POLYMERS	**126**
80	MAGNETIC DIRECTED ENERGY DEPOSITION: ASSESSMENT FOR MICROGRAVITY	**128**
82	MODELLING TOPOLOGICALLY OPTIMIZED PARTS WITH MICROSTRUCTURES	**133**
83	NUMERICAL STUDY OF HEAT DITURBUTION IN Ti-6Al-4V THIN WALLED CYLINDER DURING ELECTRON BEAM MELTING PROCESS	**137**
84	THERMAL SIMULATION OF POWDER BED FUSION PROCESS USING FINITE ELEMENT METHOD	**142**
85	THE MICROSTRUCTURE AND MECHANICAL PROPERTIES OF POROUS STRUCTURES PRODUCED FROM AlSi10Mg BY DIRECT METAL LASER SINTERING	**147**
87	ORIENTATION AND DYEING EFFECTS ON MECHANICAL STRENGTH OF THE MULTI JET FUSION PRINTED PARTS	**151**
89	EVALUATION OF GEOMETRICAL DEVIATIONS AND POROSITIES ON BOTH CFRP AND AISI 316L STEEL MATERIAL ON ADDITIVE MANUFACTURING	**155**
90	UTILIZATION OF INDUSTRIAL ADDITIVE MANUFACTURING CHALLENGES AND SOLUTIONS	**161**
91	DE-ICING USING ADDITIVELY MANUFACTURED HEATING ELEMENT	**163**

MACHINE LEARNING-BASED INTELLIGENT PATH ANALYZER TECHNOLOGY TO ACHIEVE MAXIMUM YIELD IN METAL ADDITIVE MANUFACTURING

Katharina Eissing[1], Omar Fergani[2,*]
[1] katharina.eissing@siemens.com
[2,*] omar.fergani@siemens.com

Abstract. Although very promising, additive manufacturing is still suffering from a very limited production yield compared to more traditional manufacturing process. Physics based finite element process simulation have demonstrated that the iterations on the digital twin provide an opportunity to reduce the scrap by optimizing the design, the build orientation or the supports. Unfortunately, a large part of failed build is due to issues such as overheating resulting from a sub-optimal vectors distribution and process parameters in the job-file. In this work, we have developed a new simulation technology based on a hybrid approach to detect and correct on the job file level the overheated vectors. This hybrid approach combines a physics-based meso-scale simulation and a machine learning algorithm to simulate the temperature and therefore the overheating at each vector on any layer. Based on this, multiple heuristics are implemented to correct the overheating. This lead to an optimal job file and a substantial improvement on the production yield and massive reduction of defects and recoater collision.

Keywords: machine learning, optimization, job-file, meso-scale, digital twin

1. INTRODUCTION

In metal powder bed fusion, scrap rate represents around 40% and have a substantial impact on the cost and therefore the adoption of additive manufacturing. Multiple software vendors and universities have developed finite element process simulation technology. This technology is aiming at optimizing the build preparation including the support and the part orientation to minimize the distortions. Nonetheless, other challenges leading to scrap are not related to the component level but to a sub-optimal vector and process parameters selection. To the knowledge of the authors no one has solved this problem previously. We introduce a new software technology based on a hybrid-machinery combining both physics based finite element and machine learning to training a model to predict the temperature and the overheating at each point of any vector. This will provide valuable insight on the overheating issues. Subsequently, multiple heuristics are developed to overcome these issue via the so-called corrective strategies.
In this presentation, we first introduce a highlight of the methodology, then demonstrate the capability of this approach to predict overheating. This will be demonstrated via an experiment. Finally, the overheating area will be corrected and validated via another experiment.

2. METHODOLOGY AND EXPERIEMENTS

Based on a defined combination of material and process parameters including the power range, the layer thickness speed and other machine related parameters such as the break time and the laser focus it is possible to define a large meso-scale finite element calculation to generate a large set of training and validation parameters. The generated physics-based data points are fed to a machine learning machinery that trains a model to predict the temperature at each point of a job file. Each vector on any layer is discretized to three points and the temperature is predicted at each point. Figure.1 described the methodology.

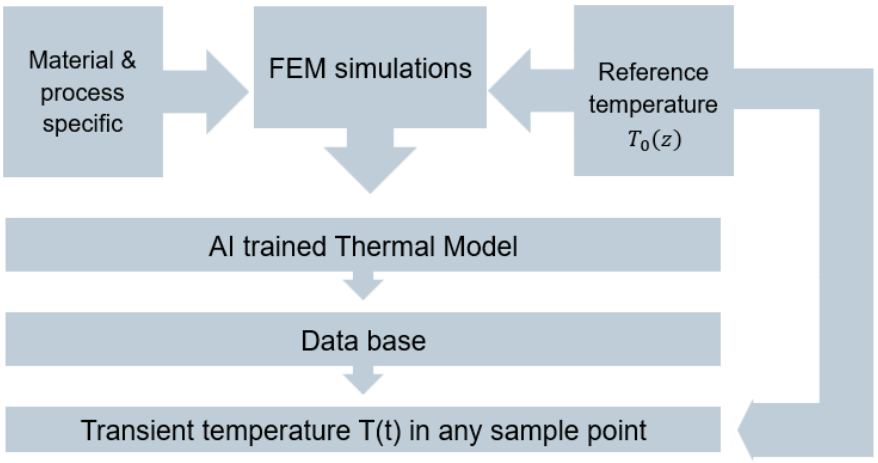

Figure 1. Intelligent path analyzer approach

The basic hypothesis is that the temperature at each is a superposition of the slow and the fast temperature. The slow temperature being the average temperature on a layer. This can be calculated with a standard finite element process simulation technology. The second component is related to specific vector properties including process parameters. Figure.2 described the basic approach from.

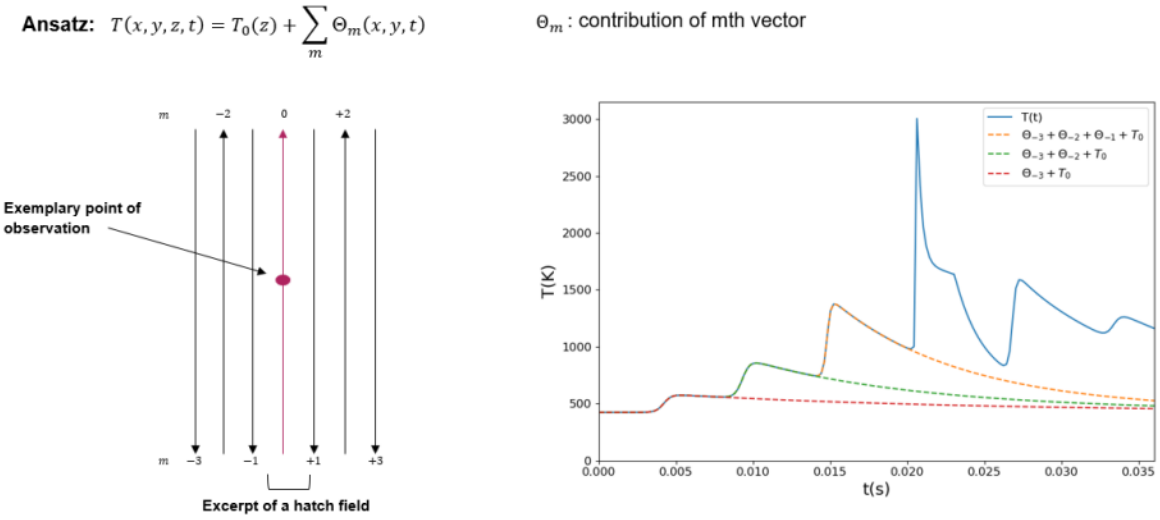

Figure 2. Hypothesis and demonstration

3. RESULTS AND DISCUSSION

This methodology was developed in closed collaboration to major machine builders where the access to the full process parameters was achieved and a validation using both printing and also monitoring was performed to insure the performance.

An elasticity study was performed to understand adaptivity of the method to a range of process parameters and we have included a calibration procedure to achieve the highest prediction fidelity. The calibration procedure requires the printing of a set of simple specimens.

The cost of computation compared to finite element is infinitely fast. On a GPU a complete job file could be simulated in few min to few hours depending on the size of the component.

The results shown in Figure 3 demonstrate the capability of the model to predict accurately the problematic vectors. The implemented corrective strategies also demonstrated the capability to solve the overheating challenges.

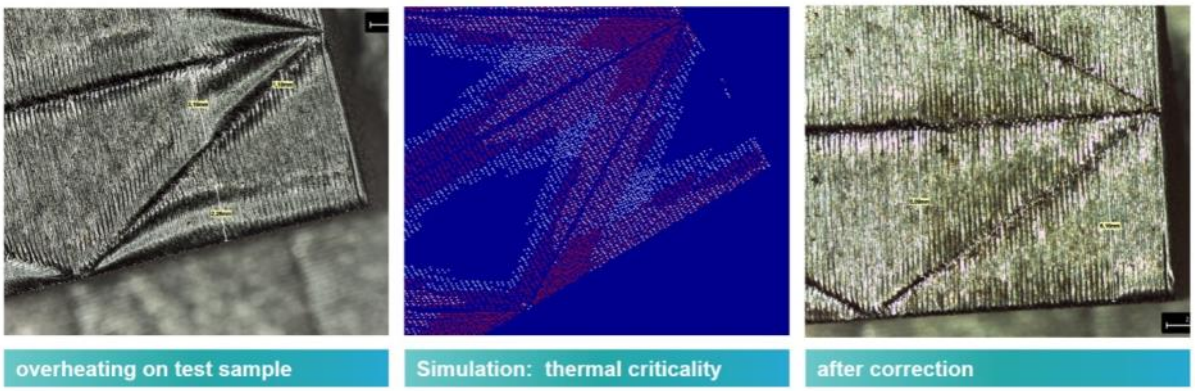

Figure 3. Before and after correction and prediction

4. CONCLUSIONS

Thanks to this new technology, Siemens have developed the most comprehensive digital twin for the additive manufacturing processes. The process iterations can be achieved fully digitally, and the scrap rate is reduced drastically. The next level of technology considers this approach combined with a meltpool monitoring to detect and react in process to the nonsystematic errors.

A FEASIBILITY STUDY ON CMT ADDITIVE MANUFACTURING TECHNIQUE

Banu Berme[1]
[1]*General Electric Marmara Research Center, banu.berme@ge.com*

Abstract. Cold Metal Transfer (CMT) is a popular additive manufacturing technique in repair and new make technologies due to its low thermal input, spatter-free metal transfer, stable arc and fast welding speed characteristics. Since it is an electric arc system, it doesn't require any laser systems resulting in low investment cost.
In this study, new make capability of CMT technique have been investigated. Effect of different variables of CMT such as wire feed speed and travel speed on the depositions have been investigated. Inconel 718 blocks were deposited for tensile test coupons, with different parameters and the formation of linear indications, voids have been observed in some parameter sets. The effect of those microstructural features on mechanical properties have been considered. Tensile tests were conducted at room temperature. Microhardness were measured before and after solution heat treatment and microstructural evaluation is correlated with the mechanical test results. In this study, those characteristic of CMT tehnique will be mentioned

Keywords: Fast welding, spatter-free, tensile test, wire feed, arc.

1. INTRODUCTION

CMT is a new type of short-circuit MIG welding process with lots of advantages compared to MIG welding as shown below [1]:

Low Heat Input: It is characterized by low heat input when compared to the conventional MIG which leads to lower distortion on the part. It improves dimensional stability. It enables the joining of thin sheet materials and dissimilar metals.

Unique wire motion: The motion of the wire is characteristic to CMT. It presents an innovative solution; motion of the electrode directly assisted by digital process control. When the arc plasma is developed the filler wire moves to the weld pool until the wire touches the weld pool and short-circuiting takes place. Then the current becomes lower and the electrode is retracted enhancing the droplet detachment and fusion with the base metal.

Higher gaps and fit-up tolerances

Spatter-free metal transfer: Ensures spatter-free metal transfer by controlling the short circuitting.

Stable arc: The arc length is acquired and adjusted mechanically. So, arc remains stable.

Speed: Welding speed is faster when compared to TIG welding.

Cold Metal Transfer is a preferred additive manufacturing repair technique since it provides controlled metal deposition and low thermal input with high-speed digital control. It is mostly preferred for building/ repair large metallic parts due to its higher deposition rates than powder additive processes. CMT has lower start-up, production, and consumable costs compared to powder-bed and powder-fed systems. There is no concrete temperature limitations for CMT. The process temperature can vary according to the melting point of the alloys, thickness of the part. While the powder processes have the advantage of fine detailed resolution, they are limited by the production rate it takes to produce these fine details.

6 axis robot + 2 axis positioner

Figure 1. CMT System

2. MATERIALS AND METHODS

CMT can be used for repair/ building of large parts. In this study, CMT process maturity is investigated on In718 alloy by the deposition of tensile test blocks. The results are compared to cast In718 mechanical properties. Single layer depositions are followed by multilayer depositions to find the optimum parameter sets.
Deposition studies started with deposition of single layer single row beads. It is followed by deposition of the multilayer, single low depositions.

a) b)

Figure 2. a) single layer b)multi layer deposition

In this study, 12 different parameter sets were tried. Each tensile test block consist of 100 layers and subjected to solution and aging heating heat treatment per AMS 5383E. Tensile tests were conducted in both X- and Z-directions. Hardness measurements were followed by microstructural investigations.

3. RESULTS AND DISCUSSION

The microstructural investigation reveals the precipitate chain formation at the center of the mechanical test blocks due to the high temperature gradients and rapid solidification rate, Figure 3. Those precipitates give the Possibility of Laves phase or other niobium precipitates (carbides) due to Cr, Nb, Mo found in SEM analysis and our high working temperature [2]. The presence of Niobium not only lowers the melting point constitutionally, but also forms low-melting precipitates during solidification. During deposition process, the bottom layers exposed to high temperatures at which those low melting point Nb-precipitates melt and form voids, incipient melting. High amount of Nb and Ti also indicates to MC and M6C type carbides.

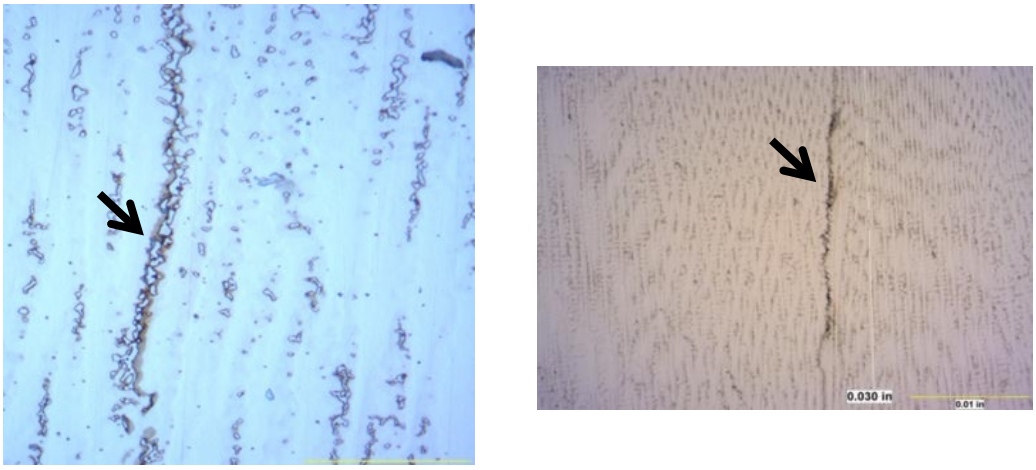

a) b)

Figure 3. a) Precipitate chains in the matrix b) void formation

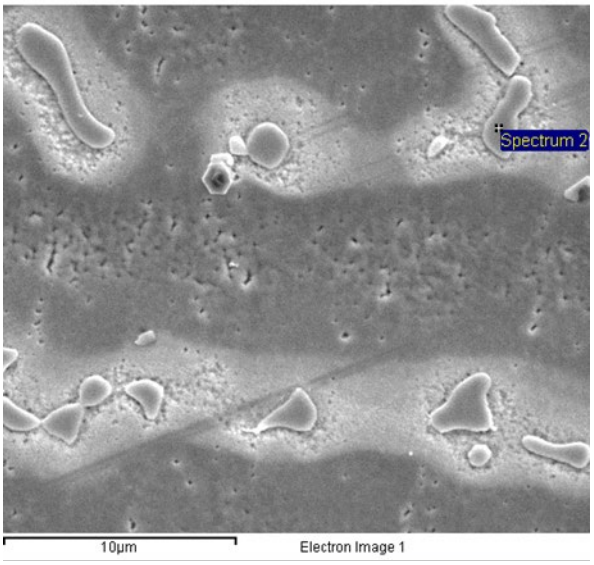

Element	Weight%
Al K	0.20
Ti K	1.04
Cr K	13.76
Fe K	12.89
Ni K	37.10
Nb L	35.01
Totals	100.00

Figure 4. SEM Analysis

Tensile test results showed that in Z direction, higher strength values could be obtained. All UTS values are between average and minimum values according to In718 cast curves. In case of YS, values in Z direction are within limits, while yield strength of X direction are mostly under mimimum limit.

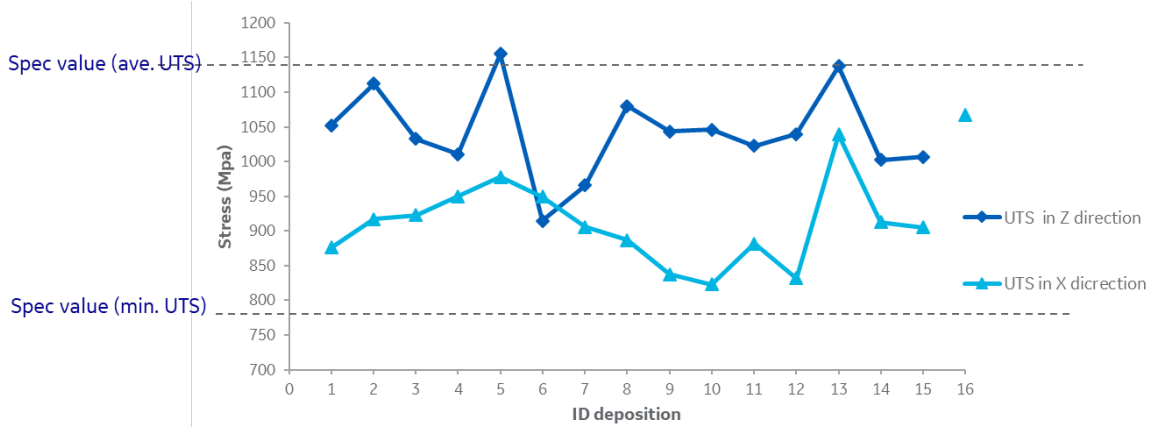

Figure 5. UTS results of the test blocks

4. CONCLUSIONS

The promising results of this study enables us to use CMT for new-make and repair processes of large components with some more improvements in the microstructure. UTS values are higher in Z direction than in X direction due to columnar grain structures and void chains. Values in both directions are above the min spec value and can be developed by better deposition, fixturing and heat treatment parameter. YS values are higher in Z direction than in X direction. However, yield properties are required to be develop by working on equiaxed grain formation by solidification rate during the process and further heat treatments. Equiaxed grain formation will increase the grain boundary amount in the microstructure and increase the strength of the part. Incipient melting was the problem to be solved to avoid void formation. Special fixture design can be planned to reduce the thermal gradients in the depositions.

REFERENCES

1. Williamson, J. ‘New Technologies Robotic GMAW’, Fronius USA LLC.
2. Dupont J.N., Lippold J. C., Samuel D.K., ‘Welding Metallurgy And Weldability of Nickel-Base Alloys.

WEIBULL DISTRIBUTION OF SELECTIVE LASER MELTED ALSI10MG PARTS FOR COMPRESSION TESTING

Hamaid M. Khan [1], M.H. Dirikolu[2], Ebubekir E. Koç[3]

[1]*Department of Mechanical Engineering, Faculty of Engineering, Istanbul University-Cerrahpaşa, 34320 Avcilar-Istanbul, Turkey, hamaid.khan@gmail.com*

[2]*Department of Mechanical Engineering, Faculty of Engineering, Istanbul University-Cerrahpaşa, 34320 Avcilar-Istanbul, Turkey, dirikolumh@istanbul.edu.tr*

[3]*Aluminum Test, Training and Research Centre, Fatih Sultan Mehmet Vakif University, Beyoğlu-Istanbul, Turkey, ekoc@fsm.edu.tr*

Abstract. The compressive strength values of selective laser melted 22 samples of AlSi10Mg were examined statistically using the Weibull distribution function at a standard processing parameter supplied by EOS. The measured strength was found to vary between 321 MPa to 382 MPa and 665 MPa to 883 MPa for compressive yield strength and compressive strength respectively.

Keywords: selective laser melting, Weibull distribution, compression testing, linear regression method, AlSi10Mg

1. INTRODUCTION

Selective Laser Melting (SLM) is a powder based variant of an Additive Manufacturing (AM) process where several tiny layers of packed powders are fused together using a guided laser to produce a solid structure. So far, a significant amount of research has been reported both numerically (Khan, Dirikolu, Koç, & Oter, 2018; Khan, Dirikolu, & Koç, 2018) and experimentally (Koc, Akca, Oter, & Coskun, 2016; Kruth, Mercelis, Van Vaerenbergh, Froyen, & Rombouts, 2005) on various aspects of AM process related to microstructure, mechanical strength, and corrosion. However, in spite of having identical processing parameters, no two samples in SLM can be claimed to have the same physical property. This is due to the processing location, environment, or orientation of parts with respect to the powder spreader (Drummer, Drexler, & Kühnlein, 2012; Olakanmi, Cochrane, & Dalgarno, 2015). Therefore, no specific strength value is applicable to identify the true mechanical behavior of the SLMed parts. A statistical analysis, on the other hand, is a viable tool to achieve the design objectives within safe parameters. Weibull distribution is based on a continuous probability distribution function to mathematically measure the probability of occurrence of different outcomes in an experiment (Birgoren & Dirikolu, 2004; Brandl, Heckenberger, Holzinger, & Buchbinder, 2012; Quercia, Chan, & Luke, 2016). It is often used in reliability and industrial engineering and failure analysis to improve the estimation approach. Several works have been reported in the determination of mechanical properties for composite materials. In AM, E. Brandl et al. (Brandl et al., 2012) used Weibull distribution to interpolate Wohler curves to investigate the fatigue strength in post heat treated samples built in different directions. In the present study, 25 cubical samples of the AlSi10Mg alloy were fabricated by the SLM process using standard EOS processing parameters. The variation in the compressive stress values of all the samples was then modeled using Weibull distribution and the results were presented in the graphical forms.

2. MATERIALS AND METHODS

The specimen in the experiment was prepared from AlSi10Mg alloys in the SLM machine, EOS M290 GmbH. A cubical sample of size 5x5x5 mm^3 was chosen for analysis and the standard processing parameter from EOS was applied in the fabrication of all 22 samples (Fig 1). The scanning parameters are presented in Table 1. The compression testing was carried out as per the ASTM E 8M-04 standard on an Instron 5982 dual column testing system with a 100 kN loading capacity.

Table 1. Processing parameters and physical values of AlSi10Mg used in the analysis.

Properties	*Values*
Laser Power	370 W
Scanning Rate	1300 mm/s
Hatching	190 µm
Layer Thickness	30 µm
Spot Size Diameter	100 µm
Scanning Strategy	Alternate, 67^0

The downward speed of 0.5mm/min was used amid room conditions during the compression tests. Table 2 lists down the compressive yield stress (0.2% offset) values for all the samples.

Fig 1. Additively manufactured 22 samples of AlSi10Mg.

Table 2. Measured compressive yield stress and strength.

S. No:	Compressive Yield Stress (MPa)	Compressive Strength (MPa)	Dimension (mm^2) (L x W)	Area (mm^2)
1	329.89	585.06	5.11 x 5.14	26.27
2	353.02	585.69	5.10 x 5.11	26.06
3	321.03	561.83	5.09 x 5.08	25.86
4	382.59	571.90	5.12 x 5.11	26.16
5	337.52	578.68	5.11 x 5.11	26.11
6	344.01	579.87	5.11 x 5.09	26.01
7	342.98	586.90	5.11 x 5.11	26.11
8	359.96	566.04	5.16 x 5.11	26.37
9	337.67	579.67	5.12 x 5.10	26.11
10	368.35	588.66	5.12 x 5.11	26.16
11	364.12	598.93	5.11 x 5.10	26.06
12	361.77	618.11	5.09 x 5.08	25.86
13	356.18	594.29	5.09 x 5.09	26.11
14	349.61	592.75	5.11 x 5.11	25.91
15	335.77	590.89	5.12 x 5.11	26.11
16	344.34	574.45	5.11 x 5.12	26.16
17	354.14	573.43	5.12 x 5.12	26.16
18	340.27	582.35	5.15 x 5.12	26.21
19	341.72	592.90	5.12 x 5.09	26.37
20	338.02	592.65	5.14 x 5.12	26.06
21	370.92	593.38	5.12 x 5.11	26.32
22	343.79	592.50	5.11 x 5.11	26.16

3. RESULTS AND DISCUSSION (HEADING 1, 11 Font Size, bold, all caps)

3.1. Weibull distribution

Weibull distribution is used to measure the characteristic compression stress values of SLM processed samples. Out of the two popular forms, the three-parameter Weibull distribution is given by (Weihull, 1951);

$$F(x;\alpha,\beta,\gamma) = 1 - \exp\left(-(\frac{x-\alpha}{\beta})^{\gamma}\right), \quad 1$$

$$\alpha,\beta,\gamma \geq 0,$$

Where, $\alpha,\beta,$ and γ are location, scale, and shape parameters respectively. If α=0, the three-parameter transforms into two-parameter Weibull distribution function;

$$F(x;\beta,\gamma) = 1 - \exp\left(-(\frac{x}{\beta})^{\gamma}\right), \quad 2$$

$$\beta,\gamma \geq 0,$$

The probability function $F(x;\beta,\gamma)$ represents that compressive strength is equal to or less than the value x. There is another term reliability $R(x;\beta,\gamma)$ that can be inferred from the equality $F(x;\beta,\gamma) + R(x;\beta,\gamma) = 1$. Here, $R(x;\beta,\gamma)$ represents the probability of compressive strength is at least equal to x.

$$R(x;\beta,\gamma) = \exp\left(-(\frac{x}{\beta})^{\gamma}\right), \quad 3$$

$$\beta,\gamma \geq 0,$$

To evaluate the scale β, and shape γ parameters of the distribution function $F(x;\beta,\gamma)$, a method of linear regression is applied where a straight line is fitted using MS Excel™ software.

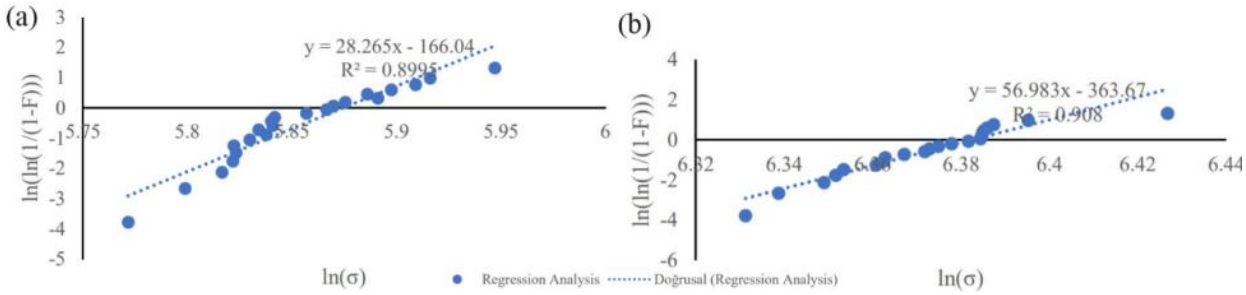

Fig 2. The regression line for (a) compressive yield stress, and (b) compressive strength.

3.2. Linear regression method

Using double logarithm, equation $F(x;\beta,\gamma) = 1 - \exp\left(-\left(\frac{x}{\beta}\right)^{\gamma}\right)$ is transformed into a straight-line form for easy evaluation.

$$\ln\left[\ln\left(\frac{1}{1-F(x;\beta,\gamma)}\right)\right] = \gamma\ln(x) - \gamma\ln(\beta), \quad 4$$

Equation 4 resembles a straight line $Y = mX + c$. The function $F(x;\beta,\gamma)$ can be estimated from the observed compression values ordered in an increasing sequence. The function $F(x;\beta,\gamma)$ is determined as;

$$F(x_i;\beta,\gamma) = (x_i - 0.5)/n, \quad 5$$

Where $n = 22$ is the total number of samples. The values $\mathrm{Y} = \ln\left[\ln\left(\frac{1}{1-F(x;\beta,\gamma)}\right)\right]$ and $X = \ln(x)$ are plotted for linear regression to estimate the parameters β and γ as shown in Fig 2. The equation thus obtained is;

$$Y = 28.265X - 166.04, \quad 6$$

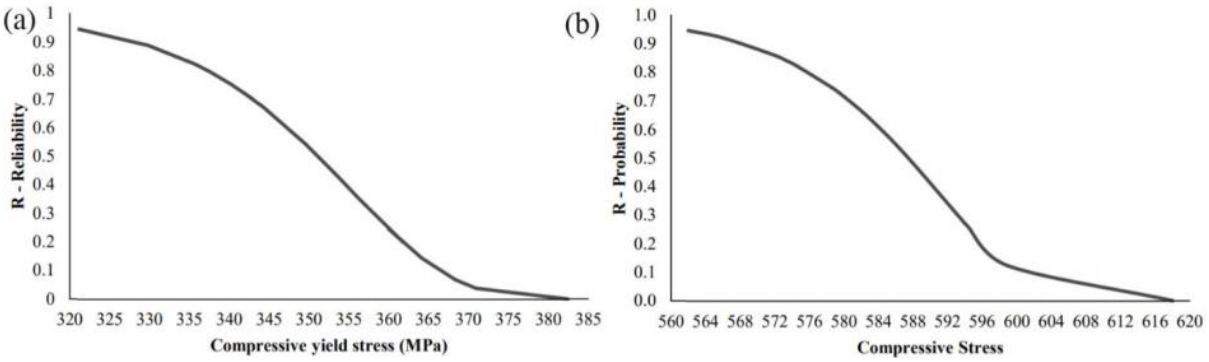

Fig 3. Weibull reliability distribution for (a) yield stress and (b) compressive strength.

Here, $m = \gamma = 28.265$ is the slope of the regression line. The shape parameter $\gamma > 0$, specifies an increasing failure rate due to compressive loading. Larger γ signifies the higher possibility of a material fracture for every unit increase in compression values. Parameter β measures the distribution scale of the data and it can be obtained from equations 4 and 6 and this founds $\beta = 355.73$ MPa. The reliability $R(x; \beta, \gamma)$ for compression stress, $x = 355.73$MPa was measured 0.3545, which is 35.45% of the tested samples have the compressive yield strength at least 355.73 MPa. A plot of $R(x; \beta, \gamma)$ is shown in Fig 4. The plot shows that 90% of the component with a compressive yield strength of about 328.08 MPa will not yield under compression loading. Table 3 lists the other important values corresponding to yield and compressive strength.

Table 3. Reliability distributions corresponding to various stress values for both compressive yield stress and compressive strength.

Parameters		Compressive yield strength		Compressive strength	
Equation		$y = 28.265x - 166.04$		$y = 17.024x - 113.71$	
$m = \gamma$		28.265		17.024	
β		355.73		795.65	
$R(x; \beta, \gamma)$		355.73	35.45%	591.20	36.74%
Lower limit, R	@x	321.03	94.65%	561.83	94.66%
Upper limit, R		382.5	0.04%	618.11	~0.00%
R = 90%		328.08 MPa		569.07 MPa	

4. CONCLUSIONS

AlSi10Mg is one of the most tested alloys in the SLM process and it is extensively used in the production of several components in automobiles, aircraft, and other industrial sectors. Weibull distribution was used here to measure the compressive yield strength and compressive strength of the tested 22 specimens of AlSi10Mg to obtain the reliability of the processed parts to withstand the variable compression loading. In the present case, the compressive yield strength and the compressive strength of the tested specimens with 90% reliability were found to be 328.08 MPa and 569.07 MPa respectively.

REFERENCES

Birgoren, B., & Dirikolu, M. H. (2004). A computer simulation for estimating lower bound fracture strength of composites using Weibull distribution. Composites Part B: Engineering, 35(3), 263–266. https://doi.org/10.1016/j.compositesb.2003.11.002

Brandl, E., Heckenberger, U., Holzinger, V., & Buchbinder, D. (2012). Additive manufactured AlSi10Mg samples using Selective Laser Melting (SLM): Microstructure, high cycle fatigue, and fracture behavior. Materials & Design, 34, 159–169.

Drummer, D., Drexler, M., & Kühnlein, F. (2012). Effects on the Density Distribution of SLS-Parts. Physics Procedia, 39, 500–508. https://doi.org/10.1016/j.phpro.2012.10.066

Khan, H. M., Dirikolu, M. H. H., Koç, E., & Oter, Z. C. C. (2018). Numerical investigation of heat

current study across different platforms in SLM processed multi-layer AlSi10Mg. Optik, 170(May), 82–89. https://doi.org/10.1016/j.ijleo.2018.05.081

Khan, H. M., Dirikolu, M. H., & Koç, E. (2018). Parameters optimization for horizontally built circular profiles: Numerical and experimental investigation. Optik, 174(August), 521–529. https://doi.org/10.1016/j.ijleo.2018.08.095

Koc, E., Akca, Y., Oter, Z. C., & Coskun, M. (2016). SELECTIVE LASER SINTERING OF ALUMINUM EXTRUSION DIES. (12).

Kruth, J.-P., Mercelis, P., Van Vaerenbergh, J., Froyen, L., & Rombouts, M. (2005). Binding mechanisms in selective laser sintering and selective laser melting. Rapid Prototyping Journal, 11(1), 26–36.

Olakanmi, E. O., Cochrane, R. F., & Dalgarno, K. W. (2015). A review on selective laser sintering/melting (SLS/SLM) of aluminum alloy powders: Processing, microstructure, and properties. Progress in Materials Science, 74, 401–477. https://doi.org/10.1016/j.pmatsci.2015.03.002

Quercia, G., Chan, D., & Luke, K. (2016). Weibull statistics applied to tensile testing for oil well cement compositions. Journal of Petroleum Science and Engineering, 146, 536–544. https://doi.org/10.1016/j.petrol.2016.07.012

Weibull, W. (1951). A statistical distribution function of wide applicability. J Appl Mech, 18, 290–293.

ADDITIVE MANUFACTURING OF CONTINOUSLY ALIGNED CARBON FIBRE STRUCTURES

Busra Karas, Patrick Fairclough, Kamran Mumtaz[1]
[1]*Department of Mechanical Engineering, The University of Sheffield, Sheffield, UK, bkaras1@sheffield.ac.uk*

Abstract. Additive Manufacturing (AM) uses a layer-by-layer building approach to create 3D components from sliced 3D CAD data. In recent years using AM to create directionally aligned composite materials has shown promise for the creation of lightweight high-performance parts. In this study, an AM process has been developed to create composite samples from directionally aligned carbon fibre sheets. A liquid binder prints onto a carbon fibre mesh, a thermoplastic powder is deposited, attaching to the binder printed areas. The process is repeated layer-by-layer with additional carbon fibre sheets until the last slice of the part is completed. The carbon fibre sheets, with thermoplastic binder are stacked together and processed using a hot press technique to the melt thermoplastic binder. Lastly, excess region of substrate layers is removed by using a sand blasting process. The influence of fibre type and hot press time on structural and mechanical properties of parts are investigated. The preliminary results show that tensile strength of the part is improved by using a combination of finer mesh size of the fibre and longer time on the hot press machine.

Keywords: Additive manufacturing, Robocasting, Composites, Carbon fibre, Thermoplastic powder

1. INTRODUCTION

Composite materials can be used to create high performance, lightweight structures, being widely used in industries such as aerospace and automotive. By combining two, or more multiple materials to produce a composite, unique mechanical properties that are superior can be achieved (Mallick, 1946). A fibre reinforced composite consists of fibres bonded to a matrix with interphases. Polymer, metal or ceramic can be used as a matrix material (Jang, 1994). Carbon fibre reinforced polymer (CFRP) composite consist of carbon fibre reinforcements and polymer matrix, which offers lightweight engineering solutions. It becomes possible to manufacture CFRP composite parts in a cost and time effective way. Additive manufacturing (AM) of composite materials has several advantages over conventional manufacturing techniques using singular materials, this includes high levels geometric customization, additional strength from fibre reinforcement, and ability to manufacture functional complex geometries with control over specific material properties (Hegab, 2016). There are commercially available systems for AM of composite materials. Many researchers have been investigating the effect of process parameters on the final composite part, as well as developing new types of composite filaments using fused deposition methodologies. Although few academic studies have been carried out in order to analyse the feasibility of the systems use fused deposition modelling like Markforged, less attention has been paid to the other systems that allow more fibre to be inserted like Composite Based Additive Manufacturing (CBAM) by Impossible Objects. This study will focus on developing a new additive manufacturing system based on CBAM process for long fibre reinforced composites.

2. MATERIALS AND METHODS

2.1. Specification of Equipment and Materials

The experimental rig consists of a Fisnar I&J 7400-LF programmable 3-axis robot. The software of RoboEdit and the I&J 7400-LF teach pendant is used to program and control the robotic arm. A Preeflow eco-PEN700 motorised precision dispenser connected with Fisnar robot provides the transfer of the ink with desired extrusion parameters. The feedstock of the manufacturing process includes deionized water as an ink, dry fabric and thermoplastic powder (PA2200). Twill weave carbon fibre sheets with 200 grams per square meter (gsm) and plain carbon fibre sheets with 90 gsm have been used to see the variance between different mesh sizes. Nylon powder (PA2200) as a thermoplastic matrix material was preferred as it has a melting point of 180° C, which is suitable for hot press process. For

post processing activities, hydraulic hot press machine has been used to melt the nylon powder and compress the stacked layers together. Sand blasting machine was used to remove the excess material around the part. Specimens were cut by tie saw and water jetting machine to have desirable sizes for tensile testing and micro CT scanning to characterize the parts.

2.2. Manufacturing Process

Carbon fibre sheets are placed into the Fisnar Robot which is programmed to move as the shape of the part. A layer of the geometry is printed on fibre sheet with deionized water. Nylon powder is deposited onto the printed sheets, this subsequently sticks to printed areas. These steps are repeated until final layer. Hot press machine is used to heat to melting temperature of polymer and compress stack to final part height. After removal of un-bonded portions of sheet fibres with sand blasting machine, the final part can be obtained.

3. RESULTS AND DISCUSSION

Two sets of experiments were performed with different types the carbon fibre sheets and hot press time. 10 layers of fibre substrate were used for each part. Parameters such as flow rate, printing speed and hot press temperature remained constant at 5.3 ml/min, 10 mm/s and 180 °C accordingly. Tensile tests were performed utilising a Tinius Olsen H5KS force tester. ASTM D3039 standards were followed by using crosshead speed of 2 mm/minute. The average of tensile strength and young's modulus of 5 specimens in each experiment are shown in Figure 1. The results indicate that the combination of using plain weave carbon fibre fabric and longer exposure time to hot press process improves tensile strength and elastic modulus of the parts.

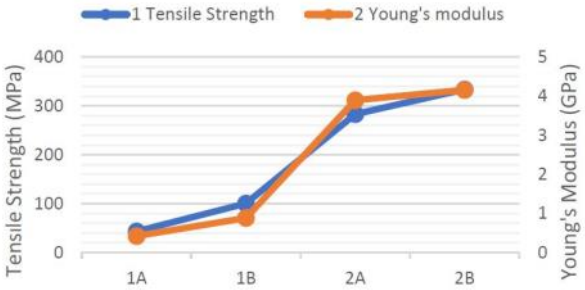

Figure 1. Comparison of tensile strength and elastic modulus of the parts (1: twill weave, 2: plain weave, A: 1-hour hot press, B: 3 hours hot press)

4. CONCLUSION

Continuous carbon fibre reinforced nylon composites were fabricated by robocasting methodology based on CBAM. Main factors that can affect the results which are the type of the carbon fibre fabric and the time period of hot press process, are investigated. In initial experiments, it was found that tensile strength of the parts with finer mesh size and that stayed longer in hot press machine is higher than the that of other parts. When it is compared with FDM methods for composites, this AM process is promising to produce strong, complex shaped composite parts with wide range of material options.

REFERENCES

Hegab, H. A. (2016). Design for additive manufacturing of composite materials and potential alloys: a review. *Manufacturing Review*. https://doi.org/10.1051/mfreview/2016010

Jang, B. (1994). *Advanced Polymer Composites Principles and Applications*. ASM International.

Mallick, P. K. (1946). *Fiber-Reinforced Composites, CRC Press, 1946.* CRC Press.

SELECTIVE LASER MELTING PROCESS DEVELOPMENT FOR ENHANCED PRODUCTIVITY WITH PH17-4 STAINLESS STEEL

Evren Yasa[1], İlker Atik[2], İpek Bayraktar[3]
[1]*Eskişehir Osmangazi University, eyasa@ogu.edu.tr*
[2]*TÜBİTAK SAGE, ilker.atik@tubitak.gov.tr*
[3]*TÜBİTAK SAGE, ipek.bayraktar@tubitak.gov.tr*

Abstract. Selective Laser Melting (SLM) is an additive manufacturing (AM) process whereby three-dimensional complex geometries can be manufactured in a layerwise manner. SLM has spiked in many industries seeking good mechanical properties, better surface finish and higher precision in comparison to other AM processes for metallic materials. However, these properties highly depend on process parameters such as laser power, scan speed, scan strategy, layer thickness, etc. One of the challenges in adopting SLM for fully functional parts is the high number of process parameters and their interactions which can easily exceed hundreds. Most often, the optimization of these parameters is experimentally done by defining a plan which specifies the number of factors, their levels and outputs. The machine vendors generally supply starting process parameter sets although these may be far from being optimized for multiple criteria. They are generally optimized for maximum density and good mechanical properties. However, surface quality, productivity and residual stresses are other important output properties that need to be considered in process parameter development. Thus, this experimental study aims at obtaining the process parameters for Ph17-4 stainless steel for increased productivity without sacrificing the density and surface quality where laser power, scan speed, layer thickness and scan spacing were taken as the main input parameters.

Keywords: Selective Laser Melting, process development, Ph17-4 Stainless Steel, productivity

1. INTRODUCTION

Selective Laser Melting (SLM) is one of the very advantageous AM processes for metallic materials in comparison to subtractive manufacturing due to the low amount of waste material, reduced lead time from design to testing, ability to create highly complex geometries including internal features, reduced need for joining processes leading to improved part life, etc. SLM has recently been increasingly adopted for manufacturing functional end-parts in diverse industries such as aerospace, defense, biomedical and others. However, to explore the full potential of SLM, some barriers still need to be overcome. One of the important limitations is the high number of process parameters that affect the part performance. These parameters do not only have direct influence on the outputs but also their interactions due to the physical phenomena occurring during the SLM process play a significant role. Although the machine vendors provide a starting set of process parameters for each material, these may be far from optimum when multiple criteria are taken into account. Generally, the given process parameters are optimized taking density into consideration since mechanical properties severely deteriorate in case of porosity at inacceptable levels. However, due to inherent nature of the SLM process, other criteria become dominant on the part performance as well. For example, due to the high cooling rates encountered in the process, residual stresses leading to part deformations or even cracks during the process become one of the problems. Moreover, especially for internal features, it is generally difficult to improve the surface quality by conventional processes. Without reaching the desired levels of surface roughness, the advantage of being able to create very complex geometries stay limited. Thus, as-built surface roughness is also critical. Moreover, productivity, as one of the bottlenecks of SLM, needs to be taken into account. Thus, this study aims to enhance the productivity rate of SLM with an experimental approach while taking the density, mechanical properties and surface quality into account for PH17-4 stainless steel starting from the standard process parameters for the given layer thickness of 30 µm.

2. MATERIALS AND METHODS

In this study, the aim is to improve the build rate for PH17-4 stainless steel in the SLM process without sacrificing the density starting from the standard process parameters for the given layer thickness of 30 µm by the machine vendor while taking surface quality also into account. Thus, cubic specimens of having dimensions of 15x15x15 mm were built under nitrogen as protective atmosphere on an SLM Solutions SLM 280 machine. The most influential parameter on the productivity is the layer thickness due to its direct effect on the total scanning and powder coating duration. Provided that the layer thickness is doubled, the total duration is halved in case the other parameters are kept constant. Thus, the layer thickness was kept constant at 60 µm while the studied parameters were the laser power (200-275-350 W), scan speed (600-800-1000-1200 mm/s) and scan spacing (0.09-0.12-0.15 mm) with a full factorial test strategy. After the production was complete, the specimens' densities were measured by the Archimedes' method while the surface quality was assessed by the surface profilometer. Moreover, hardness measurements and microstructural investigations were carried out.

3. RESULTS AND DISCUSSION

After specimens were built with 36 different sets of parameters, the density and surface quality were first evaluated. Density and roughness values were evaluated in process windows. An example is shown in Figure 1 for the laser power and scan speed. As depicted here, higher laser powers in combination with low scan speeds give desired levels of densities above 99.4% whereas the lowest surface roughness values are obtained when the scan speed is high and laser power is set to low-medium levels. The dependency of the relation between the scan speed and the density on the other parameters (laser power and scan spacing) is shown in Figure 2. For 200 W of laser power and 150 µm of scan spacing, the relationship is almost inversely linear. However, at lower scan spacing values where overlap between successive tracks is sufficient for full melting, the density's dependency on the scan speed almost vanishes. A very small portion of the findings is presented here due to page limit. Yet, the full study reports relations of many process parameters to performance criteria taking productivity into account and draws concrete results as well as the enhanced process parameter sets for enhanced build rate.

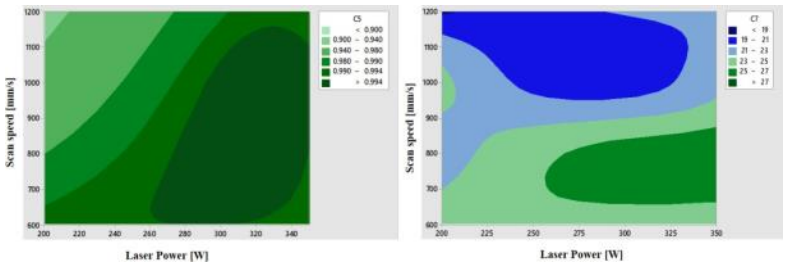

Figure 1. Process windows including scan speed and laser power for (a) density (b) R_a on top surfaces

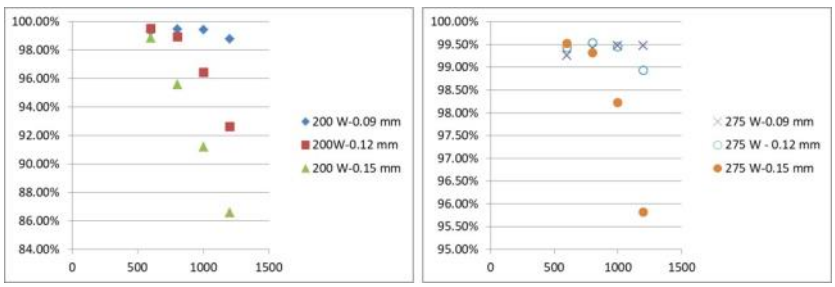

Figure 2. Density results (x-axis scan speed; y-axis relative density)

4. CONCLUSIONS

For optimizing the process parameters for a single material, density cannot be taken as the sole parameter since the process parameters also have a significant effect on production rate and surface quality. The process parameters giving highest density (medium laser power, low scan speed and low scan spacing) conflict for the best surface quality (low laser power, high scan speed and medium scan spacing). The same holds true for the build rate which depends on the scan speed and scan spacing. Thus, this study concludes that for process parameter studies, single-factor experiments are not sufficient to explore the whole relations. Moreover, it is also shown that the build rate can be almost tripled without sacrificing density if multi-criteria process development is applied.

REFERENCES

The full list of references with a detailed literature survey will be presented at the conference due to the page limit of the extended abstract.

INFLUENCE OF PROCESSING PARAMETERS ON SURFACE PROPERTIES OF SELECTIVE LASER MELTED Ti-6Al-4V PARTS

Idris Tugrul Gulenc[1], Iain Todd [2], Beverley J Inkson [3]
[1,2,3] *Department of Materials Science and Engineering, University of Sheffield, Sheffield, UK,*
[1]*ittgulenc1@sheffield.ac.uk,* [2]*iain.todd@sheffield.ac.uk*
[3]*beverley.inkson@sheffield.ac.uk*

Abstract. The effect of different processing parameters on top surface roughness and tribological performance of selective laser melting (SLM) processed Ti-6Al-4V samples is assessed in this study. Two different upskin processing parameters have been applied to the top surfaces of samples, and dry reciprocating wear tests are performed. The surfaces are characterised before and after wear tests using optical profilometry and scanning electron microscopy. The results demonstrate that upskin roughness, friction and wear of samples depend on laser scanning parameters including hatch distance between individual laser lines and volume scanning parameters of the underlying core. Therefore, both volume and upskin scanning parameters should be considered together to achieve optimum as-fabricated surface quality.

Keywords: Selective laser melting, SLM, Ti-6Al-4V, optical profilometry, tribology

1. INTRODUCTION

Additive manufacturing (AM) promises the manufacturing of near-net-shape products directly from CAD data. One of the main problems to meet this 'one-step processing' promise is surface properties. Currently, the majority of AM parts require post-machining to acquire acceptable surfaces. The morphology, microstructure and mechanical properties of a Selective Laser Melting (SLM) surface, specifically the downskin (first layer), core (sequential layers) and upskin (top surface layer), are dependant on laser melting parameters (Calignano, Manfredi, Ambrosio, Iuliano, & Fino, 2013). For direct manufacture, the surface quality needs to be improved for acceptable mechanical, tribological and aesthetic performance. Here cubes of Ti-6Al-4V have been fabricated by SLM, and the effect of using different upskin laser processing parameters has been investigated. The morphology and tribology of the upskin surface have been characterised using optical profilometry, SEM and reciprocating wear tests.

2. MATERIALS AND METHODS

Pre-alloyed Ti-6Al-4V ELI powders supplied by Renishaw plc with the particle size range of 15-45µm was used for SLM fabrication using a Renishaw AM125 with 120x120x125mm build chamber and a 200W pulsed fibre laser. Cubes of size 10x10x10mm were manufactured using the same volume parameters but different upskin scanning parameters (*Table 1*). Linear energy density and volumetric energy density were calculated according to previously defined formulations for pulsed lasers (Harrison, Todd, & Mumtaz, 2015). Samples were removed from the base plate by wire erosion. Cut samples were cleaned in an ultrasonic bath, and the top surfaces were characterised using scanning electron microscopy (SEM) and optical profilometry. Dry reciprocating wear tests in a direction parallel to the hatching directions were performed on the cube top surfaces using a 4mm Al_2O_3 ball, 4mm stroke length, 1N load and 1Hz frequency.

3. RESULTS AND DISCUSSION

Figure 1 shows optical profilometry of the top surfaces of the Ti-6Al-4V samples processed with upskin parameters A and B. The average roughness (Ra) is measured as 4.28µm and 4.17µm for sample A and B, respectively. However it is seen that that surface roughness comprises a number of components at different length-scales. Laser scanning parameters affect the roughness on one single laser scan while hatch distance is more dominant in the direction perpendicular to the hatches. Additionally, there is

another slowly modulating irregular roughness, which is thought to occur because of accretion of irregularities in the underlying volume scanning parameters.

Table 3. Upskin processing parameters

	Volumetric Energy Density (J/mm^3)	Linear Energy Density (J/mm)	Power (J/s)	Hatch Spacing (µm)	Layer Thickness (µm)	Point Distance (µm)	Exposure Time (µs)
A	476	0.57	200	40	30	70	200
B	120	0.34	200	95	30	70	120

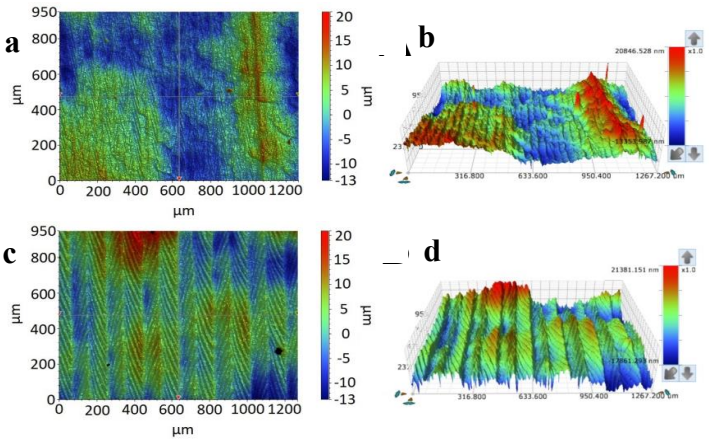

Figure 1. Top surface optical profilometry images of samples processed using (a,b) A and (c,d) B upskin parameters

The coefficient of friction (COF) increases from 0.38 to 0.56 for sample A and from 0.41 to 0.58 for sample B during the wear test. This result may be explained by the fact that asperities on the surface will limit the initial wear contact areas, but they are worn away during tests. Increased contact area from both asperity wear and tribofilm generation will potentially cause higher friction between surfaces. Increasing contact area has been reported as causing increased friction between surfaces (Ibatan, Uddin, & Chowdhury, 2015).

4. CONCLUSIONS

Surface morphology of Ti-6Al-4V selective laser melting parts is dependent both on the finishing upskin conditions and inherited roughness from the underlying core. Roughness on the upskin has different scales originated from volume scanning, laser scanning and hatch distance. Inhomogeneous SLM Surface roughness will affect the initial stages of tribological wear. Significant roughness on the upskin surface reduces the COF in initial stages of surface wear. Both the volume and upskin processing parameters must be optimised for the desired surface texture of SLM parts.

REFERENCES

Calignano, F., Manfredi, D., Ambrosio, E. P., Iuliano, L., & Fino, P. (2013). Influence of process parameters on surface roughness of aluminum parts produced by DMLS. *International Journal of Advanced Manufacturing Technology*, *67*(9–12), 2743–2751. https://doi.org/10.1007/s00170-012-4688-9

Harrison, N. J., Todd, I., & Mumtaz, K. (2015). Reduction of micro-cracking in nickel superalloys processed by Selective Laser Melting: A fundamental alloy design approach. *Acta Materialia*, *94*, 59–68. https://doi.org/10.1016/J.ACTAMAT.2015.04.035

Ibatan, T., Uddin, M. S., & Chowdhury, M. A. K. (2015). Recent development on surface texturing in enhancing tribological performance of bearing sliders. *Surface and Coatings Technology*, *272*, 102–120. https://doi.org/10.1016/j.surfcoat.2015.04.017

IMPROVEMENT MECHANICAL AND BIOLOGICAL PROPERTIES OF CoCr SCAFFOLDS FABRICATED BY SELECTIVE LASER MELTING

Emre Özeren[1] and Mirigül Altan[2*]
[1,2]*Yildiz Technical University, Department of Mechanical Engineering, Besiktas, Istanbul,34349*
[1]*emreozeren07@gmail.com,* [2*]*meksi@yildiz.edu.tr*

Abstract. Fabrication of scaffolds for biomedical applications by Selective Laser Melting (SLM) has gained wide application area due to its flexibility and accuracy in design and easy reproductions. However, the desired properties of the scaffold can change according to the patient's demand. Therefore, the step of designing of the scaffold should be considered seriously before fabrication. In this study, the properties of CoCr based scaffolds were improved by application of different structural hybrid designs within constant porosity ratio and strut diameter. The hybrid designs of scaffolds were composed of dodecahedron (DCH), grid (G), octet-truss (OCT) unit cells. In the experimental study, compression test and cell viability test were applied in order to observe the improvement of the properties of the scaffolds. It has been seen that scaffold with grid unit cell gave the highest compressive strength,65 MPa, but lowest cell viability, 54%. On the other hand, combination of all the unit cells gave 106% of cell viability and showed satisfactorily compressive strength as 57 MPa.

Keywords: Selective laser melting, scaffolds, hybrid design, mechanical strength, cell viability

1. INTRODUCTION

Scaffolds for biomedical applications are porous structures that act as a substrate and enable the cells to adhere and grow by means of porous surface. These structures should have some characteristics such as; proper porosity that enable the cells to attach to the pore network and grow through the pores and additionally, they should have appropriate mechanical properties in order to mimic the human tissue behavior [1].
Selective Laser Melting is one of the popular methods in fabricating scaffolds [1-5]. There have been several researchers focused on the design of porous scaffolds [5-10]. They have stated that the design phase of porous scaffold could enhance the biodegradability, cell biology, biomolecules design of the biomimetic scaffolds [8,9].Consequently, this allows scaffold to promote the success of clinical outcomes in musculoskeletal surgeries [7].
In this study, a novel approach was presented in designing the scaffolds as hybrid structures in order to enhance the biological and mechanical properties of the scaffolds.

2. MATERIALS AND METHODS

In designing scaffolds, CAD (3-matic and 3-matic STL software, Materialise, Belgium) and CAM software (AutoFAB and Magics software, Materialise Belgium) were used. The unit cells used in designing of the scaffolds were dodecahedron (DCH), grid (G) and octet-truss (OCT). The scaffolds in disc shape for compression test (10 x Φ20 mm) and for cell culture cytotoxicity test (5 x Φ5 mm) were fabricated on Mlab cusing 200R system from Concept Laser GmbH (Germany) equipped with a 200 W single mode Ytterbium fiber laser from IPG Photonics. During fabrication, 180 W laser power, 1500 mm/s laser speed, 60 µm hatch spacing and 30µm layer thickness were used. Three duplicates were fabricated for each type of designs. No post processing was applied to the samples.
In order to observe mechanical strength, uniaxial compression test was performed at room temperature by universal testing machines (INSTRON 5982) with 100 KN load cell with a test speed of 0.05 mm/min. Cell viability test was applied by seeding L929 fibroblast cells in the ratio of 10^5 cell/ml onto the scaffolds samples. Scanning electron microscopy (SEM, Zeiss EVO LS10) was used to determine the geometrical properties of the fabricated samples.

3. RESULTS AND DISCUSSION

The photographs of the hybrid structured scaffolds are given in Figure 1. The mechanical strength and the cell viability results of the scaffolds are reported in Table 1. It has been seen that hybrid structures did not show apparent difference on the mechanical strength of the scaffolds but when the results were examined for cell viability test, hybrid designed scaffold (G+DCH+OCT) showed improvement.

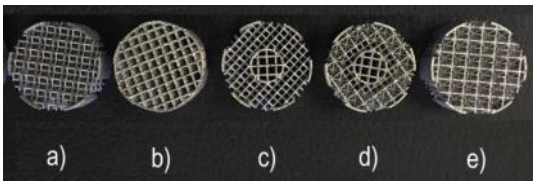

Figure 2. Hybrid designed scaffold samples for compression tests: a) DCH, b) G, c) G+DCH, d) G+DCH+OCT, e) OCT

Table 1. Mechanical and cell viability properties of the CoCr scaffolds

Sample according to unit cells	Max. Compressive Strength (MPa)	Max. Compressive Strain (mm/mm)	Elastic Modulus (GPa)	Cell viability (%)
DCH	49,3±0,2	0,203	1,45	79,51
OCT	55,5±1.4	0,204	1,16	96,54
G	65,7±0,27	0,209	1,49	53,49
G+DCH	56,5±0,5	0,205	1,37	66,35
G+DCH+OCT	57,2±0,1	0,209	1,13	106,36

4. CONCLUSIONS

This study presents the importance of designing of hybrid structures on the mechanical strenght and cell viability of the scaffolds. It has been concluded that for the fabrication of the customized scaffold depending on the patient's demand, designing of hybrid structured scaffolds within different unit cells can be used for controlling the porosity, pore size and strut diameter in order to achieve the required mechanical properties and desired biological properties. In this study, hybrid designed scaffolds gave maximally 106 % of cell viability and 57 MPa of compressive strength.

ACKNOWLEDGEMENT

The authors would like to thank to The Scientific Research Council of Yildiz Technical University (YTU-BAP) for their support in scope of the research project (Project no: FYL-2018-3222).

REFERENCES

1. 1.Munir, K. S., Li, Y., & Wen C. (2017). Metallic scaffolds manufactured by selective laser melting for biomedical applications. Metallic Foam Bone, Processing, Modification and Characterization and Properties (pp. 1-23). Cambridge, England: Woodhead Publishing.
2. Wysocki, B., Wojciech Święszkowski, W. & Kurzydłowski, K.J. (2014). Porous Titanium Scaffold Fabrication For Bone Tissue Engineering By SLM (Selective Laser Melting) Method, Fraunhofer direct digital manufacturing conference. Berlin, Germany.
3. Su, X., Yang, Y., Yu, P., & Sun, J. (2012). Development of porous medical implant scaffolds via laser additive manufacturing. Trans. Nonferrous Met. Soc. China, 22(1), 181-187. https://doi.org/10.1016/S1003-6326(12)61706-3
4. Bael, S.V., Vandenbroucke, B., Kerckhofs, G., Schrooten J. & Kruth J.P. (2009). Design and production of bone scaffolds with selective laser melting. 138th TMS Annual Meeting and Exhibition, San Francisco, USA.
5. Xiao, D., Yang, Y., Su, X., Wang, D. & Luo, Z. (2012). Topology optimization of microstructure and selective laser melting fabrication for metallic biomaterial scaffolds. Transactions of Nonferrous Metals Society of China, 22 (10), 2554-2561. https://doi.org/10.1016/S1003- 6326(11)61500-8.
6. Čapek, J., Machová, M., Fousová, M., Kubásek, J., Vojtěch, D., Fojt, J., Jablonská, E., Lipov, J., & Ruml, T. (2016). Highly porous, low elastic modulus 316L stainless steel scaffold prepared by selective laser melting. Materials Science and Engineering:C, 69 (2016), 631-639. https://doi.org/10.1016/j.msec.2016.07.027.

Fousová, M., Vojtěch, D., Jablonská, E., & Fojt, J. (2017). Promising characteristics of gradient porosity Ti-6Al-4V alloy prepared by SLM process. Journal of the mechanical behavior of biomedical materials, 69 (2017), 368–37. https://doi.org/10.1016/j.jmbbm.2017.01.043.

FAILURE ANALYSIS OF CARBON FIBER REINFORCED PA11 PRODUCED BY SLS

Serap Gümüs[1], Alperen Bayram[2], Juergen M. Lackner[3], Metin Çallı[2], Dilara Ergin[2], Wolfgang Kraschitzer[4], Roberto Krenn[4,5], Hermann Hanning[5], Şeyda Polat[1]
[1]Kocaeli University, Department of Metallurgical and Materials Engineering, Turkey, sgumus@kocaeli.edu.tr
[2]Coşkunöz R&D Center, Turkey, abayram@coskunoz.com.tr
[3]Joanneum Research Forschungsgesellschaft mbH, Austria, juergen.lackner@joanneum.at
[4]RPD Rapid Product Development GmbH, Austria, w.kraschitzer@rpd.at
[5]LSS Laser Sinter Service GmbH, 8605 Kapfenberg, Austria, hermann.hanning@lss-europe.com

Abstract. Additive manufacturing by selective laser sintering (SLS) has great potential to meet the demands of high reliability, high mechanical properties and ultra-light-weight design. Many studies target on the improvement of the properties of the SLS parts by means of using reinforcing fillers. Process parameters for SLS of polymers and theirs composites determine the final mechanical properties. In this work, failure analysis is performed on the tensile fracture surface of SLS printed carbon-Fibre reinforced polyamide 11 (PA11/CF) parts by SEM analysis to evaluate the effect of process parameters and powder properties. SEM images show a ductile fracture surface with a good interfacial bonding between CF and PA11 matrix. However, the flow of the mixed PA/CF powder over the build area by the roller, occurring layer-by layer from reservoir with defined speed and pressure,represent future optimization potential to avoid the accumulation of CFs in the matrix**.**

Keywords: *Additive Manufacturing, Selective Laser Sintering, Carbon fiber reinforced nylon 11, Crazing, interfacial adhesion.*

1. INTRODUCTION

Reducing fuel consumption leads to huge weight reduction activities in automotive industry, whereby polymers (especially thermoplastic and thermoset composite materials) significantly contributes to these goals. Conventional manufacturing has several design limitations, which favors Additive Manufacturing (AM) increasingly even in small-series production. Besides steel, Al and Ti alloys, technical focus is laid on fiber reinforced materials with enhanced properties. Selective Laser Sintering (SLS) is the commonly used AM technique due to its versatility in material design, construction and the much higher achievable mechanical strength (Goodridge, R. D., 2012). In the SLS process, a complex 3D object is built layer-by-layer by sintering/melting of powder particles by a focused laser beam. SLS is best applicable to semi-crystalline polymers like polyamides (PA12, PA6) (Dupin, S., 2012). They have a sufficiently large sintering temperature window between the crystallization (T_c) and melting temperatures (T_m). The powder bed temperature is kept within this operating temperature window during the process for preventing distortion and shrinkage cracks. For sintering and melting, the laser heats only the newly applied powder layer on top, above T_m. During SLS, only a part of the power bed is sintered to the desired component shapes, while the rest in the surrounding stays non-sintered. Nevertheless, powder storage above T_c results in aging (increase/decrease of molecular weight), which limits the re-use of powder due to the change in thermal properties. Therefore, the thermal management (accurate sensing and control of local powder bed temperature, laser power and scanning) during SLS processing is decisive.
Polymer composites, produced by SLS, are also gaining interest in the recent past to enhance the mechanical properties of the parts. However, according to pure materials some issues such types of reinforcement fiber type, its compatibility with the matrix, interfacial bonding of fiber and matrix, fiber size, length and shape, fiber orientation and homogeneity, etc., should be considered by using composite powder in SLS.
In this study, the performance of carbon fiber (CF) reinforced polyamide 11 (PA11) produced by SLS is determined by performing a series of microstructural study on fracture surface using scanning electron microscope (SEM, Jeol 6060).

2. MATERIALS AND METHODS

The SLS samples are produced from commercially available melt mixed black carbon fiber filled nylon 11 powder (PA 802-CF, ALM). The morphology of the powders is examined by using scanning electron microscope (SEM, Jeol 6060). The thermal properties of the powders are analyzed by using Differential Scanning Calorimetry (DSC, Perkin Elmer, DSC4000). The DSC analysis is a carried out in four segments. At the first segment, the powders are heated from 0 to 210°C at a heating rate of 10°C/min, then they are cooled to 0°C at cooling rate of 10°C/min. The heating-cooling segments are repeated to see the thermal aging effect on the powders. The tensile test bars are printed on a Farsoon 401selective laser sintering machine (Hunan Farsoon High-tech Co.Ltd, Changsha, Hunan, China). The tensile bars are built in the chamber as given in Figure 1 to see the variations in properties depending on the build direction. In this study, the samples oriented parallel to the x-direction (CN/C) with different tilt angle of 0˚ and 90˚ to the x-axis are discussed.
The tensile test is realized on Autograph AG-IS 100 kN Shimadzu Universal Testing Machine. Failure analysis is performed on the fracture surfaces of the samples by SEM after tensile tests, in order to evaluate the performance of the SLS samples.

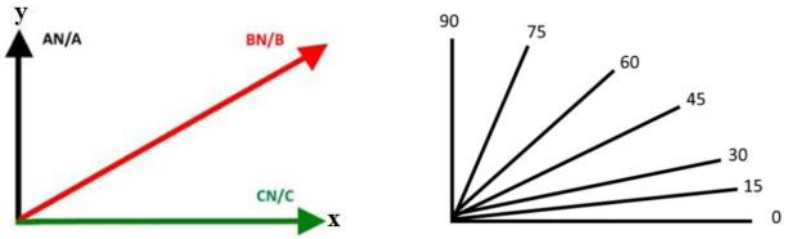

(a) (b)

Figure 1. The illustration of the manufacturing orientation and the tilt angle between part and platform of the tensile bar samples in the build chamber. The powder spreading is in the x-direction.

3. RESULTS AND DISCUSSION

Polyamides are most used polymers in SLS method because of their low processing temperature and wide processing window. However, the required mechanical properties cannot be reached without any reinforcement for many applications in aerospace, marine, automobile industries. Generally, short carbon fibers are used as reinforcing material for improving the mechanical properties of polyamides for SLS processes.
The powder properties are important for a successful processing during SLS. The SEM images of the PA/CF powder are given in Figure 2. As it seen from Fig. 2a, PA11 powder and the carbon fibers are mechanically mixed without any further chemical treatment. The powders exhibit sharp edges and corners and are far from spherical shape which is typical for cryogenic fracture production method. The particle size of the powder for a good sintering ability is generally around 45-90 μm (Goodridge, R. D., 2012). The particle size of the PA11 powder is less than 100 μm. The length of the carbon fiber is approximately < 400 μm with significant content of fractured pieces with smaller sizes. The fiber surfaces exhibit rough morphology, which is common after treatment with nitric acid (Fig. 2b). This oxidation modification method is used to improve the fiber-polymer interface by increasing the wettability between fiber and polymer by means of the introduced oxygen functional groups on the fiber surface.

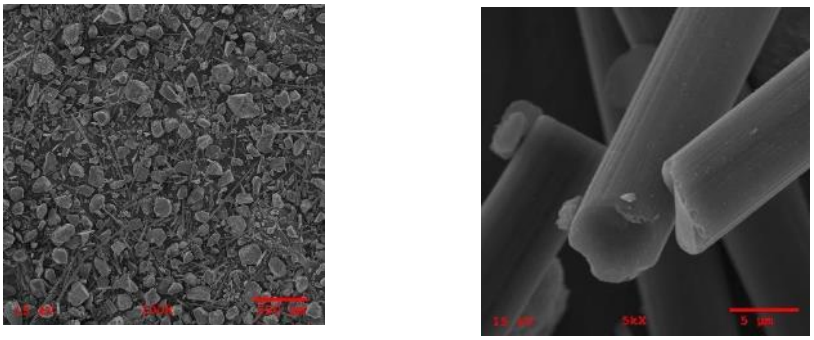

(a) (b)

Figure 2. SEM images of (a) PA/CF powder and (b) the surface of CF at higher magnification.

Figure 3 shows the SEM images of fracture surfaces of bar built in the CN/C direction with a tilt angle of 0˚ (CN-0) and 90˚ (CN-90) to the x-axis. The fracture surfaces of CN-0 samples exhibit typical ductile fracture with certain dimples (crazing) and a lot of bubbles in the microstructure (Fig. 3a and b).

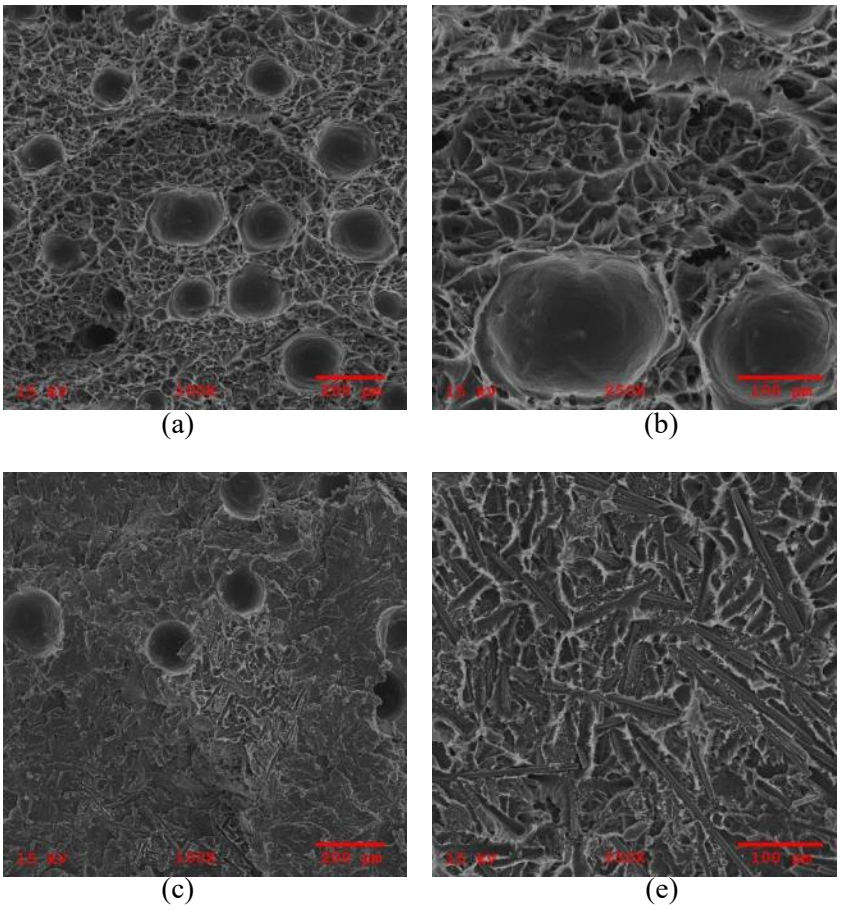

(a) (b)

(c) (e)

Figure 3. SEM images of the fracture surfaces of bar built in the CN/C (a, b) 0˚ and (c,d) 90˚ direction.

Also, the polymer residues on the carbon fibers -more evident on the fibers in CN-0 - show that the interfacial adhesion between fiber and matrix is improved by surface treatment of fibers (cohesive fracture). Crazing associated with fibrillated structure occurs at very localized plastic deformation areas and is the frequently seen fracture mechanism in thermoplastic polymers (Drummer, D., 2010; Kausch,

H. H., 1999). Crazes start by formation of small and interconnected microvoids. This interconnection between the microvoids elongate with increasing of the applied stress and finally break with a fibrillated structure appearance. Crazes are signs of higher fracture toughness because of absorbing fracture energy before cracking. As it seen from the fractograms, the craze-like structure appears prominently at the areas, where carbon fibers agglomerate (semicrystalline areas) in the polymer matrix. Thus, carbon fibers enhance the crystallization of the PA11 matrix which is also in agreement with the DSC analysis result of the PA/CF powder (Figure 4). The fibrillated structure is also seen in the fracture surface of CN-90 sample, but only in some area. The different appearance of the dimple structures (shape) in the two samples is mostly due to the fiber orientation, which is the result of movement of the roller and alignment of the PA/CF powder on platform. The structures are more spherical in the CN-0 sample (fibers are perpendicular to tensile stress) whereas they are longitudinal in CN-90 sample (fibers are parallel to tensile stress).

The individual layers, which are the result of layer-by-layer processing, are more visible in this sample (Fig. 3d).

The mechanical data obtained in the tensile test shows, that CN-0 samples exhibit better mechanical properties with a tensile strength of 62.7 ± 1.8 MPa than CN-90 with 41.6 ± 0.4 MPa. (Bayram, A., 2019) Additionally, high gas bubble densities (pores) are detected in the matrix, which are mainly accumulated at the carbon fibers. The pores are more visible in CN-0 compared to CN-90 due to the more effectively laser power, which act on larger area of higher light absorbing fiber. Probably, the pores (bubbles) are the result of the thermal decomposition of oxygen functional groups during the laser sintering process (Goh, G. D., 2019) which are introduced on the fiber surface during the oxidation modification method for improving the interfacial adhesion between the fibers and polymer. Consequently, the microstructural analysis and the mechanical data shows that the fiber orientation has more impact on the mechanical properties than the density of the bubbles.

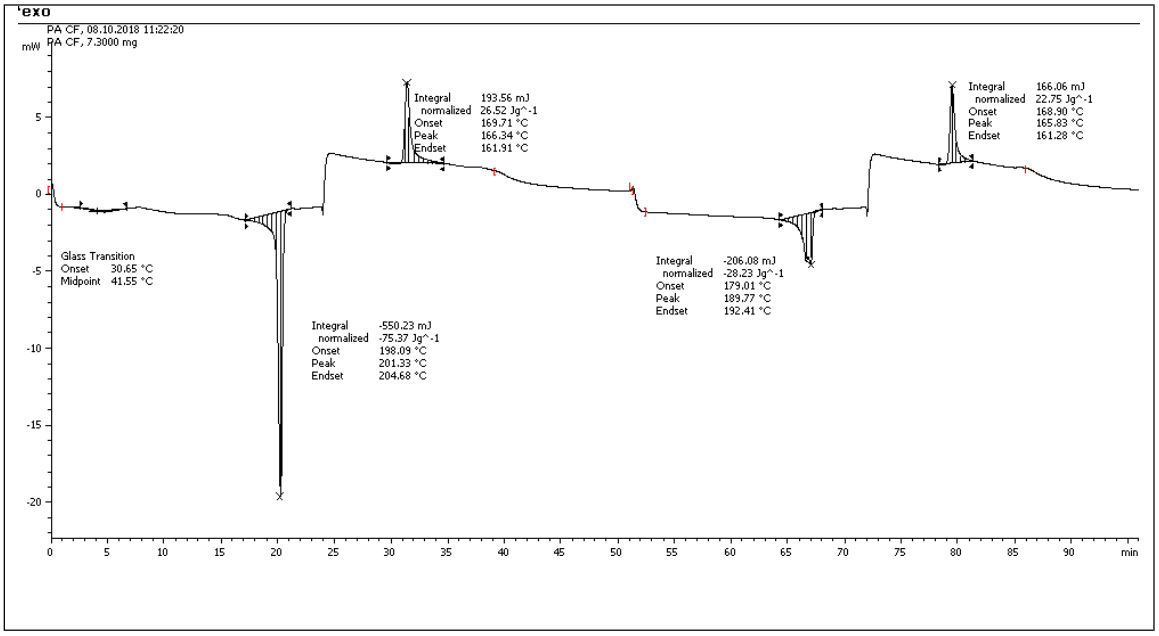

Figure 4. DSC thermogram of the PA/CF powder.

4. CONCLUSIONS

The failure analysis on tensile fracture surface of SLS PA/CF samples shows a ductile behavior with a good interfacial interaction of CF and PA11 matrix. However, carbon fiber accumulations are observed at specific areas, which is an undesired situation.

In SLS technique, determining the appropriate process parameters such part build orientation, powder bed temperature, layer thickness, laser process properties are important issues for a successful SLS

processing. The powder should have an appropriate particle size and morphology for a good flowability to spread in a thin layer over the build area. Especially, the orientation and homogeneity of the fibers, the compatibility of fiber and matrix are important issues which should be considered by using short fiber as reinforcement. As it seen from the fractograms, the material cannotspread uniformly over the the build area depending on the laying direction and printing orientation. Fibers tend to be agglomerated within the matrix. As the result, the inhomogeneity of the fibers in the final parts does only enable low mechanical properties.

Another important issue is the interfacial adhesion between carbon fibers (CF) and polymer matrix (PA) which plays a significant role on the performance of carbon fiber reinforced polymer composites. Generally, the fiber surface is modified by various surface treatment (sizing) to improve the interfacial adhesion of CF to PA. However, the introduced oxygen functional groups generated by oxidation treatment of the fiber surfaces, produce bubbles (gas pores) resulting from the gas accumulation within the composite materials due to the thermal decomposition during the laser sintering process.

It was also observed that 0° fiber orientation to x-axis has the best tensile strength compared to 90°, which gave the weakest tensile strength, which is in agreement with the literature (Goh, G. D., 2019).

ACKNOWLEDGMENT

The authors acknowledge the financial support of Eurostars E!11261 slsPEEK4smal-series project in the frame of the EUREKA initiative of the European Union and the national funding agencies in Turkey (TUBITAK) and Austria (FFG).

REFERENCES

Bayram, A., (2019). Creating material model for computer aided analysis of thermoplastic and composite materials additively manufactured by selective laser sintering process, Bursa Technical University, Institute of Natural and Applied Science.

Drummer, D., Rietzel, D., Kuhnlein F. (2010). Development of a characterization approach for the sintering behavior of new thermoplastics for selective laser sintering, Physics Procedia, 5, 533–542.

Dupin, S., Lame, O., Barres, C., Charmeau, J.-Y. (2012). Microstructural origin of physical and mechanical properties of polyamide 12 processed by laser sintering. European Polymer Journal, 48, 1611-1621.

Goh, G. D., Yap, Y. L., Agarwala, S. and Ye, W. Y. (2019). Recent Progress in Additive Manufacturing of Fiber Reinforced Polymer Composite. Advanced Materials Technologies, 4, 1800271

Goodridge, R. D., Tuck, C. J., Hague, R. J. M. (2012). Laser sintering of polyamides and other polymers. Progress in Materials Science, 57(2), 229-267.

Kausch, H. H., Gensler, R., Grein, C., Plummer, C. J. G., Scaramuzzino, P. (1999). Crazing in semicrystalline thermoplastics. Journal of Macromolecular Science, Part B Physics, 38, 803-815.

CHARACTERIZATION AND COMPRESSION TESTING OF DOUBLE GYROID LATTICE STRUCTURES PRODUCED BY DIRECT METAL LASER MELTING

Barış Kavas[1,3], Evren Yasa[2], M. Şeref Sönmez[3]
[1]*General Electric Marmara Technology Center, baris.kavas@ge.com* [2]*Eskişehir Osmangazi University, eyasa@ogu.edu.tr* [3]*Istanbul Technical University, ssonmez@itu.edu.tr*

Abstract. Lattice structures are gaining more importance to be utilized in structural part design due to their high strength to weight ratio, customizable relative density and loading-specific design opportunities, especially in the fields of aerospace, biomedical and automotive. Various unit cell designs have been studied in the literature inspired by the crystallographic unit cell structures such as FCC, BCC, etc. Mathematical surface model called "triply periodic minimal surface" also known as double gyroid is found to be a promising unit cell design for load bearing structural applications for its isotropy, continuous surface profile and homogeneity. The aim of this study is to understand the DG's compressive strength mechanism in relation to its unit cell size and relative density to be employed for aerospace applications. Cubic specimens containing different sizes of unit cells were manufactured using Direct Metal Laser Melting process on a Concept Laser M2 equipment using HAYNES® alloy powder. DMLM of this material combining excellent high-temperature strength with very good resistance to oxidizing environments up has almost never been addressed in the literature until now. Specimens were subjected to compressive testing and compressive stress-strain plots were obtained. Microstructural characteristics are also examined metallographically.

Keywords: Lattice structures, double gyroid, HAYNES®188, direct metal laser melting

1. INTRODUCTION

The main advantage of DMLM is its high precision and quality manufacturing capability. This advantage proposes a great potential for manufacturing complex geometries such as lattice structures. In the recent years, many lattice structures are proposed, mainly inspired by the atomic distribution of space groups and their combinations. Face centered cubic (FCC), base centered cubic (BCC), FCC with a truss placed in the direction of loading (FCCZ) and octet truss lattices are among the widely studied examples [1, 2].
As a novel unit cell design strategy, minimal surfaces have been proposed in the literature. Minimal surfaces are defined as surface models which have a local area minimizing in every location. That means, the sum of the principle curves passing through the location is always zero. This characteristic makes minimal surfaces very efficient in given different boundaries. By using different volume fractions, minimal surfaces models and unit cell sizes, varying mechanical properties can be obtained. Using minimal surface lattice structures for industrial applications, it is important to understand the effect of these parameters on the mechanical properties and buildability.

2. MATERIALS AND METHODS

In this study, additively manufactured lattice cellular structure comprising of one of the triply periodic minimal surface models called gyroid unit cells made of Haynes 188® alloy powder is characterized and compressively tested. For manufacturing the samples, one of the additive manufacturing modalities called direct metal laser melting system is used.
Three specimens have been printed with unit cell sizes of 6, 8 and 12 mm and compression testing is carried out on these specimens. Along with mechanical testing, witness specimens of the same configuration were printed and metallographically examined by investigating microstructural characteristics such as porosity, phases and surface roughness. Moreover, micro hardness testing was carried out on various locations of the specimens. Results and discussion are mainly focused on the relationship between microstructural properties and compressive test results. Double gyroid specific mechanical properties of HAYNES®188 produced by DMLM such as elastic moduli, specific stiffness and plateau region characteristics are among the reported outcomes.

3. RESULTS AND DISCUSSION

Modelling challenges and strategies to overcome these challenges have been documented explicitly. Ideal modelling strategy to obtain the desired volume double gyroid volume fraction is proposed. In the manufactured specimens; micro scanning and metallographical evaluations enabled to build a relationship between different unit cell sized double gyroid unit cells and buildability. Moreover, compression testing results have showed a perfect repeatability in between the specimens. Yield stress and plateau characteristics of the specimens have been documented and effect of unit cell size is showed. Energy absorption per volume is calculated and the approach for choosing the most efficient unit cell size is given.

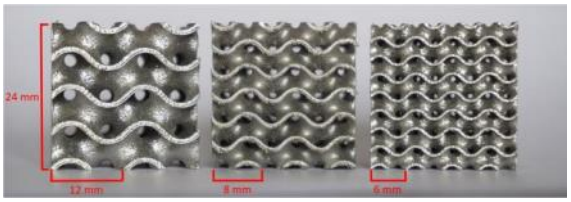

Figure 1. Manufactured double gyroid specimens for testing and characterization

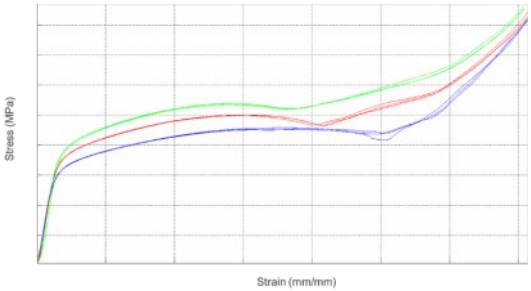

Figure 2. Obtained stress-strain curve of different unit cell size double gyroid specimens

4. CONCLUSIONS

- Overhang regions in double gyroid model is found to be challenging to print.
- Build defects in overhang areas are identified. Smaller unit cell size brings better material integrity.
- Bigger unit cell size is able to absorb more energy but yields earlier than smaller unit cell size under compression.
- Double gyroid structure with ductile material (HS188) is found to have bending dominated compressive behavior.

REFERENCES

[1] **Yan, C., Hao, L., Hussein, A., Young, P., Huang, J., & Zhu, W.** (2015). Microstructure and mechanical properties of aluminium alloy cellular lattice structures manufactured by direct metal laser sintering. *Materials Science and Engineering: A*, *628*, 238-246.

[2] **Xiong, J., Mines, R., Ghosh, R., Vaziri, A., Ma, L., Ohrndorf, A., ... & Wu, L.** (2015). Advanced micro-lattice materials. *Advanced Engineering Materials*, *17*(9), 1253-1264.

IN SITU ELEMENTAL ANALYSIS AND FAILURES DETECTION DURING ADDITIVE MANUFACTURING PROCESS UTILIZING LASER INDUCED BREAKDOWN SPECTROSCOPY

V.N. Lednev[1,2]*, P.A. Sdvizhenskii[1,2], R.D. Asyutin[3], M.Ya. Grishin[1,4], R.S. Tretyakov[3], A.Ya. Stavertiy[3], A.N. Fedorov[1], S.M. Pershin[1]

[1] *Prokhorov General Physics Institute, Russian Academy of Science, Moscow, Russia*

[2] *National University of Science and Technology MISiS, Moscow, Russia*

[3] *Bauman Moscow State Technical University, Moscow, Russia*

[4] *Moscow Institute of Physics and Technology (State University), Dolgoprudny, Moscow Region, Russia*

vasilylednev@gmail.com

Abstract. The feasibility of in situ quantitative multielemental analysis and production failures detection by laser induced breakdown spectroscopy (LIBS) has been demonstrated during direct energy deposition process in additive manufacturing. Compact LIBS probe was developed and equipped with the laser cladding head installed at industrial robot for real-time chemical quantitative analysis of key components (Ni, W) during the synthesis of high wear resistant coatings of nickel alloy reinforced with tungsten carbide particles. Owing to non-uniform distribution of tungsten carbide grains in the upper surface layer the only acceptable choice for LIBS sampling was chosen the melt pool at growing clad. No impact of LIBS sampling on cladding process and clad properties was observed according to optical and scanning electron microscopies. The feasibility of in situ LIBS quantitative elemental analysis of key components (tungsten and nickel) has been demonstrated during the cladding process. LIBS analysis results were in good agreement with offline measurements by electron energy dispersive X-ray spectroscopy and X-ray fluorescence spectroscopy.

Keywords: coaxial laser cladding, online monitoring, in-situ elemental analysis, laser induced breakdown spectroscopy

1. INTRODUCTION

Additive manufacturing opened new powerful capabilities for metal parts production including superior flexibility for producing internal structures which cannot be fabricated with traditional machinery and unique possibility to grow part with required design of chemical composition gradient (DebRoy et al., 2018). The development of online sensing and control systems is essential for the products quality improvement as well as advancement of additive manufacturing into high-value applications where component failure cannot be tolerated (Everton, Hirsch, Stravroulakis, Leach, & Clare, 2016; Kenel et al., 2016; Zhao et al., 2017): high-speed photography, optical pyrometry and high-speed X-ray imaging. However, no studies have been published so far focusing on in-situ elemental analysis during parts production by additive manufacturing.

Laser induced breakdown spectroscopy (LIBS) technique is a powerful tool which can be utilize for online quantitative multielemental analysis of synthesizing parts by additive manufacturing. Owing to remote sensing capability of LIBS to measure in situ any target which is “reachable by photons” this technique is a good candidate for online quantitative elemental analysis during additive manufacturing.

In this study we demonstrated the feasibility of in-situ quantitative multielemental analysis by LIBS during composite samples production by additive manufacturing. Specifically, our goal was to develop a remote LIBS system which is capable to quantitatively analyze both light (carbon) and heavy (tungsten, chromium, nickel) elements during composite coating synthesis by co-axial laser cladding technique. Due to low thermal depth affection, the co-axial laser cladding technique was successfully used for production/repairing high quality wear resistant coatings based on Ni-Cr-B-Si-Fe reinforced with tungsten carbide (WC) grains. However, high quality production of wear resistant coatings needs an online analysis tool to quantify tungsten and carbon in real-time due to strong influence of tungsten carbide concentration on coating mechanical properties.

2. MATERIALS AND METHODS

To fulfil this goal we designed and developed compact LIBS probe which was installed at the laser cladding head (Fig. 1). Hot solidified clad as well as a melt pool surface was sampled by LIBS probe (Fig. 2) but better analytical results were achieved in case of melt pool analysis. LIBS system was calibrated for quantitative measurements by offline analysis (Fig. 3). LIBS quantitative analysis of key components (carbon and tungsten) has been demonstrated in real-time conditions during synthesis of high wear resistant coatings of nickel alloy reinforced with tungsten carbide particles.

3. RESULTS AND DISCUSSION

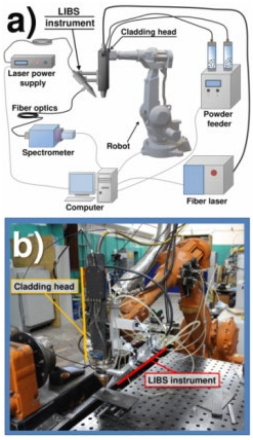

Fig.1 Scheme (a) and photo (b) of the coaxial laser cladding setup equipped with the laser induced breakdown spectroscopy (LIBS) system for in-situ elemental analysis during parts production by additive manufacturing

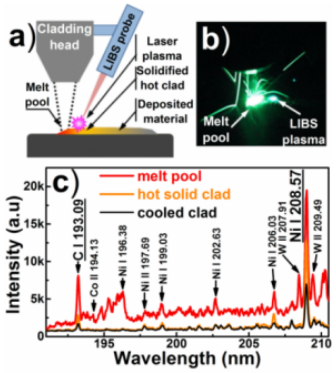

Fig. 2 Scheme of sampling spots (a), photo during hot solid clad sampling by LIBS (b) and plasma spectra (c) for different sampling spots: melt bath (red color), hot solidified clad (yellow color) and the clad cooled to the room temperature (black color)

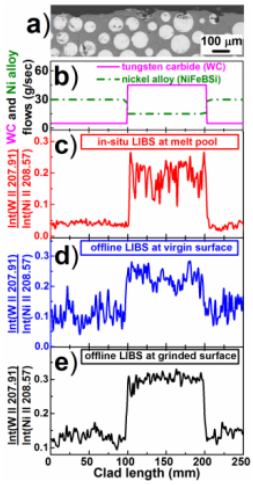

Fig.3 LIBS measurements for clad synthesized with varying concentrations of matrix (NiFeBSi) and tungsten carbide (WC): (a) – SEM image of top clad cross-section cut in the center along the cladding trajectory; (b) - flows of WC and NiFeBSi powders; (c) - in situ LIBS sampling at clad melt pool; (d) - offline LIBS sampling of solid clad; (e) – offline LIBS sampling after surface grinding.

4. CONCLUSIONS

In this study we have demonstrated the feasibility of in situ quantitative elemental analysis during direct energy deposition process in additive manufacturing. Compact LIBS (laser induced breakdown spectroscopy) probe was developed and equipped the laser cladding head installed at industrial robot for real-time chemical quantitative analysis of key components (carbon and tungsten).

REFERENCES

DebRoy, T., Wei, H. L., Zuback, J. S., Mukherjee, T., Elmer, J. W., Milewski, J. O., … Zhang, W. (2018). Additive manufacturing of metallic components - Process, structure and properties. *PROGRESS IN MATERIALS SCIENCE*, *92*, 112–224. doi:10.1016/j.pmatsci.2017.10.001

Everton, S. K., Hirsch, M., Stravroulakis, P., Leach, R. K., & Clare, A. T. (2016). Review of in-situ process monitoring and in-situ metrology for metal additive manufacturing. *Materials & Design*, *95*, 431–445. doi:https://doi.org/10.1016/j.matdes.2016.01.099

Kenel, C., Schloth, P., Van Petegem, S., Fife, J. L., Grolimund, D., Menzel, A., … Leinenbach, C. (2016). In Situ Synchrotron X-Ray Diffraction and Small Angle X-Ray Scattering Studies on Rapidly Heated and Cooled Ti-Al and Al-Cu-Mg Alloys Using Laser-Based Heating. *JOM*, *68*(3), 978–984. doi:10.1007/s11837-015-1774-0

Zhao, C., Fezzaa, K., Cunningham, R. W., Wen, H., De Carlo, F., Chen, L., … Sun, T. (2017). Real-time monitoring of laser powder bed fusion process using high-speed X-ray imaging and diffraction. *Scientific Reports*, *7*(1), 3602. doi:10.1038/s41598-017-03761-2

INVESTIGATION OF ENERGY ABSORPTION BEHAVIOR OF STIFFNESS OPTIMIZED LATTICE STRUCTURES

Recep M. Görgülüarslan[1], O. Utku Güngör[1], Erdem Erem[1], Saltuk Yıldız[1]
[1]*TOBB University of Economics and Technology, rgorguluarslan@etu.edu.tr*

Abstract. The objective of this study is to investigate the energy absorption performance of the lattice-based energy absorbers designed by a stiffness optimization process under static loadings applied in service conditions. For the optimization, first, a topology optimization process is utilized to generate unit lattice cell configurations. The energy absorber geometry is then modeled using the optimized lattice cells and a second optimization process is performed under the static bending load which produced graded lattice designs. To investigate the energy absorption behavior of these graded lattice designs, the non-linear finite element analysis (FEA) is conducted under quasi-static compression. The lattice designs are also fabricated by a Fused Filament Fabrication (FFF) printer using polylactic acid (PLA) material and the quasi-static uniaxial compression tests are performed on the fabricated designs. The FEA results are found to be in good agreement with the experimental results. Comparing to the lattice designs with uniform struts, the results show that improved energy absorption performance can be attained even though a stiffness-based optimization is utilized due to the obtained graded lattice configurations.

Keywords: *Lattice structure, topology optimization, energy absorption, fused filament fabrication.*

1. INTRODUCTION

Lattice structures fabricated by additive manufacturing (AM) techniques recently gained popularity in energy absorption applications as protective devices in packaging and blast mitigation systems (Hammetter et al. – 2013) as well as crash boxes in automotive industry (Gorguluarslan et al. – 2016). Since the lattice structures can undergo a large compressive strain at nearly a constant stress level, they can absorb a large amount of energy, thus minimizing the damage on the protected object. In the existing literature, the compressive and impact behaviors of various types of lattice structures fabricated by different AM techniques and materials have been investigated. Selective laser sintering process has been used to fabricate body-centered cubic (BCC) type lattice structures from 316L stainless steel (McKown et al. – 2008) and AlSi10Mg aluminum alloy (Gorguluarslan et al. – 2017), and face-centered cubic (FCC) type lattice structures from Ti6Al4V titanium alloy (Mines et al. – 2013). Selective laser sintering (SLS) process has been used to show the potential use of lattice structures with plastic material in body protection for impact absorption (Craddock et al. – 2012). Material extrusion process (so called Fused Filament Fabrication (FFF) or Fused Deposition Modeling (FDM)) have also been used as the AM technique by several researchers to investigate the energy absorption performance of various lattice structures fabricated by Acrylonitrile butadiene styrene (ABS) (Gautam et al. – 2018) or polylactide (PLA) materials (Sarvestani et al. – 2018).

Recently, functionally graded lattices (FGLs) have gained the attention of the researchers because of their promising opportunities in the energy absorption components. A functionally graded structure has an ordered gradient in its design and material to allow for gradually varying mechanical properties such as elastic modulus, strength and energy absorption (Miyamoto et al. – 2013). FGLs can be designed by gradually varying unit cell density or strut cross-sections along the loading direction (Grunsven et al. – 2014). Maskery et al. – 2017 investigated the energy absorption performance of BCC FGL fabricated by SLM and SLS. Al-Saedi et al. – 2018 and Yang et al. – 2019 investigated the energy absorption characteristics of the graded lattice structures fabricated by SLM, namely F2BCC lattice type from AlSi10Mg material and Gyroid lattice type from SS336L material, respectively. These studies prove that the FGLs can have better energy absorption characteristics compared to the regular lattices with uniform struts and have potential for energy absorption devices such as a crash box of an automobile.

The lattice-based energy absorbers must not only have high energy absorption performance under impact loadings but also safely withstand the static loadings in regular service conditions. In this study, we demonstrate a stiffness-based optimization framework that will consider the static loadings and will eventually result in a graded lattice design. Since the existing studies show that the FGLs designed without any optimization process have better energy absorption characteristics compared to the regular

lattice structures, we hypothesize that the FGLs obtained from the optimization under the static loading conditions will also have good energy absorption characteristics. To validate this hypothesis, the energy absorption performances of the optimized lattice designs are evaluated by nonlinear finite element analysis (FEA) under quasi-static compression and validated by compression experiments conducted on the fabricated designs by an FFF printer using PLA material. Results prove that the FGLs obtained from the stiffness-based optimization produce higher specific energy absorption performance compared to the regular lattice designs.

2. MATERIALS AND METHODS

2.1 Stiffness-based Lattice Optimization

In the stiffness-based lattice optimization processes, the geometry is filled with strut members which are modeled by using truss or beam elements for the FEA. Then, the strain energy (*SE*) of the lattice structure obtained from the FEA is minimized as the objective function to maximize its stiffness. A general optimization formulation that can be used for this optimization process can be stated by

$$\begin{aligned} &\text{Find} && \mathbf{d} \\ &\text{Minimize} && SE \\ &\text{Subject to} && V - v_f V_T \le 0 \\ & && \mathbf{F} = \mathbf{KU} \\ & && \sigma' - \sigma_{all} \le 0 \\ & && \mathbf{d}_l \le \mathbf{d} \le \mathbf{d}_u \end{aligned} \tag{1}$$

where **d** is a row vector of design variables, which are the cross-sectional lengths of each strut member. In this study, the diameter *d* of each strut is the design variable since a circular cross-section is used. The volume of the lattice structure, calculated by $V = 0.25\pi\ \mathbf{d}^2\mathbf{L}^T$ is set as a constraint in Eq. (1) and it is aimed to be equal or smaller than the total solid volume of the entire geometry, V_T, multiplied by a volume fraction value, v_f. The linear static FEA is given by $\mathbf{F} = \mathbf{KU}$ in Eq. (1) where **F** denotes the global force vector and **U** is the global displacement vector. **K** is the global stiffness matrix, which is formed by the element stiffness matrices after applying global coordinate transformations. The element stiffness matrix, **k,** is determined based on the element type used in the FEA. The Euler-Bernoulli beam element formulation (Kattan - 2008) is used to model the strut members in the FEA. Another constraint can be added to have the maximum Von mises stress calculated on each beam elements denoted by σ' is smaller than or equivalent than the allowable stress value denoted by σ_{all}. The lower and upper bound vectors of the design variables are denoted by $\mathbf{d}_l$ and $\mathbf{d}_u$, respectively.

2.2 Material Models

PLA material is considered in the design process and experimentation of this study. The mechanical properties of PLA material were obtained using dog-bone specimens, which were fabricated by the FFF 3D printer, named as Artıboyut A1 Pro, from ESUN branded PLA material, in a standard uniaxial tensile test based on ASTM D638 standard. The elastic modulus of the material was obtained from the linear section of the stress-strain data while the yield strength was obtained through %0.2 line. The material model for the beam elements was considered to follow an isotropic linear elastic material model for static FEA. The true stress-strain data was also needed to carry out the compression simulations of the lattice structures. The classical time-independent plasticity model, which uses von Mises yield surfaces with isotropic hardening, was used for the quasi-static compression FEA in ABAQUS. The plastic behavior of the material was described by defining the true yield stress as a function of true plastic strain as listed in Table 1 which were obtained from the nominal stress-strain data of experiments.

Table 1. Material properties of PLA.

Elastic Modulus	Poisson's ratio	Density	Post-yield true stress vs. true plastic strain					
2200 MPa	0.33	$1.024\text{x}10^{-9}$ ton/mm^3	Yield stress (MPa)	43.4	45.8	46.2	47.1	47.6
			Plastic Strain	0	0.0021	0.0029	0.0054	0.0067

2.3 Design Framework for the Functionally Graded Lattice Structure

The lattice design approach used in this study is illustrated in Fig. 1 and has 3 main steps:

Step 1: A discrete topology optimization (DTO) step is carried out to identify the initial topology of the unit lattice cell used for modeling the overall geometry. In the initial unit cell shown in Fig. 1(a), all the corner and face middle nodes are connected to each other with strut members. This is the combination of the so-called octet cubic (OC), simple cubic (SC), and BCC unit cell types. Hence, this configuration is called combined cubic (CC) cell in this study. The lower bounds $\mathbf{d}_l$ are set near zero in Eq. (1) to perform DTO and the struts with diameters close to the lower bound were removed. Two different loading conditions were applied in the DTO and two different lattice types were obtained. In Case 1, by applying equal compressive loads shown by F_1 in Fig. 1(a) on each corner node of the initial unit cell, the OC lattice cell was obtained. In Case 2, equal compressive loads were also applied on the middle points of each face shown by F_2 in Fig. 1(a) and the Face-Body Centered Cubic (FBCC) unit cell was obtained. The nodal force magnitudes were chosen for each case such that a unit force is applied in total.

Step 2: A rectangular energy absorber geometry of 100x40x40 mm^3 , which must withstand a static bending load of F = 100 N, is modeled by 20x20x20 mm^3 lattice cells, i.e. by CC, OC, and FBCC with uniform strut dimensions as shown in Figure 1(b). Then, the size optimization process using Eq. (1) is applied to minimize the strain energy of the entire lattice structure to determine the optimal diameter (D) of each strut. A volume fraction of 0.3 was considered in both the DTO of Step 1 and the size optimization. The maximum Von Mises stress (σ') on the struts is constrained not to exceed σ_{all} = 50 MPa to satisfy the necessary strength under the bending load. The lower and upper diameter bounds are set to 2 mm and 6 mm respectively based on the 3D printer's allowable constraints. In-house MATLAB codes have been developed to implement the linear FEA and optimization processes.

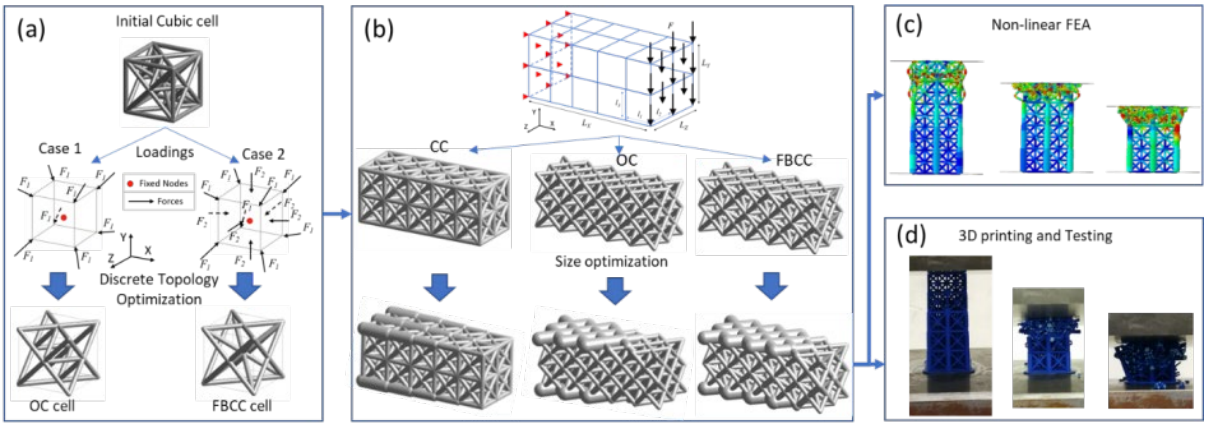

Figure 1. Design framework (a) DTO process, (b) Size optimization under bending load (c) Non-linear compression FEA (d) 3D printing and compression tests of the optimized FGLs.

Step 3: Three different FGL designs obtained in Step 2 (in Fig. 1(b)) are simulated through ABAQUS software (Fig. 1(c)) and the printed specimens by FFF printer were tested using an Instron uniaxial compression testing device with a constant velocity of 1.3 mm/min (Fig. 1(d)). In the simulations, the strut members were modeled using two-node linear Timoshenko beam element (i.e. element type B31) and 9 mesh elements were used for each. All degrees of freedom of the bottom nodes were fixed and a rigid plate was used as a compression apparatus at the top. A constant velocity is applied in the length direction of the crash box at a time period of 0.1 to simulate the compression test. A general explicit contact algorithm was defined with a friction of 0.3 for the interaction between the lattice model and the rigid shell as well as between the struts themselves.

3. RESULTS AND DISCUSSION

The stiffness-optimized FGLs after Step 1 and Step 2 have the graded diameters on the top and bottom faces decreasing from fixed end to the other end where the load is applied; while the diameters of other struts remained constant and close to the lower bound of 2 mm in general as seen in Fig 1(b). The reason

of these constant and small diameters is that the stress values were obtained lower for these struts due to the closeness to the neutral axis. On the top and bottom surfaces, on the other hand, higher stresses than the allowable one were obtained when small diameters were used. Therefore, the optimization algorithm increased the diameters to keep the stress below the allowable one. Since the stress distribution show a decreasing trend from fixed end to the tip, a graded diameter distribution was obtained as in Fig. 1(b). For each of the three FGL designs, around 41% to 54% improvement was obtained compared to the uniform lattice with equal diameters as listed in Table 2. The equal diameter value of each uniform lattice was calculated to have the same volume as the FGL design for a fair comparison. The diameters were 2.29 mm, 2.98 mm, 3.12 mm for CC, OC, and FBCC uniform lattices, respectively.

Table 2. Comparison of the strain energy (SE) results

SE ($x10^{-3}$)	Graded Lattice	Uniform Lattice	Difference (%)
CC	65	140	54
OC	126	213	41
FBCC	141	286	51

The stress-strain graphs obtained from experiment and the compression FEA are compared for each of three FGL designs in Fig. 2(a). Since the maximum compression strain was ε =0.6 in the experiment due to the limitations of the fixation plates, the comparisons are given upto this strain value. As visually seen from Fig 2(a), the FEA results are in good agreement with the experimental ones. In addition, the stress-strain curves of the FGL designs are compared with the uniform lattices (D-Equal) in Fig 2(b).

The specific energy absorption (SEA) results were obtained by dividing the area under the stress-strain curve of each design (Fig. 2) by its volume. A numerical method, namely trapezoidal rule, was used to approximate the area under the stress-strain curves. The results from experiments and FEA for FGL designs as well as the FEA results for the uniform lattices are listed in Table 3 for comparison. The comparison of experiment and FEA results for the FGL designs show similar SEA performance with differences around 10-13%, indicating a good prediction with FEA.

FEA results for the FGL designs and uniform lattices were also compared by calculating the SEA upto the densification strain denoted by ε_d in Table 3. The densification strains were determined from the curves in Fig. 2(b) by choosing the point when the continuous increase of the stress begins. Those values were 083, 085, and 0.82 for the CC, OC, and FBCC FGL designs, respectively; while they were 0.79, 0.81, 0.77 for the CC, OC, and FBCC uniform lattices, respectively. The differences of the results between the graded and uniform lattices given in Table 3 show that the graded CC and FBCC structures have better energy absorption performance with 27.3% and 20.1% increase, respectively. However, the difference was less than 1% for the OC lattice, meaning the FGL design did not have an improvement. Nevertheless, the performance of the graded OC is better in terms of the difference between the initial peak stress and the plateau stress, since it is seen from Fig. 2(b) that all the graded lattice structures have smaller initial peak stress values than the uniform lattices which is desired for energy absorbers.

Table 3. SEA results

SEA ($x10^{-5}$)	Graded-Experiment $\varepsilon = 0.6$	Graded-FEA $\varepsilon = 0.6$	Difference (%)	Graded-FEA $\varepsilon = \varepsilon_d$	Uniform - FEA $\varepsilon = \varepsilon_d$	Difference (%)
CC	2.41	2.12	11.94	3.36	2.64	27.3
OC	2.37	2.13	10.20	3.57	3.59	-0.56
FBCC	1.57	1.78	12.98	2.75	2.29	20.1

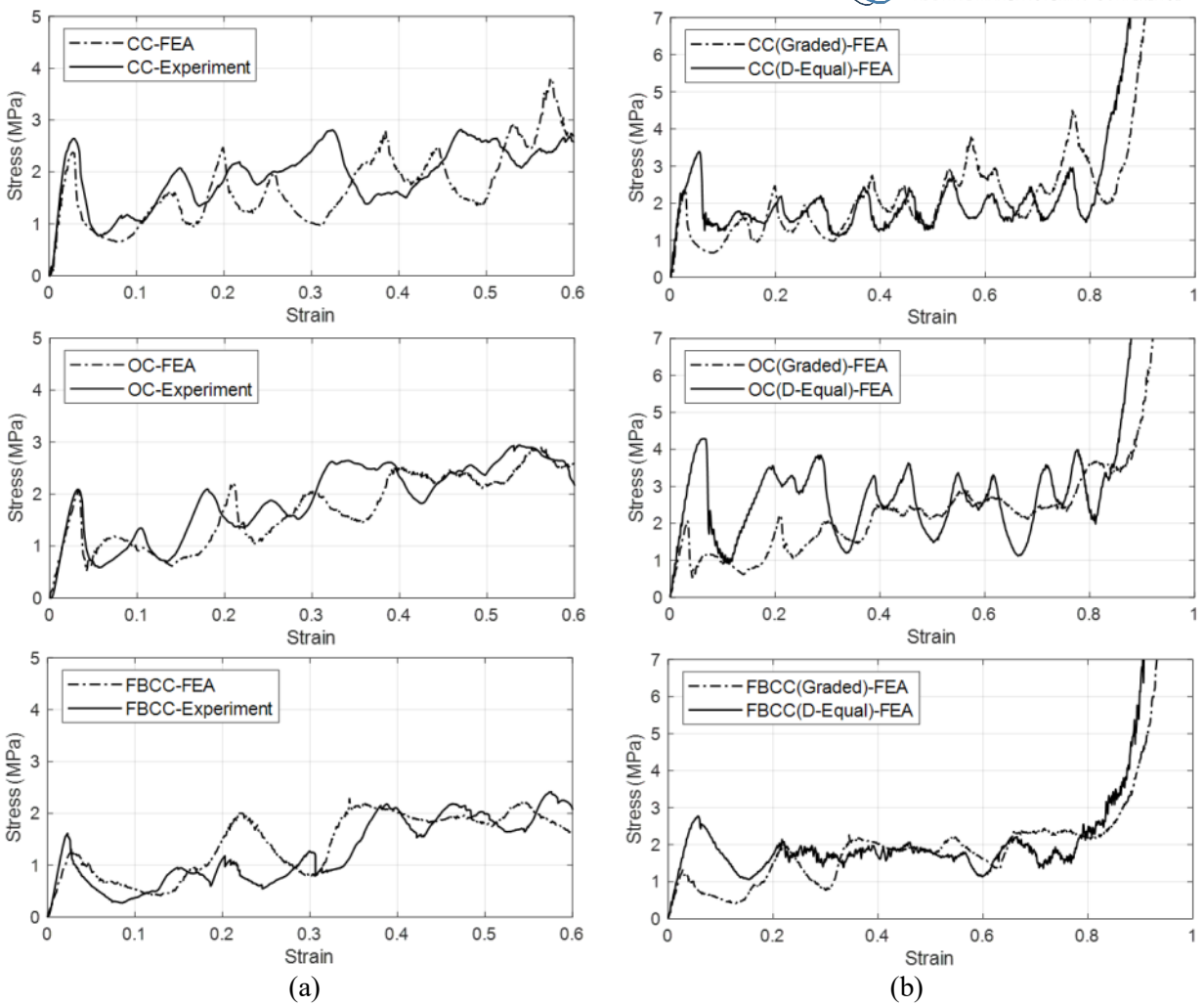

Figure 2. Stress-strain graphs for CC, OC, and FBCC lattice types; (a) comparison of FEA results with experiment, (b) comparison of graded and uniform (D-Equal) lattice FEA results.

4. CONCLUSIONS

The results of this study prove that although a stiffness optimization process was used under static bending load to obtain graded lattice designs, their energy absorption is still improved compared to the uniform lattice structures. Future work includes integrating the nonlinear FEA to the optimization process to further improve the energy absorption performance of the lattice structures.

REFERENCES

Hammetter, C.I., Rinaldi, R.G. and Zok, F.W. (2013). Pyramidal lattice structures for high strength and energy absorption. Journal of Applied Mechanics, 80, 041015. http://www.doi.org/10.1115/1.4007865

Gorguluarslan, R.M., Gandhi, U.N., Mandapati, R. and Choi, S.K. (2016). Design and fabrication of periodic lattice-based cellular structures. Computer-Aided Design and Applications, 13, 50-62. https://doi.org/10.1080/16864360.2015.1059194

McKown, S.S.S.S., Shen, Y., Brookes, W.K., Sutcliffe, C.J., Cantwell, W.J., Langdon, G.S., Nurick, G.N. and Theobald, M.D. (2008). The quasi-static and blast loading response of lattice structures. International Journal of Impact Engineering, 35, 795-810. https://doi.org/10.1016/j.ijimpeng.2007.10.005

Gorguluarslan, R.M., Choi, S.K. and Choi, H.J. (2017). International Design Engineering Technical Conferences and Computers and Information in Engineering Conference, American Society of

Mechanical Engineers, Uncertainty Quantification and Validation of Lattice Structures Fabricated by Selective Laser Melting (pp. V001T02A085-V001T02A085).

Mines, R.A.W., Tsopanos, S., Shen, Y., Hasan, R. and McKown, S.T. (2013). Drop weight impact behaviour of sandwich panels with metallic micro lattice cores. International Journal of Impact Engineering, 60, 120-132. https://doi.org/10.1016/j.ijimpeng.2013.04.007

Brennan-Craddock, J., Brackett, D., Wildman, R. and Hague, R. (2012). The design of impact absorbing structures for additive manufacture. Journal of Physics: Conference Series, 382, 012042. http://doi.org/10.1088/1742-6596/382/1/012042

Gautam, R., Idapalapati, S. and Feih, S. (2018). Printing and characterisation of Kagome lattice structures by fused deposition modelling. Materials & Design, 137, 266-275. https://doi.org/10.1016/j.matdes.2017.10.022

Sarvestani, H.Y., Akbarzadeh, A.H., Niknam, H. and Hermenean, K. (2018). 3D Printed Architected Polymeric Sandwich Panels: Energy Absorption and Structural Performance. Composite Structures. https://doi.org/10.1016/j.compstruct.2018.04.002

Miyamoto, Y., Kaysser, W.A., Rabin, B.H., Kawasaki, A., Ford, R.G. (2013) Functionally Graded Materials: Design, Processing and Applications.

Grunsven, W.V., Hernandez-Nava, E., Reilly, G.C. and Goodall, R. (2014). Fabrication and mechanical characterisation of titanium lattices with graded porosity. Metals, 4, 401-409. https://doi.org/10.3390/met4030401

Maskery, I., Hussey, A., Panesar, A., Aremu, A., Tuck, C., Ashcroft, I. and Hague, R. (2017). An investigation into reinforced and functionally graded lattice structures. Journal of Cellular Plastics, 53, 151-165. https://doi.org/10.1177/0021955X16639035

Al-Saedi, D.S., Masood, S.H., Faizan-Ur-Rab, M., Alomarah, A. and Ponnusamy, P. (2018). Mechanical properties and energy absorption capability of functionally graded F2BCC lattice fabricated by SLM. Materials & Design, 144, 32-44. https://doi.org/10.1016/j.matdes.2018.01.059

Yang, L., Mertens, R., Ferrucci, M., Yan, C., Shi, Y. and Yang, S. (2019). Continuous graded Gyroid cellular structures fabricated by selective laser melting: Design, manufacturing and mechanical properties. Materials & Design, 162, 394-404. https://doi.org/10.1016/j.matdes.2018.12.007

Kattan, P.I. (2008). MATLAB Guide to Finite Elements: An Interactive Approach.

THE EFFECT OF PROCESSING PARAMETERS ON THE MICROSTRUCTURE AND MECHANICAL PROPERTIES OF SLS PEKK

Serap Gümüs[1], Alperen Bayram[2], Juergen M. Lackner[3], Metin Çallı[2], Dilara Ergin[2], Wolfgang Kraschitzer[4], Roberto Krenn[4,5], Hermann Hanning[5], Seyda Polat[1]
[1]*Kocaeli University, Department of Metallurgical and Materials Engineering, Turkey, sgumus@kocaeli.edu.tr*
[2]*Coşkunöz R&D Center, Turkey, abayram@coskunoz.com.tr*
[3]*Joanneum Research Forschungsgesellschaft mbH, Austria, juergen.lackner@joanneum.at*
[4]*RPD Rapid Product Development GmbH, Austria, w.kraschitzer@rpd.at*
[5]*LSS Laser Sinter Service GmbH, 8605 Kapfenberg, Austria, hermann.hanning@lss-europe.com*

Abstract. The demands of ultra-light-weight design for decreasing fuel consumption and consequently decreasing greenhouse emissions are pressing needs in different industry applications. The automotive and aeronautic industries are forced to search for alternative materials and manufacturing methods. Additive manufacturing technique has great potential to meet such demands and selective laser sintering (SLS) is the dominantly used one for high durability needs of even large size polymer parts due to its versatility in material design, construction and the much higher achievable mechanical strength compared to e.g. fused deposition or stereolithography. In this work, a series of microstructural investigations on fracture surfaces of SLS polyetherketoneketone (PEKK) is performed to obtain insight about the effect of the laser power on the final microstructure and mechanical properties. Thereby, the improved Thermomelt technology was applied, reducing the process temperature of powder bed and simultaneously increasing the laser power significantly, which minimizes the powder aging at otherwise high temperatures and enables the use of standard SLS equipment.

Keywords: *Additive Manufacturing, Selective Laser Sintering, PEKK, layer-by-layer processing, anisotropic properties.*

1. INTRODUCTION

The increasing need for environmentally friendly production methods by decreasing fuel consumption and consequently decreasing greenhouse emissions is met by light-weight design. The automotive and aeronautic industries are forced to search for alternative materials and manufacturing methods. Conventional manufacturing has several design limitations, which favors additive manufacturing (AM) increasingly even in small-series production. Thus, rather all automotive and OEM part producers have nowadays components and tools produced by AM processes at least in prototyping and as manufacturing aids. Selective laser sintering (SLS), one of the highly versatile additive manufacturing (AM) technology, is seen as the most preferred and used manufacturing method due to the possibility of producing light-weight materials with advanced geometries in high mechanical quality (durability) and large sizes. Using of high-strength polyetherether ketone (PEEK) based structural and functional components in car bodywork is seen as candidate for tomorrow's electric and self-drivimg cars with need for low weight, even due to still high material costs. PEEK is an advanced semi-crystalline thermoplastic belonging to the poly aryl ether ketone (PAEK) family. The PAEK family are known with its high temperature performance, high chemical and oxidation resistance. AM of PAEK polymers is economically seen as a key future technology for cost-efficient production of high-quality components in small-series as alternative to conventional used materials. However, the high melting temperature of PEEK leads to high processing time and consequently high costs. Nowadays, polyetherketoneketone (PEKK) is mostly preferred material, because it is easy to process due to its lower melting temperature and enables similar mechanical performance. It is well applicable in the novel, patented Thermomelt process, which reduces powder bed temperature by increased laser power. This minimizes powder aging and enables also the production at medium temperature SLS equipment, which is widely used in industry. In this study, microstructural investigations on tensile fracture surfaces of SLS produced PEKK is performed to determine the effect of process parameters on the final microstructure as well as mechanical properties.

2. MATERIALS AND METHODS

The SLS-ThermoMelt samples are produced in different condition (oxygen content and laser power) from commercially available PEKK powder (KEPSTANTM PEKK 6003, Arkema, France). The morphology of the powders is examined by using scanning electron microscope (SEM, Jeol 6060). The thermal properties of the powders are analyzed by using Differential Scanning Calorimetry (DSC, Perkin Elmer, DSC4000). The DSC analysis is carried out in two segments. At the first segment, the powders are heated from 0 to 350°C at a heating rate of 10°C/min, then they are cooled to 0°C at cooling rate of 10°C/min. The glass transition temperature (T_g) and melting temperature (T_m) could be determined from the DSC-thermogram.
The tensile test bars are printed on a Farsoon 401 sintering machine (Farsoon optimized by LSS, Kapfenberg, Austria).
The tensile test is realized on Autograph AG-IS 100 kN Shimadzu Universal Testing Machine. Failure analysis is performed on the fracture surfaces of the samples by SEM after tensile tests, in order to evaluate the failure mechanism.

3. RESULTS AND DISCUSSION

In SLS, the powder properties such particle size and shape, are important for a good spreading on the platform of the chamber, successful sinterability with good fusion and final surface quality. Nowadays, the general problem in SLS is the availability of adequate polymer material in powder form with an appropriate particle size and morphology. The polymers are not produce directly in powder form and should converted by an appropriate method to the required shape for good sintering. The SEM images of the PEKK powder at different magnification are given in Figure 1. The powders exhibit a coagulated structure of small particles. While the small powder particles are less than 10 µm, the size of the big agglomerates exceed 100 µm. The small powders show an undesired shape, far from sphericity, being probably produced by cryogenic grinding. The particle size of the powder for a good sintering ability is generally around 45-90 µm [Goodridge, R. D., 2012].

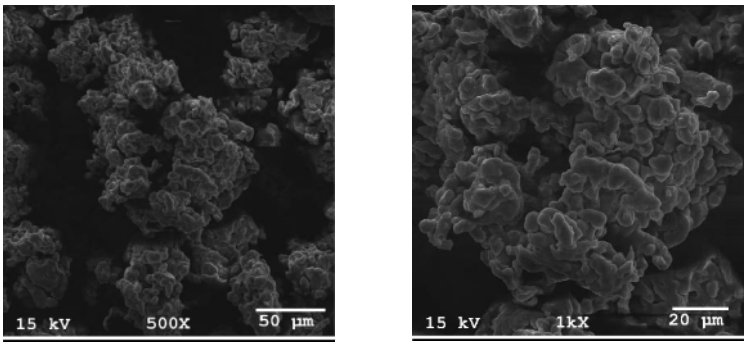

(a) (b)

Figure 1. SEM images of PEKK6003 powder at different magnification.

The DSC thermogram of the PEKK 6003 is given in Figure 2. Here, only the heating step is given because no peak can be detected at the cooling step. The heating step show a T_g at 159.8˚C and a main melting temperature at 294.3˚C. Additionally, a small broad endothermic peak is detected near 225˚C. The presence of multiple and broaded melting peaks suggests that the powder contains polymer chains with different molecular weight.

Figure 3a, c and Figure 3b, d show the fracture surfaces of SLS-ThermoMelt PEKK 6003 processed with a laser power of 37 W and 47 W, respectively. The effect of the different laser power on the microstructure properties is clearly seen by exhibiting different fracture morphology. Multiple parallel gaps are visible in the fracture surface of the sample processed at lower laser power which is

a sign of weak bonding of the individual sintering layers (Fig 3a). It is clearly seen that the powders are fused to each other within the same layer, whereas it is not the same between the adjoining layers.

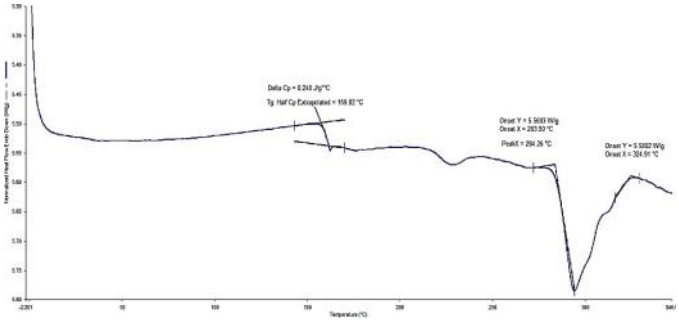

Figure 2. DSC heating thermogram of the PEKK powder.

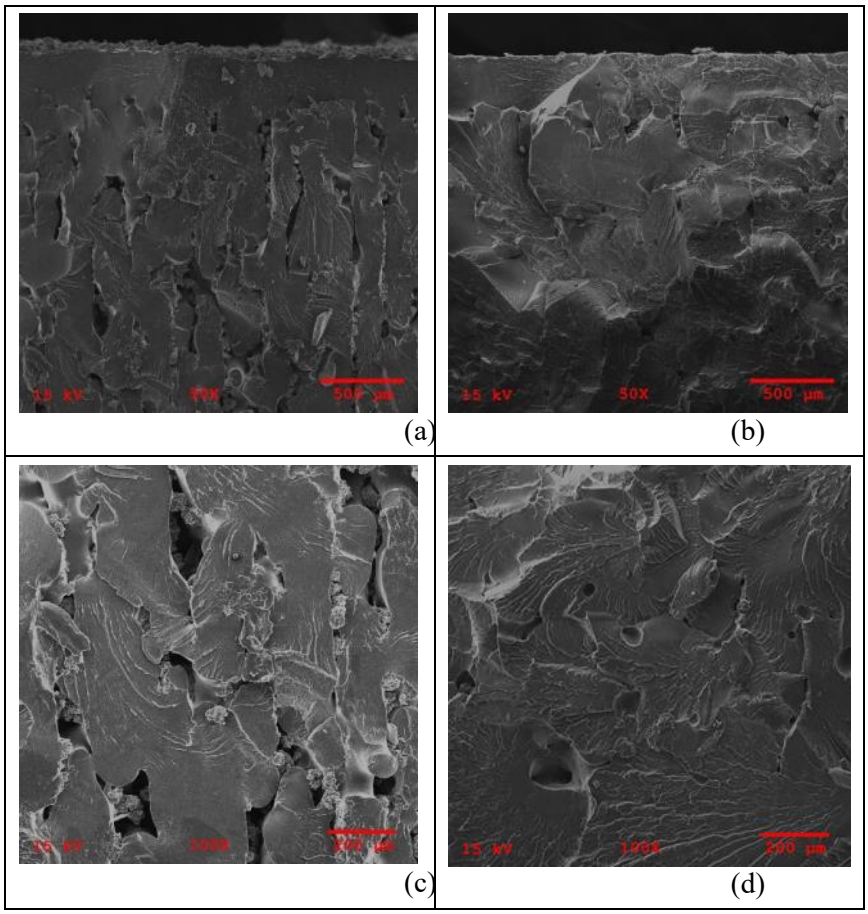

Figure 4. SEM images of the fracture surfaces of the SLS PEKK 6003 produced with a laser power of (a, c) 37 W and (b, d) 47 W.

In SLS process, the parts are produced directly from 3D CAD models by building them in layers and processed by layer-by-layer sintering. One of the main cause for this undesirable structure is the improper particle size, shape and morphology of the powders. Ideal powder should have high sphericity for a good flowability, processability [Drummer, D., 2010; Dupin, S., 2012]. However, availability of polymers in powder form with high sphericity for laser sintering is the main problem.

They are not produced directly in powder form, rather indirectly by co-extrusion processes, precipitation process or cryogenic milling. Generally, flowability agents like silica are usually added which could also act as defects. The other main cause for great gaps between the individual layers is the insufficient heat supply. It leads to non-predicable, low fatigue strength and part lifetime. Accurate sensing and control of local powder bed temperature, laser power are the main precautions to reduce these undesirable

phenomena.
The layer-by-layer process structure is not more visible at the fracture surface processed at higher laser power. However, some pores are apperead in the microstructure, which is probably due to the local excessive heat supply and consequently polymer degradation. Both sample exhibit a brittle fracture mode.

The tensile bars are built flat, parallel to the x-axis of the platform. Tensile strength and elongation at break for the sample printed with lower laser power is 61.2 MPa and % 2.57, whereas the values are 58.5 MPa and %1.80 for that with higher laser power, respectively. A decrease in tensile strength and in elongation at break is observed with increasing the laser power. The major issues in SLS processing is the anisotropic mechanical properties of the laser sintered parts according to their build position, which is the result of the layer-by-layer processing nature. Thus, the gaps between the individual layer have a little effect on the tensile test, because the layers are 0˚ orientated to x-axis and the stress is applied along to each of the layers in the sample during tensile test. On the other hand, higher laser power allows the layers to fuse together, whereas some pores are appeared in the structure. The tensile test data show that the pores has more adversely effect on the mechanical properties.

4. CONCLUSIONS

In this study, a series of microstructural investigations on fracture surfaces is performed to obtain insight about the effect of the laser power on the final microstructure and mechanical properties. It is seen that low and high laser power has distinctive adverse effect. The mechanical properties are a function of the build orientation. Parts built parallel to the x-axis show the highest tensile strength. The stress act along on each of the individual layer and is distributed evenly during tensile test. Each layer will fail at weak points and small defects while the stress builds up along the layers. Consequently, the pores resulting from degradation of polymer due to the local high heating have more effect on tensile properties than the gaps orientated along the applied stress. The weakest properties will be experienced, when stress is applied perpendicular to this layers with the gaps.
Therefore, accurate sensing and control of local powder bed temperature, laser power, laser fill scan spacing, laser beam speed, powder properties are the main precautions to reduce these undesirable effects.

ACKNOWLEDGMENT

The authors acknowledge the financial support of Eurostars E!11261 slsPEEK4smal-series project in the frame of the EUREKA initiative of the European Union and the national funding agencies in Turkey (TUBITAK) and Austria (FFG).

REFERENCES

Drummer, D., Rietzel, D., Kuhnlein F. (2010). Development of a characterization approach for the sintering behavior of new thermoplastics for selective laser sintering, Physics Procedia, 5, 533–542.

Dupin, S., Lame, O., Barres, C., Charmeau, J.-Y. (2012). Microstructural origin of physical and mechanical properties of polyamide 12 processed by laser sintering. European Polymer Journal, 48, 1611-1621.

Goodridge, R. D., Tuck, C. J., Hague, R. J. M. (2012). Laser sintering of polyamides and other polymers. Progress in Materials Science, 57(2), 229-267.

Kausch, H. H., Gensler, R., Grein, C., Plummer, C. J. G., Scaramuzzino, P. (1999). Crazing in semicrystalline thermoplastics. Journal of Macromolecular Science, Part B Physics, 38, 803-815.

ON THE OPTIMIZATION OF METAL SPATTER SWEEPING IN SELECTIVE LASER MELTING

Ahmet Yusuf Gürkan[1], Mehmet Bursa[1], Evren Yasa[2], Erdem Öğüt[1,3,4]
[1]*FİGES Engineering, Istanbul, Turkey*
[2]*Eskişehir Osmangazi University, Eskisehir, Turkey*
[3]*Leibniz Institute of Photonic Technology, Jena, Germany*
[4]*Friedrich Schiller University, Jena, Germany*
Corresponding author: erdem.ogut@figes.com.tr

Abstract. Selective Laser Melting (SLM) is one of the widely utilized additive manufacturing processes used to manufacture fully functional metal parts with fine details and good mechanical properties. There are many process parameters affecting the final part quality. Some of these parameters, e.g. the amount of leftover oxygen in the chamber, raw material quality, build direction, are well addressed in the literature for a wide of materials. However, the factors influencing the inert gas circulation quality are less studied although sweeping metal spatter out of the process chamber is crucial as metal spatter can interfere with the laser beam or end up in the virgin metal powder, being the cause of various process flaws. In this study, the interaction of inert gas flow with metal spatter microparticles is investigated using a Discrete Phase Model (DPM) of Computational Fluid Dynamics. A three-dimensional design of the SLM build chamber is utilized in DPM analyses. AISI 316L stainless steel microparticles with various diameters (50 μm, 100 μm), angles of injection (45°-135°), and injection velocities (0.5-10.0 m/sec) are investigated as a function of gas flow rate. It is demonstrated that for particles injected with identical velocities and diameters the angle of injection (perpendicular, upstream, and downstream) has no significant effect on particle trajectory; thus, the number of particles leaving the process chamber. It is shown that particle mass and injection velocity, designating particle kinetic energy, have a major effect on particle trajectory at constant gas velocity.

Keywords: Selective Laser Melting, Metal Spatter, Computational Fluid Dynamics

1. INTRODUCTION

Selective Laser Melting is an additive manufacturing process whereby the metallic powder is selectively scanned and melted under protective atmosphere to be able to create complex 3D parts in a layerwise manner. One of the most critical aspects in order to manufacture fully functional metallic parts by the SLM process without inacceptable defects is the management of the protective gas flow. However, this effect is generally underestimated in the process development phase. It is not taken as a primary process variable but it can be encountered while searching for the root cause of process variability between the mechanical properties of parts built on different locations of the base plate, the gas flow rate as was the case for the study by De Bruycker et al. [1] Especially, in the phase of component development for the SLM process, it is crucial to study the effect of distinguished design concepts involving the gas circulation due to its direct effect on metal spatter and defects occurring inside the material. Thus, this study aims to investigate the effect of different particle size, injection angles and injection velocities as a function of flow rate in SLM of AISI 316L stainless steel using a Discrete Phase Model (DPM) of Computational Fluid Dynamics (CFD).

2. MATERIALS AND METHODS

The CFD analysis, using finite volume method, utilized Navier-Stokes (N-S) equations under incompressible flow assumption. The pressure-velocity pair is considered with the Coupled Algorithm. The Coupled Algorithm uses a modified time-dependent solution algorithm. The time step is specified as $\Delta t=CFL/(u/L)$ where "Δt" is a measure of the user-specified Courant-Friderich-Lavy number, "L" is the cell size, and "u" is the local velocity.

Turbulence effects are included via the k-ε Realizable model, which is a two-equation turbulence approach [2]. The area around the walls of the SLM build chamber is handled with the Enhanced Wall Treatment algorithm. The gradient between the cells was calculated by cell-based least squares method. Pressure separation is performed by the PRESTO! method [3]. Momentum and turbulence equations are separated by the Second Order Upwind method [4]. Discrete Phase Modeling (DPM) approach [5] was used to include the size, velocity and injection direction of spatter particles into the simulations. Metal spatter was represented by spherical particles and calculations were performed with the Langrangian approach. Spatter particles injected into the production cabinet are affected by the velocity of the inert gas flow, while not affecting the overall flow area; in other words, a one-way interaction modeling is considered.

3. RESULTS AND DISCUSSION

The dimensions, injection vectors, and velocities of the spatter particles are shown in Figure 1b. Spatter particles were injected on the baseplate from 9 different locations covering the whole surface.
Three cases were studies where the gas flow rate increases at each case, namely, 40.7 m^3/hr, 203.5 m^3/hr, and 404.2 m^3/hr. Spatter diameter, velocity and direction are set to various levels obtained from experimental studies in the literature. In Case-1, the injection direction affects the number of particles exiting the build chamber through the outlet channel. This leads to the fact that the design of the inlet and outlet channels is critical for effective cleaning of metal spatter. Among the particles sitting in the second row on the baseplate, those injected in the same direction as the inert gas can leave the chamber more easily while those injected perpendicular or opposite to the flow cannot be sweeped out. When the injection rate is 1.00 m/s particles are in general able to leave the chamber, while for 2.00 m/s almost all particles stayed in the chamber. In Case-2, all of the particles injected at 45° and 135° were able to leave the system. As the perpendicular injection velocity is increased to 2 m/s, which is 4 times the kinetic energy, almost none of the particles were able to exit through the exhaust line. In Case-3, only particles at a single location on the baseplate remained in the chamber for an injection velocity of 5 m/s and a particle size of 50 μm.

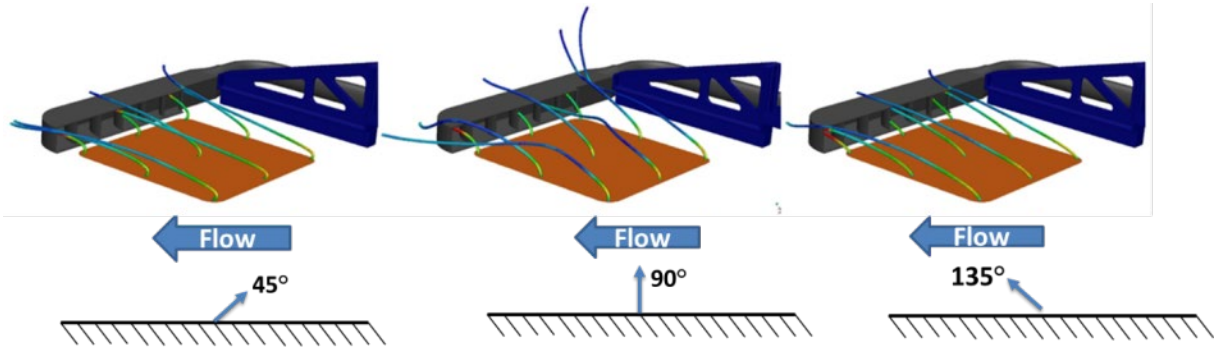

Figure 4. Case-1: Injection of metal spatter particles at various angles. Injection rate is 0.5 m/s and particle size is 100 μm.

4. CONCLUSIONS

This study shows that the design of inlet and outlet of SLM equipment shall be based on scientific studies with the help of CFD tools rather than trial-and-error approach in order to sweep the metal spatter efficiently from the melt pool area and the protective glass. Our study involving three different cases also demonstrate the importance of gas flow rate, spatter's diameter, velocity and direction, among which the gas flow rate is the only controllable factor by the process engineer.

REFERENCES

[1] E. De Bruycker , F. Thielemans, M. Caruso, S. Nardone, 2019, Ensuring and validating process stability for qualification of large industrial SLM machine, 4th Workshop On Metal Additive Manufacturing, 27-28th May, Leuven, Belgium.
[2] Blazek, J. (2001). Computational Fluid Dynamics: Principles and Applications. Oxford, UK: Elsevier.
[3] Patankar, S. V. (1980). Numerical Heat Transfer and Fluid Flow. Washington, DC: Hemisphere.
[4] Barth, T. J., & Jespersen, D. (1989). The design and application of upwind schemes on unstructured meshes. Technical Report AIAA-89-0366. AIAA 27th Aerospace Sciences Meeting. Nevada:Reno.
[5] Wilcox, D. C. (1998). Turbulence Modeling for CFD. California: Inc. La Canada.

PROCESSING OF NdFeB BY SELECTIVE LASER MELTING

Kubra Genc[1], Kamran Mumtaz[2], Iain Todd[3]
[1]*Depertmant of Mechanical Engineering, University of Sheffield, Sheffield,S1 4BJ,UK* kgenc1@sheffield.ac.uk
[2]*Depertmant of Mechanical Engineering, University of Sheffield, Sheffield,S1 4BJ,UK* k.mumtaz@sheffield.ac.uk
[3]*Department of Materials Science and Engineering, University of Sheffield, Sheffield,S1 4BJ,UK*
iain.todd@sheffield.ac.uk

Abstract. The aim of this project is to improve the density and the magnetic properties of the NdFeB magnets using by Selective Laser Melting (SLM). The main disadvantages of the SLM NdFeB magnets are firstly the porosity of the samples due to the intermetallic structure of the NdFeB, secondly the residual thermal stresses due to fast cooling rate of the SLM process. The main objective of this project is to reduce the porosity and the internal cracks of the SLM- NdFeB magnets by process parameters and the heated bed. It was found that low energy densities, between 50 to 100 kJ/m^3, provide reasonably dense samples than the high energy densities. Based on the Archimedes density test results, up to 95% dense samples were obtained. Moreover, the maximum remanence value was 0.658 T, tested by Helmholtz coil and Fluxmeter. However, there were some defects observed mostly on the edge of the samples. It is assumed that the thermal differences between the building platform and the melted powder might cause these defects. Therefore, for the future studies heated bed SLM is going to be used to reduce the thermal differences.

Keywords: NdFeB, SLM, Laser Beam Melting, Additive Manufacturing, Permanent Magnets

1. INTRODUCTION

NdFeB magnets have been used in various areas. Since NdFeB magnets have high energy product, BH_{max}, and they can keep their magnetism for long period, they are highly demanded within the application areas which permanent magnets are used (LaSalle 2014).
In this project NdFeB magnets were produced by the selective laser melting. SLM, is one of the powder bed additive manufacturing (AM) methods which enables to complex part geometry without tooling cost and material waste (Anderson et al. 2013). The production of the complex shaped magnets is difficult by the conventional techniques due to their brittle structure (Jaćimović et al. 2017). With this aspect selective laser melting is a promising technique to produce NdFeB magnets.

2. MATERIALS AND METHODS

In this study commercial MQP-S-20001-070 NdFeB powder (supplied by Magnequench) was used. The morphology of the powder was checked by the SEM, Hitachi TM 3000.The samples were printed in 10*10*5 mm^3 sizes by the Selective Laser Melting "Aconity Mini" which uses continuous-mode laser. The densities of the samples were analyzed by the Archimedes density test. The magnetic properties were tested with Helmholtz coil and the Fluxmeter.

3. RESULTS AND DISCUSSION

It was found that there were no successful parts obtained over around 125kJ/m^3 energy densities due to the boiling of powder. Therefore, energy densities were reduced, below 100 kJ/m^3. Figure 1 shows some of the successful samples. However, there were some defects seen mostly on the sample edges and the bottom of the sample, pointed by red arrows in Figure 1. It is assumed that the temperature difference between platform and the melted powder causes these defects. It was observed that defects reduce as the printing progresses. The printing parameters were summarized in Table 1.

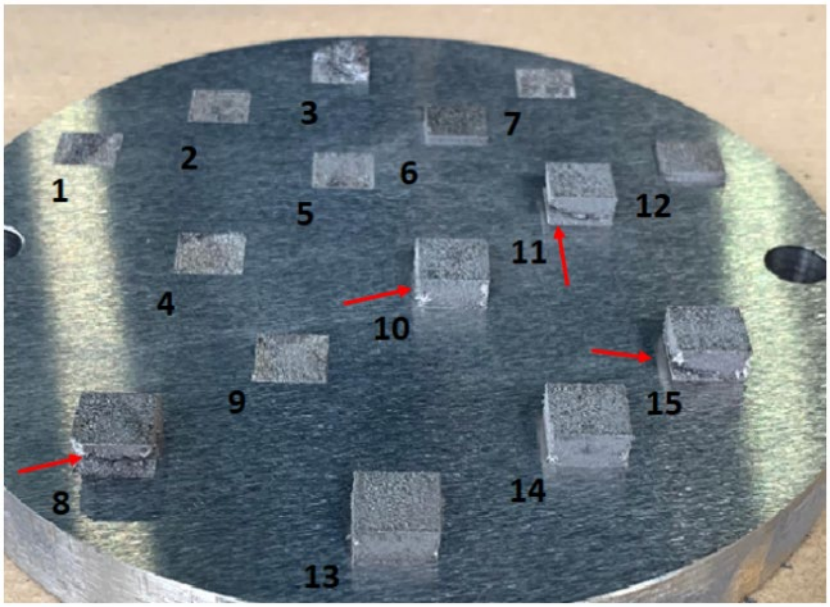

Figure 1. Sample photos of the NdFeB Magnets printed by SLM, from sample 1 to 15.

Table 1. Summary of the printing parameters

Parameter	Value
Hatch distance, µm	20
Layer thickness, µm	30
Laser power, Watt	40 -100
Laser speed, mm/s	1000-3000
Energy density, J/mm^3	50-83

4. CONCLUSIONS

- There were no successful samples printed by the high energy density scan parameters, above 125 kJ/m^3. Samples felt apart during the cleaning of surrounded powder by brush.
- Some defects seen in the samples, mostly on the edges which are possibly due to the thermal differences between built platform and the melted powder.
- Up to 95 % dense samples were obtained by the lower energy densities below 100 kJ/m^3.
- The maximum obtained remanence is 0.658 T.

Further studies will focus on the heated bed to decrease the residual thermal stress.

REFERENCES

Anderson, K. et al. 2013. “Simultaneous Multi-State Equine Business Education Program.” *Journal of Equine Veterinary Science* 33(5): 389. https://linkinghub.elsevier.com/retrieve/pii/S073708061300261X.

Jaćimović, Jaćim et al. 2017. “Net Shape 3D Printed NdFeB Permanent Magnet.” *Advanced Engineering Materials* 19(8).

LaSalle, University of. 2014. “Magnetic Susceptibility.” *Notes* (May): 4–7.

LASER INDUCED BREAKDOWN SPECTROMETRY FOR ONLINE ANALYSIS OF METAL PARTICLES FEEDSTOCK DURING LASER METAL DEPOSITION PROCESS

Pavel A. Sdvizhenskii[1,2], Vasily N. Lednev[1,2], Roman D. Asytin[3], Mikhail Ya. Grishin[1,4], Sergey M. Pershin[1]
[1]*Prokhorov General Physics Institute, Russian Academy of Sciences, Moscow, Russia*
[2]*National University of Science and Technology MISiS, Moscow, Russia*
[3]*Bauman Moscow State Technical University, Moscow, Russia*
[4]*Moscow Institute of Physics and Technology (State University), Dolgoprudny, Moscow Region, Russia*
E-mail: pausdw@gmail.com+9

Abstract. Laser induced breakdown spectroscopy (LIBS) has been used for elemental analysis of metal powder jet during coating synthesis by coaxial laser cladding. Coaxial laser cladding is an additive manufacturing technology (laser direct metal deposition) based on part build-up process with metal powder melting by powerful continuous wave laser. A compact and lightweight LIBS probe has been designed to equip the laser cladding head installed on an industrial robot.
Samples of wear resistant coatings (nickel alloy matrix reinforced with tungsten carbide particles) synthesized with variable proportions of powder flows were deposited while LIBS analysis was carried out. Deposited tracks were cooled, cut off and analyzed by X-ray fluorescence spectroscopy in laboratory conditions. The LIBS system was calibrated for quantitative analysis of major components.

Keywords: laser induced breakdown spectrometry, coaxial laser cladding, metal particle analysis.

1. INTRODUCTION

Additive manufacturing is a promising technology that allows to create parts with unique characteristics and properties. For aviation industry, industrial engineering plays a major role production parts with designed gradients of elemental composition (Hofmann et al., 2014). Therefore, synthesis of compositional graded parts requires rapid elemental analysis. However, high reproducibility of the product's properties is difficult to achieve. Real time monitoring of metal powder feedstock used in additive manufacturing will be good for possible failures detection during metal processing part. Optical spectroscopy is a low cost but powerful alternative for real-time monitoring of additive manufacturing processes.
Laser induced breakdown spectroscopy (LIBS) can be a good choice for developing instrument for online quantitative multielemental analysis of metal particle feedstock during additive manufacturing process.

2. MATERIALS AND METHODS

The experimental setup was based on coaxial laser cladding setup. Continuous wave ytterbium doped fiber laser beam (1070 nm, 2 kW, YLS-5 by IPG Photonics) was focused by quartz lens (F=200 mm) 20 mm above the target surface. Coaxial cladding head (YC-50 by Precitec) was manipulated by industrial robot arm (IRB-2400 by ABB). Cladding head was equipped with the compact LIBS probe (Lednev et al., 2018). The experiment setup for cladding and LIBS probe is shown in Figure. 1. Laser beam of diode pumped solid state Nd:YAG laser (1064 nm, 5 ns, 130 mJ/pulse, $M^2 \approx 90$, 10 Hz) was focused by quartz lens (F=280 mm) through the pierced aluminum mirror to the samples surface.

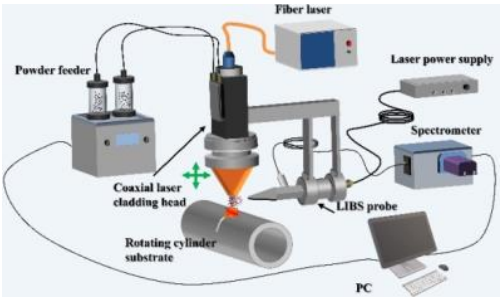

Figure 1. Scheme of the coaxial laser cladding setup equipped with the laser induced breakdown spectroscopy (LIBS) system for analysis of metal powder flow

Plasma emission was collected and transferred to the entrance of fiber optic cable. Fiber optics output fit the entrance slit of the Czerny-Turner spectrograph (Shamrock 303i, Andor) equipped with the intensified CCD camera (iStar, Andor).

3. RESULTS AND DISCUSSION

LIBS sampling was carried out at different areas of gas-powder jet at coaxial nozzle but greater intensity and better signal reproducibility was achieved at jet waist.
The emission of laser plasma induced at powder particles was significantly lower compared to that for bulk sample. LIBS signals reproducibility for metal particles was also poorer compared to conventional ablation of metal target. The process of LIBS metal particle analysis during deposition is illustrated in Figure 2

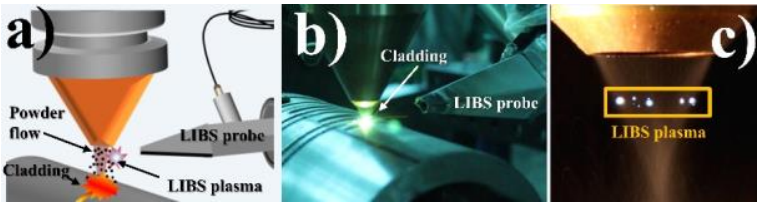

Figure 2. Scheme (a) and photo (b) of metal particle feed analysis during deposition. LIBS plasma photo (c) on metal powder flow. Calibration curve (d) for tungsten by laser induced breakdown specrtometry

Spectral range, plasma emission gating and spectra averaging were selected to improve the LIBS signal reproducibility. The LIBS system was calibrated for quantitative analysis of major components.

4. CONCLUSIONS

Samples of wear resistant coatings (nickel alloy matrix reinforced with tungsten carbide particles) synthesized with variable proportions of powder flows were deposited while LIBS analysis was carried out. Deposited tracks were cooled, cut off and analyzed by X-ray fluorescence spectroscopy in laboratory conditions. A good agreement with LIBS results is achieved.

REFERENCES

Hofmann, D. C., Roberts, S., Otis, R., Kolodziejska, J., Dillon, R. P., Suh, J. O., … Borgonia, J. P. (2014). Developing gradient metal alloys through radial deposition additive manufacturing. *Scientific Reports*, *4*. https://doi.org/10.1038/srep05357

Lednev, V. N., Dormidonov, A. E., Sdvizhenskii, P. A., Grishin, M. Y., Fedorov, A. N., Savvin, A. D., … Pershin, S. M. (2018). Compact diode-pumped Nd:YAG laser for remote analysis of low-alloy steels by laser-induced breakdown spectroscopy. *JOURNAL OF ANALYTICAL ATOMIC SPECTROMETRY*, *33*(2), 294–303. https://doi.org/10.1039/c7ja00319f

INFLUENCE OF BUILD ORIENTATION ON RESIDUAL STRESSES IN 3D PRINTED PARTS

Prabhat Pant[1], Ru Peng[1], Johan Moverare[1], Kjell Simonsson[1], Sören Sjöström[1]
[1]*Dept. of Management and Engineering, Linköping University, Sweden*
prabhat.pant@liu.se

Abstract. Additive manufacturing has great potential in manufacturing of complex geometry parts, which are optimized with respect to functionality. Parts manufactured using the powder bed fusion process including selective laser melting (SLM) often show build-direction dependent mechanical behavior. In this work the influence of build-direction on residual stresses in IN718 bars printed with the SLM process are studied using lab-scale XRD and the results are compared to simplified finite element simulations. The purpose of the work is to increase understanding of the influence of printing condition on the behavior of SLM parts.

Keywords: *Additive manufacturing, Inconel718, Residual stresses, XRD, FE simulation*

1. INTRODUCTION

During manufacturing of parts by a layer-by-layer approach using laser and powder bed, residual stresses (RS) are generated, owing to the thermal gradient induced in the parts. Residual stresses are stresses that remain inside the part in a self-balanced state when no external loads are applied to it. Depending upon the distribution of the RS, it can both be useful and detrimental for the mechanical performance of the part. Compressive residual stresses near the surface of a part are known to increase the fatigue life by slowing down the crack formation and propagation whereas tensile residual stresses can lead to failure of the part well below its estimated fatigue durability. Additionally, the higher level of RS can lead to deformation and cracks in part during printing. Additive manufacturing offers a great deal of flexibility in the selection of processing parameters to achieve parts of good quality at the end and one of the parameters is the build direction. Proper planning with regard to build direction is not only important to utilize the printing area to its maximum but also for the mechanical properties as well. Previous work has shown that depending upon the build orientation the mechanical properties varies(Bean et al., 2019; Deng, Peng, Brodin, & Moverare, 2018). In this work, we investigate the residual stresses generated in parts with different printing orientations and significance of RS with anisotropic properties reported earlier.

2. MATERIALS AND METHODS

Two rectangular bars of dimensions of 80mm x 11mm x 11 mm and 80mm x 15mm x 11mm respectively were printed out of Inconel 718 powder using the laser-based powder bed fusion process (LPBF) in two build orientations, namely vertically (VB) and horizontally (HB), respectively. Printing of the part was done using an EOS M290 machine with base plate preheated to 80°C and a 40µm thickness for each layer. The standard manufacturing parameters recommended by EOS were used. After the printing, the parts were removed from the base plate for the residual stress measurement. X-ray diffraction was utilized to measure the stress using the so-called Sin $^2\psi$ technique. Here diffraction peaks were measured at multiple tilt-angles from ψ = -55° to ψ = +55°. The measurement was done at side surface at mid-length of the bars. In order to obtain the RS depth profile, layers were removed in subsequent steps from the side surface into the bulk using electrolytic polishing and stresses were measured for each layer. With the Cr source diffraction peaks from {220} planes of the matrix γ-phase were measured. The obtained peaks were fitted using pseudo-voigt function the material and the inter-planer distance was calculated from the Bragg's law and the X-ray elastic coefficients (XEC) E_{220} = 280 MPa and ν_{220} =0.298(Chen et al., 2017) were used for calculation of the stress. Correction for the stress redistribution due to the material removal was also done for the measured data(SAE, n.d.).

A simple transient FE analysis model was developed for the prediction of residual stresses using the Abaqus software and utilizing the element deactivation and activation technique. Instead of using a moving heat source as in real build, temperature is used as a load. A temperature of 1500 K was used for the entire part at the beginning of the simulation. The build process was further simplified by combining multiple layers of print into one combined layer. Initially, the entire part is deactivated and each combined layer is activated after certain amount of time. Time for each layer activation is calculated based on laser speed used in the real print. Time for the re-coater to apply new layer of powder and the part to move inside the powder bed is also incorporated into the model in between layer activation. Heat loss to environment is modeled through radiation and via conduction through the base plate. At last the base plate was also removed with element deactivation with proper implementation of boundary conditions to restrict rigid body motion. Results from the simulations are extracted at the integration points of the elements at the same location as measured experimentally.

3. RESULTS AND DISCUSSION

The depth profiles from the XRD as seen in **Figure 1** reveal that for the build direction of the horizontally built sample high tensile residual stresses prevail in a significantly thick surface layer until the depth of 2100 µm, which gradually change to compressive towards the bulk of the material thereafter. At the surface 800 MPa was measured. Whereas for the transverse direction, it shows compressive stress in a small layer near the surface and after 300 µm it becomes tensile stress which remains in a magnitude of around 200 MPa until the depth of 2200 µm.
From the simulation, higher tensile RS are predicted in the build direction compared to the transverse direction. Prediction of the stress distributions from the FE model are similar to the experimentally measured one. From FE model, magnitude of the predicted residual stresses in the building direction at the surface are higher than the experimentally measured ones. For the transverse direction, the agreement between experiments and simulations is very good except the very near surface where compressive stresses have been measured which is not captured by the model.

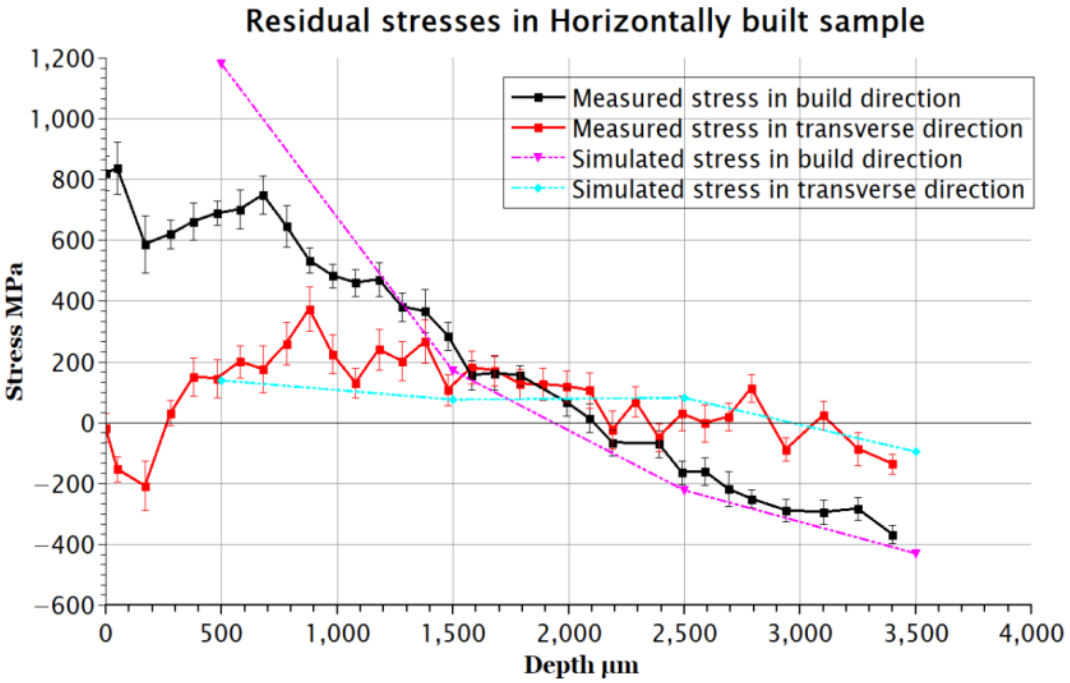

Figure 5. Residual stress distribution for the horizontally built sample.

For the vertically built (VB) sample (see **Figure 2)** tensile residual stresses were observed in the build direction for a thick surface layer of 1600 µm and changes to compressive thereafter. For the transverse direction, residual stresses measured were also in tension near the surface until the depth of 2100 µm and

changes to the compressive stress thereafter. Here, the tensile residual stress measured in build direction is almost 4 times higher than the transverse direction at the surface; also, in general the tensile stress measured is lower in transverse direction than in build direction. The simplified FE simulation also predicts the similar trend of higher RS in build direction for the VB and lower in the transverse direction. Here also magnitude of the predicted stresses in build direction are higher than measured experimentally and the slope of the stress distribution is steeper than the experimentally measured profile. As for the transverse direction, the predicted stresses are also higher than measured values in the region close to the surface.

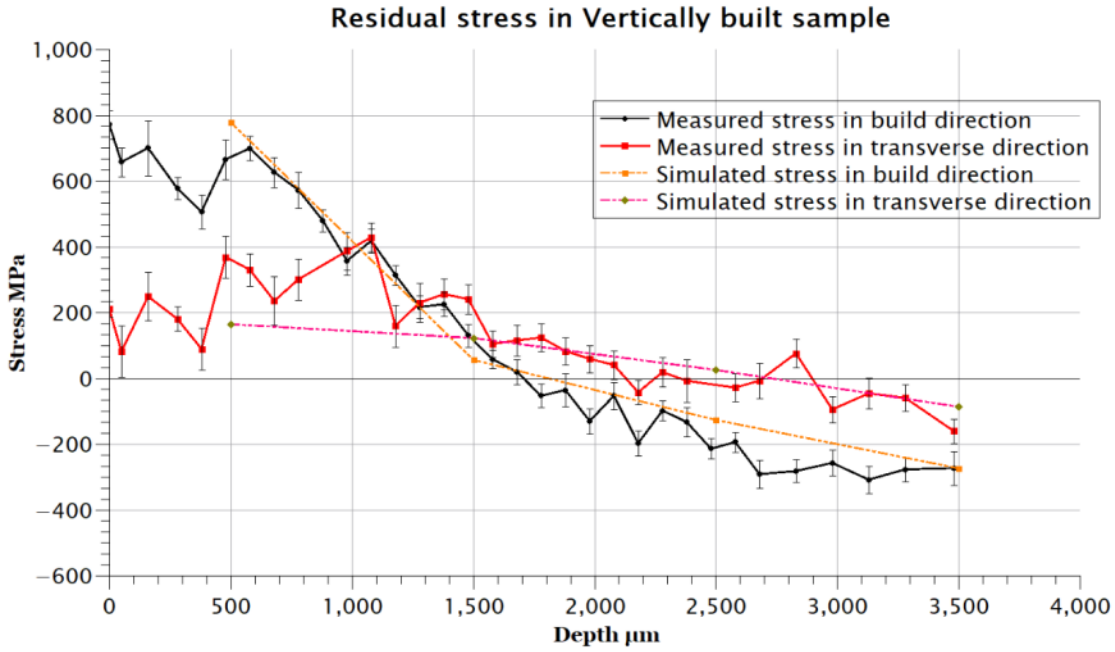

Figure 6. Residual stress distribution for the vertically built sample

Comparing the stress distributions for the build direction for VB and HB samples there is a steeper slope for the VB samples moving from surface to bulk of the sample than compared to the HB sample. In addition, for the transverse direction, the stresses were lower for the horizontally build sample than the vertically built samples. Nonetheless, the largest tensile residual stresses were observed to be associated with the build direction in both samples. One of the factors that attribute to the fact that RS in build direction is higher than in other direction is that in build direction the heat dissipation is greater due to heat transfer from the new build layer to the base plate via conduction and also the radiation from the surface. Whereas in transverse direction the heat dissipation is through the loose powder that will cause lower heat loss from the surface thus results in lower RS.

Due to a strong interaction between the sample and base plate during printing, larger residual stresses would be expected in the samples before removal from the base plate. As the samples were detached from the base plate, the impact of the removal is greater for the sample built in the horizontal direction due to the larger surface in contact with the base plate(Thiede et al., 2018). So, the difference between the two samples could be attributed to a larger effect from cutting when the samples were removed from the plate.

The observed high tensile residual stress in build direction can be one of the factors that can affect the mechanical properties in the build direction in real load case scenario. Samples investigated in this work are from the same batch as of samples investigated in previous work (Deng et al., 2018) and they have shown different mechanical properties for different build orientation. These higher levels of tensile residual stresses in the sample can be a contributing factor for the apparent mechanical anisotropy reported in previous works in as-built state and after heat treatment (Bean et al., 2019; Deng et al., 2018).

4. CONCLUSIONS

Generally, tensile residual stress has been observed near the surface and this can have a negative effect in part performance in real load case scenario. It was observed that the tensile residual stress zone can be very big in contrast to the general understanding of tensile residual stress confined near the surface layers only. Higher tensile RS were observed from both measurement and simulation in the build direction in comparison to the transverse direction for both build orientations with HB sample having somewhat smaller section of tensile zone in build direction. In case of the transverse stress, for VB it was dominantly tensile near the surface but compressive for HB near surface. Residual stress plays significant role in determining the mechanical properties and built orientation seems to have an impact on the level of the residual stress generated. Proper selection of build orientation is necessary with regard to real world application of the part being manufactured. The simplified FE model can reasonably predict residual stresses distribution in shorter time and higher level of the stress predicted by the model can be due to idealized conditions during simulations and material properties used. The simplified model can be further extended for use in complex parts to identify the best possible orientation and the critical areas with respect to residual stresses and refine the process parameter for better mechanical properties.

ACKNOWLEDGMENT

This research is funded by the Swedish Foundation for Strategic Research (SSF) within the Swedish national graduate school in neutron scattering (SwedNess).

REFERENCES

Bean, G. E., McLouth, T. D., Witkin, D. B., Sitzman, S. D., Adams, P. M., & Zaldivar, R. J. (2019). Build Orientation Effects on Texture and Mechanical Properties of Selective Laser Melting Inconel 718. *Journal of Materials Engineering and Performance*, *28*(4), 1942–1949. https://doi.org/10.1007/s11665-019-03980-w

Chen, Z., Lin Peng, R., Moverare, J., Widman, O., Gustafsson, D., & Johansson, S. (2017). Effect of Cooling and Shot Peening on Residual Stresses and Fatigue Performance of Milled Inconel 718. In *Residual Stresses 2016* (Vol. 2, pp. 13–18). https://doi.org/10.21741/9781945291173-3

Deng, D., Peng, R. L., Brodin, H., & Moverare, J. (2018). Microstructure and mechanical properties of Inconel 718 produced by selective laser melting: Sample orientation dependence and effects of post heat treatments. *Materials Science and Engineering A*, *713*(October 2017), 294–306. https://doi.org/10.1016/j.msea.2017.12.043

SAE (Ed.). (n.d.). *Residual Stress Measurement by X-Ray Diffraction, 2003 Edition*. Retrieved from https://www.sae.org/publications/books/content/hs-784/2003/

Thiede, T., Cabeza, S., Mishurova, T., Nadammal, N., Kromm, A., Bode, J., … Bruno, G. (2018). Residual Stress in Selective Laser Melted Inconel 718: Influence of the Removal from Base Plate and Deposition Hatch Length. *Materials Performance and Characterization*, *7*(4), 20170119. https://doi.org/10.1520/MPC20170119

EVALUATION OF ALTERNATIVE PARAMETERS TO DESCRIBE THE QUALITY OF ADDITIVELY MANUFACTURED ALUMINIUM ALLOY SURFACES

Buchenau, Theresa[1], Amkreutz, Marc[2], Brüning, Hauke[3], Norda, Michael[4]
Fraunhofer Institute for Manufacturing Technology and Advanced Materials IFAM, Bremen, Germany
[1] *theresa.buchenau@ifam.fraunhofer.de*
[2] *marc.amkreutz@ifam.fraunhofer.de*
[3] *hauke.bruening@ifam.fraunhofer.de*
[4] *michael.norda@ifam.fraunhofer.de*

Abstract. Recent developments in metal additive manufacturing offer new possibilities for various applications by enabling lightweight, biomimetic designs. Reductions in material waste and manufacturing process duration are viable. When qualifying additively manufactured metal parts, especially the surface quality is challenging. Characteristic for metal additive manufacturing surfaces are powder particle agglomerations, sub- surface voids and undercuts. The special nature of those surfaces cannot be described by means of commonly used surface parameters like arithmetic mean height (Ra / Sa) and maximum profile height (Rz / Sz, ISO 4287 and ISO 25178). Therefore, in this work, less common parameters described in the aforementioned standards are considered in order to find a set of parameters to characterize metal additive manufacturing surfaces.
For selected aluminium alloys and a laser beam melting process, surface parameters obtained from a structured light scan were examined statistically. Furthermore, sample densities have been determined following Archimedes' principle.
Ultimately, the aim is to find a set of parameters enabling a holistic description of additively manufactured metal surfaces and their characteristic features. The correlation of printing parameters with standardized surface parameters and results of alternative surface characterization methods as well as fatigue life are subject to further investigation.

Keywords: Surface Quality, Metal Additive Manufacturing

1. INTRODUCTION

Additive manufacturing technologies enable lightweight, functionally integrated designs and development of biomimetic structures. They contribute to the reduction of material waste and decrease in overall process durations. The benefits make additive manufacturing interesting for applications in the aerospace industry. A major challenge when qualifying additively manufactured parts for aerospace applications is posed by the surface quality and its assessment, especially on complex geometries.
Characteristic for the as-built surface condition of metal parts manufactured by a laser beam melting process are agglomerations of partially melted powder particles, resulting in a high initial surface roughness (Townsend et. al. 2016). Surface quality plays an important role when looking at cyclically loaded parts, since rougher surfaces are more prone to crack initiation, or when protective coatings have to be applied. In as-built quality (without application of surface treatments), particle agglomerations complicate the application of the tactile surface detection method, which is currently most commonly used for surface roughness measurements. Furthermore, this method fails to capture a representative portion of the evaluated surface, as they only take a linear profile measurement. An interesting alternative is posed by optic methods like laser scanning confocal microscopy, structured light scan or light scattering measurement (Townsend et. al. 2016).
In this paper, the effect of laser beam melting process parameters applied to an aluminium alloy powder on resulting surface quality, assessed by means of structured light 3D scan, is discussed. The results have been assessed considering commonly used parameters like arithmetic mean height (Ra / Sa) and maximum profile height (Rz / Sz) as well as less frequently considered values as suggested in ISO 4287 and ISO 25178, with focus on areal data representation. Furthermore, density measurements have been performed according to Archimedes' principle and evaluated with respect to the parameter variation.
Ultimately, the aim is to find a set of parameters enabling a holistic description of additively manufactured metal surfaces and their characteristic features.

2. MATERIALS AND METHODS

2.1 Manufacturing of Samples

The samples have been manufactured in a laser beam melting (LBM) process on an EOS M270 with a laser diameter of 100µm. First sets of tested printing parameters have been based on literature examples (DebRoy et al. 2018) and adjusted to fit the available equipment. Based on the workability, one set of parameters has been selected, specified in Table 1. Subsequently, layer thickness, hatch distance and scan speed have been varied within the capabilities of the printer.

Table 1. Base printing parameters

Layer thickness	Hatch distance	Scan speed	Laser power
30 µm	0.12 mm	900 mm/s	195 W

The samples are cubic and have a size of approximately 10 mm x 10 mm x 10 mm. The selected aluminium alloy is AlSi7Mg0.6. Figure 1 shows microscopic images of a sample surface in as-built condition, where particle agglomerations are clearly visible.

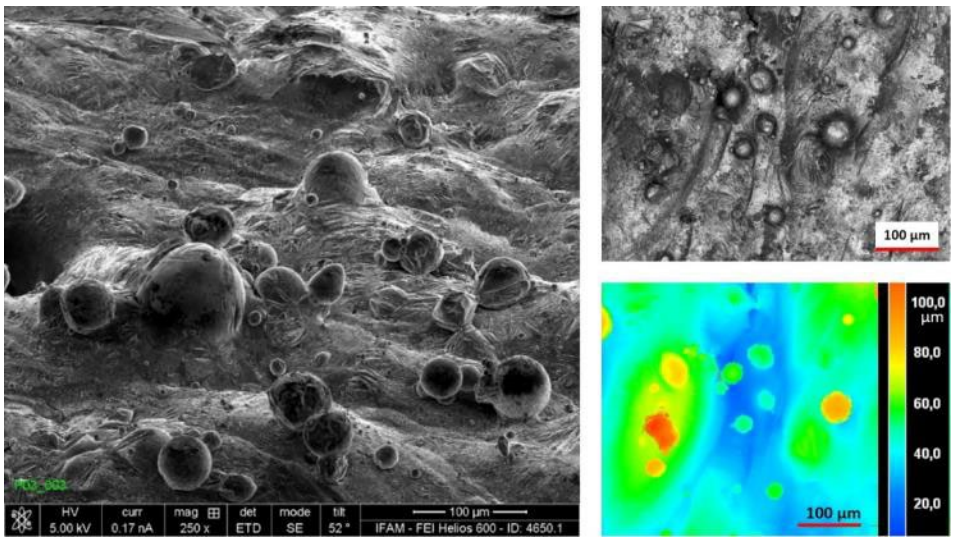

Figure 1. *Left:* Scanning electron microscope image showing agglomerations of partially melted powder particles of different sizes on the sample surface in as-built condition. *Right:* Laser scanning confocal microscope image and corresponding height representation**.**

2.2 Surface Characterisation

Areal surface characterization parameters have been determined according to ISO 25178 (Leach 2016), based on the data obtained from structured light 3D scan (Bhushan 2001). The measurements were performed using the Keyence VR-3100 structured light scanning microscope.
Selected parameters have been evaluated for multiple samples per set of printing parameters, 11 to 16 samples for layer thickness variation, three for scan speed variation and hatch distance. The latter will not be discussed but is mentioned for the sake of completeness.
In this work, in addition to Sa and Sz, the focus is on three parameters associated with the material ratio curve, given in Figure 2 (Leach 2016), namely Sk, Smr1and Smr2. Sk is the core material height of the profile, which is determined by the main slope line's intersection with a vertical line at 0% and 100%. Spk and Svk are the peaks and valleys outside the core. From those mentioned intersections, horizontal lines are drawn to meet the curve, defining Smr1 and Smr2 on the horizontal axis (Leach 2016).

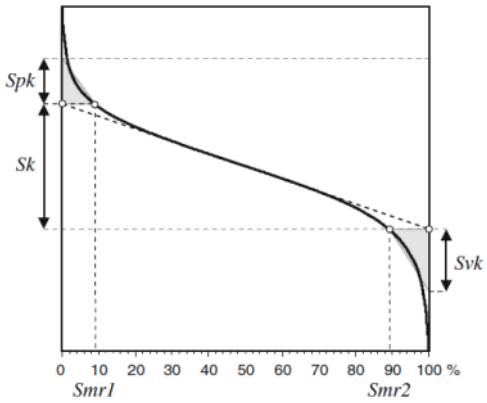

Figure 2. Material ratio curve - Determination of Sk with Spk and Svk, Smr1 and Smr2

2.3 Density Measurements

The densities for selected samples have been measured based on Archimedes' principle (Brown 1984). For each sample, three measurement have been taken and three samples for every set of parameters have been tested.

3. RESULTS AND DISCUSSION

3.1 Surface Characterisation

Commonly used parameters for surface quality assessment are the profile arithmetic mean height Ra and maximum profile height Rz with their areal extensions Sa and Sz. When describing additively manufactured metal surfaces, these parameters show very high standard deviations for samples manufactured using the same printing parameters. They react sensitively to local irregularities resulting in large standard deviations for samples manufactured using the same set of printing parameters. Table 2 shows mean values and standard deviations of selected surface characterisation parameters for base parameter samples (sides with same orientation w.r.t. the coater). The resulting values for Sk and Smr2 indicate, that even much lower standard deviation values are possible and give a clearer possibility to identify distinct manufacturing conditions.

Table 2. Mean, standard deviation and percentage standard deviation, 11 samples, base parameters, measured on the same sample side w.r.t. the coater

	Sa / µm	**Sz / µm**	**Sk / µm**	**Spd / 1/mm²**	**Smr1 / %**	**Smr2 / %**
MEAN	12.70	428.04	29.95	64.26	14.99	92.12
ST-DEV	1.46	61.18	1.47	3.65	0.82	0.58
% dev	*11.48*	*14.29*	*4.91*	*5.68*	*5.44*	*0.63*

The visualisations in Figure 3 show the dependences of ISO 25178 surface parameters and the variation of layer thickness. While the standard deviation for Smr2 and Sk remain below 1 % and 5 %, respectively, standard deviations for Sa reach over 20 %, for Sz even as high as 35 %.
As observable in Figure 3, when looking at sample quantities of 11 to 16 pieces, especially for the Sz values, high variations can be observed. The parameter gives the absolute height difference between the highest peak and lowest valley within the considered area, meaning it is very sensitive to outliers and hence cannot be used as a robust measure for the overall surface condition.
Considering the Smr1 (no graph) and the Smr2 parameters, containing information on the percentage of material outside core Sk, namely peaks and valleys, give a better overall indication and show better reproducibility across the set of samples (refer to Table 2, "% standard deviation"). One point to be

considered when looking at Smr2 is that its value is quite high and therefore the percentage standard deviation is low, while absolute standard deviation values are in the same order of magnitude for both, Smr1 and Smr2.

Similar to Sz, Sa is influenced by local features (its value is the average absolute profile height), even though the effect is much smaller. If it is expected, that the same printing parameters results in similar surface characteristics, this parameter with a possible standard deviation of more than 20 % is hardly reproducible for the chosen manufacturing condition.

The profile core height Sk (derived from the main slope of the material ratio curve in Figure 2), however, appears to be a robust parameter showing good reproducibility across the examined sets of samples. This is due to the main slope being hardly dependent on insular extreme values.

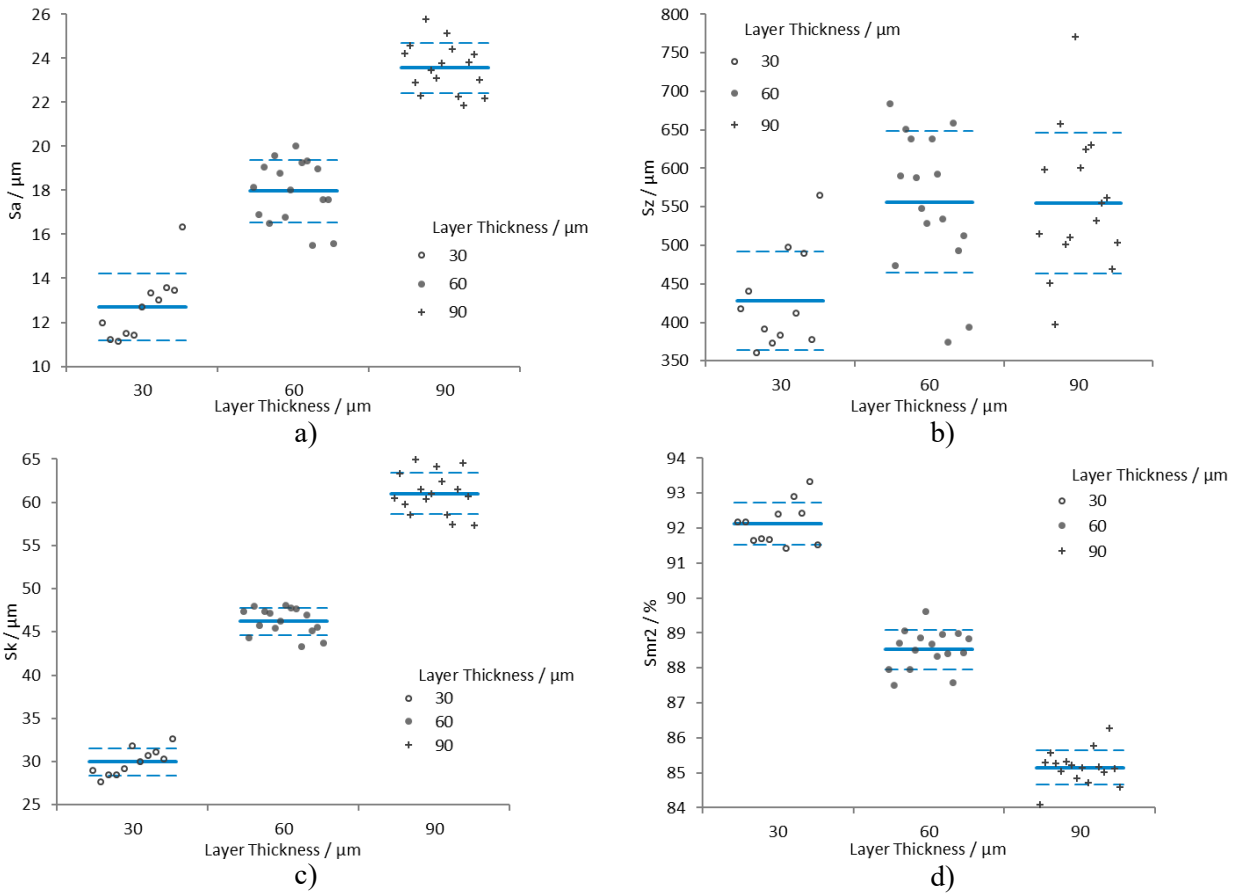

Figure 3. Mean value ± 1 SD for Sa (a), Sz (b), Sk (c) and Smr2 (d), variation of layer thickness

3.2 Density

The densities show a clear dependence on the variation of printing parameters, shown in Figure 4 for layer thickness and scan speed. Graph a) gives distinct densities with small variations for each set of samples, the density decrease is higher from 60 µm to 90 µm than from 30 µm to 60 µm, presumably due to internal voids caused by the applied laser power not being sufficient to properly melt through the entire 90 µm layer. With an AlSi7Mg0.6 material density of 2.68 g/cm³ (SLM Solutions) and a measured density for 30 µm layer thickness of 2.656 ± 0.003 g/cm³, a relative density of nearly 98 % is reached.

For the scan speed variation, a decreasing density trend with increasing speed can be observed for the first three sets. At 2000 mm/s and 2500 mm/s the density remains in the similar (i.e., within the standard deviation of 2000 mm/s). When increasing the scan speed even further (3500 mm/s have been tested), the samples crumble when touched, presumably due to the energy brought into the powder layer not being sufficiently high to melt it properly at high scan speeds.

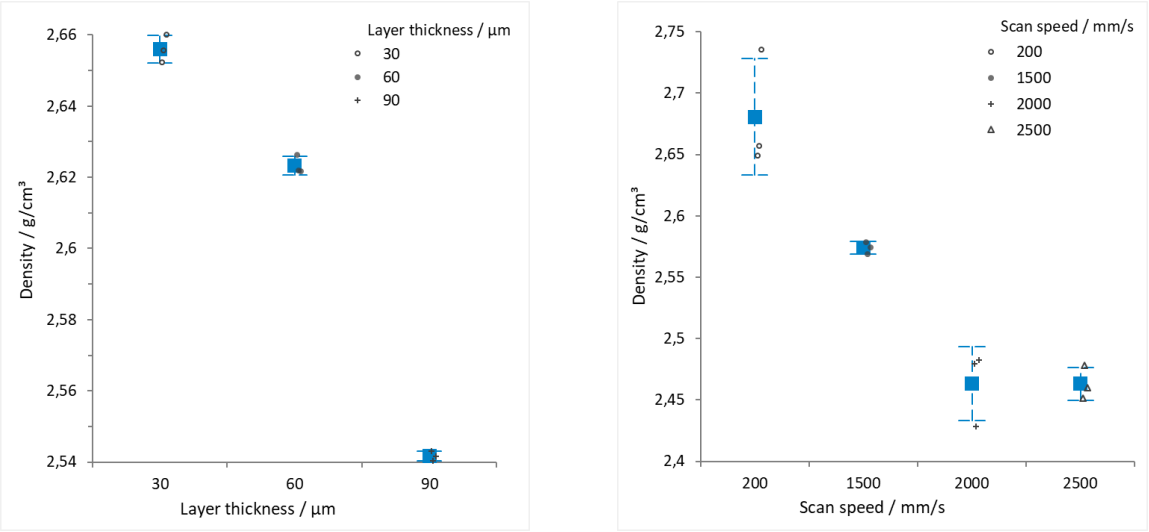

a) b)

Figure 4. Dependence of sample density on layer thickness and scan speed

4. CONCLUSIONS

Given similar surface characteristics are expected for the same set of printing parameters, the commonly used surface characteristics Sa and Sz show large deviations. More robust options for a description of the surface quality are Sk, Smr1 and Smr2, derived from the material ratio curve.
It has to be kept in mind that the definition of a "good" surface is still pending. The evaluation of mechanical properties and correlations between standard parameters and results of alternative surface characterisation methods is subject to further investigation.

REFERENCES

Bhushan, B.V. (2001). Surface Roughness Analysis and Measurement Techniques.
Brown, R.P. (1984). Taschenbuch Kunstoff-Prüftechnik (p. 122). München, Wien: Carl Hanser Verlag.
Debroy, T., Wei, H. L., Zuback, J. S., Mukherjee, T., Elmer, J. W., Milewski, J. O., Zhang, W. (2018). Additive manufacturing of metallic components – Process, structure and properties. *Progress in Materials Science*, *92*, 112-224. https://doi.org/10.1016/j.pmatsci.2017.10.001
International Organization for Standardization (2005). ISO 4287 - Geometrical Product Specifications (GPS) - Surface texture: Profile method.
International Organization for Standardization (2012). ISO 25178 - Geometrical product specifications (GPS) Surface texture: Areal.
Leach, R. (2016). Characterisation of Areal Surface Texture. Berlin: Springer Berlin.
SLM Solutions. Datasheet AlSi7Mg0.6. Retrieved from https://www.slm-solutions.com/de/produkte/zubehoer-verbrauchsmaterialien/slmr-metallpulver/ , June 2019.
Townsend, A., Senin, N., Blunt, L., Leach, R. K., & Taylor, J. S. (2016). Surface texture metrology for metal additive manufacturing: a review. Precision Engineering, 46, 34–47. doi:10.1016/j.precisioneng.2016.06.001

DESIGN AND VALIDATION OF GRADED POROUS STRUCTURES PRODUCED BY POWDER BED FUSION PROCESS

Mustafa Kaş[1] and Oguzhan Yilmaz[2]

[1] *Advanced Manufacturing Technologies Research Group, Mechanical Engineering Department, Gazi University, Maltepe, Ankara, Turkey, mustafakas@gazi.edu.tr*

[2] *Advanced Manufacturing Technologies Research Group, Mechanical Engineering Department, Gazi University, Maltepe, Ankara, Turkey, oguzhanyilmaz@gazi.edu.tr*

Abstract. Porous structures are formed by the repetition of the lattice elements in regular and/or stochastic manner. These are commonly used in production of lighter and more durable structures which have great importance mainly in aerospace for lighter aircraft components and medical implants for creating biocompatible designs. In this study, the design and validation of graded porous structures is presented. The porous structures are produced by powder bed fusion process which eliminates the constraints of traditional production techniques. Pores became functionally graded by designs which are inspired by the nature and validated by numerical analyses. Functionally graded structures are designed by changing the strut diameters by which increasing and decreasing the strut diameters from inside to outside in the porous structure. The designs were characterized by some laboratory tests using calipers, precision scales, SEM-EDS and uniaxial compressive devices for physical and mechanical properties of the samples produced by selective laser melting process. The obtained results were evaluated in the scope of producibility, porosity, maximum compression stress and elastic modulus.

Keywords: Additive manufacturing, selective laser melting, porous structures

1. INTRODUCTION

The interest for metallic lattice structures with regular and/or variable unit cell architecture which are almost impossible or difficult to manufacture using conventional techniques, is increasing day by day. Additive manufacturing allows to produce mechanically more robust, economically cheaper and lighter structures and thus optimized porous structures can be designed. In the optimization of porous structures, the studies have been carried out on the parameters such as lattice structure type, size and strut diameter which determines the pore size. Larger pore size is preferred when light weight is aimed, and small pore size is preferred when strength is required. The density of the porous structure can be changed according to design achievements. Functionally graded porous structure (FGS) can be obtained by continuously or graded changing the density in a porous structure. This work aims therefore to design graded porous structures using biomimetic approaches and tested for validation.

2. MATERIALS AND METHODS

Lattice structures were manufactured using Enavision powder bed fusion process machine commercialized by Ermaksan Makina Inc., Bursa, Turkey. 10 to 45 µm spherical Ti-6Al-4V grade 5 titanium powder was used and all processing parameters (laser power, scan speed, hatch spacing, layer thickness and scan strategy) were kept constant for all samples. Cubic porous specimens were built with a 24 mm dimensions, as specified in ISO 13314 [1]. The rhombic dodecahedron unit cell was used as the micro-architecture for all test samples, with a constant and changing strut diameter of 0.3 mm and 0.4 mm.

Table 1. Dimensions of the designed lattices

Design	Unit Cell Length, H	L1	L2	d1	d2
1. A	3 mm	24 mm	12 mm	3 mm	-
2. B	3 mm	24 mm	12 mm	3 mm	4 mm
3. C	3 mm	24 mm	12 mm	-	4 mm
4. D	3 mm	24 mm	12 mm	3 mm	4 mm

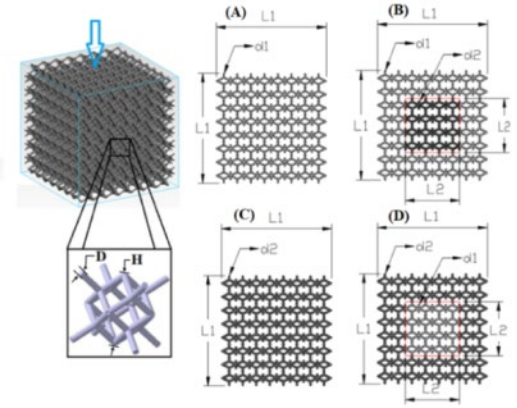

Figure 7. 3D and sectional view of the designed lattices (A, B, C, D)

Procedures to determine physical properties can be divided into two categories; macro-dimensional investigations and micro-dimensional investigations. Macro examinations consist of caliper length, precision scales, weight measurements and micro-scale examinations Microscopic observations of the samples were made on SEM, JEOL JSM-6500F scanning microscope. Static mechanical testing of four cubic samples and sixteen series of lattice structures for each sample was carried out in accordance with the standard ISO 13314. The compression tests were conducted by an INSTRON 3369 mechanical testing machine (50 kN load cell) with a constant deformation rate of 10^{-3} s^{-1}.

3. RESULTS AND DISCUSSION

Dimensional accuracy of porous structures relative to the CAD model was checked and differences were observed in terms of strut dimensions. The surface morphology and porosity of the solid struts showed dissimilarities from CAD design. Strut diameters were lower and pore sizes were higher in all samples. Because the porosity ratio depending on the density affects the mechanical properties where the strut diameter is highly prominent factor for lattice structure design. Since the Design C has higher density and it gives % 17.3 better strength and Design A has the lowest stiffness. In functionally porous structures, Design D with higher strut diameter and it showed better mechanical properties than Design B. It can be concluded that mechanical properties of all test parts were affected by unit cell design. Possible defects that affect the properties of the sample might be the reason of unmelted powder particles due to scanning parameters, as well as inhomogeneous laying of the powder layer.

4. CONCLUSIONS

In this study, the strut diameter was investigated for Ti-6Al-4V rhombic dodecahedron structure and the physical and mechanical properties of the test parts were obtained. The strut diameter of all samples increased by 50-60 µm compared to the CAD design, while the pore measurements showed a decrease in diagonal diameter of 70-110 µm. The density of the sample increases with increasing strut diameter and test parts showed better mechanical properties. An increase in density of 0.34 g / cm^3 resulted with a 23% increase in compressive strength. Design B and D are improved 4.4% and 1.3% mechanical properties, respectively, in the transition direction in porous structures.

REFERENCES

1. International Organization for Standardization. (2011). Mechanical testing of metals -- Ductility testing - Compression test for porous and cellular metals (ISO/DIS Standard No. 13314). Retrieved from https://www.iso.org/standard/53669.html.

EVALUATION OF TANTALUM ALLOY WITH TITANIUM IN UNIVERSAL POWDER BED SYSTEM (UPB) FOR ELECTRON BEAM MELTING PROCESS

Ahu CELEBI[1], Stefan GULIZIA[2], Christian DOBLIN[3], Darren FRASER[4], Leon PRENTICE[5]
[1]*CSIRO, Commonwealth Scientific and Industrial Research Organization, Manufacturing, Clayton, Melbourne, VIC 3168, Australia,*
[2]*MCBU, Manisa Celal Bayar University, Engineering Faculty, Manisa ahu.celebi@cbu.edu.tr*
[2]*CSIRO, Commonwealth Scientific and Industrial Research Organization, Manufacturing, Clayton, Melbourne, VIC 3168, Australia, stefan.gulizia@csiro.au*
[3]*CSIRO, Commonwealth Scientific and Industrial Research Organization, Manufacturing, Clayton, Melbourne, VIC 3168, Australia, christian.doblin@csiro.au;*
[4]*CSIRO, Commonwealth Scientific and Industrial Research Organization, Manufacturing, Clayton, Melbourne, VIC 3168, Australia, darren.fraser@csiro.au*
[5]*CSIRO, Commonwealth Scientific and Industrial Research Organization, Manufacturing, Clayton, Melbourne, VIC 3168, Australia, leon.prentice@csiro.au*

Abstract. Electron beam melting (EBM) is a powder bed fusion additive manufacturing (AM) technique that produces three-dimensional (3D) parts by fusing metallic powders with a high-energy electron beam. Powder has been major issue for the properties of the final parts. Hence, establishing the effect of the powder characterization is important for producing parts of quality. In this study; Ta-60Ti, Ta-50Ti, Ta-40Ti was a blend of tantalum and titanium powders. The blend of powder was characterized in terms of the particle size distribution (PSD), bulk density, tap density, flowability in Hall Funnel flowmeter and particle morphology. In addition, a universal powder bed (UPB) system was used to characterize the powder behavior raking because the UPB system allows a quick assessment of the powder spreading behavior in AM processes. Surface roughness's of the powder after raking with universal powder bed (UPB) system, the microstructural heterogeneity, defect distributions were investigated.

Keywords: *Additive Manufacturing, Electron Beam Melting Process, Universal powder bed (UPB) system*

1. INTRODUCTION

Additive manufacturing (AM) processes are being used more and more often to manufacture industrial metal or polymer products for a broad range of applications. One category of AM process technology is powder bed fusion (PBF) [1]. Generally, metallic PBF parts have high strength [2] and nearly 100% density, directly out of the machine, a result of fully melting the powder particles [3]. PBF processes are currently the most common AM technology used by aerospace and medical implant industries for producing complex, parts with tight dimensional and surface roughness tolerances, which require process control and tracking to ensure high product quality [4].
The importance of the powder feedstock has been underlined by leaders in the field of AM Technologies [5]. The powder feedstock is characterized by mechanical, thermal, optical and chemical properties on the surface of individual powder particles; by morphology, granulometry and resulting flowability of bulk powder; and by the resulting packing density, surface uniformity and effective thermal and mechanical properties of the deposited powder layer. Herbert (2016) overviews important metallurgical aspects in the different stages of powder handling and treatment during the SLM process, i.e., in the sequence from powder storage, to spreading in the machines, to melting, solidification, and post-processing [6]. Tan et al. (2017) extend this overview to more general aspects with a special focus on the influence of powder morphology and granulometry [7].
Powder bed recoating is the first step in forming each layer. As such, powder properties can be viewed as the "parent" properties for the manufacturing process. Although powder properties are extrinsic, they significantly interact with many intrinsic properties to govern how a polymer performs throughout the manufacturing process and are essential to produce consistent, predictable, high quality parts. Drummer, et al. present four important powder properties [8], that is (i) spherical particles for flowability, (ii) small surface area to volume ratio for good packing efficiency, (iii) good control over the particle size

distribution with no particles below 1 µm and the average particle size between 10 µm and 120 µm, (iv) the Hausner ratio (i.e., the ratio between tap and bulk density [9] should be less than 1.25. This corresponds to a sphericity of at least 0.60 [10]. It is important to recognize that powder properties are very sensitive to the measurement method employed and environmental conditions during measurement [11, 12]. Powder properties are dependent on the shape, size, and size distribution of the powder particle population.

Unfortunately, very few contributions have studied the interplay of the aforementioned powder particle, bulk and layer properties during the powder recoating process in metal additive manufacturing [13]. In the recent work by Mindt et al. (2016), the influence of the blade gap on the resulting powder layer has been investigated. Their work showed that small blade gaps in the range of the maximal powder particle diameter or below can lead to a considerably decreased packing density [14]. Haeri (2017) investigated the influence of different recoating device geometries. While the studies were based on polymer materials, a transferability of general results to metal powders was claimed by the author. Volume forces such as gravity decrease cubically with particle size, while typical adhesive forces decrease linearly with particle size [15]. Consequently, the cohesiveness of bulk powder increases with decreasing particle size [16]. Typical (adhesive) surface energy values measured for metals as well as typical powder particle size distributions applied in metal additive manufacturing suggest that adhesion might be an important factor governing the flowability of bulk powder [17]. Furthermore, Foster et al. studied a variety of other defects related to powder bed processes including insufficient powder spread on the processing table and interaction between large particulates with the coater arm [18].

The quality of powder layers, specifically their packing density and surface uniformity, is a critical factor influencing the quality of components produced by powder bed metal additive manufacturing (AM) processes. Powder bed-based products usually display increased surface roughness. Although there are research about surface roughness's sintered parts [19], there is not any previous investigation about surface roughness's of the powder after raking before sintering. The UPB system allows a quick assessment of the powder spreading behavior in AM processes. The present work investigates surface roughness's of the powder after raking before sintering, present in three different Ta-Ti alloys (Ta-60Ti, Ta-50Ti, Ta-40Ti) by the UPB. The powder characteristics examined, were the packing, bulk and tap density as well as the flow efficiency of the powder samples.

2.EXPERIMENTAL METHODS

2.1. Materials

Three blended tantalum and titanium powders were used: Ta-60Ti, Ta-50Ti, Ta-40Ti alloys. Commercially pure titanium and tantalum powders are used. The tantalum powders (HC Starck), are fused and crushed with an angular morphology. According to the specification less than 1 wt% + 90µm and less than 5 wt% - 45 µm. Laser particle size analysis (Malvern Mastersizer S) is shown in Figure 1a. The d_{10}, d_{50} and d_{90} were = 66, 103 and 144 µm, respectively. The commercially pure titanium powder particles (Grade 2 ASTM 348, AP&C) is nominally -106+45 micron spherical powder. Hitachi TM3030Plus Tabletop operating at an accelerating voltage of 15 kV was used to examine the morphology and surface features of both Tantalum powders and alloys at various magnifications. Backscattered electron micrograph of Ta powder is given in Figure 1b. Ta (90/45) and CP Ti were mixed for at least 12 h in tumble mixer and 60 rpm to generate mixtures containing 40, 50 and 60 weight (wt) % Ta.

a. 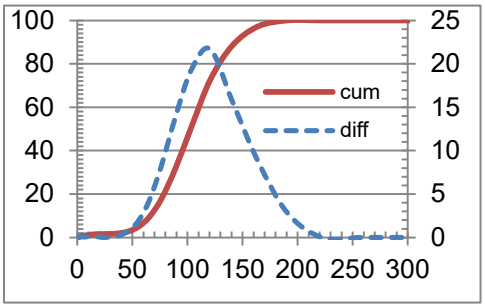

b. 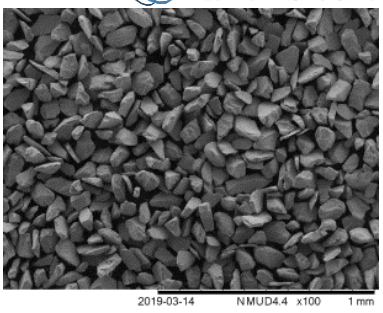

Figure 1.a. Laser particle size distribution **b.** Backscattered electron micrograph of Ta powder (HC Stark- Amperlit 150.002 90/45 µm).

2.2. Flowability, Haussner Ratio, Bulk and Tap Density Measurements

Flowability is an important indicator to assess the performance of powder in powder-bed AM systems, and it has a strong influence on the powder layer forming process and hence on the uniformity of the built-up components. Hall funnel is used according to the ASTM B855-06 [20] for the volumetric flowability test. This procedure was repeated three times and the average values were reported. To exclude the influence of moisture on flowability measurements, powders and devices were dried in a vacuum oven at 90 C for 4 h, and tests were conducted in a fume cupboard immediately after taking them out of the oven.

The bulk density of powders was measured by an Arnold meter according to the ASTM B703-05 [21]. The tap density of powders was measured based on the ASTM standard B527-06 [22]. A 10 mL glass cylinder is used based on the tested apparent density. The cylinder is placed on a tapping apparatus (EU 42E2/110S; J. Engelsmann AG, Ludwigshafen am Rhein, Germany) and tapped until no further decrease in the volume of the powder could be seen (approximately 1000 tappings). The powder volume was read directly from the cylinders. The bulk and tap densities of each powder were measured three times and averaged. The ratio between the poured and tapped bulk densities, called Hausner ratio (HR), classifies the powder's flowability [23]. The Hausner ratio is calculated between tap and apparent density of the powder according to ASTMD7481 standard [24] is widely considered a good predictor of flowability. It numerically compares static density measurements of the powder in its most densely-packed state (i.e., tap density) to powder in a loosely packed state arising from a standardized flow condition (i.e., apparent density).

2.3. Powder Behavior of Powders on UPB

The UPB is the stand-alone internal mechanism of an ARCAM machine in which the performance of powders including their flowability can be evaluated before using them in an actual ARCAM machine. The UPB was controlled by a Siemens SINUMERIK 808D programmable logical controller (Siemens AG, Berlin, Germany). Blended alloys were spread by raking on the stainless steel base plate (210 mm x 210 mm) of the UPB. The standard raking speed of the Arcam A1 EBM machine, which is 14 m/min (233.33 mm/s), was employed on the UPB. Each alloy generated a different surface texture, the layouts of which were investigated by a digital camera and a microscope (Olympus LEXT OLS4100) at various magnifications.

3. RESULTS AND DISCUSSION

3.1. Flowability, Haussner Ratio, Bulk and Tap Density Measurements

Powder diameter affects the flowability of the powder. As particle diameter reduces, the powder rheological properties improve until below 25 µm, at which point the surface energy of the powders begins to inhibit flow, instead of facilitating the flow behavior [25]. A freely flowing powder resulting in high packing density of the powder bed inside the build piston is imperative for producing fully dense, defect free final parts. The melting and consolidation steps may be more intuitively linked to defect-free

final parts of high density but having a densely packed powder bed prior to powder particle fusion is important as it minimizes the void space between particles that must be filled during the coalescence step to create a fully dense part. When discussing density as it relates to powder processing, there are three types of density to be considered (a) true density of the powder particle, (b) theoretically most dense packing arrangement for a given particulate shape and size distribution (i.e., tapped density), and (c) the packing density generated from recoating conditions (i.e., bulk density). Table 1 shows the average flowability, Haussner Ratio, bulk and tap density of cpTi, tantalum and titanium-tantalum mixed powders. The results show that the TiTa mixed powder has better flowability compared to the non-spherical tantalum powder. However, the blended powder flowability is still lower compared to the cpTi powder. Tantalum has a high density of 16.6 g/cm^3. The powder volume increases for a specific weight of the powder mixture by mixing tantalum powder with cpTi powder, as compared to processing pure tantalum powder, due to the lower density of cpTi (4.51 g/cm^3). The bulk density and measured tap densities of TiTa mixed powder is tabulated in Table 1. Flowability is an important concern in EBM, as uniform powder deposition is required for production of parts with high relative density. Spherical powder is ideally desired. However, the tantalum powder has irregular shape, as its high melting point of 2996 °C restricts the production of spherical powder economically. Hence, the overall flowability is improved by mixing the tantalum powder with spherical cpTi powder. The spherical titanium particles roll easier during powder depositions and acts as a medium by pushing the tantalum particles along. The Hausner ratio considered a good predictor of flowability should be less than 1.25 [25]. The Hausner ratio for all TiTa mixed powders tested was less than than 1.25 for (see Table 1).

Table 1. The average flowability, Haussner Ratio, bulk and tap density of CP Ti, tantalum and titanium-tantalum mixed powders.

Sample	Volume fraction Ta	Hall Flow time (s)	Vol, mL	Mass, g	Bulk density, g/cc	Tap density, g/cc	Haussner ratio
Ta-60Ti	15.3	24,1	20	91,1	4,56	5,50	1,11
Ta-50Ti	21.3	26,5	20	107,8	5,39	5,89	1,09
Ta-40Ti	28.9	28,5	20	113,45	5,67	6,18	1,11
Cp Ti	0	25,4	20	52,9	2,64	2,89	1,09
Ta	100	28,1	20	154,1	7,71	9,27	1,20

3.2. Blended Ta-Ti alloys characterization

Due to the complex nature of powder, powder flow behavior is difficult to predict from solid particulate shape alone without considering the gas around the particulates in the bed and the historical packing and loading conditions of the powder. Therefore, while powder size and shape are primary parameters informing secondary extrinsic properties, like powder flow, it is more practical to directly evaluate the powder flow properties for predicting process performance.

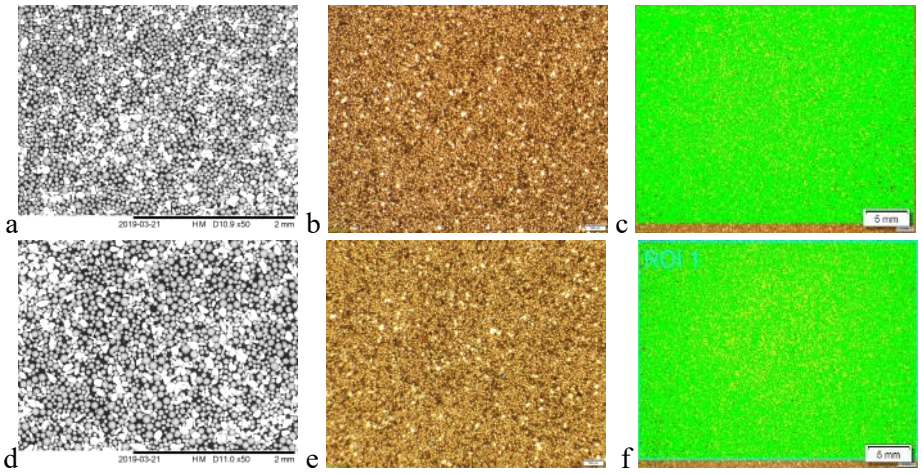

Figure 2. SEM images after mixing (50x) a. Ta-60Ti d. Ta-50Ti g. Ta-40Ti, Optic microscope images after raking by UPB (5x) b. Ta-60Ti e. Ta-50Ti h. Ta-40Ti, OLYMPUS Stream software report c. Ta-60Ti f. Ta-50Ti ı. Ta-40Ti.

Scanning electron microscopy (SEM) images after mixing showed powder size and shape in Figure 2.a, 2.d, 2.g. for Ta-60Ti, Ta-50Ti, Ta-40Ti alloys are presented below. The resolution of the SEM pictures is 50x magnification for each alloy sample in order to allow the basic comparison of dispersing powder and the shape of the particles by optical observation. Furthermore, each alloy microscope picture after raking by UPB is given Figure 2.b, 2.e, 2.h. The magnification of the microscope pictures is 5x for each sample. The Ta can be identified by bright spots in the optical images (Figure 2.b, 2.e, 2.h). As seen, especially in the low magnification images, bright specks of Ta can be seen throughout the images indicating uniform distribution. OLYMPUS Stream software was used for analyzing volume friction on each alloy microscope pictures. The results of volume friction for Ta-60Ti, Ta-50Ti, Ta-40Ti alloys was found 14.36 %, 20.39 % and 26.76 % respectively. OLYMPUS Stream software report pictures for Ta-60Ti, Ta-50Ti, Ta-40Ti alloys are given in Figure 2.c, 2.f, 2.ı respectively. The segregation of the powders in the mixtures can occur because of the huge density difference between tantalum and titanium. OLYMPUS Stream software and SEM image results proved that showing no segregation of titanium and tantalum in the powder mixture.

The most immediate method to test the performance of powder is applying the powder onto a powder bed fusion process. Therefore, the UPB was developed by CSIRO to observe the powder behavior during the raking of the powder bed. On the UPB, a powder spreading system is formed by four rakes with 0.9-mm-wide teeth and 0.1-mm-wide gaps, which interstitially overlap with each other. The powder stocked in two stainless steel hoppers is gravity fed and the rake fetches the powder. The powder is then raked across the base plate. During particle movement, surface particles will rearrange to a minimum of potential energy under the uniform drive given by the motion of the rake. The kinetic energy of the spreading particles is mostly used to overcome local friction resistances among particles, achieving the minimum energy configuration. Figure 3a, b, c shows the surface topographies of three tested powders on the UPB Ta-60Ti, Ta-50Ti, Ta-40Ti alloys respectively.

Figure 3. Images after raking by UPB

UPB was set up such that the comb just touched the original build plate across the whole surface. The original build plate has a grit blasted surface finish and no provision for ex-situ analysis of small sections of the bed. A small layer of powder was laid in front of the rake and powder raked once over the build plate at 100% speed. A uniform layer was created as seen Figure 3.b, c when illuminated with low incident light. The build plate was lowered to a 50µm gap every layer and the process repeated each mixed powder. The powder looked uniform on the build plate in Figure 3. Large particles like Ta will sometimes "plow" instead of "tumble" during recoating. This can cause layer scarring as it disrupts the smooth powder bed surface as can be seen Fig 3.c.

REFERENCES

1. ASTM F2792 2012 Standard Terminology for Additive Manufacturing Technologies (West Conshohocken, PA: ASTM International)
2. Levy G N, Schindel R and Kruth J P 2003 Rapid manufacturing and rapid tooling with layer manufacturing (LM) technologies, state of the art and future perspectives CIRP Ann. 52 589–609
3. Kruth J P, Levy G, Klocke F and Childs T H C 2007 Consolidation phenomena in laser and powder-bed based layered manufacturing 2007 CIRP Ann. 56 730–60
4. Campbell J, Bourell D and Gibson J 2012 Additive manufacturing: rapid prototyping comes in age Rapid Prototyping J. 18 255–8
5. King, W., 2017. Modeling of Powder Dynamics in Metal Additive Manufacturing: Final Powder Dynamics Meeting Report.
6. Herbert, R., 2016. Viewpoint: metallurgical aspects of powder bed metal additive manufacturing. J. Mater. Sci. 51, 1165–1175.
7. Tan, J., Wong, W., Dalgarno, K., 2017. An overview of powder granulometry on feedstock and part performance in the selective laser melting process. Addit. Manuf. 18, 228–255.
8. Drummer D, Medina-Hernández M, Drexler M, Wudy K. Polymer Powder Production for Laser Melting Through Immiscible Blends. Procedia Eng 2015;102:1918-25.
9. Van den Eynde M, Verbelen L, Van Puyvelde P. Assessing polymer powder flow for the application of laser sintering. Powder Technol 2015;286:151-5.
10. Zou RP, Yu AB. Evaluation of the packing characteristics of mono-sized non-spherical particles. Powder Technol 1996;88:71-9.
11. Verbelen L, Dadbakhsh S, Van den Eynde M, Kruth J-P, Goderis B, Van Puyvelde P. Characterization of polyamide powders for determination of laser sintering processability. Eur Polym J 2016;75:163-74.
12. Berretta S, Ghita O, Evans KE. Morphology of polymeric powders in Laser Sintering (LS): From Polyamide to new PEEK powders. Eur Polym J 2014;59:218-29.
13. Whiting, J., Fox, J., 2016. Characterization of feedstock in the powder bed fusion process: sources of variation in particle size distribution and the factors that influence them. International Solid Freeform Fabrication Symposium, Austin, Texas, USA
14. Mindt, H., Megahed, M., Lavery, N., Holmes, M., Brown, S., 2016. Powder bed layer characteristics: the overseen first-order process input. Metall. Mater. Trans. A: Phys. Metall. Mater. Sci. 47, 3811–3822.
15. Haeri, S., 2017. Optimisation of blade type spreaders for powder bed preparation in additive manufacturing using DEM simulations. Powder Technol. 321, 94–104.
16. Walton, O., 2008. Review of adhesion fundamentals for micron scale particles. Kona Powder Part. J. 26, 129–141.
17. Herbold, E., Walton, O., Homel, M., 2015. Simulation of Powder Layer Deposition in Additive Manufacturing Processes Using the Discrete Element Method (Technical report). Lawrence Livermore National Laboratory.
18. B.K. Foster, E.W. Reutzel, A.R. Nassar, B.T. Hall, S.W. Brown, C.J. Dickman, Optical, Layerwise Monitoring of Powder Bed Fusion. 2015 Annual Solid Freeform Fabrication, Austin. In: University of Texas at Austin, pp. 295–307 (2015)
19. H. Meier and C. Haberland, Experimental Studies on Selective Laser Melting of Metallic Parts, Mat.-wiss. u. Werkstofftech, 2008, doi: 10.1002/mawe.200800327
20. ASTM B855-06, Standard Test Method for Volumetric Flow Rate of Metal Powders Using Arnold Meter and Hall Funnel (West Conshohocken, PA: ASTM, 2006)
21. ASTM B703-05, Standard Test Method for Apparent Density of Powders Using Arnold Meter (West Conshohocken, PA: ASTM, 2005).
22. ASTM B527-06, Standard Test Method for Determination of Tap Density of Metallic Powders and Compounds (West Conshohocken, PA: ASTM, 2006).
23. Schmid, M., Levy, G., Amado, F., Wegener, K., 2013. Flowability of Powders for Selective Laser Sintering (SLS) investigated by Round Robin Test., pp. 95–99.
24. ASTM International, 2009. Standard test methods for determining loose and tapped bulk densities of powders using a graduated cylinder. In: ASTM D7481. ASTM International.
25. A Review of the Process Physics and Material Screening Methods for Polymer Powder Bed Fusion Additive Manufacturing Authors: Camden A. Chatham, Timothy E. Long, Christopher B. Williams

A METALLURGICAL PHASE TRANSFORMATION MODEL APPLIED TO DIRECTED ENERGY DEPOSITION ADDITIVE MANUFACTURING OF Ti-6Al-4V

Cengiz Baykasoğlu[1*], Öncü Akyıldız[2], Merve Tunay[3]

[1*] *Hitit University, Department of Mechanical Engineering, Çorum, Turkey, cengizbaykasoglu@hitit.edu.tr*
[2] *Hitit University, Dept. of Metallurgical and Materials Engineering, Çorum, Turkey, oncuakyildiz@hitit.edu.tr*
[3] *Hitit University, Department of Mechanical Engineering, Çorum, Turkey, mervetunaycetin@hitit.edu.tr*

Abstract. This paper presents 3D finite element (FE) implementation of a generalized metallurgical phase transformation kinetic model for predicting evolution of volumetric phase fractions during both diffusional and diffusionless phase transformations of Ti-6Al-4V in a typical Directed Energy Deposition (DED) additive manufacturing (AM) process. The metallurgical model is enabled to describe the dissolution, formation and recovery of alpha (Widmanstätten, colony/basketweave, massive/martensitic and grain boundary) and beta phases. The benchmark simulation results showed that the evolution of phase fractions during DED process of Ti-6Al-4V could be effectively simulated using the proposed thermo-metallurgical model.

Keywords: *directed energy deposition, finite element modeling, solid-state phase transformation, Ti-6Al-4V*

1. INTRODUCTION

Predicting and controlling of microstructural features during large scale metal AM processes is one of the challenging issues. Recent studies showed that the use of density type microstructural models in conjunction with FE based macro scale thermal models is a powerful tool for enabling this challenging task (Thompson et al. 2015). In this modeling approach, density fields such as phase fractions of different phases are computed using transient thermal field data via phase transformation kinetic models (Kelly and Kampe, 2004; Crespo, 2011; Murgau et al. 2012; Irwin et al., 2016). In the present work, a generalized thermo-metallurgical model based on the most recent observations and formulations in literature is proposed and implemented to Laser Engineering Net Shaping (LENS) process which is one of the representative commercial forms of DED (Mudge and Wald, 2007; Palčič et al., 2009). The proposed model enables prediction of grain boundary, Widmanstätten colony/basketwave, massive and martensitic alpha, and beta phase fractions during solid state phase transformations for a wide range of processing conditions.

2. MATERIALS AND METHODS

The transient thermal FE model is developed to simulate LENS process of five layers single wall Ti-6Al-4V part having a width of 2.45 mm, using the commercially available FE software ABAQUS (Figure 1). The material deposition during process is modelled using inactive/active element method. A double ellipsoid heat source model is used to describe the laser heat source (Goldak et al., 1984). Different user subroutines (e.g., USDFLD and DFLUX) are written and optimized using PYTHON and FORTRAN and embedded in Abaqus in order to define the geometry, microstructural features and heat source input. The AM process parameters are selected as same in Baykasoglu et al. (2018).

Ti-6Al-4V is a heat treatable alloy, and the morphologies of α- and β- phases can substantially change depending on the thermal cycles during deposition processes (Kelly and Kampe, 2004). During a cooling event, if the calculated temperature is below the martensite start temperature (T_{MS}) and the cooling rate is higher than the critical cooling rate (CCR), then massive or martensitic phase transformations are considered using a discrete form of Koistinen–Marburger equation (Koistinen and Marburger, 1959). If the temperature is above the T_{MS} or the cooling rate is lower than CCR, then diffusional phase transformations using modified Johnson-Mehl-Avrami-Kolmogorov (JMAK) equations that account

incomplete phase transformations for varying initial concentrations are employed (Johnson and Mehl, 1939; Avrami, 1939; 1940; 1941). In addition, Widmanstätten α phase is divided into colony and basketwave morphologies based on an intragranular nucleation temperature (T_{IG}). During heating, if the amount of massive phase is higher than the expected amount, the massive phase is dissolved to its equilibrium value while forming Widmanstätten alpha and beta phases according to a discrete JMAK formulation. If the total diffusional α-phase fraction, is above its equilibrium value, α-phases decompose into ß phase following a parabolic ß growth rate function. The microstructure model is verified and validated using the primary and secondary heat treatment curves and the corresponding phase fraction evolutions given in Kelly and Kampe, (2004) and Murgau et al. (2012).

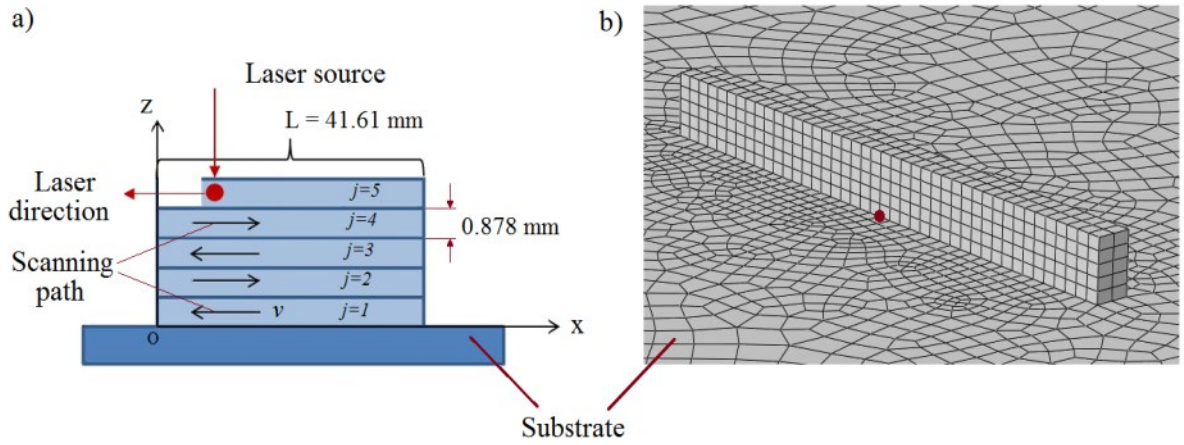

Figure 1. The finite element model and an illustration of laser deposition process.

3. RESULTS AND DISCUSSION

In the numerical analysis, the beta transus, intragranular temperature and martensite start temperature are considered as T_{β}=1000 ºC, T_{IG}=825 ºC and T_{ms}=800 ºC, respectively. The time evolution of the temperature and phase fractions at the sample integration point shown in Figure 1b is given in Figure 2. When Figure 2 is examined, it is observed that α- and β- phases transforms continuously during the thermal cycles. Throughout the additive manufacturing process, a total of five peaks occur in the temperature profile of the point taken from the first layer. The first peak corresponds to the deposition of Layer 1, where the others correspond to that of upper layers. In each step, primary heating or heating above T_{β} takes place. Therefore, as can be seen from the figure clearly, the total α phase fraction goes down to 0 and the β phase fraction goes up to 1 at the peak points.

The colony-α phase fraction increases continuously, as the time elapsed during cooling from beta transus (T_{β}) to T_{IG} increases until the fifth layer where it almost remains unchanged afterwards. On the other hand, the massive-α phase fraction reaches about 0.7 in the first cooling cycle due to high cooling rate, and this value decreases as the cooling rate decreases in subsequent cycles.

Temperature, martensite-α, colony-α and basketwave-α phase fraction distributions over the sample at different time steps corresponding to bottom, middle and top layers of the single wall structure are seen in Figure 3. It is seen that martensite α phase is formed in all layers of the single wall structure. Colony α and basketwave α phase ratios have values that are approximately zero in regions exposed to high temperatures.

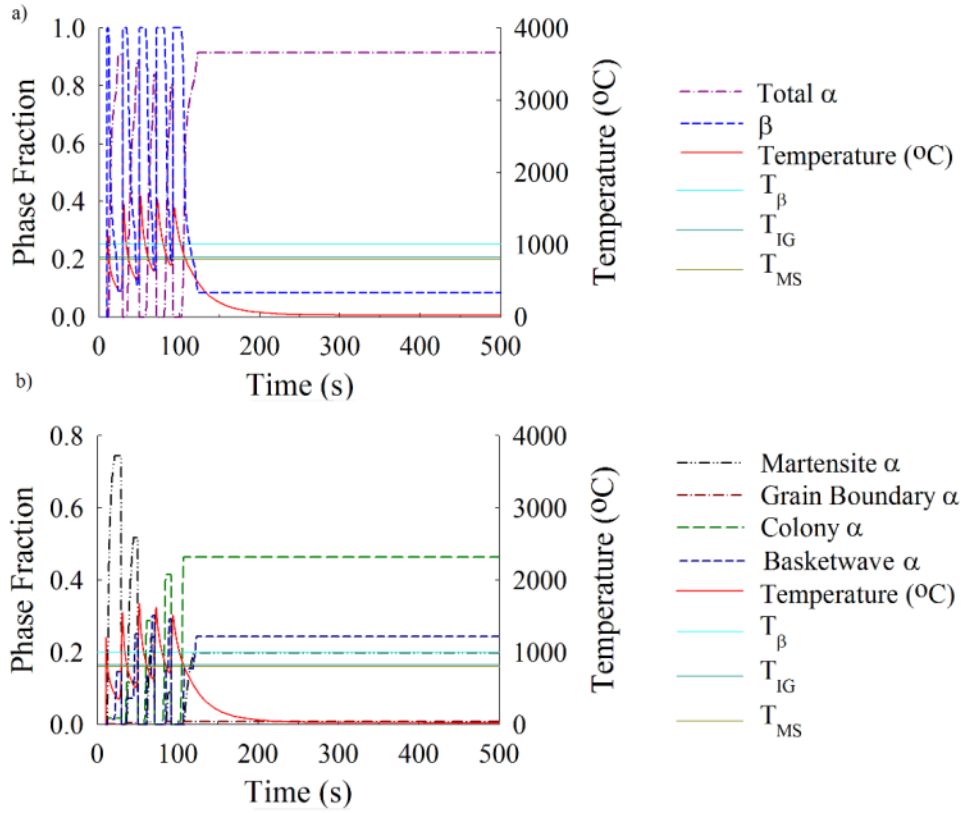

Figure 2. The time evolution of the temperature and phase fractions at the sample integration point.

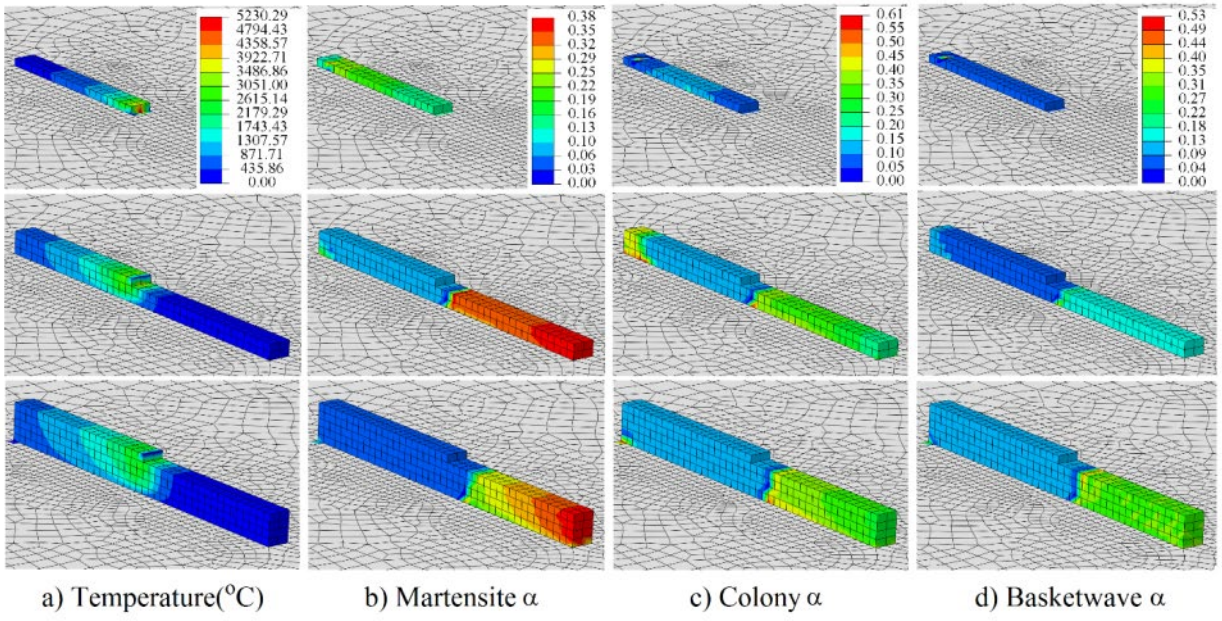

Figure 3. a) Temperature, b) martensite α, c) colony α and d) basketwave α phase fraction evolutions during layer by layer deposition.

4. CONCLUSION

This paper presents a comprehensive thermal-microstructural model to describe both diffusional and diffusionless phase fraction evolutions for Ti-6Al-4V alloy in DED processes. The simulation results demonstrated that the proposed model is able to capture the evolution of phase fractions of Ti-6Al-4V during all proposed solid state transformations.

ACKNOWLEDGMENT

This research is supported by The Scientific and Technological Research Council of Turkey (TUBITAK) under the grant number 217M638.

REFERENCES

Avrami, M. (1939). Kinetics of Phase Change. I General Theory, Journal of Chemical Physics 7, 1103-12.

Avrami, M. (1940). Kinetics of Phase Change. II Transformation-Time Relations for Random Distribution of Nuclei, Journal of Chemical Physics 8, 212-24.

Avrami, M. (1941). Kinetics of Phase Change III. Granulation, phase change, and microstructure, Journal of Chemical Physics 9, 177-84.

Baykasoglu C., Akyildiz O., Candemir D., Yang Q., To A.C. (2018). Predicting microstructure evolution during directed energy deposition additive manufacturing of Ti-6Al-4V. J Manuf Sci E, 140(5), 051003.

Crespo, A., (2011), Convection and Conduction Heat Transfer, INTECH Open Access Publisher, Rijeka, Croatia, Chap. 15.

Goldak, J., Chakravarti, A., and Bibby, M., (1984), A New Finite Element Model for Welding Heat Sources, Metall. Trans. B, 15(2), pp. 299–305.

Irwin, J., Reutzel, E. T., Michaleris, P., Keist, J., and Nassar, A. R., (2016), Predicting Microstructure From Thermal History During Additive Manufacturing for Ti-6Al-4V, ASME J. Manuf. Sci. Eng., 138(11), p. 111007.

Johnson, W. A., Mehl, R. F. (1939). Reaction kinetics in processes of nucleation and growth, Transactions of the AIME 135, 416.

Kelly, S. M., & Kampe, S. L. (2004). Microstructural evolution in laser-deposited multilayer Ti-6Al-4V builds: Part II. Thermal modeling. Metall and Mater Trans A, 35(6), 1869-1879.

Koistinen, D. P., Marburger, R. E. (1959). A general equation prescribing the extent of the austenite-martensite transformation in pure iron–carbon alloys and plain carbon steels, Acta metall. 7 59–60.

Mudge, R. P., and Wald, N. R., (2007). Laser Engineered Net Shaping Advances Additive Manufacturing and Repair, Weld. J., 86(1), pp. 44–48.

Murgau C.C., Pederson R., Lindgren, L. E., (2012). A Model for Ti–6Al–4V Microstructure Evolution for Arbitrary Temperature Changes. Model and Simulation Material Science and Engineering, 20(5).

Palčič, I., Balažic, M., Milfelner, M., and Buchmeister, B., (2009). Potential of Laser Engineered Net Shaping (LENS) Technology, Material Manufacturing Processes, 24(7–8), pp. 750–753.

Thompson,S.M., Bian L., Shamsaei N., Yadollahi A. (2015). An Overview of Direct Laser Deposition for Additive Manufacturing; Part I: Transport Phenomena, Modeling and Diagnostics, Additive Manufacturing 8, 36 62.

PRODUCTION OF PRIMECAST® POLYSTYRENE BY SELECTIVE LASER SINTERING (SLS) METHOD AND DEVELOPMENT OF SURFACE ROUGHNESS OF SINTERED PARTS

Burçin Özbay[1,2], Gökhan Özer[1], M. Enes Bulduk[1], Gürkan Tarakçı[1], Zafer Çağatay Öter[1], Ebubekir Koç[1]
[1]*ALUTEAM, Fatih Sultan Mehmet Vakif University, Istanbul, Turkey, burcinozbay@gmail.com*
[2]*Department of Polymer Science and Technology, Istanbul Technical University, Istanbul, Turkey*

Abstract. Selective laser sintering (SLS) is one of a popular method of additive manufacturing technique. In this study, PrimeCast® was used, which is a trade name of polystyrene material of EOS Company, for the production of rapid prototyping to create investment casting patterns via the SLS process. The research examines how will be the surface roughness properties of the sintered samples by changing the energy density values. Various energy densities have been processed in the manufacturing processes of SLS of PrimeCast®. TGA (Thermogravimetric Analysis), DSC (Differential Scanning Calorimetry) and, SEM (Scanning Electron Microscopy) analysis were done. On the other hand, surface roughness values were measured to the sintered samples after processing and after coating by injection wax (infiltration). It was observed that there is a significant change at surface roughness while intensity of energy density increases. Also, there is a definite surface roughness improvement measured after wax coating which names as infiltration process.

Keywords: *PrimeCast®, Polystyrene, SLS, Surface Roughness.*

1. INTRODUCTION

Nowadays, some advanced techniques have been developed to fabricate prototypes, experimental models, etc. Selective laser sintering (SLS) is one of these advanced methods which processes especially improved polystyrene powders for the fabrication of investment casting models.
Using polystyrene materials such as PrimeCast, CastForm, etc. instead of traditional investments casting, additive manufacturing techniques decreases the cost and also provides time saving due to the elimination of pre-shell stage (N.P. Nkhasi1, 2017).
Rapid Prototyping (RP) chain is CAD 3-D Modelling (STL File Conversion), sending to RP system computer, RP Fabrication (Layer-by-layer building), Post-Processing (Cleaning, hardening, finishing), prepared 3-D Physical Part, respectively (C.M. Cheah, 2005).
In literature there was only a related study could be found. Ku et al. were used CastForm polystyrene material to investigate how various densities effect the porosity values of the laser energy density (Ku, 2002).
PrimeCast® polystyrene material provides good dimensional accuracy, high surface quality, good strength, etc. for use as investment casting pattern. One of an important feature of this material is the residue content after casting step is very low and the residue material powder, which is not sintered in SLS processing step, can be reused for many times (EOS GmbH, 2019).

2. MATERIALS AND METHODS

The used polymer is EOS PrimeCast® 101 which is an investment casting pattern polystyrene. To cover the sintered samples injection wax was used. Selective laser sintered specimens were produced by EOS Formiga P 110 system under a laser power range from 6 W to 22,626 W in a part bed temperature (Tb) of 89 °C with different hatch distance (scan spacing) (mm) and scan speed (mm/s) values. There were two productions have been done.
After producing the samples by SLS, wax infiltration has been done. Firstly, the wax was preheated to 80-85 °C on a hotplate until complete melting of the wax. Then the temperature was kept around 75-

80 °C. The sintered specimens were fixed vertically in the wax bath by using a set of metal cables. Figure 1 illustrates the steps of wax infiltration of sintered samples. Figure 1-a shows the samples while preheating the parts near to wax temperature to avoid any stress cracks. Figure 1-b shows the pre-heated parts in the hot wax, and Figure 1-c demonstrates dripping the samples after was infiltration.

a) b) c)

Figure 1. a-Preheating the parts; b-Dipping the sintered samples to melt wax; c- Leaving to drip in the oven.

3. RESULTS AND DISCUSSION

There are some chosen parameters and their surface roughness properties listed as below with comparison with EOS default parameters of PrimeCast® (given as basic and fine). The surface roughness properties were measured, before and after wax coating, at least 3-4 different points of the samples.

Table 1. Some chosen processing parameters and surface roughness measurement values before and after wax coating

Sample Name	Laser Power (W)	Scan Speed (mm/s)	Hatch Distance (mm)	Energy Density (J/mm^3)	Average Surface Roughness (µm)
Z_2	21	2400	0,15	0,583	17,108 (before) 9,687 (after)
Z_3	21	2500	0,15	0,560	16,493 (before) 6,200 (after)
Z_6	21	2600	0,15	0,538	16,124 (before) 7,867 (after)
Y_6	20	2000	0,15	0,666	15,760 (before) 7,742 (after)
X_3	basic	-	-	-	18,111 (before) 5,121 (after)
X_5	fine	-	-	-	19,317 (before) 6,805(after)

As can be seen from *Table 1* surface roughness values are significantly decreased after the wax coating step. Surface roughness values of sintered materials with default parameters (basic and fine); also the parameters, which were detected by our study, named as Z_3 and Z_6 samples were measured after wax coating as almost one third.

4. CONCLUSIONS

It can be said that these created patterns have a positive dewaxing response which is resulting in substantially improved surface quality for investment cast prototypes. Also, there is a significant

development for surface roughness values via changing the energy density and doing infiltration step. However, the study will continue with cast investment process works.

ACKNOWLEDGMENT

The authors are grateful to Fatih Sultan Mehmet Vakif University-Aluminium Test Training and Research Center (ALUTEAM) and Istanbul Technical University for their supports.

REFERENCES

C.M. Cheah, C. C. (2005). Rapid prototyping and tooling techniques: a review of applications for rapid. Int J Adv Manuf Technol, 308-320.

EOS GmbH. (2019, Temmuz 01). EOS Materials Plastic Technical Data-PrimeCast 101. https://eos.materialdatacenter.com/eo/en adresinden alınmıştır

Ku, C. G. (2002). Selective Laser Sintered CastFormTM Polystyrene with Controlled Porosity and its Infiltration. Solid Freeform Fabrication Proceedings, 107-114.

N.P. Nkhasi1, W. d. (2017). Effectiveness Of Primecast® And PMMA Additive Manufacturing Processes To Produce Patterns For Investment Casting. 19th Annual International RAPDASA Conference, (s. 189-200).

INFLUENCE OF HOT ISOSTATIC PRESSING AND SUBSEQUENT HEAT TREATMENT ON MECHANICAL PROPERTIES OF DIRECT METAL LASER SINTERED ALSI10MG ALLOY

Onur Ertuğrul[1], Zafer Çagatay Öter[2], Mustafa Safa Yılmaz[2], Ezgi Şahin[1], Mert Coşkun[2], Gürkan Tarakçı[2], Ebubekir Koç[2]

[1]*Izmir Katip Celebi University, Dept of Materials Science and Engineering, Izmir, Turkey,*
onurertugrul@gmail.com , ezgi.sahin26@hotmail.com

[2]*Aluminum Test, Training and Research Center, Fatih Sultan Mehmet Vakif University, Istanbul, Turkey,*
zcoter@fsm.edu.tr , msyilmaz@fsm.edu.tr, mcoskun@fsm.edu.tr, gtarakci@fsm.edu.tr, ekoc@fsm.edu.tr

Abstract. In this work, hot isostatic pressing and subsequent T6 heat treatment, by using two different aging durations (4h and 12h), were applied to laser sintered AlSi10Mg materials to evaluate the effects of secondary process combinations on properties of DMLS AlSi10Mg alloy. Relative densities and open porosities were determined using Archimedes method. As-built, HIPed and HIP+heat treated samples were characterized by optical microscopy and SEM. Mechanical properties were evaluated with tensile tests. HIP process does not alter the amount of surface pores, however it has a positive influence on closed pores. HIPed samples indicate the microstructure of the aluminum matrix surrounded by a network of micron size and spherical Si based precipitates. Additional heat treatment results in larger precipitates. After HIP process, the material is getting softer having too much ductility. Heat treatment including 4h of aging results in higher yield and tensile strength but decreased ductility compared to as-built material. 12h aged sample shows the best combination of strength and ductility. As-built samples show a ductile fracture, however HIP process results in more ductile fracture surface with dimple structure. The fracture surfaces of the heat-treated samples show more flat fracture surface showing a clevage type fracture.

Keywords: Hot isostatic pressing; T6 heat treatment, AlSi10Mg, Additive manufacturing, Mechanical properties

1. INTRODUCTION

AlSi10Mg is the most common aluminum alloy used in AM due to its suitability to the process, good mechanical properties, low thermal expansion coefficient and superior corrosion resistance (Girelli et al., 2019;Delahaye et al., 2019). The high cooling rates in laser sintering process lead to a more homogeneous distribution of more fine-grained and silicon-rich eutectic compounds, in contrast to the usual microstructure of Al-Si casting alloys. This difference results in superior mechanical properties such as higher tensile strength and higher ductility compared to conventional casting products (Itturioz, 2018).

Many studies have been carried out to clarify the microstructure and mechanical properties of the AlSi10Mg alloy parts. The use of the subsequent heat treatment to develop the mechanical properties is important because the effect of the heat treatment on the microstructure of AM materials is enormous, and studies on this subject has been increased in recent years (Girelli et al., 2019). Also, HIP has been an important post process for many materials in AM. This is because it helps to reduce the internal pores and surface pores, thus allowing increased the fatigue strength (which is very critical in aluminum parts) as well as tensile and corrosion properties. The only disadvantage of the HIP process is the high cost. In this study, AlSi10Mg parts produced by DMLS technique have been heat treated with HIP process and then subsequent T6 heat treatments have been applied in order to improve the properties.

2. MATERIALS AND METHODS

Commercial gas atomised EOS AlSi10Mg powder, with an average particle size of 35±5 µm, was used. Cylindirical tensile test samples were produced in horizontal direction using DMLS powder bed technology, with an EOS M290 system. The as-built samples were then undergone to HIP process, and subsequent heat treatments were applied to HIPed samples. HIP process was performed under pressure of

100 MPa at 500˚C for 75 min under argon atmosphere. After all the samples were HIPed, T6 heat treatment consists of solutionizing and artificial aging (with two different aging time) was applied. First, samples were solutionized at 540˚C for 2 h, then quenched in water at 80˚C. In artificially aging at 180˚C, two different aging time of 4 h and 12 h were selected. The relative density and the surface porosity of samples in as-built, HIPed and HIP + heat-treated condition were measured in ethanol using Archimedes principle. Densities, open porosities and roughness values of the samples are measured in order to see if there is a change in the surface properties. The samples are characterized by optical microscopy and SEM in order to understand the mechanical behaviours.

3. RESULTS AND DISCUSSION

Table 1. Density and porosity values of the samples. T6 indicates the heat-treated samples.

Material	Relative Density (%)	Open Porosity – Archimedes (%)	Surface roughness (µm)
As-built	98.8 ± 0.2	0.7 ± 0.3	12.7 ± 1.6
HIPed	98.7 ± 0.3	1.4 ± 0.5	12.1 ± 0.7
HIP+4h aged	98.7 ± 0.2	1.3 ± 0.4	13.1 ± 0.8
HIP+12h aged	98.9 ± 0.3	1.1 ± 0.3	12.6 ± 1.5

Table 2. Mechanical properties of the samples.

Material	Yield Strength(MPa)	UTS (MPa)	Strain (%)
As-built	208 ± 17	301 ± 18	11.8 ± 1.8
HIPed	108 ± 3	176 ± 1	25.0 ± 0.5
HIP+4h aged	308 ± 25	345 ± 1	5.8 ± 1.7
HIP+12h aged	254 ± 9	306 ± 9	8.7 ± 3.3

4. CONCLUSIONS

HIP process does not alter the density and increases the surface porosity very slightly. After HIP process, the material is having significant amount of ductility with having quite low yield and tensile strength. 4 hours of aging yields improved yield and tensile strength, but low ductility. 12 hours of aging gives a good strength-ductility combination. These samples are more ductile than the samples aged for 4 hours.

REFERENCES

Delahaye, J., Tchoufang Tchuindjang, J., Lecomte-Beckers, J., Rigo, O., Habraken, A.M., Mertens, A. (2019). Influence of Si precipitates on fracture mechanisms of AlSi10Mg parts processed by Selective Laser Melting. Acta Mater., 175, 160-170.

Girelli, L., Giovagnoli, M., Tocci, M., Pola, A., Fortini, A., Merlin, M., La Vecchia, G.M. (2019). Evaluation of the impact behaviour of AlSi10Mg alloy produced using laser additive manufacturing. Materials Sci. Eng. A, 748, 38-51.

Iturrioz, A., Gil, E., Petite, M.M., Garciandia, F., Mancisidor, A.M., San Sebastian, M. (2018). Selective laser melting of AlSi10Mg alloy: influence of heat treatment condition on mechanical properties and microstructure. Welding in the World, 62, 885-892.

TRANSIENT MELT POOL MODELING FOR THE ABRUPT PROCESS PARAMETER CHANGE IN SELECTIVE LASER MELTING PROCESS

Emrecan Soylemez
Department of Mechanical Engineering, Istanbul Technical University, Gumussuyu, 34437, Beyoglu, Istanbul, Turkey, esoylemez@itu.edu.tr

Abstract. Selective laser melting (SLM) is a powder bed fusion metal additive manufacturing (AM) process favored for its near-net-shape part promise. However, the deposition rate of this process is relatively slow compared to alternative metal processes. Enhancing the building rate of SLM is viable by controlling the beam diameters and process parameters simultaneously. Shifting of these parameters require a transition period for the melt pool to respond. This study focused on the melt pool transition when a high deposition rate process parameter combination changed to a high precision process parameter combination and vice versa. Thermal finite element analysis was used to predict the behavior and response of the melt pool.

Keywords: selective laser melting, deposition rate, transient melt pool modeling

1. INTRODUCTION

Selective laser melting (SLM) is the most commonly used metal additive manufacturing (AM) process. However, it is still a slower manufacturing process than conventional techniques. Selective laser melting process performance on the production speed can be evaluated by the deposition rate (*DR*) (Clymer, Cagan, & Beuth, 2017). Powder layer thickness, hatch spacing, and laser beam scanning velocity are the parameters to calculate the deposition rate. However, increasing these parameters is not a solution due to the laser fusion physics limitations. Melt pool geometry should be kept under control to avoid defective parts. The defocusing of the laser beam produces uniform energy distribution on the melt pool. It also presents benefits of high *DR* where the precision is not critical, and moderate *DR* where the precision is significant, such as the outer surface of the part when shifting the focused laser beam diameter (Schleifenbaum, Meiners, Wissenbach, & Hinke, 2010). Thinner and tighter sections, smooth surfaces, and controlled microstructure regions of the part can be printed by process parameters at lower speeds, and the rest can be manufactured in a shorter time with different process parameters. Variation of the process parameters on the same scanning line require a deeper understanding of the melt pool behavior for the process control (Fox & Beuth, 2013). This also helps to control the melt pool with feedback systems while monitoring the melt pool. This study focuses on the melt pool geometry response on the same layer of the SLM when the process parameter changes on the continuous line.

2. MATERIALS AND METHODS

A 3D finite element analysis (FEA) model was built up to estimate the single bead melt pool geometry of Ti-6Al-4V. After reaching the steady state melt pool geometry, process parameters were shifted while the laser kept moving to investigate the melt pool geometry reaction to it. Table 1 presents the process parameters that were used in this study. Melt pool geometries of the simulation predictions were compared to the defocused experimental results as seen in Table 1 where the beam diameter was equal to 220 µm.

Table 1. Single bead steady state melt pool geometry experimental results.

Power (W)	Velocity (mm/s)	Depth (µm)	Width (µm)
370	400	170	340
250	800	52	198
200	400	67	229

Experimental set up details can be found in (Soylemez, 2018). Transient melt pools were investigated for the cases seen in Table 2.

Table 2 Transient single bead process parameters.

Case	Initial Power (W)	Initial Velocity (mm/s)	Final Power (W)	Final Velocity (mm/s)
1	200	400	370	400
2	370	400	200	400
3	250	800	370	400
4	370	400	250	800

3. RESULTS AND DISCUSSION

Figure 1 shows the melt pool geometry after shifting the process parameters from 370 W and 400 mm/s to the 250 W and 800 mm/s. This case can be interpreted as a region where a thin layer of an overhang structure is started to be built, an outside surface of an inner channel, or a region where fatigue strength is critical. Transition of the melt pool presents that melt pool width and depth that reduce linearly. Transition region length for the cases 1, 2 and 3 was found to be ~ 250 µm, and for case 3 it was 146 µm.

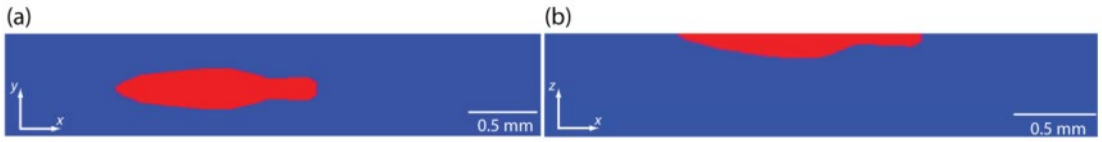

Figure 1. Melt pool snapshot view after process parameters changed from 250 W and 800 mm/s to 370 W and 400 mm/s. **(a)** Top view of the melt pool in the *x-y* plane **(b)** section view in the *x-z* plane

4. CONCLUSIONS

Single bead simulations calibrated by the experimental results were run to understand the melt pool transient response. Melt pool length experimental measurements should be conducted to check the melt pool length predictions by the simulation in the future study to improve the response time of the transient melt pool. These findings can be used to improve the feedback and feedforward controlling systems.

5. ACKNOWLEDGMENTS

The author thanks Prof. Ebubekir Koc and Mr. Mert Coskun at Fatih Sultan Mehmet University for their assistance in conducting the SLM experiments. The author appreciates the guidance of Dr. Michael Gouge and Prof. Sualp Ozel on the Netfabb Simulation practices. This work was carried out at Istanbul Technical University EKAM laboratory supported by ISTKA under Grant TR10/18/YMP/0005 “Additive Manufacturing Education and Research Center”. The author gratefully acknowledges The Scientific and Technological Research Council of Turkey (TÜBİTAK) through Project No: 216M033 for their financial support.

REFERENCES

Clymer, D. R., Cagan, J., & Beuth, J. (2017). Power–Velocity Process Design Charts for Powder Bed Additive Manufacturing. *Journal of Mechanical Design*, *139*(10), 100907. doi:10.1115/1.4037302

Fox, J., & Beuth, J. (2013). Process Mapping of Transient Melt Pool Response in Wire Feed E-Beam Additive Manufacturing of Ti-6Al-4V. *Proceedings 2013 Solid Freeform Fabrication Symposium*,

(August), 675–683.
Schleifenbaum, H., Meiners, W., Wissenbach, K., & Hinke, C. (2010). Individualized production by means of high power Selective Laser Melting. *CIRP Journal of Manufacturing Science and Technology*, *2*(3), 161–169. doi:10.1016/j.cirpj.2010.03.005
Soylemez, E. (2018). *Modeling the Melt Pool of the Laser Sintered Ti6Al4V Layers with Goldak's Double-Ellipsoidal Heat Source*. In *Proceedings of 29th Solid Freeform Fabrication Symposium* (pp. 1721–1736). Austin, TX. Retrieved from

CERAMIC COMPOSITE COATING AND LASER SURFACE MELTING OF COCR ALLOY, AND ITS CHARACTERIZATION

Murat Isik[1, 2], Amit Bandyopadhyay[2], Anish Shivaram[2], Jose D. Avila[2], William S. Dernell[3], and Susmita Bose[2]
[1]*Faculty of Engineering and Natural Sciences, Sabanci University, 34956 Tuzla, Istanbul Turkey*
[2]*School of Mechanical and Materials Engineering, Washington State University, 99164-2920, Pullman, WA, USA*
[3]*College of Veterinary Medicine, Washington State University, 99164-2920, Pullman, WA, USA*
E-mail: murat.isik@wsu.edu, imurat@sabanciuniv.edu, amitband@wsu.edu, anishshivaram89@gmail.com, jose.avila@wsu.edu, wsdernell@wsu.edu and sbose@wsu.edu

Abstract. Cobalt-chromium (CoCr) alloys are widely preferred for artificial hip and knee joints applications since they perform excellent mechanical properties in addition to their economic advantages when compared to titanium-based alloys. However, there are still issues regarding its biocompatibility such as toxic Co and Cr ion release. In the current research, addressing the issue through laser engineered net shaping (LENS™) coating of biocompatible calcium phosphate (CaP) on CoCr alloy was aimed (Coatings are referred as CCM_{CaP}). Following this procedure, another CoCr alloy plate was treated with laser surface melting (LSM) using LENS™ set up ($CoCr_{LP}$). Samples were studied from the aspect of phase identification, microstructural investigation, and biocompatibility. A drastic increase of wear resistance, almost by 5 times, was detected in $CoCr_{LP}$. Formation of a phosphorous-based tribofilm layer is observed in the case of CCM_{CaP}. No cytotoxic effect was realized during the *In vitro* cell-material interactions study. Enhanced osteoid formation was found for the CCM_{CaP} through the Sprague Dawley rat and rabbit *in vivo* study.

Keywords: CoCr alloys, Load-bearing implants, Microstructure, Surface Modification, Biocompatibility.

1. INTRODUCTION

Alloys comprised of CoCr alloys are preferred in biomedical applications for example hip and knee joints as a consequence of their outstanding mechanical and wear properties (Chiba, Kumagai, Nomura, & Miyakawa, 2007). Contrariwise, the use of these implants still may induce problems, namely wear-induced osteolysis, a difference of modulus between the bone and implant, and metal ion release increasing the risk of various type of cancer formation because of bio-tribo corrosion (Fisher et al., 2004; Heneghan, Langton, & Thompson, 2012). Suppression of ion leaching and augmented biocompatibility can be achieved by coating of biomedical implants with bioactive ceramics such as hydroxyapatite (HA). Based on taking previous studies as a reference (Roy, Vamsi Krishna, Bandyopadhyay, & Bose, 2008; Zhang et al., 2011), it was hypothesized that coating application using HA can supports cell proliferation and raise hardness. In this study, simultaneous improvement of wear resistance and biocompatibility was targeted via HA coating on CoCr alloy (CCM_{CaP}), and laser surface melting of CoCr alloy ($CoCr_{LP}$) was also conducted. A bio-tribometer, scanning electron microscopy (SEM) and X-Ray diffraction (XRD) was used for studying tribological properties and microstructure. Moreover, the biocompatibility of $CoCr_{CaP}$ was evaluated through *in vitro* cell tests and *in vivo* studies.

2. MATERIALS AND METHODS

CoCr alloy (Stellite 6B) and HA powders with a size distribution ranging between 49-150 μm were attained from Corrosion Materials Inc. and Berkeley Advanced Biomaterials Inc. Premixed CoCr alloy and HA powder composites were processed using a Laser Engineered Net Shaping system (LENS™ 750, Optomec Inc., Albuquerque, NM) on a CoCr plate (Biodur® CCM Plus® Alloy). The surface melt geometry was of 10 mm diameter at 8.5 mm/s scan velocity using 450W laser power for single laser pass samples. Microstructural imaging was conducted following chemical etching of specimens using an SEM (FESEM, FEI-SIRION, OR, USA). Samples were analyzed with XRD for identifying the phases (PANalytical X'pert Pro MPD XRD). Hardness test was carried out using a Vickers microhardness tester with a load of 500 g and dwell time of 15 s. Ball-on-flat wear tests were conducted using a fully

automated tribometer (NANOVEA, Microphotonics Inc., CA USA) in deionized (DI) water at room temperature.

3. RESULTS AND DISCUSSION

Micrographs of $CoCr_{LP}$ at the different regions of the specimen is demonstrated in Figure 1. Regions corresponded to unmelted zones has a coarse-grained microstructure comprised of carbides near grain boundaries. However, in the case of regions close to the solidification front, dendritic structure with very fine honeycomb texture exists. Dendritic grains are aligned along the radial direction of the melt pool. Irregular network structure morphology with CaP phase presence is spotted at CCM_{CaP} (Sahasrabudhe, Bose, & Bandyopadhyay, 2018). XRD analysis detected γ phase peaks whereas peaks regarding fcc→hcp phase transformation was not observed with LSM application.

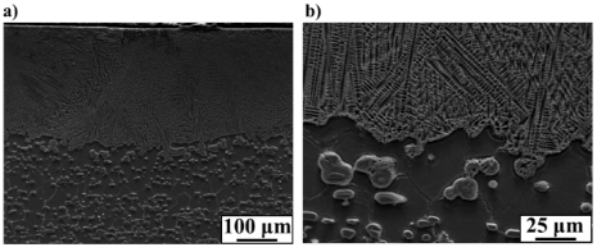

Figure 1. Optical Micrographs of $CoCr_{LP}$ a) Low magnification image of entire cross section and b) High magnification image of the interface between solidification front and heat affected zone (HAZ).

Application of LSM induces an improvement in the hardness from 314.5±13.0 HV (parent microstructure regions of CoCr alloy) to 425.5±6.0 HV (LSM surface). By comparison, final wear rates of CCM_{CaP} (5.16×10^{-7} mm^3/Nm) and $CoCr_{LP}$ (3.07×10^{-7} mm^3/Nm) are less than CoCr alloy (0.90×10^{-4} mm^3/Nm) without any treatment. Improvement in wear resistance is attributed to dendritic microstructure in $CoCr_{LP}$ while it corresponds to tribofilm layer formation at CCM_{CaP}.

4. CONCLUSIONS

CoCr alloys are one of the most preferred candidates among the metallic materials for biomedical applications although its toxic ion release is still a major concern. It was determined in our study that the addition of CaP to CoCrMo for coating increases wear resistance and biocompatibility at the same time. Formation of tribofilm is major mechanism for enhancement on wear resistance in the case of CCM_{CaP} whereas very fine dendritic microstructure is responsible for $CoCr_{LP}$. Decreased wear rates reduce ion leach for treated samples, therefore, results in enhanced biocompatibility, cell proliferation and spread with no toxic effect.

REFERENCES

Chiba, A., Kumagai, K., Nomura, N., & Miyakawa, S. (2007). Pin-on-disk wear behavior in a like-on-like configuration in a biological environment of high carbon cast and low carbon forged Co-29Cr-6Mo alloys. *Acta Materialia*, Vol. 55, pp. 1309–1318. https://doi.org/10.1016/j.actamat.2006.10.005

Fisher, J., Hu, X. Q., Stewart, T. D., Williams, S., Tipper, J. L., Ingham, E., … Berry, G. (2004). Wear of surface engineered metal-on-metal hip prostheses. *Journal of Materials Science. Materials in Medicine*, *15*(3), 225–235.

Heneghan, C., Langton, D., & Thompson, M. (2012). Ongoing problems with metal-on-metal hip implants. *BMJ*, *344*(feb28 1), e1349–e1349. https://doi.org/10.1136/bmj.e1349

Roy, M., Vamsi Krishna, B., Bandyopadhyay, A., & Bose, S. (2008). Laser processing of bioactive tricalcium phosphate coating on titanium for load-bearing implants. *Acta Biomaterialia*, *4*(2), 324–333. https://doi.org/https://doi.org/10.1016/j.actbio.2007.09.008

Sahasrabudhe, H., Bose, S., & Bandyopadhyay, A. (2018). Laser processed calcium phosphate reinforced CoCrMo for load-bearing applications: Processing and wear induced damage evaluation. *Acta Biomaterialia*, *66*, 118–

128. https://doi.org/10.1016/j.actbio.2017.11.022

Zhang, M. Y., Ye, C., Erasquin, U. J., Huynh, T., Cai, C., & Cheng, G. J. (2011). Laser Engineered Multilayer Coating of Biphasic Calcium Phosphate/Titanium Nanocomposite on Metal Substrates. *ACS Applied Materials & Interfaces*, *3*(2), 339–350. https://doi.org/10.1021/am100962m

A NEW DESIGN APPROACH FOR ADDITIVE MANUFACTURING OF SATELLITE COMPONENTS

Mehmet Emin BADIR[1,2], Akın DAGKOLU[1], Emirhan SOGUTKIRAN[1,2], Oguzhan YILMAZ[1]
[1]*Advanced Manufacturing Technologies Research Group (AMTRG), Department of Mechanical Engineering, Faculty of Engineering, Gazi University, Maltepe, 06570, Ankara, TURKEY*
[2]*TÜBİTAK UZAY Space Technologies Research Institute, METU Campus, 06800, Ankara, TURKEY*

Abstract. In today's industrial studies it is almost imperative to apply topology optimization in order to increase the specific strength in the design of parts and systems to be used in aerospace applications. In this optimization technique, the strength of the part can be increased while its mass being reduced at the same time by changing the material distribution within the part. Topology optimization design approach gives almost impossible to produce geometries by traditional manufacturing techniques. Manufacturing of such optimized products also become feasible with the use of additive manufacturing methods. This work presents a redesign approach for satellite reaction wheel bracket using topology optimization and DMLS (Direct Metal Laser Sintering) technique. Biomimetic design approach is used in order to qualify the part for space and earth conditions such as working under combined 20G acceleration and having a natural frequency of minimum 300 Hz by mimicking the tree branches and elephant feet shape. The optimum design of part shows that its weight is reduced by 47% and the Von-Mises stresses within the part is reduced at about 58%.

Keywords: Additive Manufacturing, Satellite Technologies, Topology Optimization

1. INTRODUCTION

Topology optimization lies under the structural optimization subject with size optimization and shape optimization processes. In size and shape optimization processes the work part is structurally optimized by changing its geometrical dimensions and outer shape. But topology optimization process optimizes the part with changing the distribution of the material within the work part [1]. Topologically optimized designs often have complex features which are hard to manufacture by traditional subtractive manufacturing methods. This manufacturing complexity leads to usage of additive manufacturing technologies. In Direct Metal Laser Sintering DMLS method, which is decided to be used in this study, fine metal powders (10-40um) get sintered with laser scanning and this laser melting process takes place for every layer of metal powder that laid on the built area [2]. Since the additive manufacturing (AM) is a relatively new generation of manufacturing technology and contains different methods, different design approaches are included in the literature. One of these design approaches is biomimetic design approach and it is used as the main design factor in this study. The biomimetic design approach takes its reference from biologic forms from nature and integrates the features of these forms to the mechanical designs. In this study, elephant feet and tree branches geometries are used as a reference design inspiration.

2. MATERIALS AND METHODS

In this work, the topologically optimized part is manufactured using EOS M290 DMLS machine available in ALUTEAM Center (Fatih Sultan Mehmet Vakıf University). AlSi10Mg metal powders with the size of 10-40um are used in the production. The selected alloy powder has the similar mechanical properties with Al 6000 series alloy which is currently preferred in space applications. The powder bed fusion process is performed using 370W laser power, 1300 mm/s laser scan speed, 0.19 mm hatch distance and 30um layer thickness during the process. 7515 layers are built in total with block support type. The production time is 47.5 hours. Afterwards, sand blasting, surface grinding and coating are performed as post-processing operations. The geometrical dimensioning and tolerancing are obtained using optical and contact measuring devises in order to validate the deformations and distortions which could be seen on critical features on the part after production.

3. RESULTS AND DISCUSSION

A typical design and analysis procedure is conducted in this work. Definition of the boundary conditions that form the assembly relations of the part, load cases acting on the part at its working conditions and geometrical constraints are set as the first step of the developed design workflow which is to be used for the inputs of the topology optimization process. Iteratively carrying through these optimization process on a commercial analysis and optimization tool, the final model has been created based on Design for Additive Manufacturing (DfAM) and biomimetic design approach. With accomplishing this optimization task, it is found that the bracket part is lightened by 47%, von-Mises stresses that occur within the part is reduced by 58% and its minimum natural frequency mode raised as high as 300 Hz.

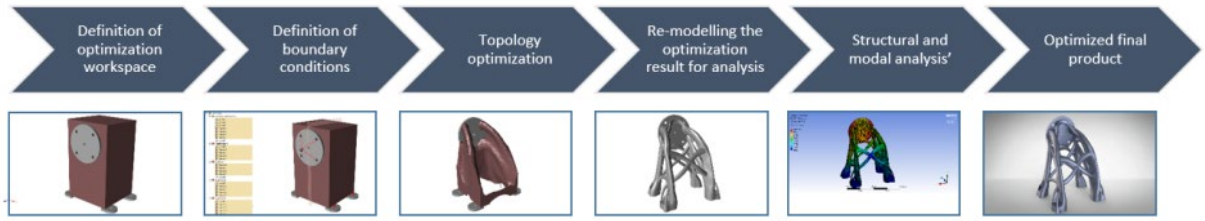

Figure 8: Topology optimization workflow

Manufacturing of the final optimized part is conducted on an EOS M290 DMLS powder bed fusion machine with the predetermined manufacturing parameters which are laser power, scanning speed, scan spacing, layer thickness, support structures and positioning of the part on the substrate. The optical scanning of the manufactured bracket part shows that the geometrical differences those may be occurred during manufacturing process lie within the predetermined tolerances. Also the density measurements conducted by Archimedes' Principle and X-Ray imaging show that the relative density of the DMLS sample which produced with the same parameters is not lower than 98%.

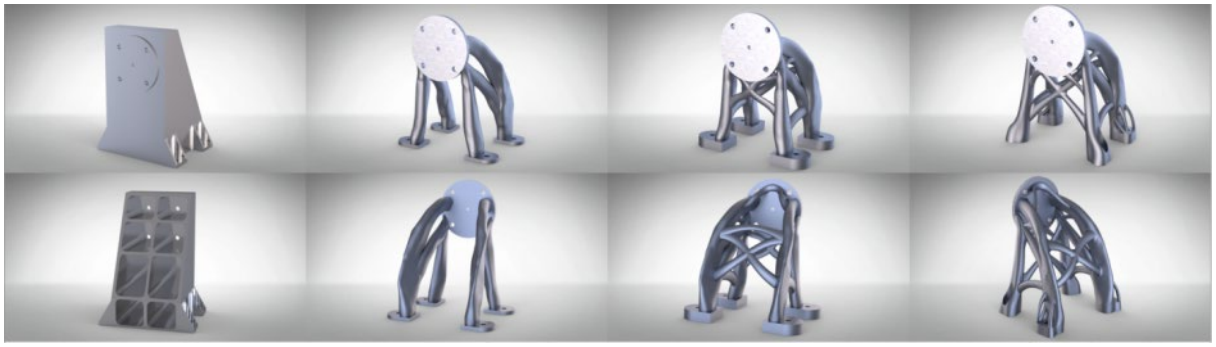

Figure 9 : Optimization steps of bracket part

4. CONCLUSIONS

Light weighting by topology optimization and more homogeneous stress distribution by biomimicry are achieved in this study. In addition, lowering waste (lower buy-to-fly ratio) and saving valuable material, examining complex design capabilities by AM for space applications is also gained. It is found that the optimized part weight reduced from 2.32 to 1.27 kg. The natural frequency is improved from 279 Hz to 301 Hz. On the other hand, the proposed design approach eliminates the von-Mises stresses at critical regions and maximum 76 MPa is obtained on the AM model while the traditional design has 185 MPa. Archimedes method confirmed the volumetric density and optical measurements have shown that the AM part has almost no defects that might be caused by DMLS process. Environmental analyzing and vibration tests are to be planned in order to simulate the launching and space conditions to qualify the process and design for space applications.

REFERENCES

1. Behrouz Ahmadi-Nedushan, Yazd Univ. “Differences among Size, Shape and Topology Optimization” https://www.researchgate.net/post/Differences_among_Shape_Size_and_Topology_optimization, 2014
2. Yicha Zhanga, Alain Bernard, Ravi Kumar Gupta, Ramy Harik, 2014, “Evaluating the Design for Additive Manufacturing: A Process Planning Perspective”, Procedia CIRP 21 144 – 150, 2014

VALIDATION OF DYNAMIC MODELS OF ADDITIVE MANUFACTURED PARTS USING SELECTIVE LASER MELTING METHOD

Akin Orhangul[1], Kenan Y. Sanliturk[2]
[1]*TUSAS Engine Industries, Inc.,*
akin.orhangul@tei.com.tr
[2]*Istanbul Technical University,*
sanliturk@itu.edu.tr

Abstract. This paper investigates the use of modal analysis & testing as a non-destructive validation technique for additively manufactured (AM) metal parts using Selective Laser Melting (SLM) method. For most engineering components, vibration plays a major role. In practice, most of the additive manufacturing users focus on basic mechanical properties of components. However, it is also necessary to examine the vibration characteristics of additively manufactured parts as they are mostly subjected to dynamic loads in their operational environments. The Frequency Response Function (FRF) is dependent on both the geometry and the material properties of the component as well as the presence of any defects. This allows the FRF to serve as a fingerprint for a given part. Once the reference fingerprint is established, FRF can be used to qualify the additively manufactured parts.
Finite element models and the corresponding results are obtained for conventional and additively manufactured parts. Natural frequencies and mode shapes are obtained using FE models for both conventional and AM parts. Then, vibration tests are performed on structures manufactured using AM and the conventional methods for comparison purposes. Natural frequencies and damping levels are obtained from measured FRFs for both conventional and AM parts. By comparing experimental and theoretical results, FE models of conventional and AM parts are verified and updated according to the natural frequencies identified from FRFs. This process allowed estimation of more accurate material properties, yielding more realistic and representative FE models for AM parts.

Keywords: Selective Laser Melting, Vibration Testing, Finite Element Analysis, Natural Frequency, Damping

1. INTRODUCTION

The use of additive manufacturing process has increased rapidly in the last decade. Nowadays, final products, rather than prototypes, are being manufactured using Additive Manufacturing (AM) Technologies including various parts of industrial machines, motor vehicles, aero engines etc. It is extremely important that structures manufactured by AM technologies provide sufficient level of strength which should be comparable or better than that which can be obtained by casting or forging processes. For example, an aero engine part operates in harsh environments and should survive under extreme dynamic excitations and static loads. However, various parameters in SLM process, such as scan speed and layer thickness, affect the mechanical properties of the parts manufactured. This makes development of reliable theoretical models difficult. Therefore, there is a need for developing validated theoretical models for parts that are manufactured via AM technologies so as to simulate various mechanical tests and make appropriate design changes or modifications during the design stage. Since it is not feasible to make prototypes for every possible design options, it is logical to make simulations using validated FE models of structures manufactured by AM technology.
Changing the process parameters of SLM to obtain desired mechanical properties is one of the subjects studied in the literature [1]. Obtaining different mechanical properties using different process parameters in order to make less stiff implants in especially biomedical applications is considered as one of the major advantages of SLM process. Providing the required strength and stiffness values with reduced weight is also an important advantage of SLM process in other industrial applications [2, 3]. Spierings et al. have associated mechanical properties such as Young's modulus with porosity as shown in Figure 1. This is considered as an advantage, which makes it possible to obtain different mechanical properties at different regions of the parts [2].

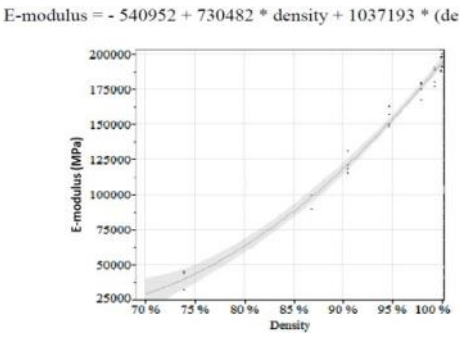

Figure 1. Dependency of Young's modulus on material density [2].

2. MATERIALS AND METHODS

The values of Density, Poisson's ratio and Young's modulus are needed in order to model both conventionally and additively manufactured parts. Young's modulus (E), shear modulus (G) and Poisson's ratio properties are measured according to ASTM E1876-15 standard (Standard test method for dynamic Young's modulus, shear modulus, and Poisson's ratio by impulse excitation of vibration). The density of the material is determined using Archimedes' principle which is described in BS EN ISO 3369:2010 (Impermeable sintered metal materials and hard metals – Determination of density) standard. A hot rolled and solution heat treated plate manufactured according to AMS 5599F (Nickel Alloy, Corrosion and Heat Resistant, Sheet, Strip, and Plate 62Ni – 21.5Cr – 9.0Mo – 3.7 (Cb+Ta) Annealed) standard is used as conventional sample in material tests. In order to provide repeatability, 2 high density and 2 low density samples are manufactured using additive manufacturing process. In this paper, material properties are estimated via updating FE models using natural frequencies identified from measured FRFs.

3. RESULTS AND DISCUSSION

Comparisons of experimental natural frequency results for conventional, high density AM and low density AM parts which are beam structures with dimensions of 10 mm height, 25 mm width and 300 mm length are given in Figure 2.

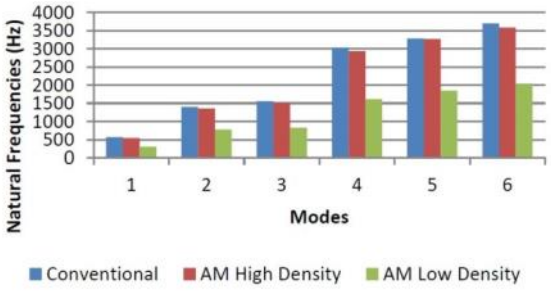

Figure 2. Comparisons of experimental natural frequency results for conventional, high density AM and low density AM parts

From the results, it is obvious that conventional structure has the highest natural frequencies whereas AM low density has the lowest natural frequencies. It is also seen from these results that the natural frequencies of AM high density structure are quite close to that of the structure manufactured via conventional method.

Loss factors which are estimated from measured FRFs for all 3 structures for the first 6 elastic modes are given in Figure 3. It is obvious that low density AM part has the highest level of damping. Porosity level of AM low density structure is 20 % and it is anticipated that this high level of damping is related to the porosity. On the other hand, the structure manufactured via conventional method has

the lowest damping. This result indicates that AM has the advantage of increasing the material damping, a phenomena which may well be exploited in critical applications.

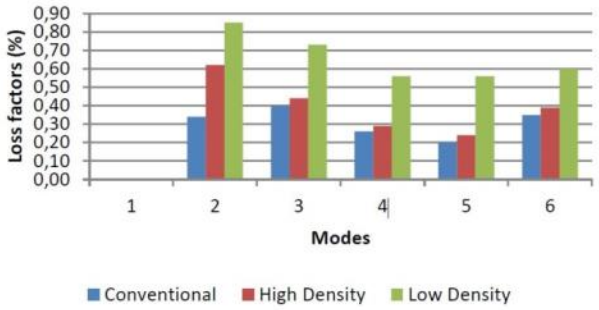

Figure 3. Comparisons of loss factors for 3 structures.

Comparison of Young's moduli for all 3 structures is given in Figure 4. It is seen that Young's modulus strongly depends on porosity, higher levels of porosity leading to very substantial reduction in Young's modulus.

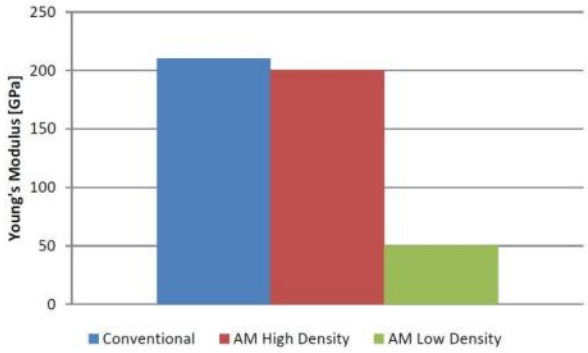

Figure 4. Comparison of Young's moduli for all 3 structures.

The dependency of Young's modulus on material density of structures manufactured via AM is also investigated. The limited number of results obtained in this research are presented in Figure 5. It is seen that the Young's modulus and density of the AM high density part are almost the same as those of the conventional part. It is clear from Figure 5 that Young's modulus decreases with decreasing density showing similar trend with *Figure 1*. One can infer that a part that has a density between AM high density and AM low density part, it will have a Young's modulus between 50 GPa and 200 GPa.

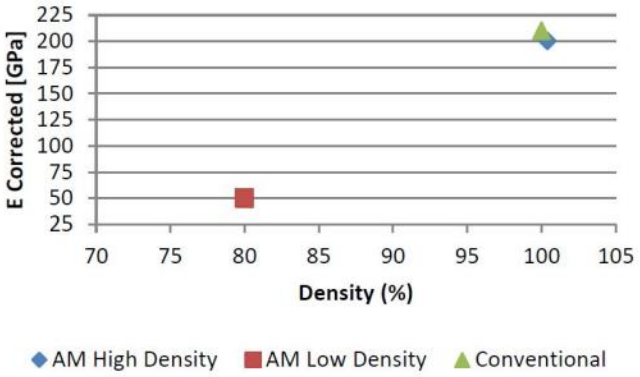

Figure 5. Dependency of Young's modulus on IN625 material density.

4. CONCLUSIONS

- In terms of measured natural frequencies, there is up to 2.8% difference between parts manufactured by conventional methods and parts manufactured by AM technology. If this level of variation in natural frequencies is acceptable, parts manufactured by AM technology can be used as counterparts for parts manufactured by conventional methods.
- It is obvious from experimental and theoretical (FE) results that natural frequencies shift to lower values when porosity levels increase.
- It is seen that one can manufacture a specific part that has a specific Young's modulus and density/porosity value by adjusting process parameters with powder bed AM technology.
- Young's modulus of an AM part can be estimated via vibration tests and FE analysis.
- Damping levels increase with increasing porosity levels for parts manufactured by AM technology.
- It is possible to manufacture a specific part that has a specific damping level by adjusting AM process parameters. According to damping level requirement for a part that will be designed, it is possible to tune damping level by varying density/porosity levels by adjusting AM process parameters.

Suggestions for future work are listed below:

- Parts that have varying density levels can be manufactured and vibration tested.
- Conventional parts consisting of multiple subparts can be manufactured as single piece part using AM technology. One can manufacture single piece part using AM technology and try to observe effects of welding or bolt/nut coupling used in conventional parts on damping levels.
- Parts with different build directions should be manufactured and vibration tested in order to understand and model the anisotropy in AM technology.

REFERENCES

[1] **Sierra M.** (2013). Additive Manufacturing at ITP, Date retrieved: 09.01.2015, adress: http://www.lortek.es/files/fab-aditiva/additive-manufacturing-in-itp-ik4-lortek.pdf.

[2] **Spierings, A. B., Wegener K., Levy G.** (2012). Designing material properties locally with additive manufacturing technology SLM, Symposium on Freeform Fabrication, Austin, TX, USA, August 2012.

[3] **Yadroitsev, I., Thivillon L., Bertrand Ph., Smurov I.** (2007). Strategy of manufacturing components with designed internal structure by selective laser melting of metallic powder,Applied Surface Science, 254/4, pp.980-983.

THERMAL PROCESS SIMULATION FOR DIRECT ENERGY DEPOSITION ADDITIVE MANUFACTURING PROCESS

Kerem Dörtkaşlı[1,2,3], Eralp Demir[1,2,3]
kdortkasli@sabanciuniv.edu, eralpd@sabanciuniv.edu
[1]*Integrated Manufacturing Technologies Research and Application Center, Sabanci University, 34956, Istanbul, Turkey.*
[2]*Composite Technologies Center of Excellence, Sabanci University-Kordsa, Istanbul Technology Development Zone, Sanayi Mah. Teknopark Blvd. No:1/1B, Pendik, 34906, Istanbul, Turkey.*
[3]*Faculty of Engineering and Natural Sciences, Sabanci University, Tuzla, 34956, Istanbul, Turkey.*

Abstract. The objective of this work is development of an additive manufacturing (AM) simulation method for the directed energy deposition (DED) process using finite element method (FEM). Due to its capabilities, DED process has been widely used in different industries for metal AM. Yet, repeatability with achievement of high-quality products for each production is still not enough. High cooling rate and solidification repeatedly at every build layer that occur in parts during manufacturing with high thermal gradients result as residual stress generation in part and distortion that can cause detrimental effects on parts. For this purpose, thermal DED process simulation model is developed for Inconel 718 metallic parts and its verification will be achieved by commercial software for the comparison of accuracy and effectiveness of model's results in computational time.

Keywords: Additive manufacturing, process modeling, thermal model, direct energy deposition, finite element method.

1. INTRODUCTION

Thermal gradients in high values with high rate cooling and heating cycles give rise to residual stress accumulated in additively manufactured parts as a result of local laser heat source during melting layers of metal powder successively. Thermomechanical process simulation development by using Finite Element Method (FEM) can be effective solution to diminish residual stresses and distortions by indicating them beforehand by giving an opportunity to change/modify the manufacturing parameters and plan. Prediction of residual stress generation and/or distortions by conducting additive manufacturing (AM) process as a thermo-mechanically coupled boundary problem is the focus of finite element modeling (Michaleris, 2014). As a result, with an effective model, by avoiding the application of the trial and error method, the loss of time and money can be avoided. The main and most important reason of the residual stress formation is the thermal gradients formed between the building substrate and deposited layer (Denlinger and Michaleris, 2016). Residual stresses in parts that are produced due to AM, lead to formation of distress, delamination between deposited layers, distortion and loss of tolerances in geometry. For both static and fatigue mechanical properties of materials, residual stresses are negatively affected by residual stresses (Klingbeil et al., 2002). Preheating of base plate before manufacturing, optimization of scanning strategies, optimization of process parameters and build orientation, hatch pattern, island scanning on base plate are some of the applications to reduce residual stress in AM parts (DebRoy et al., 2018). In this study a thermal model is developed to compute the transient temperature distributions inside an additively manufactured part using a commercial finite element software as the very first step to estimate the residual stresses.

2. MATERIALS AND METHODS

This study presents the thermal solution of thermo mechanical process modeling currently being developed with Inconel 718 built material and AISI 316 stainless steel base plate for Direct Energy Deposition (DED) process. The methods for the thermal process simulations are explained as in the below for the thermal model. Figure 1 shows thermal process simulation in commercial finite element software MSC.Marc®.

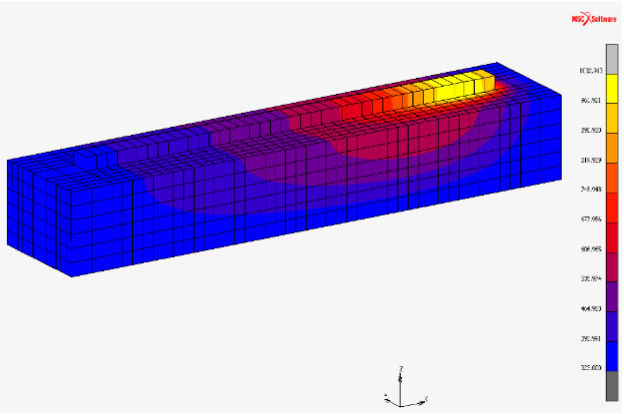

Figure 10

Thermal Model

Thermal model includes solution of transient energy balance relation for a given moving heat flux. In equation (1); $\rho, C_p, T, q, \dot{Q}$ represent mass density, specific heat, temperature, heat flux vector and heat input, respectively. The heat flux vector and heat input are computed at position x and at time t.

$$\rho c_p \frac{\partial T}{\partial t} = -\nabla \cdot q(x,t) + \dot{Q}(x,t) \quad (1)$$

Goldak's double ellipsoid model is used as the heat input as shown in Equation (2). $\dot{Q}$ is the heat input per unit volume, P is the laser beam power and η is the efficiency factor, r_x, r_y, r_z represent laser spot radii in $x, y,$ and z respectively. Moving heat flux is implemented using DFLUX subroutine.

$$\dot{Q}(x,t) = \frac{6\eta\sqrt{3}p}{\Pi\sqrt{\pi}r_x r_y r_z} \exp\left(-\frac{3x^2}{{r_x}^2}\right) \exp\left(-\frac{3x^2}{{r_y}^2}\right) \exp\left(-\frac{3x^2}{{r_z}^2}\right) \quad (2)$$

The heat flux vector, q, is computed using the temperature gradients as given in Equation (3).

$$q(x,t) = -k\nabla T \quad (3)$$

The corresponding heat transfer rate from the surfaces, Q_{Conv}, is computed using an effective convection coefficient, h, and ambient temperature, T_{amb} and radiative heat loss, Q_{rad}, where ε is emissivity and K_B is Boltzmann constant, computed as shown in Equations (4) and (5), respectively. Convection coefficient is applied to the surfaces using UFILM subroutine.

$$Q_{Conv}(x_s,t) = h(T - T_{amb}) \quad (4)$$

$$Q_{rad}(x_s,t) = K_B\varepsilon\left(T - {T_{amb}}^4\right) \quad (5)$$

UACTIVATE subroutine is used for element activation in conjunction with the 5% criterion (Yang et al.,2016)

3. RESULTS AND DISCUSSION

Mesh refinement study reveals convergence of the results after certain mesh refinement level. A relatively coarse mesh is used for base plate when compared with built material. 8 noded hexahedra elements (Hex 8) are used in the simulations. Number of divisions along the build material should be known for total number of elements used in mesh. Hence, a factor generated to reduce the size of the elements to see the effect of number of elements in mesh (both for activated and deactivated elements) and mesh refinement on process model. This factor also correlated with the sub element division of build

layer parallel to build direction (along x direction). In addition, factors such as scale factor of base plate along each direction, size of plate along each direction and number of divisions along build direction are the input variables used in the code generated in MATLAB®.

The node that is from the element at the middle of the generated first layer selected as location to investigate temperature distribution during whole process. Convergence of temperatures with mesh refinement could be concluded from Figure 2.

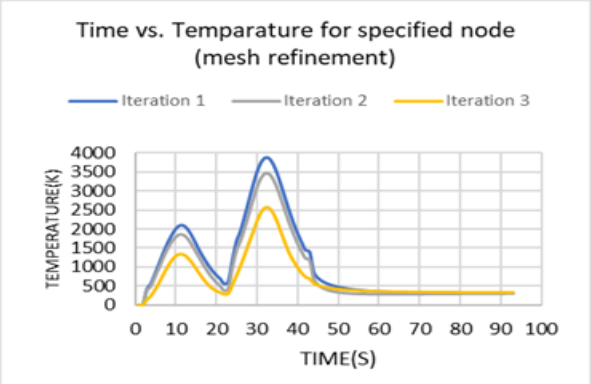

Figure 2

Figure 3 shows the effect of laser power (LP) for the selected mesh refinement (level 3 in Figure 2). As the energy input increases peak temperatures and the overall thermal energy of the system also increases as expected.

The effect of other parameters such as layer thickness (LT), build direction (BD) and laser spot size (SS) will also be investigated in this study.

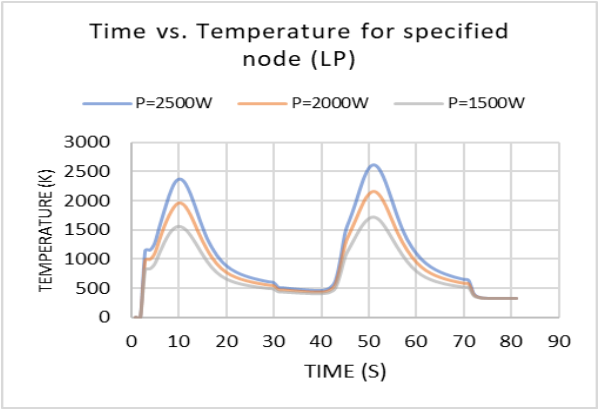

Figure 3

3.1 Abbreviations and Acronyms

AM;	Additive Manufacturing
DED;	Direct Energy Deposition
FEM;	Finite Element Method
AISI;	American Iron and Steel Institute
LP;	Laser Power
LT;	Layer Thickness
BD;	Build Direction
SS;	Laser Spot Size

4. CONCLUSIONS

The purpose of this study is to develop a thermal computational model for DED process to predict thermal history of the built part. The effect of mesh refinement and laser power are presented. The presented work will be later used to predict residual stresses and distortions.

REFERENCES

DebRoy, T., Wei, H. L., Zuback, J. S., Mukherjee, T., Elmer, J. W., Milewski, J. O., ... & Zhang, W. (2018). Additive manufacturing of metallic components–process, structure and properties. *Progress in Materials Science*, *92*, 112-224.

Denlinger, E. R., & Michaleris, P. (2016). Effect of stress relaxation on distortion in additive manufacturing process modeling. *Additive Manufacturing*, *12*, 51-59.

Klingbeil, N. W., Beuth, J. L., Chin, R. K., & Amon, C. H. (2002). Residual stress-induced warping in direct metal solid freeform fabrication. *International Journal of Mechanical Sciences*, *44*(1), 57-77.

Michaleris, P. (2014). Modeling metal deposition in heat transfer analyses of additive manufacturing processes. *Finite Elements in Analysis and Design*, *86*, 51-60.

Yang, Q., Zhang, P., Cheng, L., Min, Z., Chyu, M., & To, A. C. (2016). Finite element modeling and validation of thermomechanical behavior of Ti-6Al-4V in directed energy deposition additive manufacturing. *Additive Manufacturing*, 12, 169-177.

TOPOLOGY OPTIMIZATION AND FINITE ELEMENTAL ANALYSIS FOR AN INCONEL 718 ENGINE MOUNTING BRACKET MANUFACTURED VIA ELECTRON BEAM MELTING

Murat Isik[1,a], Erdal Kisa[1,b], Bahattin Koc[1,2,c], Mehmet Yildiz[1,2,d], Baris Pehlivanogullari[3,e], Akin Orhangul[3,f], Ozgur Poyraz[3,g] and Guray Akbulut[3,h]

[1]*Integrated Manufacturing Technologies Research and Application Center, Sabanci University, Istanbul Technology Development Zone, Sanayi Mah. Teknopark Blvd. No: 1/1B, Pendik, 34906 Istanbul* [2]*Faculty of Engineering and Natural Sciences, Sabanci University, 34956 Tuzla, Istanbul Turkey*

[2]*Tusas Engine Industries Inc., 26003, Eskisehir, Turkey*

E-mail: [a]imurat@sabanciuniv.edu, [b]erdalkisa@sabanciuniv.edu, [c]bahattinkoc@sabanciuniv.edu, [d]meyildiz@sabanciuniv.edu, [e]baris.pehlivanogullari@tei.com.tr, [f]akin.orhangul@tei.com.tr, [g]ozgur.poyraz@tei.com.tr, [h]guray.akbulut@tei.com.tr

Abstract. In recent years, there is a growing interest in additive manufacturing (AM) technologies for aerospace industries because it offers direct digital manufacturing of highly complex fully functional critical components. Among the all AM techniques, electron beam melting (EBM), a powder bed fusion process, is one of the most promising methods because of its freedom production of complex geometries as well as improved mechanical properties. EBM can be used to manufacture functional critical components in aerospace applications such as brackets for serving as engine mounts. For brackets or engine mounts, it is critical to damper vibration and also support the weight of the engine during service. Therefore, the mechanical properties of the brackets are very critical as well as the weight reductions without sacrificing the dynamic mechanical properties. In this work, topology optimization methods are used to optimize geometry of an engine bracket for its lightweight and high-performance. The topology optimization of the engine bracket was done using ANSYS and OptiStruct software. Reduction in the weight of the engine mounting taking into account of design and material layout was determined and compared between two software. In addition, the effect of different loading conditions on the topology optimization of the EBM-built Inconel 718 bracket was studied.

Keywords: Inconel 718, Electron Beam Melting, Topology Optimization, Finite Elemental Analysis.

1. INTRODUCTION

Inconel 718 alloy has recently become one of the most popular metallic materials in applications for the aerospace industry (Mercer, Soboyejo, & Soboyejo, 1999) since they present unique mechanical properties and strong resistance to high temperatures (Xu, Murray, Hyde, & Clare, 2018). Conventional methods (CM) are nowadays being suppressed by additive manufacturing (AM) techniques, electron beam melting (EBM) is one of those, has serious advantages over conventional manufacturing since the processing of complex IN718 parts induce difficulties in manufacturing (Sadowski, Ladani, Brindley, & Romano, 2016). However, EBM-built components can be still improved by reducing the weight while keeping its required mechanical properties. Topology optimization (TO) is an approach for optimization of body structures calculating optimum material distribution within a design domain for a given set of loads, boundary conditions and constraints (Bendsøe & Sigmund, 2004). Because the geometry generated by the TO method could be complex, conventional manufacturing methods cannot be used to manufactured TO parts. AM or EBM methods can be used to manufacture such structures under manufacturing constraints. In this study, additively manufactured EBM bracket was topologically optimized for its lightweight under realistic load conditions.

2. MATERIALS AND METHODS

Material properties for the bracket were designated as orthotropic-elastic for conducting analyses. The initial weight of the engine mounting bracket is calculated as 1.1509 kg. Hex20 elements were used in the finite element analysis of bracket. Each element was defined by 20 nodes having three degrees of freedom

(ux, uy and uz) per node. Overhang angle was taken as 45˚.The minimum feature size or unit length was set at 1 mm. A load of 20 kN is applied with angles such as 0˚, 45˚, 60˚, 75˚ and 90˚. The bracket holes were constrained in 6 degrees of freedom in three-dimension space as a boundary condition. The manufacturing constraint was set as symmetrical. The other boundary conditions were determined as; 3 mm minimal unit length, a minimal weight reduction of ≈%30, and to robust characteristic resistance of the structure. Inconel 718 material was selected as the manufacturing material. Density, elastic modulus, Poisson's ratio and shear modulus values were accepted as 8220 kg/m3; E_x:149 GPa, E_y:149 GPa and E_z:125 GPa; ν_x:ν_y:ν_z: 0.3; and Gx: 57.3 GPa, Gy: 57.3 GPa and Gz:48.07 GPa. Topology optimization (TO) was done using ANSYS and OptiStruct software and the results are compared.

3. RESULTS AND DISCUSSION

Figure 1 and Figure 2 shows the results obtained by Ansys and OptiStruct software respectively. Hex20 elements for Ansys (Fig. 1 a) and Hex8 was used for OptiStruct (Fig. 1 a) and Fig. 2 a)) respectively. The original bracket was subjected to 90˚ angled load along the Z axis. The stress levels of the original bracket were represented in Fig. 1 b) and Fig. 2 b) where maximum (max) equivalent stress (σ_E) is around 524.8 MPa with deformation of max 0.084 mm and 279.0 MPa with deformation of max 0.059 for OptiStruct . TO was realized where minimum stress concentrations are observed. The topologically optimized bracket is given in Fig. 1 b) (Ansys) and Fig. 2 b) (OptiStruct). The purpose was to lessen the weight of the bracket without changing its function. It has been found that the total weight reduction for bracket with an applied load of 90˚ was achieved around %35.98 with Ansys and %32.9 with OptiStruct . In addition, bracket with TO was subjected to 90˚ load to see the stress levels (Fig. 1 d) and Fig. 2 d)) which was targeted to follow the same trend as that of the original bracket (Fig. 1 a)). In TO applied model, the max σ_E and deformation are determined 386.35 MPa and 0.086 mm with Ansys and 274.3 MPa and 0.070 mm with OptiStruct respectively.

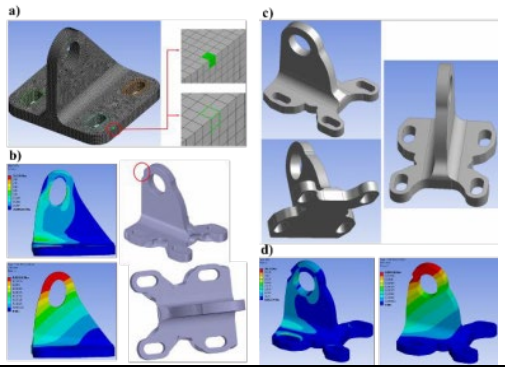

Figure 1. a) Meshed model of original bracket in Ansys,
b) Equivalent stress and deformation of the original bracket under 90˚ load along Z axis and TO applied bracket model,
c) Revised model for notch removal near the hole in TO applied model, d) Equivalent stress and deformation of bracket with TO under 90˚ load along Z axis.

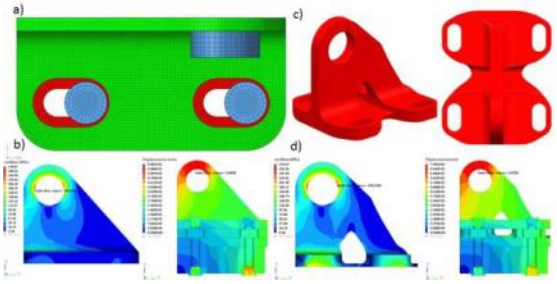

Figure 2. a) Meshed model of original bracket in OptiStruct , b) Equivalent stress and deformation of the original bracket under 90˚ load along Z axis,
c) TO applied bracket model, d) Equivalent stress and deformation of bracket with TO under 90˚ load along Z axis.

4. CONCLUSIONS

A TO method was developed to reduce weight of an engine bracket under realistic loads. The additively manufactured bracket using EBM under manufacturing constraints considered. Compared to conventional manufacturing methods, the complex geometry from TO result can be manufactured with EBM without difficulty. There is a big reduction in the weight by %35.98 compared to the original bracket while maintaining full functionality and the mechanical requirements of the bracket.

REFERENCES

Bendsøe, M. P., & Sigmund, O. (2004). *Topology Optimization*. https://doi.org/10.1007/978-3-662-05086- 6

Mercer, C., Soboyejo, A. B. O., & Soboyejo, W. O. (1999). Micromechanisms of fatigue crack growth in a forged Inconel 718 nickel-based superalloy. *Materials Science and Engineering A*, Vol. 270, pp. 308– 322. https://doi.org/10.1016/S0921-5093(99)00214-2

Sadowski, M., Ladani, L., Brindley, W., & Romano, J. (2016). Optimizing quality of additively manufactured Inconel 718 using powder bed laser melting process. *Additive Manufacturing*, *11*, 60– 70. https://doi.org/10.1016/j.addma.2016.03.006

Xu, Z., Murray, J. W., Hyde, C. J., & Clare, A. T. (2018). Effect of post processing on the creep performance of laser powder bed fused Inconel 718. *Additive Manufacturing*, *24*, 486–497.

MICROSTRUCTURE AND EFFECT OF HOLE ON MECHANICAL PROPERTIES OF INCONEL 718 BUILT VIA DIRECT METAL LASER SINTERING

Murat Isik[1,a], Bahattin Koc[1,2,b], Mehmet Yildiz[1,2,c]
[1]*Integrated Manufacturing Technologies Research and Application Center, Sabanci University, Istanbul Technology Development Zone, Sanayi Mah. Teknopark Blvd. No: 1/1B, Pendik, 34906 Istanbul* [2]*Faculty of Engineering and Natural Sciences, Sabanci University, 34956 Tuzla, Istanbul Turkey*
E-mail: [a]*imurat@sabanciuniv.edu,* [b]*bahattinkoc@sabanciuniv.edu, and* [c]*meyildiz@sabanciuniv.edu*

Abstract. In this study, the microstructure of direct metal laser sintering (DMLS) fabricated Inconel 718 alloy (IN718) and subsequently heat treated condition ($IN718_{HT}$), and the effect of hole presence on its mechanical properties were investigated. Besides the manufacturing $IN718_{HT,}$ a batch of the tensile test specimens with a hole in the center was produced using DMLS ($IN718_{OHT}$) whereas other batch were built without a hole, where it was applied through a drilling process ($IN718_{DH}$), following the DMLS processing. Further, understanding possible reasons behind the differences in mechanical properties between at IN718, $IN718_{OHT}$ and $IN718_{DH}$ was targeted. Microstructure analysis of IN718 specimen presents scan layers and columnar grains oriented towards building direction. On the other hand, subjecting DMLS built specimen to a heat treatment drastically alter the microstructure where scan layers completely disappear and some of the equiaxed grains and building direction oriented columnar grains co- exist at $IN718_{HT}$ which illustrates superior UTS (≈1295 MPa), and yield stress (≈1061 MPa) values with 13% elongation at failure. The UTS, yield stress and elongation of $IN718_{OHT}$ are 1293 MPa, 970 MPa, and 4.79%. Further investigation will be undertaken to reveal the mechanical behavior of $IN718_{OHT}$ and $IN718_{DH}$ and to elucidate its correspondence with microstructure.

Keywords: Inconel 718, DMLS, Microstructure, Mechanical Properties, Open Hole Specimen.

1. INTRODUCTION

Inconel 718 (IN718), a nickel-based super alloy, have been preferred in applications such as turbine disks (Mercer, Soboyejo, & Soboyejo, 1999) and jet engines owing to their exceptional mechanical properties and heat resistance (Xu, Murray, Hyde, & Clare, 2018). It has been broadly manufactured into structural components using direct metal laser sintering (DMLS), which is one of the most promising additive manufacturing methods, since processing IN718 through conventional methods has difficulties (Sadowski, Ladani, Brindley, & Romano, 2016). DMLS enable manufacturers to build structural components with special desired geometries consists of holes on the bodies without the formation of notches and defects. On the other hand, hole drilling operations have some certain complications just as naturally induced defects around the hole and the necessity of achieving expected tolerances. The stress concentration around the hole is known to start failure when they are used in applications (Gopalakrishna, Narasimha Murthy, Krishna, Vinod, & Suresh, 2010). Therefore, it is crucial to study the mechanical properties of IN718 and holed geometries, and to establish its relationship to microstructure.

2. MATERIALS AND METHODS

Inconel 718 powder used in this study was EOS NickelAlloy IN718 product with an average particle size of 40 µm. Subsequently, DMLS built alloy was subjected to heat treatment according to AMS 5664 standard ($IN718_{HT}$). Microstructural characterization was conducted on the transverse plane from the build direction following the cross-sectioning. The electrochemical polishing procedure was directed using an aqueous solution of HCl at an applied potential for 5 V around 5-10 seconds. Operation of microstructural observation was completed with Nikon Clemex LVN100ND optical microscope (OM). The surface quality of the alloys was studied via Nano Focus uSurf Non-Contact 3D Profilometer.

Hardness test was carried out using an AFFRI 206 EX/206 EXS Rockwell tester. Tensile test on $IN718_{HT}$ and $IN718_{HT}$ was conducted according to ASTM E8 and D6766 standards using Digital Image Correlation (DIC). Inconel 718 alloys were analyzed by X-ray (XRD) (D2 Phaser BRUKER XRD Machine). The performed range selected between 0˚-110˚ for XRD analyses.

3. RESULTS AND DISCUSSION

Figure 1 exhibits the microstructure of DMLS built IN718 and where columnar grain structure growth along building direction with the existence of scan layer track is visible. However, in the case of $IN718_{HT}$, scan layers are vanished but columnar grains still remains. On a previous study, it was mentioned that subjecting IN718 alloy to a heat treatment may not cause the formation of equiaxed grains owing to presence of excessive amount of secondary phases and carbides, where they act as grain boundary pinners, constraining grain growth unlike the case of Inconel 625 alloy (Raghavan et al., 2017). The surface morphology investigation on IN718 exposes Ra and Sa values were around 4,8 µm and 40 µm for the surface perpendicular to building direction while they are 6,4 µm and 23 µm for the lateral plane. XRD analysis did not detect the δ phase.

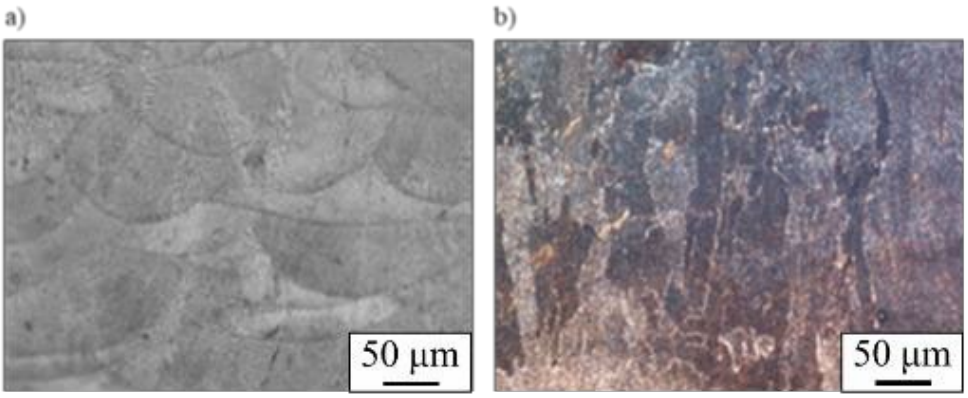

Figure 1. Optical Microscope Images of a) IN718 and b) $IN718_{HT}$.

Figure 2 suggests the strain evolution of $IN718_{OHT}$ specimen at where maximum strain appears on the hole edges and specimen fractures from hole exterior zones. UTS of $IN718_{HT}$ and $IN718_{OHT}$ are almost identical (1295 MPa and 1293 MPa) whereas yield stress and elongation decrease at $IN718_{OHT}$ (970 MPa and 4.73%) compared to those of $IN718_{HT}$ (1061 MPa and 13%).

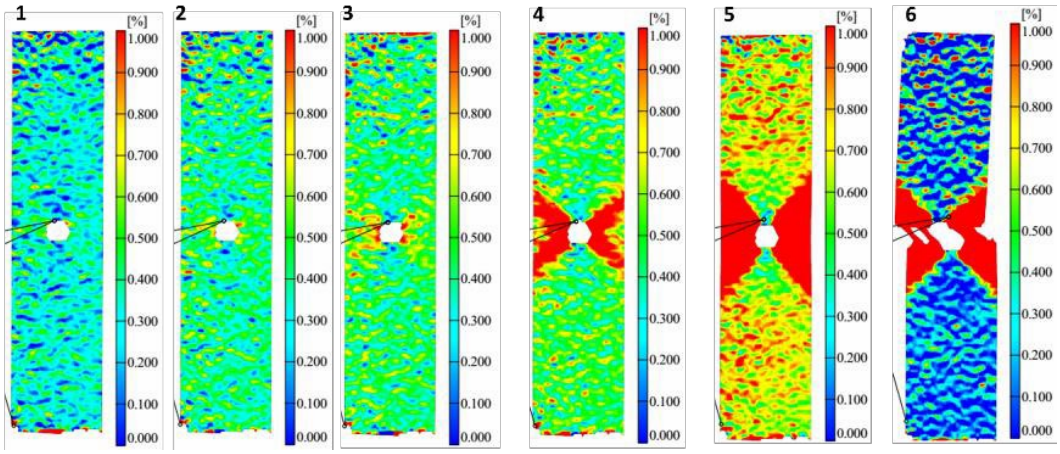

Figure 2. Strain Evolution of OHT Inconel 718 Specimen During Tensile Test.

4. CONCLUSIONS

Fabrication of DMLS processed parts carries a great deal of potential for future applications in various types of industries. However, the enhancement of the product quality in the process is still an ongoing process which requires careful examination of parts manufactured by this method. In this study, microstructure and mechanical properties of $IN718_{HT}$ and $IN718_{OHT}$ were investigated and the results compatible with the literature was obtained. In the future, studies on $IN718_{HT}$ and $IN718_{DH}$ will further be proceeded.

REFERENCES

Gopalakrishna, H. D., Narasimha Murthy, H. N., Krishna, M., Vinod, M. S., & Suresh, A. V. (2010). Cold expansion of holes and resulting fatigue life enhancement and residual stresses in Al 2024 T3 alloy - An experimental study. *Engineering Failure Analysis*, Vol. 17, pp. 361–368. https://doi.org/10.1016/j.engfailanal.2009.08.002

Mercer, C., Soboyejo, A. B. O., & Soboyejo, W. O. (1999). Micromechanisms of fatigue crack growth in a forged Inconel 718 nickel-based superalloy. *Materials Science and Engineering A*, Vol. 270, pp. 308–322. https://doi.org/10.1016/S0921-5093(99)00214-2

Raghavan, S., Zhang, B., Wang, P., Sun, C. N., Nai, M. L. S., Li, T., & Wei, J. (2017). Effect of different heat treatments on the microstructure and mechanical properties in selective laser melted INCONEL 718 alloy. *Materials and Manufacturing Processes*, Vol. 32, pp. 1588–1595. https://doi.org/10.1080/10426914.2016.1257805

Sadowski, M., Ladani, L., Brindley, W., & Romano, J. (2016). Optimizing quality of additively manufactured Inconel 718 using powder bed laser melting process. *Additive Manufacturing*, *11*, 60–70. https://doi.org/10.1016/j.addma.2016.03.006

Xu, Z., Murray, J. W., Hyde, C. J., & Clare, A. T. (2018). Effect of post processing on the creep performance of laser powder bed fused Inconel 718. *Additive Manufacturing*, *24*, 486–497.

PRINTABLE DENSITY LIMITS OF ADDITIVELY-MANUFACTURED STRUCTURED FOAMS

Niyazi Tanlak[1]
[1]*Turkish Aerospace (TA) Teknopark Istanbul Branch, Istanbul 34906, Turkey, e-mail:Niyazi.Tanlak@tai.com.tr*

Abstract. Additive manufacturing methods like powder bed fusion are used to print lattice structures. Yet, there are limits for printing these structures. The relative density of the unit-cell is a good indicator of whether it is appropriate for printing. The printable range has two constraints: The minimum printable density and the maximum printable density. The minimum printable radius of the additive manufacturing machine is the main factor for the former while trapped powder within an inclusion is the primary factor for the higher printable density limit. These limits are found by using numerical methods for different lattice types and sizes, machine precision, and powder lump size.

Keywords: Structured foams, Additive manufacturing, Printable relative density, Lattice, Powder bed fusion,

1. INTRODUCTION

By the time a foam-like structure is formed out of a solid, the single-valued properties of that solid are extended. Those properties are the strength, stiffness, electrical/thermal conductivity and diffusivity, and so forth (Ashby, 2005). Because of this property extension, foams are used in many engineering practices. The property extension can be made more controllable by the introduction of structured foams, a unit-cell (or a network of struts) repeats itself throughout a domain. Yet, structured foams are known to be hard to be manufactured by using conventional tools. At this point, additive manufacturing (AM) offers what is not possible in the manufacturing of them, previously.

Contrary to the common belief of a cellular structure is always printable, structured foams face printing problems. The printable density limits of unit-cell (*a.k.a.* lattice) types are not known fully. With powder bed fusion methods, printability of a structured foam is in control of unit-cell shape [(Sing, Yeong, Wiria, & Tay, 2015), (Loh, et al., 2015), (Rehme & Emmelmann, 2006)], relative density of a lattice (*i.e.* volume fraction) [(Sing, Yeong, Wiria, & Tay, 2015), (Loh, et al., 2015), (Rehme & Emmelmann, 2006), (Van Bael, et al., 2011), (Hao, Raymont, Yan, Hussein, & Young, 2011)], strut inclination [(Abele, Stoffregen, Klimkeit, Hoche, & Matthias Oechsner, 2015) (Wang, et al., 2017), (Leary, et al., 2016), (Mazur, et al., 2016), (Weißmann, et al., 2017)], powder particle size [(Zhang, Wei, & Cheng, 2014), (Yan, Hao, Hussein, Young, & Raymont, 2014)], powder material[(Sing, Yeong, Wiria, & Tay, 2015), (Loh, et al., 2015), (Van Bael, et al., 2011), (Hazlehurst, Wang, & Stanford, 2013), (Leary, et al., 2016) (Mazur, et al., 2016)], machine precision (Van Bael, et al., 2011), laser power [(Sing, Yeong, Wiria, & Tay, 2015), (Loh, et al., 2015), (Qiu, Yue, & Adkins, 2015), (Tsopanos, et al., 2010), (Yan, Hao, Hussein, Young, & Raymont, 2014), (Van Bael, et al., 2011) (Pattanayak, et al., 2011) (Tsopanos, et al., 2010)], laser spot size[(Zhang, Wei, & Cheng, 2014), (Van Bael, et al., 2011) (Yan, Hao, Hussein, Young, & Raymont, 2014)], laser scanning speed [(Sing, Yeong, Wiria, & Tay, 2015), (Loh, et al., 2015), (Qiu, Yue, & Adkins, 2015), (Tsopanos, et al., 2010)], layer thickness [(Van Bael, et al., 2011)], and hatch spacing [(Zhang, Wei, & Cheng, 2014)].

Machine precision is the main factor for the lower relative density limit together with unit-cell size. On the other hand, powder lump size as well as unit-cell size are the main factors defining the higher relative density limit. An important point worth mentioning here is that entrapment of powder within an inclusion allows, formally speaking, the manufacture. But the mass of such structured-foam will be higher than that of the intended one, which is considered to be improper. To fully unleash the potential of property extension effect, the printable range of volume fraction ought to be known in advance. For this reason, this paper investigates the bounds of manufacturing structured-foams with powder bed fusion techniques. Yet, it can cover other AM methods.

2. MATERIALS AND METHODS

This study's main objective is to unearth the printable range of volume fraction for given unit-cell type (See **Figure 1**), and size, powder lump size, and machine precision. At first instance, the problem is targeted by assuming the bed full of infinitesimally thin powder and infinite production. This assumption will provide the ideal case and it will be the pivot point to attack the problem of finite size powder and finite precision production.

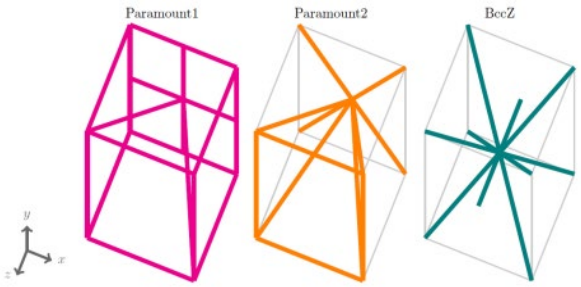

Figure 1. Unit-Cell Types

To evacuate the unused powder out, the void volume (the unused space in the unit-cell) has to be monolithic. Only this way, the unused powder can find an escape route. Hence, the problem of finding the upper printable density limit for the infinitesimal powder reduces to find the highest density of the unit-cell having monolithic void volume. To find that, the methodology proposed by Tanlak *et al.* (Tanlak, De Lange, & Van Paepegem, 2017) is employed. After finding the limit for the infinitesimal case, the problem of the finite size powder can be solved by reducing the critical relative radius as much as the powder lump radius. Then, based on the relative radius, the corresponding relative density can be found.

A commercial CAE software, Abaqus/CAE, is employed with Python language to objectify the proposed methods in this work. Each unit-cell is considered to be confined within cubic space as depicted in **Figure 1** (For Paramount unit cells (Chang, 2010)). Moreover, all the struts within a unit-cell have to have the same circular cross-section according to the assigned relative density.

3. RESULTS AND DISCUSSION

3.1 Infinitesimal Powder and Infinite Precision Production

As mentioned in the previous section, production with infinite precision is assumed. The lower printable limit is, therefore, zero. The resultant higher printable density limit, ρ_{high}, and its reciprocal values of relative strut radius, r_h', are provided in **Table 1**. Since the powder is so small and the machine used in AM has infinite precision, ρ_{high} is not controlled by the unit-cell size, L. Among the lattices at hand, BccZ lattice is the one reaching the highest printable density, which almost covers the whole density range. The struts of BccZ stem from the center and the cavities remain connected almost up to their disappearance when strut radius grows steadily. On the other hand, Paramount-1 is the one reaching the thickest strut cross-section.

Table 1 Highest relative density and the corresponding relative radius for the unit-cells.

Lattice Type	r'/L	ρ_h
Paramount-1	0.4000	0.9783
Paramount-2	0.3241	0.9467
BccZ	0.3553	0.9906

The corresponding solid -depicted with red- and void volumes -depicted with blue- are shown graphically in Table 3.

Table 2 Solid and void volume assemblies for critical radius.

Paramount1	Paramount2	BccZ
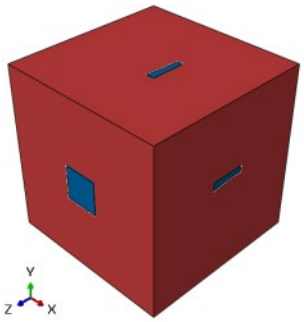	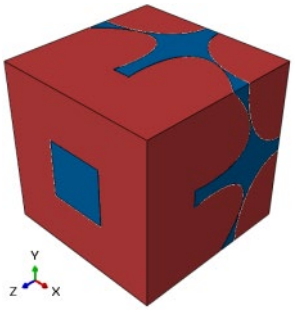	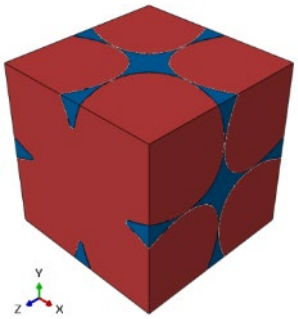

3.2 Finite Size Powder and Finite Precision Production

Unlike the previous case, here we are subject to machine precision and the powder size; ergo, there will be a lower as well as a higher printable limit. Since the combination of machine precision, powder size, unit-cell size is endless, it is necessary to build a non-dimensionalized plot enabling to find the corresponding printability limits for given r_{min}, r_{lump} , L. In **Figure 2**, such a plot is provided, whose $\frac{r_{min}}{L}$ and $\frac{r_{lump}}{L}$ are put on abscissa together. But, they are mutually independent of each other. The relative density values in **Figure 2**, are cut-off at the corresponding ρ_{high} of each unit-cell.

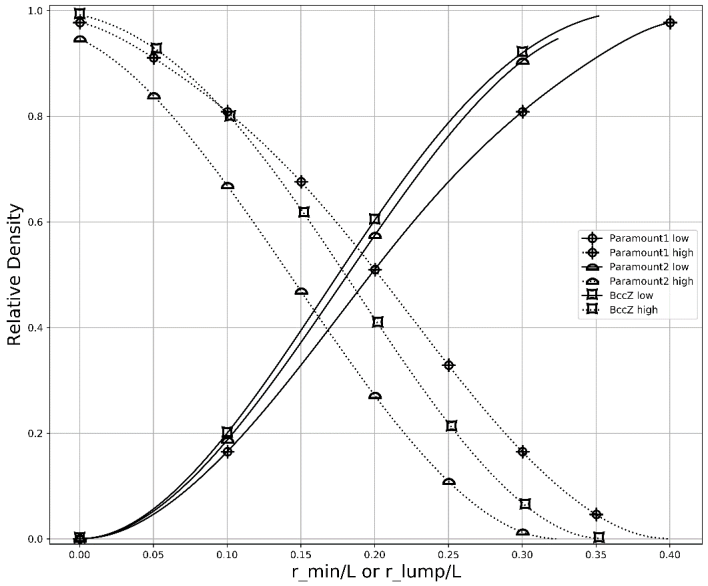

Figure 2. Printable Density Range of Selected Unit-Cells in Dimensionless Form.

A careful look at **Figure 2** will reveal that as the cell size increases while all other factors remain the same, the printable range gets closer to the infinitesimal case. When cell size decreases, the upper and lower limit curves of each unit-cell draw near to each other, in other words, the range of printable density gets narrower, till the two curves intersects, which, in turn, means that solely one density value is printable. From that point on, any unit-cell value is not printable. In order to produce structured-foams with precision, it is paramount to use optimal processing parameters. Hence, finding optimized parameters for each unit-cell will make the range of printable density closer to those discovered in this research.

4. CONCLUSIONS

To sum up, the printable volume fraction range is mainly controlled by unit-cell size, size of powder lump, and machine precision. The printable range grows and approaches to infinitesimal powder case when unit-cell size increases and all else the same. Contrarily, the printable range narrows when the machine precision worsens and the powder lump size increases, *c. p.* A nondimensionalized plot is created to find the printable density range for a unit-cell, cell size, lump size, and the minimum printable radius easily.

REFERENCES

Abele, E., Stoffregen, H. A., Klimkeit, K., Hoche, H., & Matthias Oechsner. (2015). Optimisation of process parameters for lattice structures. *Rapid Prototyping Journal, 21*, 117-127.

Ashby, M. (2005). The properties of foams and lattices. *Philosophical Transactions of the Royal Society A-Mathematical Physical and Engineering Sciences*, 15=30.

Chang, P. (2010). *An Improved Size, Matching, and Scaling Synthesis Method for the Design of Meso-Scale Truss Structures.* Atlanta: Georgia Institute of Techology.

Hao, L., Raymont, D., Yan, C., Hussein, A., & Young, P. (2011). Design and Additive Manufacturing of Cellular Lattice Structures. *Innovative Developments in Virtual and Physical Prototyping*, 249–254.

Hazlehurst, K., Wang, C. J., & Stanford, M. (2013). Evaluation of the stiffness characteristics of square pore CoCrMo cellular structures manufactured using laser melting technology for potential orthopaedic applications. *Materials Design, 51*, 949-955.

Leary, M., MaciejMazur, Elambasseril, J., McMillan, M., Chirent, T., Suna, Y., . . . Brandt, M. (2016). Selective laser melting (SLM) of AlSi12Mg lattice structures. *Materials and Design, 98*, 344-357.

Loh, L.-E., Chua, C.-K., Yeong, W.-Y., J. Song, M. M., Sing, S.-L., Liu, Z.-H., & Zhang, D.-Q. (2015). Numerical investigation and an effective modelling on the selective laser melting (SLM) process with aluminium alloy 6061. *International Journal of Heat and Mass Transfer*, 80: 288–300.

Mazur, M., Leary, M., Sun, S., Vcelka, M., Shidid, D., & Brandt, M. (2016). Deformation and failure behaviour of Ti-6Al-4V lattice structures manufactured by selective laser melting (SLM). *Int J Adv Manuf Technol, 84*, 1391–1411.

Pattanayak, D. K., Matsushita, T., Takadama, H., Fukuda, A., Takemoto, M., Fujibayashi, S., . . . Kokubo, T. (2011). Fabrication of Bioactive Porous Ti Metal with Structure Similar to Human Cancellous Bone by Selective Laser Melting. *Bioceramics Development and Applications, 1*, 1-3.

Qiu, C., Yue, S., & Adkins, N. J. (2015). Influence of processing conditions on strut structure and compressive properties of cellular lattice structures fabricated by selective laser melting. *Mat Sci Eng A, 628*, 188-97.

Rehme, O., & Emmelmann, C. (2006). Rapid manufacturing of lattice structures with Selective Laser Melting. *Proceedings of SPIE 6107: 61070K. 1–61070K. 12.*

Sing, S., Yeong, W., Wiria, F., & Tay, B. (2015). Characterization of titanium lattice structures fabricated by selective laser melting using an adapted compressive test method. *Exp Mechan*, 56: 735–748.

Tanlak, N., De Lange, D. F., & Van Paepegem, W. (2017). Numerical prediction of the printable density range of lattice structures. *Materials and Design*, 549–558.

Tsopanos, S., Mines, R. A., McKown, S., Shen, Y., Cantwell, W. J., Brooks, W., & Sutcliffe, C. J. (2010). The influence of processing parameters on the mechanical properties of selectively laser melted stainless steel microlattice structures. *J Manuf Sci Eng, 132*.

Van Bael, S., Kerckhofs, G., Moesen, M., Pyka, G., Schrooten, J., & Kruth, J. P. (2011). Micro-CT-based improvement of geometrical and mechanical controllability of selective laser melted Ti6Al4V porous structures. *Materials Science and Engineering: A, 528*, 7423-7431. doi:http://dx.doi.org/10.1016/j.msea.2011.06.045

Wang, D., Wu, S., Fu, F., Mai, S., Yang, Y., Liu, Y., & Song, C. (2017). Mechanisms and characteristics of spatter generation in {SLM} processing and its effect on the properties . *Materials & Design , 117*, 121-130. doi:https://doi.org/10.1016/j.matdes.2016.12.060

Weißmann, V., Drescher, P., Bader, R., Seitz, H., Hansmann, H., & Laufer, N. (2017). Comparison of Single Ti6Al4V Struts Made Using Selective Laser Melting and Electron Beam Melting Subject to Part Orientation. *Metals, 7*, 91-113.

Yan, C., Hao, L., Hussein, A., Young, P., & Raymont, D. (2014). Advanced lightweight 316L stainless steel cellular lattice structures fabricated via selective laser melting. *Materials & Design, 55*, 533-541. doi:10.1016/j.matdes.2013.10.027

Zhang, S., Wei, Q., & Cheng, L. (2014). Effects of scan line spacing on pore characteristics and mechanical properties of porous Ti6Al4V implants fabricated by selective laser melting. *Materials Design*, 185-193.

GENERATIVE TOPOLOGY OPTIMIZATION FOR METAL ADDITIVE MANUFACTURING

M. Furkan Polat [1,2, a] and Bahattin Koç [1,2,b]

[1]*Integrated Manufacturing Technologies Research and Application Center, Sabanci University, Istanbul Technology Development Zone, Sanayi Mah. Teknopark Blvd. No: 1/1B, Pendik, 34906 Istanbul* [2]*Faculty of Engineering and Natural Sciences, Sabanci University, 34956 Tuzla, Istanbul Turkey*

Emails:[a]*mfurkan@sabanciuniv.edu* and [b]*bahttinkoc@sabanciuniv.edu*

Abstract. The main goal of this study is to investigate the possible improvement for the topology optimization for structural parts by using generative design algorithms. The idea is to get an insight from topology optimization solutions and carry them into algorithm-based CAD environment. Since topology optimization algorithms are bounded with certain constraint and this optimization has iterative solution techniques, the global optimal 3D design cannot be reached with only topology optimization. Therefore, it is possible to reach more desired and better design solutions with algorithmic design methods because algorithmic design method enables us to search more complex geometry then topology solution. Moreover, new constrains can be added to the algorithmic design part rather than topology optimization in order to keep topology optimization time shorter. In other words, adding new constraints into the topology optimization process is quite costly but not for generative algorithm-based CAD design. One of the goals of this study is to make additional constraints less costly in terms of computational manner.

Keywords: Generative Design, Topology Optimization, Computational Design, Design Optimization

1. INTRODUCTION

Topology optimization is a design optimization method such that it can search the best material distribution among the design space with given boundary conditions. Objective of this optimization can be both compliance minimization and mass minimization. In 2001, Ole Sigmund [3] published an article about 2D topology optimization algorithm based on input parameters, design space, constraints, objective function, sensitivity analysis and filtering operations. In 2014 Liu and Tovar [1] modified the previous study in 3D form. The output of that algorithm gives a STereoLithography (STL) mesh file as an output. Many studies in the literature have improved the initial algorithm in order to add new manufacturing constraints. However, since all those optimization processes include an iterative Finite Element Method (FEM) calculations, each extra constrain brings too much computational cost. In addition, the solution methodology cannot guarantee global optimal solution, so although topology optimization is very powerful optimization method in practical use it has a few drawbacks. When someone wants to add a new manufacturing constrain or try to search new possible design solution, he/she has to put much more computational effort on it.

Generative design is not an iterative optimization method like topology but it is a kind of search algorithm that looks for alternative solution geometry within the given constraint and chose the best solution [2]. It has the same objective with topology optimization, but it can find better solution because it can search different local optimum points. Generative design is one of the investigation methods applied by typically altering design geometry parametrically [2]. In recent years topology optimization has been used to design generator instead of parameterization tool [4].

2. MATERIALS AND METHODS

In this study, 60x20x22 mm design space was used and the boundary conditions are taken as the same with Liu and Tovar's [1] study. This boundary condition is very common in literature, so in order to compare our result with literature this input parameters were chosen. Also, this study includes commercial software comparison with our results. ANSYS Topology Optimization was used to obtain static structural response of optimized geometry. First, 3D topology optimization algorithm [1] was run

with MATLAB in order to obtain artificial density distribution over the design domain. After getting those artificial density, Rhinoceros was used to create iso curves on the artificial density domain. Those curves lie on the planes perpendicular to the main skeleton of the design domain. Main skeleton is a Bezier curve starting from fix boundary ends on the line the external force applied on it. The control points were chosen as an area weighted centroid of the iso curves. Those curves stand for the topology optimization solution. In other words, those curves are very close to topology optimization solution surface geometry. Secondly, certain 2D primitive geometries were chosen as auxiliary geometries. In this study, circles and ellipses were used to section curves. The exact position of those auxiliary curves perpendicular to the main skeleton curve of the design domain. After this point, our algorithm creates the possible geometries by using auxiliary curves and main skeleton curves. In this step, building direction, force and boundary regions, material properties and optimization parameters have some effects on the output.

3. RESULTS AND DISCUSSION

Generative design using topology optimization solution can enable us to discover better geometrical solutions in shorter time and adding new constrain into the generative design process is less costly compared to topology optimization algorithm. In addition, since our algorithm runs based on NURBS surface generation, final geometry does not need and post process operation for manufacturing preparation. On the other hand, topology optimization solutions have to be modified accordingly because most of the time the optimal geometry in topology optimization does not convenient for manufacturing even for additive manufacturing. It can be seen in figure 1 better compliance or the lower mass with the same compliance can be obtained with generative design approach. However, life cycle and dynamic strength of the material should be studied as well in the further studies.

Figure 1. Generative Topology Optimization of typical 3D beam geometry

4. CONCLUSIONS

Generative design solutions can increase the effectiveness of the topology optimization in different aspects. Therefore, algorithm-based geometry creation based on topology optimization methods will provide wide range of optimization for everyone. Our algorithm can be enhanced with deep learning algorithms in order to get better solution each time.

REFERENCES

[1] Liu, K., & Tovar, A. (2014). An efficient 3D topology optimization code written in Matlab. Structural And Multidisciplinary Optimization, 50(6), 1175-1196. doi: 10.1007/s00158-014-1107-x

[2] Shea, K., Aish, R., & Gourtovaia, M. (2005). Towards integrated performance-driven generative design tools. Automation In Construction, 14(2), 253-264. doi: 10.1016/j.autcon.2004.07.002

[3] Sigmund, O. (2001). A 99 line topology optimization code written in Matlab. Structural And Multidisciplinary Optimization, 21(2), 120-127. doi: 10.1007/s001580050176

Matejka, J., Glueck, M., Bradner, E., Hashemi, A., Grossman, T., & Fitzmaurice, G. (2018). Dream Lens: Exploration and Visualization of Large-Scale Generative Design Datasets. In Proceedings of the 2018 CHI Conference on Human Factors in Computing Systems (p. 369). ACM.

THE EFFECT OF POST PROCESSING ON SURFACE PROPERTIES OF AS-PRINTED AND HEAT TREATED Ti-6Al-4V ALLOY PRODUCED BY ELECTRON BEAM MELTING

Tolga Berkay Sirin[1*], Yusuf Kaynak[2], Evren Tan[3], Berkay Gümüş[4]
[1] *Department of Mechanical Engineering, Marmara University, 34722 Goztepe Campus-Istanbul, Turkey,* tolga.sirin94@gmail.com
[2] *Department of Mechanical Engineering, Marmara University, 34722 Goztepe Campus-Istanbul, Turkey,* yusuf.kaynak@marmara.edu.tr
[3] *ASELSAN A.Ş., Yenimahalle, Ankara, Turkey,* evrentan@aselsan.com.tr
[4] *ASELSAN A.Ş., Yenimahalle, Ankara, Turkey* berkaygumus@aselsan.com.tr

Abstract. This study presents the effects of post-processing on the surface aspects of as-printed and heat treated Ti-6Al-4V alloy fabricated by electron beam melting additive manufacturing. As a post-processing operation, finish milling operation with various feed rate and cutting speed is chosen. As-printed specimens were heat treated considering β-transus temperature. Therefore, 950 and 1050 °C were used and consequently two different microstructures were produced. All these three specimens were post-processed to examine final surface and subsurface characteristics. Surface roughness calculations including Ra and Rz, topography image examinations, microhardness measurements, phase transformation with XRD analyses, and reciprocating wear tests were carried out and presented in this work. This extensive and systematic works illustrate that heat treatment alters microstructural characteristics of as-printed sample remarkably. Besides, the surface and subsurface characteristics obtained from heat-treated and as-printed specimen shows profound difference. Work hardening and resulting wear resistance induced from both heat treatment and post processing operation.

Keywords: post-processing operation, Ti-6Al-4V, Electron Beam Melting, Heat Treatment, Wear Resistance

1. INTRODUCTION

Ti–6Al–4V is the most prevalent α + β dual-phase titanium alloy in engineering industry. Due to ist light weight, high strength-to-weight ratio, low elastic modulus, good biocompatibility and outstanding corrosion resistance (Li, Li, Bai, Liu, & Kuai, 2018; Murr et al., 2009), Ti–6Al–4V, has been used in aerospace, sporting goods, orthopedic biomedical implants and devices, marine and offshore, etc (Carroll, Palmer, & Beese, 2015). Recent studies reported that components made of Ti-6Al-4V alloys can be successfully fabricated by additive manufacturing (AM). Although there are many AM methods, Electron Beam Melting (EBM) is one of the frequently preferred one to fabricate components made of Ti–6Al–4V. It is also preferred since the EBM's vacuum environment eliminates the titanium's high affinity for oxygen and provides a more uniform and consistent production (Tan et al., 2015). Along with the advantages which additive manufacturing brings, there are also many problems such as high surface roughness, dimensional deviation and residual stress. These problems may be overcome by optimizing process parameters. In addition to the optimization on process parameters, post-processing operations can be conducted. Application of some post-processes such as machining (Kaynak, Kitay, & Processing, 2018), shot peening, sand blasting, drag finishing (Kaynak & Kitay, 2019), vibratory surface finishing, and chemical polishing (Łyczkowska, Szymczyk, Dybała, Chlebus, & Engineering, 2014; Pyka et al., 2012) can improve mechanical properties and eliminate other problems. In this study, as-printed and heat treated Ti-6Al-4V specimens fabricated by EBM was post-processed to improve surface properties.

2. MATERIALS AND METHODS

Specimens produced by electron beam melting using ARCAM EBM A2X machine under vacuum environment and Ti–6Al–4V powder was utilized for the manufacturing process. Square prism specimens 10 mm in edge and 30 mm in height were printed for testing. Heat treatment was applied as

secondary treatment. As-built specimens were heat treated at 1050 ºC, 1h / water quenched (WQ-1) and 950 ºC, 1h / water quenched (WQ-2), respectively. In the finish milling test, various cutting speeds and feed rate were used. Sliding wear tests were carried out as per the ASTM G133 wear test standard. A tungsten carbide ball (ISO K20 (G10) (WC 94%, CO 6%)) with a diameter of 6 mm was used for the reciprocating wear test.

3. RESULTS AND DISCUSSION

The microstructures of as-built and heat treated material are given in Figure 1. Primarily acicular α-plate and Widmanstätten-like structures were observed in the microstructure, while coarse, plate-like (acicular) α with some intergranular β characteristic was also observed locally of as-built Ti-6Al-4V specimen. In the WQ-2 heat treatment condition, a remarkable change on the microstructure of specimen was observed because of the fact that high heat treatment temperature. Similar microstructures were observed in the heat-treated specimen as in the as-built specimen, but it is clearly seen that grain boundaries are formed.

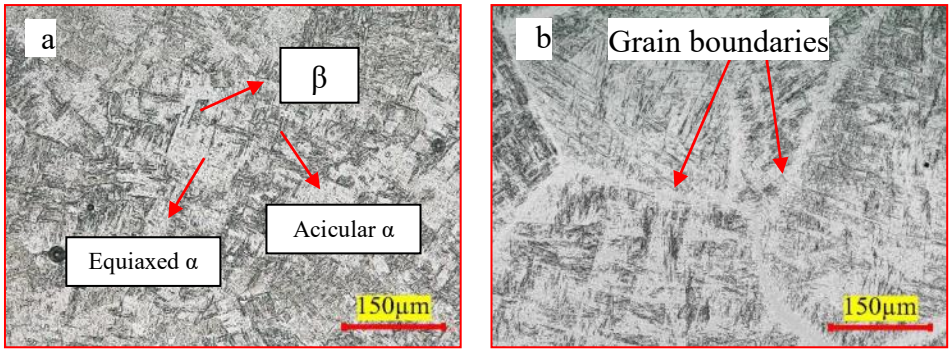

Figure 1. As-printed (a) and Heat Treated (1050 ºC, 1h / WQ) (b) Ti-6Al-4V specimen

The microhardness of the as-printed and heat-treated specimens was measured and found as approximately 333 (±11) and 420 (±15) HV, respectively. In the heat treated condition, the microhardness was increased by 26% as compared to the as-built specimen.

4. CONCLUSIONS

It is evident that as-printed specimens fabricated by EBM cannot be used without post processing operation since they have very rough surfaces (much higher than R_a= 20 µm). Furthermore, to obtain homogeneous microstructure heat treatment is also required. However, this work addresses the critical question whether post processing need to be implemented before or after heat treatment. Furthermore the advantages of implementing post processing before or after heat treatment in terms of wear resistance, surface mechanical and microstructural properties were demonstrated.

REFERENCES

Carroll, Beth E, Palmer, Todd A, & Beese, Allison M %J Acta Materialia. (2015). Anisotropic tensile behavior of Ti–6Al–4V components fabricated with directed energy deposition additive manufacturing. *87*, 309-320.

Kaynak, Yusuf, & Kitay, Ozhan %J Additive Manufacturing. (2019). The effect of post-processing operations on surface characteristics of 316L stainless steel produced by selective laser melting. *26*, 84-93.

Kaynak, Yusuf, Kitay, Ozhan %J Journal of Manufacturing, & Processing, Materials. (2018). Porosity, surface quality, microhardness and microstructure of selective laser melted 316L stainless steel resulting from finish machining. *2*(2), 36.

Li, Bao-Qiang, Li, Zhonghua, Bai, Peikang, Liu, Bin, & Kuai, Zezhou %J Metals. (2018). Research on Surface Roughness of AlSi10Mg Parts Fabricated by Laser Powder Bed Fusion. *8*(7), 524.

Łyczkowska, E, Szymczyk, P, Dybała, B, Chlebus, E %J Archives of Civil, & Engineering, Mechanical. (2014). Chemical polishing of scaffolds made of Ti–6Al–7Nb alloy by additive manufacturing. *14*(4), 586-594.

Murr, LE, Quinones, SA, Gaytan, SM, Lopez, MI, Rodela, A, Martinez, EY, . . . Wicker, RB %J Journal of the mechanical behavior of biomedical materials. (2009). Microstructure and mechanical behavior of Ti–6Al–4V produced by rapid-layer manufacturing, for biomedical applications. *2*(1), 20-32.

Pyka, Grzegorz, Burakowski, Andrzej, Kerckhofs, Greet, Moesen, Maarten, Van Bael, Simon, Schrooten, Jan, & Wevers, Martine %J Advanced Engineering Materials. (2012). Surface modification of Ti6Al4V open porous structures produced by additive manufacturing. *14*(6), 363-370.

Tan, Xipeng, Kok, Yihong, Tan, Yu Jun, Descoins, Marion, Mangelinck, Dominique, Tor, Shu Beng, . . . Chua, Chee Kai %J Acta Materialia. (2015). Graded microstructure and mechanical properties of additive manufactured Ti–6Al–4V via electron beam melting. *97*, 1-16.

HEAT TREATMENT TEMPERATURE-INDUCED MICROSTRUCTURE, MICROHARDNESS AND WEAR RESISTANCE OF INCONEL 718 PRODUCED BY SELECTIVE LASER MELTING

Yusuf Karabulut[1*], İlyas İnce[2], Emre Tascioglu[3], Yusuf Kaynak[4]

[1] *Department of Mechatronics System Engineering, Türkisch-Deutsche Universität, 34820 Beykoz , Istanbul, Turkey, yusuf.karabulut@tau.edu.tr*
[2] *Department of Mechanical Engineering, Istanbul-Cerrahpasa University, 34320 Avcılar Campus-Istanbul, Turkey, ilyas.ince@thy.com*
[3] *Department of Mechanical Engineering, Marmara University, 34722 Goztepe Campus-Istanbul, Turkey, emre_tascioglu@hotmail.com*
[4] *Department of Mechanical Engineering, Marmara University, 34722 Goztepe Campus-Istanbul, Turkey, yusuf.kaynak@marmara.edu.tr*

Abstract. Additive manufacturing (AM) has been becoming more widespread and its usage area has been increasing in different industries. However, the mechanical and microstructural properties of the metal parts printed by additive manufacturing required further investigation. In this study, various heat treatment temperatures were applied to Inconel 718 produced by selective laser melting (SLM) to examine the effects of heat treatment temperature on microstructure, microhardness and wear behavior of the printed specimens. Moreover, the microhardness and wear response of printed specimens were compared with the wrought Inconel 718. The results provide strong evidence that heat treatment temperature is capable of altering microstructural aspects of printed parts substantially and thus microhardness and wear resistance is induced. Comparative study also provides evidence that printed Inconel 718 can have much higher wear resistance performance than conventionally produced Inconel 718 if printed Inconel 718 can be treated by an appropriate heat treatment temperature.

Keywords: Selective laser melting; heat treatment; wear behavior; microstructure

1. INTRODUCTION

The additive manufacturing method is a new generation production method that allows engineers to design complex parts that are difficult to produce by conventional methods (Kranz, Herzog, Emmelmann, Kranz, & Herzog, 2015). It is more cost-effective since there is no chip as in conventional manufacturing methods (Zhang, Dembinski, & Coddet, 2013). In addition, additive manufacturing has the ability to produce prototypes of designed parts quickly (Kruth, Leu, & Nakagawa, 1998). Additive manufacturing method, has become widespread especially in aerospace, automotive and medical fields due to its advantages compared to traditional methods (Gibson & Rosen, n.d.). Selective laser melting (SLM) is one of the most preferred among the various additive manufacturing methods (Craeghs, Thijs, Verhaeghe, Kruth, & Humbeeck, 2010). Although, it has some advantages over traditional methods, this new production method has to overcome some problems including high surface roughness, poor ductility, dimensional deviation, and formation of residual stresses in the processed parts (Bhaduri et al., 2017). These problems were tried to be addressed by arranging the process parameters such as laser power, scan speed, layer thickness, scan spacing, scanning pattern etc. Some post-processing operations have been applied to improve the mechanical properties and surface quality of the components produced by additive manufacturing, such as electrochemical polishing (Su, Jeong, & Park, 2019), shot-peening (AlMangour & Yang, 2016), turning (Yu, Li, Wang, & Zeng, 2018), heat treatment (Shindo et al., 2012) etc. Inconel 718 is a Ni-based super alloy with excellent resistance to oxidation and abrasion, which can maintain mechanical properties up to high temperatures and has a good fatigue life (Qi, Azer, & Ritter, n.d.). Hence, it is widely used in aerospace, in energy and in automotive industries for various applications. Therefore, Inconel 718 is a candidate for industrial applications of SLM produced parts (Zhao, Chen, Lin, & Huang, 2008).
In this study, heat treatment was applied to Inconel 718 specimens produced by SLM method at different temperatures.

2. MATERIALS AND METHODS

The specimens were composed of Renishaw standard gas atomized Inconel 718 powder and produced by the selective laser melting using Renishaw AM250 under Ar atmosphere. A round bars 15 mm in diameter and 25 mm in length was printed for testing. The detail of the building parameters for the specimens is presented in Table 1. Wrought Inconel 718 was received as round bar of 15 mm diameter as extruded condition. As post-process operation heat treatments were conducted using a vertical furnace under atmosphere. As-built specimens were heat-treated as follows: 600 ºC, 2h/air cooling (HT-1) and 1100 ºC, 2h/air cooling (HT-2). A reciprocating tribometer was used to conducted dry sliding wear tests as per ASTM G133 wear test standard. The dry sliding wear tests performed for 40 minutes under 5 N contact load and with 6 mm stroke length. A tungsten carbide ball (WC 94%, CO 6%) with a diameter of 6mm was utilized for the reciprocating wear test.

Table 1. SLM building parameters

Particle size of powder	14-45 µm	Point Distance	70 µm
Layer Thickness	60 µm	Exposure Time	80 µs
Power	200 W	Hatch Distance	90 µm

3. RESULTS AND DISCUSSION

Cellular dendritic structures and columnar grain structures are obviously observed in the microstructure of as-built Inconel 718 specimen. Figure 1 presents the microstructures of as-built material and wrought material. No substantial change in the microstructure of the specimen under the HT-1 condition was observed. Melting pools and melting pool boundaries with cellular dendritic structures are still clear. In the HT-2 condition, the microstructure of specimen has changed significantly because of the high heat treatment temperature. Cellular dendritic structures and columnar grain structures are not seen in microstructure. Different heat treatment temperatures have different impact on the microstructure of the Inconel 718 material fabricated by SLM. The microstructure of specimens is affected more as the heat treatment temperature increases.

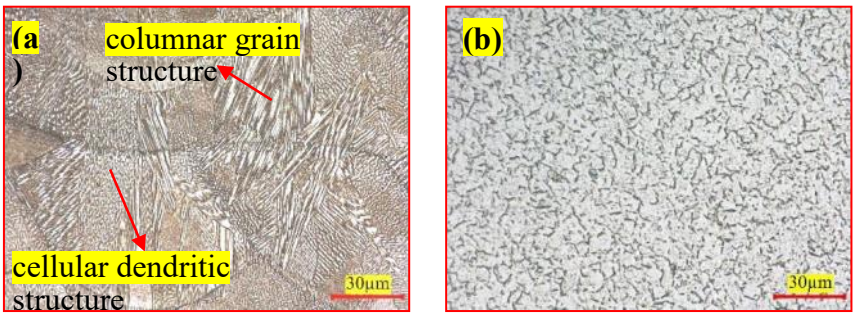

Figure 1. As-built (a) and wrought Inconel 718 specimen

The microhardness of the wrought specimen was measured approximately 323 HV. The microhardness of the SLM as-built specimen is almost equal to the microhardness of the wrought specimen. In the HT-1 condition, the microhardness value was 342 HV with an increase of 8% compared to the as-built specimen. The microhardness value was measured as 268 HV in the HT-2 condition and this value was approximately 15% less than the as-built specimen.

As-built material, heat-treated and wrought specimen have been found to exhibit different behaviors from the wear behavior perspective. The wear resistance of the as-built specimen is lower than the wrought one. The wear depth of the as-built specimen was measured to be approximately 27 µm, while the wrought specimen was measured to be 23 µm. Post processing operations are considered necessary to improve the wear resistance of specimens produced by the SLM method.

The wear rate of wrought specimen was calculated as 4.4 mm^3/Nm, while the wear rate of as-built specimen was calculated as 4.6 mm^3/Nmm. As a result of HT-1 and HT-2 heat treatments, the wear rates were calculated as approximately 4.1 and 4.7 mm^3/Nm, respectively. Wear rates showed very consistent results with the microhardness changes examined in the previous section.

4. CONCLUSIONS

In this study, the influence of various heat treatment temperatures on microstructure, microhardness and wear behavior of Inconel 718 produced by SLM was investigated and compared with the results of as-built and wrought specimens. The heat treatment should be applied at high temperatures (> 900 °C) to alter the microstructure of the SLM Inconel 718. The heat treatment applied at low temperatures increased the microhardness while the heat treatment applied at high temperatures reduced microhardness of SLM Inconel 718. This study showed that different heat treatments have different effects on wear behavior of SLM Inconel 718.

REFERENCES

AlMangour, B., & Yang, J.-M. (2016). Improving the surface quality and mechanical properties by shot-peening of 17-4 stainless steel fabricated by additive manufacturing. *Materials & Design*, *110*, 914–924.

Bhaduri, D., Penchev, P., Batal, A., Dimov, S., Leung, S., Sten, S., … Dong, H. (2017). Applied Surface Science Laser polishing of 3D printed mesoscale components. *Applied Surface Science*, *405*, 29–46. https://doi.org/10.1016/j.apsusc.2017.01.211

Craeghs, T., Thijs, L., Verhaeghe, F., Kruth, J.-P., & Humbeeck, J. Van. (2010). A study of the microstructural evolution during selective laser melting of Ti–6Al–4V. *Acta Materialia*, *58*(9), 3303–3312. https://doi.org/10.1016/j.actamat.2010.02.004

Gibson, I., & Rosen, D. (n.d.). *Additive Manufacturing Technologies*.

Kranz, J., Herzog, D., Emmelmann, C., Kranz, J., & Herzog, D. (2015). Design guidelines for laser additive manufacturing of lightweight structures in TiAl6V4 Design guidelines for laser additive manufacturing of lightweight structures in TiAl6V4, *14001*. https://doi.org/10.2351/1.4885235

Kruth, J. P., Leu, M. C., & Nakagawa, T. (1998). Progress in additive manufacturing and rapid prototyping. *CIRP Annals - Manufacturing Technology*, *47*(2), 525–540. https://doi.org/10.1016/S0007-8506(07)63240-5

Qi, H., Azer, M., & Ritter, A. (n.d.). Studies of Standard Heat Treatment Effects on Microstructure and Mechanical Properties of Laser Net Shape Manufactured, *2*. https://doi.org/10.1007/s11661- 009-9949-3

Shindo, P. W., Martinez, E., Gaytan, S. M., Murr, L. E., Amato, K. N., Medina, F., … Collins, S. (2012). Microstructures and mechanical behavior of Inconel 718 fabricated by selective laser melting. *Acta Materialia*, *60*(5), 2229–2239. https://doi.org/10.1016/j.actamat.2011.12.032

Su, U., Jeong, K., & Park, W. (2019). High - Quality Surface Finishing of Industrial Three - Dimensional Metal Additive Manufacturing Using Electrochemical Polishing. *International Journal of Precision Engineering and Manufacturing-Green Technology*, (0123456789). https://doi.org/10.1007/s40684-019-00019-2

Yu, H., Li, F., Wang, Z., & Zeng, X. (2018). Fatigue performances of selective laser melted Ti-6Al-4V alloy: Influence of surface finishing, hot isostatic pressing and heat treatments. *International Journal of Fatigue*. https://doi.org/10.1016/j.ijfatigue.2018.11.019

Zhang, B., Dembinski, L., & Coddet, C. (2013). Materials Science & Engineering A The study of the laser parameters and environment variables effect on mechanical properties of high compact parts elaborated by selective laser melting 316L powder. *Materials Science & Engineering A*, *584*, 21–31. https://doi.org/10.1016/j.msea.2013.06.055

Zhao, X., Chen, J., Lin, X., & Huang, W. (2008). Study on microstructure and mechanical properties of laser rapid forming Inconel 718, *478*, 119–124. https://doi.org/10.1016/j.msea.2007.05.079

ON THE EFFECT OF UNFIXED PROCESS VARIABLES ON MECHANICAL PROPERTIES IN SELECTIVE LASER MELTING

Evren Yasa[1], Kıvılcım Ersoy[2], Barış Koç[3]
[1]*Eskişehir Osmangazi University, Mechanical Engineering, eyasa@ogu.edu.tr*
[2]*FNSS Defence Systems, Ankara, Kivilcim.Ersoy@fnss.com.tr*
3FNSS Defence Systems, Ankara, Baris.Koc@fnss.com.tr

Abstract. Selective Laser Melting, a type of additive manufacturing (AM) processes, is a technology whereby functional metallic end-parts can be produced with high geometrical complexity and reduced lead times in comparison to conventional manufacturing. Defense industry, as well as other leading sectors such as aerospace, biomedical and automotive, is interested in AM processes since these technologies allow on-demand production with high levels of customization, complexity and flexibility. This leads to an improved supply chain reactivity and reduces the inventory. Moreover, AM processes are suitable to address the needs of small volume of tailored components and spare parts for the systems damaged in operations in the defence industry. Thus, this study investigates the use of Selective Laser Melting for structural applications in land-based defence vehicles by studying the effect of various build orientations and amount of heat input on tensile properties. Moreover, a case study of a structural bracket from FNSS part portfolio is presented.

Keywords: Selective Laser Melting, mechanical testing, land-based defence vehicles

1. INTRODUCTION

Space and defense organizations are exploring Additive Manufacturing processes especially to provide on-demand manufacturing for the functional end-use parts at the point of use. Allowing on-demand manufacturing also has great importance on the supply-chain management because all supply chains aim to deliver the right part, to the right place at the right time and in the right quantity [1]. For defence applications, where most of the maintenance and repair work needs to be handled far from a center, individually customization of low-quantity parts produced on-demand and at its actual point of use enhances the value of a given supply-chain. AM technologies benefit from these advantages and are considered as revolutionary processes. However, there are some challenges to be overcome such as part testing and qualification. There are many studies in the literature addressing the mechanical properties of additively manufactured parts in order to enable these technologies to be used not only for non-structural parts or prototypes but also for load-carrying structural parts.

Table 1. Microhardness values achieved in various studies of AISI 316L stainless steel after SLM

Reference	Condition	Microhardness [HV]
[2]	As built	325
[3]	As built	255-265
[4]	As built – various planes	237-262
[5]	As built	245±21
[6]	As built	210-220
[7]	As built	200-260
[8]	As built	250-280
[9]	As built	210-240
[10]	As built – various planes	240-300
[11]	As built	220-225
[12]	As built	215-255

Selective Laser Melting (SLM), one of the powder-bed fusion processes preferred widely, utilizes a high energy laser beam to selectively scan and fully melt metallic powder particles in a layerwise manner. The material range with the SLM process is quite wide ranging from titanium alloys, aluminum alloys, nickel superalloys, precious metals, and iron-based alloys. One of the most widely studied materials with the SLM process in literature is AISI 316L stainless steel. It has been tested by many researchers as-built and also in different heat treated conditions. As shown in Table 1, the values obtained by different researchers for the microhardness of AISI 316L are quite different ranging from 200 to 325 HV [2-14]. However, to enable these AM processes for critical applications, the designers shall know the effect of various unfixed

process variables on the part quality and mechanical properties once the directly controllable process parameters, e.g. scan speed, laser power, etc., are optimized and frozen. This study therefore is focused on the influence of variables such as the build orientation or the amount of heat input per layer on tensile properties. These process variables depends on many factors such as part geometry, nesting, maximum build envelope, residual stresses, support design, etc. and cannot be fixed beforehand for all parts with different geometries to be manufactured.

2. MATERIALS AND METHODS

The parts were manufactured on an EOS M280 machine at the facilities of Materialise from AISI 316L stainless steel powder using the process parameters optimized for maximum density for dynamic applications by Materialise. Tensile test sub-size specimens per ASTM E8 were produced at 6 build orientations as shown in Figure 1. The sub-size specimens were chosen due to the smaller size. Different build orientations are obtained in a systematic manner by changing the angles of rotation for the tensile specimen as Figure 2 depicts. Moreover, the thickness of the specimens was varied and a thick block was manufactured from which test specimens were wire-EDMed. This is carried out to test the effect of heat input per layer to the specimen on the tensile properties. All specimens were peripherally machined to final geometry and only stress-relief heat treatment was applied. The tested specimens' notations are listed in Table 2.

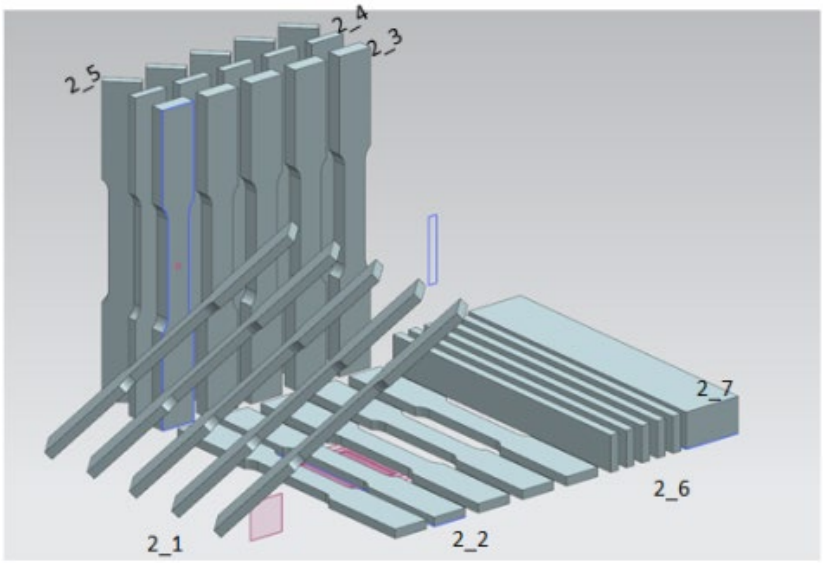

Figure 1. Build orientations of the tensile specimens

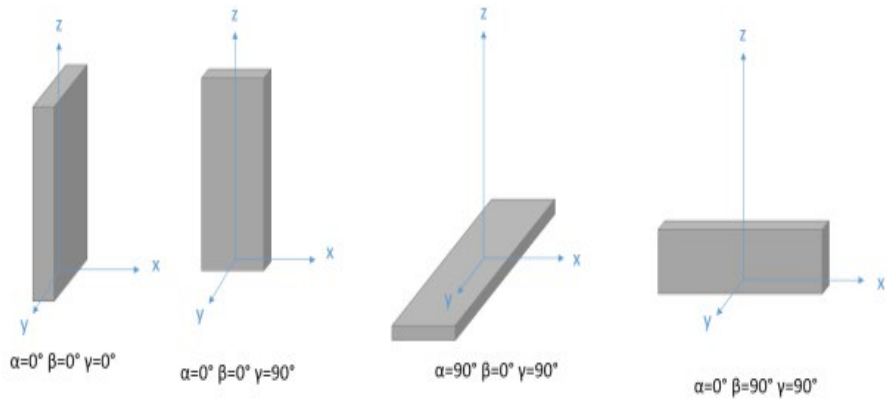

Figure 2. Angle of rotations with respect to three axes where z represents the build direction

Table 2. List of tested specimens

#	Thickness	Orientation	Factor
2_1	3 mm	45-45-0°	45 degrees with two axes
2_2	3 mm	0-90-0°	Horizontal lying coupons - long side aligned with the coater direction
2_3	5 mm	0-0-0°	Vertical standing coupons-short side aligned with the coater direction - specimen thickness
2_4	3 mm	0-0-0°	Vertical standing coupons-short side aligned with the coater direction
2_5	3 mm	0-0-45°	Vertical standing coupons 45 degrees with respect to coater direction
2_6	3 mm	0-90-90°	Vertical lying coupons
2_7	3 mm from thicker block	0-90-90°	Thickness of the produced specimen
1_1	5 mm	90-45-0°	Horizontal lying coupons 45 degrees with respect to coater direction
1_2	3 mm	90-45-0°	Horizontal lying coupons 45 degrees with respect to coater direction - specimen thickness

3. RESULTS AND DISCUSSION

Figure 3 shows the result of one configuration (2_1) for the inclined specimens for five repetitions. As the strain-stress curve shows, the results are quite reliable for the repetitions. This is valid for other configurations as well. Table 3 lists the results for different build orientations for the same sample thickness. Vertically standing specimens (2_4), of which the tension direction coincides with the build direction exhibit a slightly lower yield strength in comparison to the other two build directions. The alignment with respect to the coater direction does not seem to affect the results significantly in terms of yield strength when the results of 2_5 and 2_4 are compared taking the standard deviations into account. Moreover, inclining the specimens (2_1) does not seem to change the yield strength. The highest yield strengths are achieved by the horizontally lying coupons (2_2 and 1_2) regardless of the alignment with respect to the coater direction. When the ultimate tensile strengths are compared taking the build direction into account, it is seen that the standard deviations are much less in comparison to the yield strength values. This leads to the fact that the manufacturing defects in specimens are more influential on the yield strength. The highest tensile strengths are again achieved by the coupons where the build direction is not same with the tensile direction (2_2, 2_6 and 1_2). 45 degrees inclined specimens (2_1) exhibit slightly lower UTS whereas the lowest UTS values are exhibited by the vertically standing coupons. The difference in average UTS values is approximately 80 MPa which is 14% clearly showing the anisotropy. Regarding the area reduction, vertically standing specimens show a higher ductility. Young moduli are more or less the same except specimens numbered as 2_5.

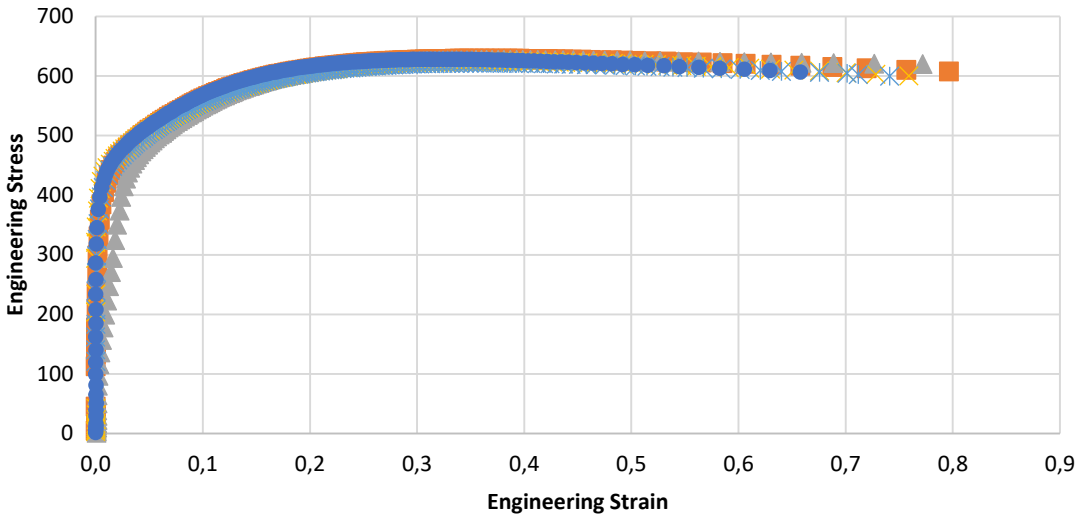

Figure 3. The strain-stress curve for the inclined specimens (2_1) for 5 repetitions

Table 3. Effect of build orientation on tensile properties with standard deviations

#	Thickness [mm]	Orientation	Factor	YS [MPa]	UTS [MPa]	A%	Young Modulus [GPa]
2_2	3 mm	0-90-0°	Horizontal lying coupons - long side aligned with the coater direction	416.01±22	647.84±5	21±1%	20.2±0.7
2_4	3 mm	0-0-0°	Vertical standing coupons-long side aligned with the coater direction	378.19±14	574.33±4	25±1%	19.3±1.1
2_6	3 mm	0-90-90°	Vertical lying coupons	403.36±5	648.97±6	22±1%	20.5±0.4
2_1	3 mm	45-45-0°	45 degrees with two axes	382.69±25	623.93±4	23±1%	19.9±0.6
2_5	3 mm	0-0-45°	Vertical standing coupons 45 degrees with respect to coater direction	361.42±16	569.13±2	25±0.4%	17.8±0.4
1_2	3 mm	90-45-0°	Horizontal lying coupons 45 degrees with respect to coater direction -specimen thickness	407.78+8	639.37+3	26±1%	20.6±0.7

The effect of specimen thickness is tested with batch numbers of 2_3 versus 2_4 and 1_1 versus 1_2 for different orientations. 2_3 and 2_4 are vertical standing coupons of which the short side of the cross-section is aligned with the coater direction. 1_1 and 1_2 are horizontally lying coupons of which the long side has 45 degrees of rotation with respect to the coater direction (see Figure 1). Specimens 2_3 and 1_1 has a thickness of 5 mm whereas specimens 2_4 and 1_2 have a thickness of 3 mm. The results show that specimen thickness does not necessarily change the yield or the ultimate tensile strengths taking the standard deviations into account. However, the Young Modulus and area reduction are significantly affected by the change of specimen thickness as depicted in Table 4. The effect is even more pronounced for vertically standing specimens.

The effect of the specimen thickness in relation to the heat input per scan layer is tested with specimen numbered as 2_6 and 2_7. In this case, another orientation was used as shown in Figure 1. The final specimen thicknesses were the same as 3 mm for both configurations. However, the initial parts built by the SLM process had different dimensions. For both sets, the specimens were built as rectangular prisms and the final geometry was cut by WEDM from these geometries. No significant difference is observed in any of the results for these two sets including area reduction and Young modulus as seen in Table 4.

Table 4. Effect of specimen thickness on tensile properties with standard deviations

#	Thickness	Orientation	Factor	A%	Young Modulus [GPa]
2_3	5 mm	0-0-0°	Vertical standing coupons-short side aligned with the coater direction -specimen thickness	30.82%	13.94
2_4	3 mm	0-0-0°	Vertical standing coupons-short side aligned with the coater direction	25.00%	19.33
1_1	5 mm	90-45-0°	Horizontal lying coupons 45 degrees with respect to coater direction -specimen thickness	25.51%	15.48
1_2	3 mm	90-45-0°	Horizontal lying coupons 45 degrees with respect to coater direction	22.45%	20.58
2_6	3 mm	0-90-90°	Vertical lying coupons SLM built part dimensions: 103x3x12 mm	21.55%	20.54
2_7	3 mm	0-90-90°	Thickness of the produced specimen- SLM built part dimensions: 103x20x12 mm	20.75%	19.74

Proceeding the tests, a structural bracket was manufactured and tested against technical requirements at FNSS with success.

4. CONCLUSIONS

This study has shown the feasibility of the SLM process for fully functional parts from AISI 316L stainless steel parts for load-carrying applications. The tensile properties were investigated of SLMed parts for unfixed process parameters such as the build orientation and scan area per layer leading to different heat input conditions. In addition to consolidated process parameters such as scan speed, laser power, scan strategy, etc., these parameters are critical for the success of the process because depending on the part size, residual stresses, support design, build rate, etc., these cannot be consolidated for every geometry to be built. The results show that the obtained mechanical properties are satisfactory for real life applications However, it is also shown that the vertically standing specimens are more prone to manufacturing defects. For further investigations, microstructural investigations and testing dynamic part properties will be carried out.

REFERENCES

1. M. J. Louis, T. Seymour, J. Joyce, 3D opportunity in the Department of Defense by Deloitte Consulting LLP.
2. Yasa, E., Kruth, J.-P., 2011, Microstructural investigation of Selective Laser Melting 316L stainless steel parts exposed to laser re-melting, Procedia Engineering 19 (2011) 389 – 395.
3. Kaynak, Y., Kitay, O., 2018, Porosity, Surface Quality, Microhardness and Microstructure of Selective Laser Melted 316L Stainless Steel Resulting from Finish Machining, J. Manuf. Mater. Process. 2018, 2, 36; doi:10.3390/jmmp2020036
4. Yusuf, S.M., Chen,Y., Boardman, R., Yang,S., Gao, N., Investigation on Porosity and Microhardness of 316L Stainless Steel Fabricated by Selective Laser Melting, Metals 2017, 7, 64; doi:10.3390/met7020064
5. Kluczyński,J., Śnieżek, L., Grzelak, K., Mierzyński, J., 2018, The influence of exposure energy density on porosity and microhardness of the SLM additive manufactured elements, Materials 2018, 11, 2304; doi:10.3390/ma11112304.
6. Sun, Z., Tan,X., Tor,S.B., Wai, Y.Y., 2016, Selective laser melting of stainless steel 316L with low porosity and high build rates, Materials and Design, doi:10.1016/j.matdes.2016.05.035.
7. Luo, J.P.; Jia, X.; Gu, R.N.; Zhou, P.; Huang, Y.J.; Sun, J.F.; Yan, M.,2018, 316L Stainless Steel Manufactured by Selective Laser Melting and Its Biocompatibility with or without Hydroxyapatite Coating. Metals 2018, 8, 548.
8. Wang, D.; Song, C.H.; Yang, Y.Q.; Bai, Y.C., 2016, Investigation of crystal growth mechanism during selective laser melting and mechanical property characterization of 316L stainless steel parts. Mater. Des. 2016, 100, 291–299.
9. Liverani, E.; Toschi, S.; Ceschini, L.; Fortunato, A., 2017, Effect of SLM process parameters on microstructure and mechanical properties of 316L austenitic stainless steel. J. Mater. Process. Technol. 2017, 249, 255–263.
10. Chen, W.; Yin, G.; Feng, Z.; Liao, X., 2018, Effect of Powder Feedstock on Microstructure and Mechanical Properties of the 316L Stainless Steel Fabricated by Selective Laser Melting. Metals 2018, 8, 729.
11. Cherry, J.A., Davies, H.M., Mehmood, S., Lavery, N.P., Brown, S.G.R., Sienz, J., 2015, Investigation into the effect of process parameters on microstructural and physical properties of 316l stainless steel parts by SLM. Int. J. Adv. Manuf. Technol. 76, 869–879.
12. Tolosa, I., Garciandia, F., Zubiri, F., Zapirain, F., Esnaola, A., 2010, Study of mechanical properties of AISI 316 stainless steel processed by “selective laser melting”, following different manufacturing strategies. Int. J. Adv. Manuf. Technol. 2010, 51, 639–647.

A PROCESS PLANNING STUDY IN WIRE ARC ADDITIVE MANUFACTURING

Ahmet Suat Yıldız[1], Enes Gebel[2], Barış Koç[1], Ahmet Ali ŞEN[2], Oğuzhan Yılmaz[3]
[1]*FNSS Defense Systems, Ankara, ahmet.yildiz@fnss.com.tr, baris.koc@fnss.com.tr*
[2]*Intecro Robotics, Ankara, enes.gebel@intecro.com.tr,* ali.sen@intecro.com.tr
[3]*Gazi University, Mechanical Engineering Department, oguzhanyilmaz@gazi.edu.tr*

Abstract. Wire arc additive manufacturing (WAAM) is attracting people from the manufacturing industry, due to its potential to fabricate large metal components with low cost and short production lead time. The WAAM parts can be an alternative to large casting and machined parts which have high buy to fly ratios. In order to fabricate a part, the process planning is needed. This paper introduces a process planning strategy of a structural ring part. The path planning, step over and layer numbers were calculated according to the weld bead geometry which is result of welding parameters. The half of the fabricated part were machined to the desired dimensions and no visible defects detected.

Keywords: Wire arc additive manufacturing, process planning

1. INTRODUCTION

Additive manufacturing (AM) is a near-net-shaped manufacturing technology used for producing final solid objects by depositing the material layer by layer from powder or wire feedstock via melting them using beam or arc heat source. AM technology promises remarkable reduction in lead time, cost and machined material *(Yilmaz & Ugla, 2016)*. Wire Arc Additive Manufacturing (WAAM) is becoming popular in industry and academia due to its production ability of large components with medium geometric complexity *(Cunningham, et al., 2018)*. It is the combination of arc heat source and wire feedstock. WAAM system uses the standard welding equipment including welding power source, torches and wire feeding systems. Motion is performed with either robotic systems or computer numerical controlled gantries *(Williams, et al., 2016)*. WAAM has a higher deposition rate compared to powder bed fusion, but less resolution and complexity. Metal wires are cheaper than metal powders having suitable properties for AM, hence large components could be economically produced with WAAM *(Ding, Pan, Cuiuri, & Li, Wire-feed additive manufacturing of metal components: technologies, developments and future interests, 2015)*. Process planning which means selecting the right welding parameters and path planning is very important in order to fabricate a high-quality part. In this study, process of a structural ring geometry was planned and manufactured with WAAM. It is intended to replace some industrial casting and machined parts with WAAM parts.

2. MATERIALS AND METHODS

WAAM hardware used in the process has 6-axis KUKA KR30 HA robot arm motion system. The 'Fronius TPS400i' with CMT welding process is used as a welding power supply. The depositing speed and weld path were controlled by robot, while other parameters, such as voltage and current, were controlled with CMT power supply by selecting the wire feed speed. The CMT torch was fixed on the robotic arm and hold vertical to the substrate during the deposition. In the process, hot rolled structural mild steel S355 with 20 mm thickness was used as a substrate. The 1.2 mm diameter wire material ER120S-G according to AWS A5.28 was used as welding wire. This material is a low alloy high strength steel which is commonly used for large vehicle, crane and high strength pressure vessel manufacturing. Wire feed and travel speed welding parameters were selected according to the previous study and kept constant during the deposition (Suat Yildiz, Koc, & Yilmaz, 2019). The resulting weld bead width and height of these parameters were known from the study. According to this information, the step-over and layer numbers were calculated to reach the required hollow thickness and the height of the ring geometry. Ring dimensions was targeted as

300 and 220 mm outer and inner diameter respectively, after the machining process. The first weld pass started from the outer and directed inside with a defined step over distance after the end of each circle path by overlapping the previous weld as shown in Figure 1. The step over distance was calculated according to the empirical formula (Ding, Pan, Cuiuri, & Li, A multi-bead overlapping model for robotic wire and arc additive manufacturing (WAAM), 2015). Dwell time was selected as 1 minute between each layer to avoid the heat accumulation and collapse of the part. Path planning was prepared by offline programming and the generated robot code was transferred to the robot controller.

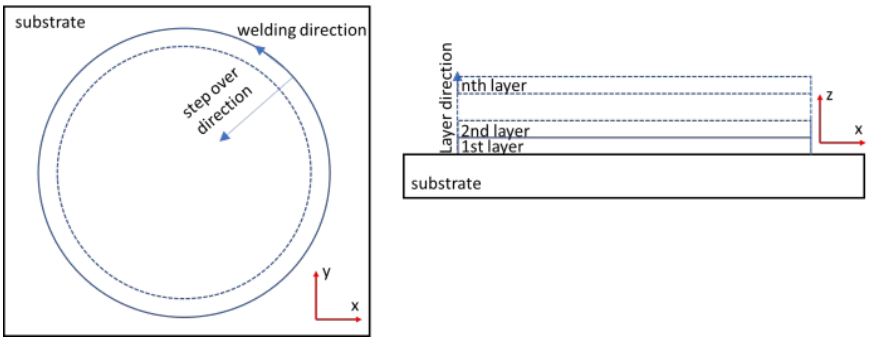

- **Figure 11.** Deposition strategy of the ring geometry

3. RESULTS AND DISCUSSION

The produced ring geometry is shown in Figure 2. The half of it was machined. The machined surface has no defects such as porosity, crack and lack of fusion. The machining dimensions were different for inner (6.5 mm), outer (2.5 mm) and upper (7 mm) surfaces. In order to have a better buy to fly ratios, machining distances should be kept minimum. The step over distance were not enough, since the layer height varied from outside to inside of the ring.

Figure 2. Produced ring geometry with WAAM

4. CONCLUSIONS

A systematical process planning was prepared and applied to fabricate a structural part with WAAM. The step-over distance effect was seen on the top of the part. It will be optimized in the future. Half of the part was machined to the desired dimensions. No visible quality problems on the machined sides were seen. The machining distance varied and was too much for upper and inner surfaces. The control of this distance will be performed in the future. The microstructure and mechanical properties of the part will also be examined.

REFERENCES

Cunningham, C., Flynn, J., Shokrani, A., Dhokia, V., Flynn, J., Shokrani, A., & Dhokia, V. (2018). Invited Review Article: Strategies and Processes for High Quality Wire Arc Additive.

Ding, D., Pan, Z., Cuiuri, D., & Li, H. (2015). A multi-bead overlapping model for robotic wire and arc additive manufacturing (WAAM). *Robotics and Computer-Integrated Manufacturing, 31*, 101-110.

Ding, D., Pan, Z., Cuiuri, D., & Li, H. (2015). Wire-feed additive manufacturing of metal components: technologies, developments and future interests. *International Journal of Advanced Manufacturing Technology*.

Suat Yildiz, A., Koc, B., & Yilmaz, O. (2019). *Building strategy effect on mechanical properties of high strength low alloy steel in wire + arc additive manufacturing.*

Williams, S., Martina, F., Addison, A., Ding, J., Pardal, G., & Colegrove, P. (2016). Wire + Arc Additive Manufacturing. *Materials Science and Technology*.

Yilmaz, O., & Ugla, A. (2016). Shaped metal deposition technique in additive manufacturing: A review. *Proceedings of the Institution of Mechanical Engineers, Part B: Journal of Engineering Manufacture, 230*(10), 1781-1798.

MEASURING HAZE, TRANSMITTANCE AND COLOUR OF CLEAR 3D PRINTED STEREOLITHOGRAPHY RESINS

Darragh Fitzpatrick[1], Ory Hajatpour[2], David Branagan[3]
[1]*darragh.fitzpatrick@henkel.com*
[2]*ory.hajatpour@henkel.com*
[3]*david.branagan@henkel.com*

Abstract. The purpose of this report is to describe the development process of a test method that accurately quantifies 3D printed polymers for haze, transmittance and colour. The need for the development of this test method is at the forefront of the evolution of standards and practices in the additive manufacturing industry. Standardizing of a method developed for haze, transmittance and colour is critical for quantitative assessment of printed resins. The resulting method is particularly applicable for development and formulation of stereolithography (SLA) resins denoted as aesthetically clear or near clear and low in colour.

Keywords: 3D printing, Haze, Transmittance, Colour.

1. INTRODUCTION

As with all methods of testing in the 3D printing industry they are evolving and becoming standardised. However, it is not unexpected to find gaps in the materials testing. There is a need for specific 3D Printing or Additive manufacturing methods as there are differences to those printed specimens against that of cast cured materials or molded plastics where there are no artefacts of the printing process. For 3D polymers it is important to establish what is needed to be measured and then align that with existing ASTM standards. The most logical place to look for existing standards is the Plastics Industry.
To establish a repeatable and reproducible test method, the plastics industry has two very relevant standards, ASTM D1746-15 Standard Test Method for Transparency of Plastic Sheeting [1] and ASTM D1003-13-1 Standard Test Method for Haze and Luminous Transmittance of Transparent Plastics [2]. ASTM D1003-13-1 was seen as the most appropriate as it utilizes instrumental techniques to generate measurements such as a specific haze meter, spectrophotometry or colorimetry. The measurement of colour can be performed on the same 3D printed test specimen using a colorimeter.
The dimension of the test specimen was not the only consideration. Printed test specimen requires a standardised print method. The orientation of the model during the print cycle should be like for like for comparative results. Printing the specimen with upright along the z-axis, 90° to the x y, as per Figure 1 (c), was chosen to be ideal. In this orientation the stacking of the layers is uniform. Effects of layering will be evident on the test surfaces.

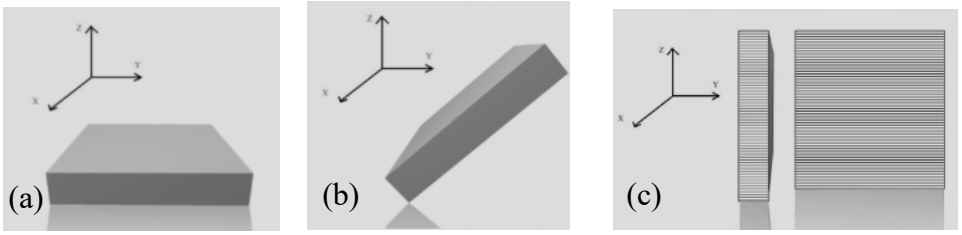

Figure 1: Possible print orientations of the test piece.

2. MATERIALS AND METHODS

Initial testing was carried out on two SLA printers, both a Laser (SLA) and Digital Light Process (DLP) based. 3D printed test pieces of the dimensions, 40mm x 40mm x7mm, were printed upright on the z axis. Uncoated samples were tested for haze, transmittance and colour, using a colourometer, as well as,

samples which were coated with the respective resin to become more visibly transparent. This was to investigate the impact of surface haze.
The ultra-clear 3D resin Loctite 3D 3820 was used to print these test pieces.

3. RESULTS AND DISCUSSION

Variation across printers is shown, particularly by the degree of haze and diffusion of light. Total transmittance is not significantly different on the two printed specimens; however, the type of transmittance is changed with the different print methods. This is perhaps a result of the sharpness of the resolution with the SLA light. The post-treatment of the surfaces of the specimen has little effect on colour but it has significant effects on the haze. The clear resin was then tested where one printed specimen was coated with a itself to become visually transparent and the other sample was uncoated. This was to investigate reduction of the surface haze which is an artefact of the printing process. A predictable clear difference is demonstrated in the coated v. uncoated specimen. The colour while not unaffected is determined by the material and not the printer. Coating of material after the printing process has a major effect on the appearance. The coated clear resin showed a major decrease in the haze values. This would indicate that the haziness in the specimen is generated at the surface of this product through the printing process. It was also interesting that the colour in B* yellowness increased. This is to do with the intensity of colour increase with a less hazy surface.

Table 1: Testing data for DLP v SLA printed test specimen.

Test	Indication	DLP Printer	SLA Printer
L	Dark 0-100 Bright	88.005	87.13
A	-Green+Red	-4.86	-5.48
B	-Blue+Yellow	5.905	5.11
Haze	% Haze	49.385	73.29
Transmittance	Y Total	87.42	87.48
Transmittance	Y Diffuse	43.245	64.11

Table 2: Testing data for uncoated and coated test specimen.

Test	Indication	Uncoated	Coated
L	Dark 0-100 Bright	88.005	88.39
A	-Green+Red	-4.86	-4.9
B	-Blue+Yellow	5.905	6.64
Haze	% Haze	49.385	3.93
Transmittance	Y Total	87.42	89.98
Transmittance	Y Diffuse	43.245	3.54

4. CONCLUSIONS

From our testing we have reached a standardized repeatable practice where any deviations of test results come from external influences on the test method, an example of which is the effect of treating the specimen after printing with a coating. A protocol of standard practice is followed when comparing two materials; Printer Selection, Specimen Dimensions, Printed Orientations, Print Layer thickness, Post Print Preparation, Test Instrument & settings.
With this approach the selected ASTM D1003-13-1 adapted herein from the plastics industry is suitable method that can be applied to 3D Printing for development of clear resins and as guidance for the end user.

REFERENCES

[1] https://www.astm.org/Standards/D1746.htm
[2] https://www.astm.org/Standards/D1003.htm

MECHANICAL PROPERTIES OF 3D PRINTED PARTS MADE OF RECYCLED POLYMERS

Ali Alperen BAKIR[1], Resul ATİK[1], Sezer ÖZERİNÇ[1,2]
[1]*Middle East Technical University, Department of Mechanical Engineering, Ankara, Turkey alprnbkr@gmail.com*
[2]*Middle East Technical University, Department of Micro and Nanotechnology, Ankara, Turkey*
ozerinc@metu.edu.tr

Abstract. In this study, we investigated the mechanical properties of specimens made of recycled PET, to assess the suitability of this material for applications that require high mechanical strength. We explored the effect of infill and raster orientation on the tensile strength and elastic modulus. Increasing the infill parameter improved mechanical strength and increased elastic modulus. Raster orientations parallel, perpendicular and diagonal with respect to the loading direction also resulted in different mechanical behavior. The best mechanical performance was observed for the parallel orientation with a tensile strength of 48.4 MPa and an elastic modulus of 1.73 GPa. The results show that the use of rPET as a 3D printing filament material provides good printing quality with high mechanical strength, making rPET an environmentally friendly alternative to standard filament materials.

Keywords: 3D printing, fused deposition modeling, recycled PET, mechanical properties

1. INTRODUCTION

3D printing has become an effective way of prototyping miscellaneous engineering components in a quick and economical fashion [1]. As a significant fraction of parts manufactured by 3D printing is rapidly discarded, effect of the 3D printing industry to environment is a concern. Recently, various filament manufacturers have focused on recycled filaments to reduce the waste material [2]. One of the promising types of recycled filaments is based on polyethylene terephthalate (PET), which is the most commonly used plastic for beverage packaging. In this study, we investigated the mechanical properties of 3D-printed specimens made of recycled PET (rPET), to assess the suitability of this material for applications that require high mechanical strength.

2. MATERIALS AND METHODS

An Ultimaker 2+ 3D printer that uses fused deposition modeling technology printed the specimens in standard tensile testing geometry. 3 different types of specimens were considered with raster orientations being parallel, perpendicular and diagonal with respect to the loading axis.
A Zwick/Roell Z250 tensile testing machine is used for mechanical characterization, at a displacement rate of 5 mm/min. For each geometry, 5 identical specimens were prepared and tested. Both the filament and printed specimens were characterized by using a Rigaku Ultima IV X-ray diffractometer using the θ-2θ geometry.

3. RESULTS AND DISCUSSION

Figure 1 shows representative stress-strain data for each specimen type. The parallel specimen is shown separately as it exhibits a much higher elongation at break.

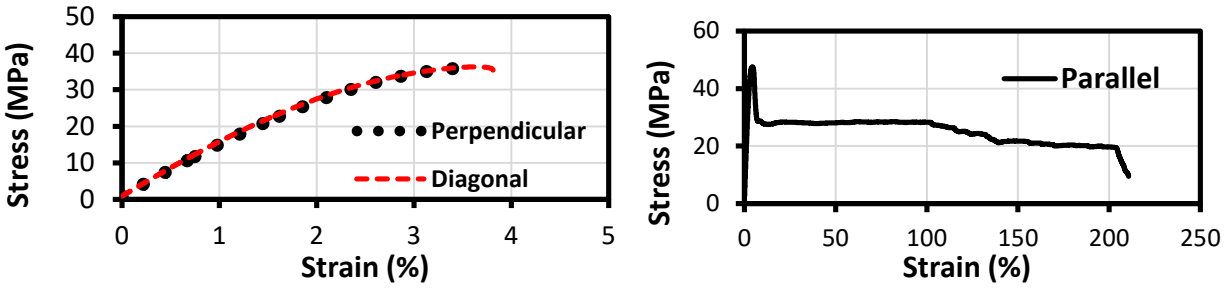

Figure 1. Stress-strain behavior of representative specimens with different printing orientations. (a) perpendicular and diagonal, (b) parallel.

The perpendicular sample forms a fracture surface normal to the loading direction, whereas the diagonal sample exhibits failure over a surface oriented at 45° relative to the loading direction. The parallel sample shows high plasticity through the deformation of the printed lines of polymer along their deposition path. Average mechanical properties of the specimens for the three printing orientations are summarized in Table 1. Parallel configuration provides the highest ultimate tensile strength (UTS) and exhibits an outstanding ductility reaching 142%.

Table 1. Average values of ultimate tensile strength and elongation at break for rPET.

Printing orientation with respect to loading direction	UTS (MPa)	σ_{UTS} (MPa)	Elongation at break (%)	St. Dev	Youngs Modulus	St. Dev
Parallel	48.4	0.6	142	80	17.3	0.5
Diagonal	35.8	1.0	7.9	5.2	14.1	1.0
Perpendicular	33.3	2.4	3.3	1.2	14.4	2.4

4. CONCLUSIONS

The best combination of rPET mechanical properties was observed for the parallel printing orientation with a tensile strength of 48.4 MPa and an elongation at break above 100%. Therefore, in order to obtain the best performance in applications, parts should be printed with raster lines being parallel to the direction of operational loading. The results show that the use of rPET in 3D printing applications combines high mechanical strength with outstanding ductility, making rPET an environmentally friendly alternative to other popular filament materials.

REFERENCES

[1] Gibson, I. (2014). Additive Manufacturing Technologies. New York: Springer.
[2] Kreiger, M. A., Mulder, M. L., Glover, A. G., & Pearce, J. M. (2014). Life Cycle Analysis of Distributed Recycling of Post-consumer High Density Polyethylene for 3-D Printing Filament. Journal of Cleaner Production 70, 90-96.

MAGNETIC DIRECTED ENERGY DEPOSITION: ASSESSMENT FOR MICROGRAVITY

Peter Smith[1], Adam Clare[2], Joel Segal[3]
[1]*peter.smith2@nottingham.ac.uk*
[2]*adam.clare@nottingham.ac.uk*
[3]*joel.segal@nottingham.ac.uk*

Abstract. Additive manufacturing in space has potential to resolve dependability and redundancy issues on long duration space flight missions. The primary difficulty in powder use in microgravity is controlling its placement. This work proposes using a magnetic field to constrain ferromagnetic powders and aims to investigate the effects of this process terrestrially. This study shows that magnetic field assisted catchment can be improved when a ferromagnetic steel is used. Single layer tracks were produced by directed energy deposition under varying magnetic conditions. The mass of each track was measured to determine powder catchment, with focus variation microscopy used to examine profiles and surface roughness of the tracks. The effect of the magnetic field on the geometry of tracks produced, surface roughness and catchment efficiency was analysed. The improvement in powder catchment efficiency suggests that the process may aid powder capture in microgravity. The production of steep sided tracks may also yield improved surface roughness of sidewalls manufactured by directed energy deposition.

Keywords: Magnetic, microgravity, additive, manufacturing, DED

1. INTRODUCTION

Current reliability strategies for technologies in-space will not be suitable for long term missions to Mars (Stormgren, 2016), and additive manufacturing (AM) in space has been suggested as a solution. Wire feed AM processes have been the subject of research due to the ease of manipulating wires in microgravity (Watson, 2002). This work proposes an alternative approach, using a magnetic field to control ferromagnetic powders for directed energy deposition (DED) in reduced gravity.
Magnetically assisted DED (MADED) has potential to improve powder catchment efficiency, enabling powder capture in microgravity. Powder DED is considered for in-space applications due to the smaller quantity of powder which must be controlled at a given time and simplified scalability compared to powder bed methods. The reduction in post-machining required by wire feed additive manufacturing methods is also an advantage (Frazier, 2014).
An additional benefit is that magnetic assistance may be used to improve surface roughness in sidewalls, due to the steeper sides which can be created by improving catchment at the edge of the melt pool. This work examines the effect of a magnetic field on track geometry, powder catchment and surface roughness.

2. MATERIALS AND METHODS

A magnetic chuck, conventionally used for work holding during grinding, was used to apply the magnetic field lines of dense magnetic flux across the substrate. Experiments were conducted with and without the presence of a magnetic field to determine its effects. 1 mm thick mild steel was used as the substrate material to allow the magnetic field to permeate sufficiently through the substrate. AISI 4340 steel powder was used as the cladding material due to its magnetic permeability and its level of understanding in the DED community. The powder used was gas atomised and determined by the manufacturer to have a diameter of 32-75 µm. A 2kW diode pumped laser was used as the laser source, with laser power set to 600 W, with a standoff distance of 10 mm, and a spot size of diameter 1.5 mm.

Single layer tracks were produced, at powder flow rates of 9.2-23 g/min, collinearly and perpendicular to the lines of dense magnetic flux. The mass of each track was measured. Surface maps of 1.5-2 mm sections of track were analysed by focus variation microscopy.

3. RESULTS AND DISCUSSION

3.1 Track Geometry

Track geometry was observed to change based on the magnetic condition. In X-axis tracks, broad sections were observed where the tracks bisected the areas of high magnetic flux density (shown in figure 1). The mean cross sectional profile of each measured section was determined from the surface maps, allowing the track geometry to be quantified (Figure 2).

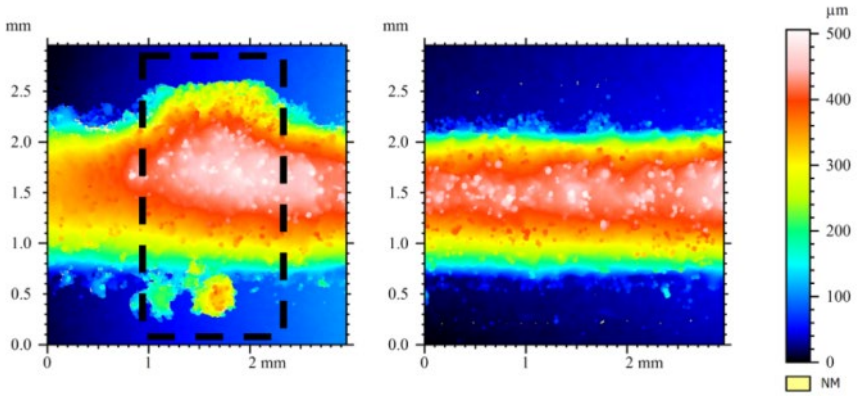

Figure 1. Surface maps showing broad track sections (left) with magnetic assistance and (right) without magnetic assistance. Dashed box shows the area used to construct the mean profile (figure 2).

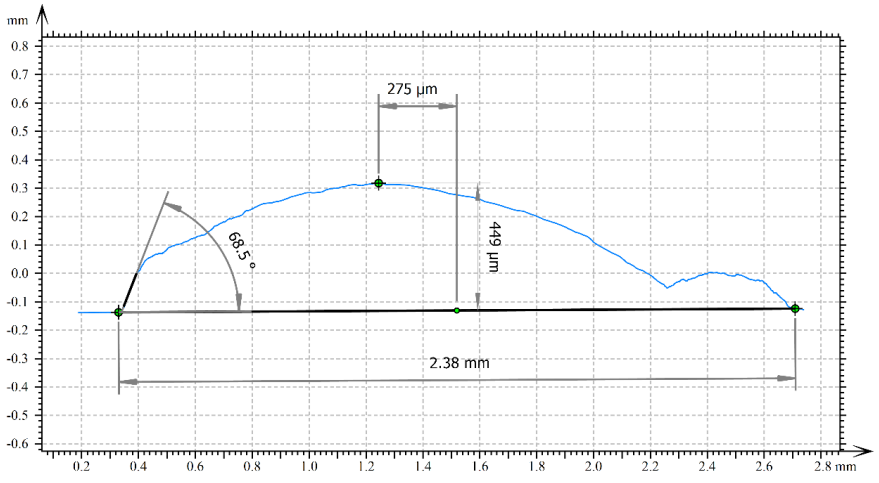

Figure 2. Measurements of the above DED track, showing the maximum tangent angle being measured on the steep side of the track.

On the wider track sections, a steep track side was observed consistently on one side of the track, with partially connected islands on the opposite side (shown in Figure 2). The effect of increasing powder quantity to produce a steep sided track has been previously been shown to improve sidewall surface roughness (He, 2013). Increasing the powder catchment at the edge of the pool using a magnetic field is a novel approach to reproducing this steep sided track. Figure 3 illustrates that the addition of a magnetic field has a greater effect on track angle than increasing powder catchment alone, this is likely because the magnetic field draws additional powder to the edge of the melt pool specifically rather than over the whole melt pool, as has been demonstrated previously.

The steep side being consistently observed on the same side of the track is believed to be as a result of phenomenon noted by Eisenbath et al. where an out of focus powder stream leads to uneven deposition (Eisenbath, 2019).

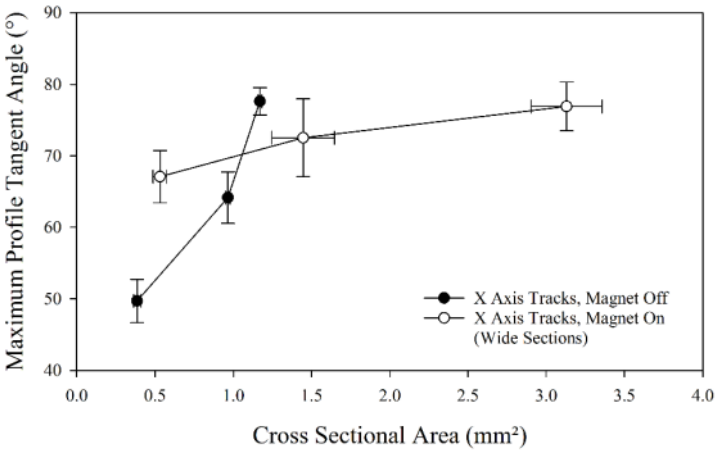

Figure 3. Magnetic assistance can increase track sidewall angle more than increasing powder catchment alone.

3.2 Powder Catchment

Figure 4 indicates that magnetic assistance has a positive effect on powder catchment. With increased mass being accompanied by greater cross-sectional area, with the exception of the narrow sections on X-axis tracks. This change shows that powder catchment is only affected when the powder flow traverses the areas of high magnetic flux. The increase in catchment due to the magnetic field is greatest when the powder is consolidated along lines of dense magnetic flux. Compared to without magnetic assistance, powder catchment was improved by up to 62% (by weight) in this condition. This effect is more significant at greater powder flow rates. Increased powder catchment suggests MADED could be used to

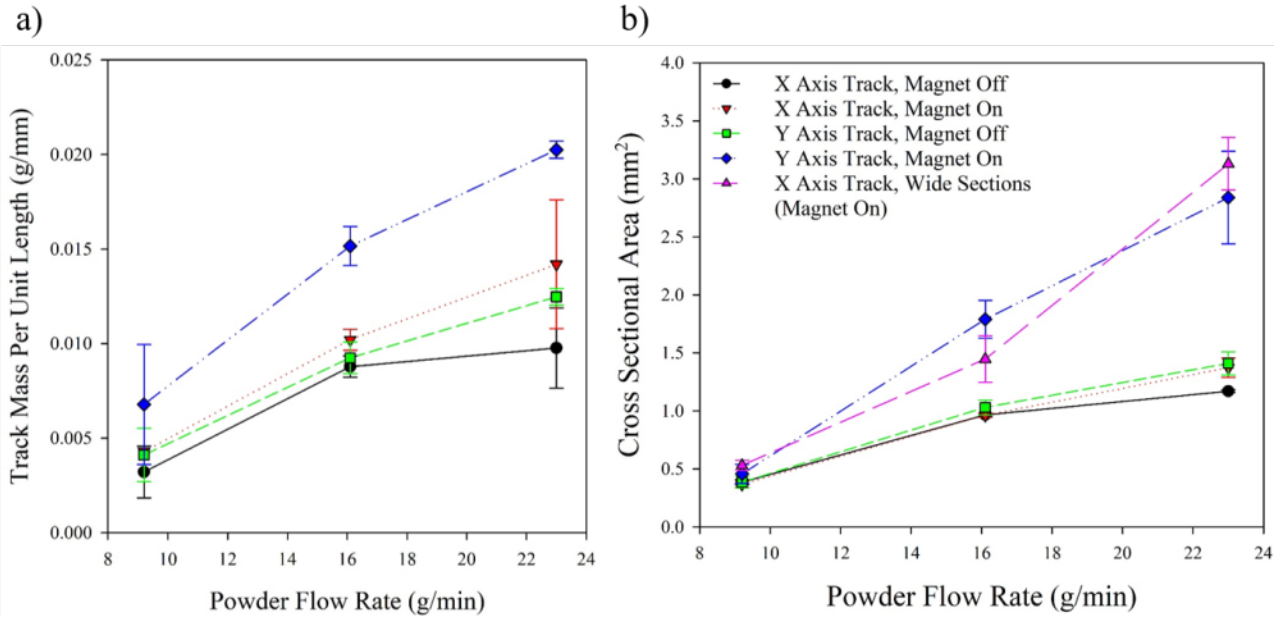

Figure 4. The increase in track mass is accompanied with increased cross sectional areas. When the wide sections are separated from the rest of the track the difference in catchment becomes clear.

constrain powder in microgravity.

3.3 Surface Roughness

Surface roughness increases at greater powder flow rates and the effect appears to be exaggerated when magnetic assistance is applied. Surface roughness is clearly linked to powder catchment rather than specifically to magnetic assistance, as shown by the similarity between figures 4 and 5. As magnetic assistance increases a greater proportion of the powder is only partially melted onto the surface of the track, because laser power (and therefore heat input) remained constant. Partially melted powder can be seen in the scanning electron microscopy (SEM) image of the track cross section in figure 6.

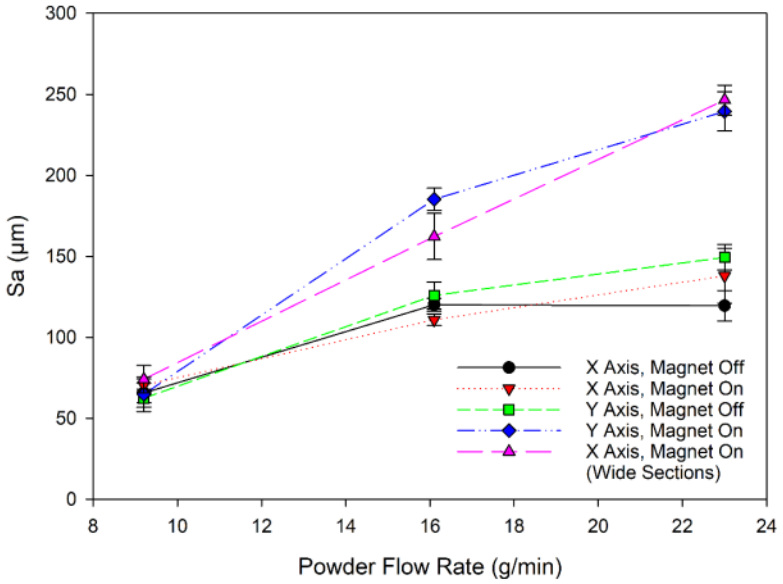

Figure 5. Arithmetic mean height (Sa) increase with flow rate

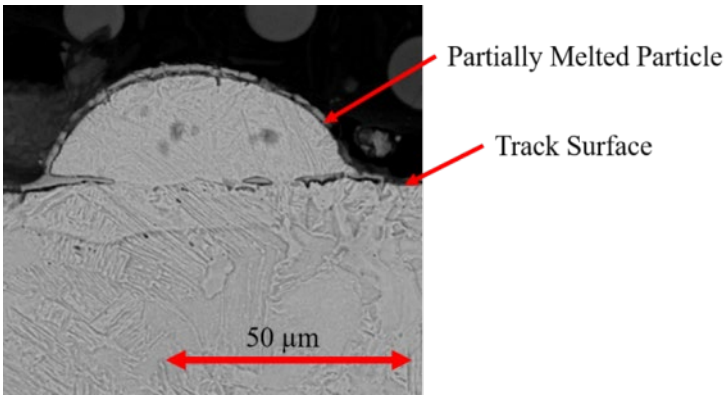

Figure 6. SEM image showing partially melted powder attached to a cross section of the track, the powder diameter is within the range expected of the powder.

4. CONCLUSIONS

MADED was found to increase powder catchment by up to 62%, by weight. This means that there is potential for magnetic assistance to improve the material efficiency of the DED process. Increased powder catchment also suggests that magnetic assistance could be used to constrain powders for additive manufacturing in microgravity environments, although significant research is required to determine the true effects of microgravity on this process.

The addition of a magnetic field was also used to draw more powder to the edge of the melt pool locally, this resulted in tracks with steeper sides with a greater effect than increasing the powder flow rate alone.

There is potential for this product to improve surface roughness of multi-layer walls. More work is required to investigate whether this effect can be replicated along many layers using shaped or pulsed magnetic and electrostatic fields.

Further analysis of the effect of magnetic assistance on material properties and microstructure in ferromagnetic powders is also required to determine whether hardness and strength are affected.

REFERENCES

He, B., Li, D., Zhang, A., Ge, J., Do, X., Xie, H., Yang, H., (2013). Influence of Powder Flow on Sidewall Quality of Solid Parts in Laser Metal Direct Forming. International Journal of Advanced Manufacturing Technology, 68, pp 2703-2711.

Eisenbath, D., Esteves, P.M.B, Wirth, F., Wegener, K. (2019). Spatial Powder Flow Measurement and Efficiency Prediction for Laser Direct Metal Deposition. Surface & Coatings Technology, 362, pp 397-408.

Frazier, W.E, (2014). Metal Additive Manufacturing: A Review. Journal of Materials Engineering and Performance, 23, pp 1917-1928.

Stormgren, C., Goodliff, K., Cirillo, W., & Owens, A. (2016). The Threat of Uncertainty - Why Using Traditional Approaches for Evaluating Spacecraft Reliability Are Insufficient. AIAA Space, Long Beach, Retrieved from www.arc.aiaa.org/doi/10.2514/6.2016-5307.

Watson, J., Taminger, K., Hafley, R., & Peterson, D. (2002). Development of a Prototype Low-Voltage Electron Beam Freeform Fabrication System. Solid Freeform Fabrication, Austin, Retrieved from www.ntrs.nasa.gov/search.jsp?R=20030012711

MODELLING TOPOLOGICALLY OPTIMIZED PARTS WITH MICROSTRUCTURES

Damla Ozkapici[1], Ulas Yaman[2]
[1]*Defense System Technologies, ASELSAN, dozkapici@aselsan.com.tr*
[2] *Department of Mechanical Engineering, Middle East Technical University, uyaman@metu.edu.tr*

Abstract. In this study, a topologically optimized part is remodeled with microstructures to increase its strength-to-weight ratio. Firstly, the Solid Isotropic Material with Penalization (SIMP) method is applied on the selected part. The SIMP method finds the optimum material distribution in a design domain and creates solid-void formations whose densities are 0 or 1. Setting a higher penalization factor in the method avoids having regions with intermediate densities which are difficult to manufacture with the conventional fabrication methods. However, those density regions can be manufactured by using Additive Manufacturing (AM) technologies. Thus, maintaining the intermediate density regions on the optimized part may result in a better performance. In order to investigate the idea, in this study, the SIMP method is applied with and without penalization and the entire design domain is filled with variable types of microstructures, each having wall thicknesses proportional to the density. Results of the proposed method are compared with the parts optimized by different techniques through finite element analysis. In addition, these parts are manufactured via Electron Beam Melting type of AM and mechanical tests are performed.

Keywords: *additive manufacturing, microstructures, topology optimization, SIMP, EBM*

1. INTRODUCTION

Additive Manufacturing (AM) methods fabricate parts by adding layers of material on top of each other in contrast to the conventional methods that create structures through subtractions of initial material block. One of the greatest advantages provided by these technologies is that complex geometries can be manufactured easily while the conventional methods remain incapable of producing such intricate artifacts (Gibson et al., 2014).

Topology Optimization (TO) is one of the specialized fields utilizing the advantages of AM. Optimization goals are set in a way to increase the performance of the overall part, such as maximizing the compliance and/or minimizing the weight. Although the method suggests significant improvements on the performance of the part, it was not that applicable in terms of manufacturing in recent years since the optimization usually ended up with complex geometries (Zegard et al., 2016). However, advances in AM technologies led this field to develop rapidly. There are several techniques used for TO. Homogenization method is one of the earliest studies in the field, introduced by Bendsøe and Kukuchi (Bendsøe et al., 1988). In this method, the optimization problem is solved for the optimum distribution of microcells, composed of material and micro-voids, in a reference domain based on the finite element analysis (FEA) done in accordance with the optimization goal. The method resulted with topologies having nearly precise shapes. Another similar optimization method is the Solid Isotropic Material Penalization (SIMP) (Bendsøe, 1989; Rozvany et al., 1992). It utilizes a penalization factor (PF) to avoid formation of regions with intermediate densities. In a recent study, Yaman et al. (2018) proposed a method called Variable Thickness Approach where they benefitted from the intermediate densities by applying the SIMP method with no penalization. After obtaining the density values of finite elements, the method covers the design domain with a surface of varying thickness.

Genetic algorithms aim to find the optimal solutions that fit the best according to the optimization objective in a population of candidate solutions. Jakiela et al. (2000) applied the method on cantilever plates. The authors' work resulted with multiple topologies in contrast to the previously mentioned methods ending up with a single solution. There are no regions with intermediate densities in the resulting topologies. It is also seen that there are some unconnected microstructures.

In this study, we propose an approach for improving the performance of the parts already optimized with the SIMP method. As opposed to the conventional approach, our method intends to use the intermediate densities instead of avoiding them. The method also presents a novel technique to obtain stable topologies with fully connected elements.

2. PROPOSED METHOD

2.1 Geometry and Boundary Conditions

In this study, the geometry and the boundary conditions are the same as the cantilever plate example used in the work of Jakiela et.al (2000) for comparison purposes. In their work, the edges of the cantilever have a ratio of 1.6. This ratio is also preserved here and a 96mm x 60mm rectangle is used as the initial geometry. Left edge of the rectangle is fixed and a load is applied at the middle of the right edge. The geometry and boundary conditions are defined in Rhinoceros3D and Grasshopper3D software accordingly.

2.2 SIMP Topology Optimization

After introducing the geometry and the boundary conditions, the design domain is discretized into finite elements. Then, the PF and the volume fraction constraints are set in the TopOpt ("TopOpt Plugin for Grasshopper3D", 2019), a plug-in for Grasshopper3D, before the optimization. TopOpt takes the discretized domain, constraints, loading conditions and some optimization settings like volume fraction and PF as inputs, and then gives the density distribution throughout the design domain as the output. Finally, the volume constraint is set to 0.25 as it is in the work of Jakiela et.al (2000) and the optimization is executed. As a result, densities of all the finite elements are obtained.

2.3 Microstructures

Using the data obtained from the SIMP, the entire domain is filled with microstructures where each one has a volume proportional to the density of the region it covers. There are three types of microstructures used in this study as shown in Figure 1. The properties of the microstructures are summarized in Table 1. The regions with densities lower than 0.25 are set to void.

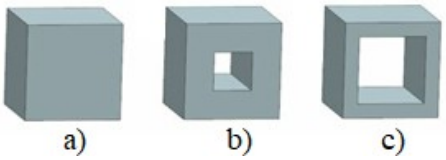

Figure 1. Utilized microstructures.

Table 1. Properties of microstructures.

Microstructures	Outer Dimensions(mm)	Inner Dimensions(mm)	Wall Thickness(mm)	Area Ratio(%)	Density Region
(a)	3×3	NA	NA	100	0.75-1
(b)	3×3	1.2×1.2	0.9	84	0.5-0.75
(c)	3×3	2.1×2.1	0.45	54	0.25-0.5

2.4. Connectivity Analysis

In this step, the topology is checked against the unconnected elements. A microstructure is considered as unconnected if it does not share an edge with a neighbor cell. This type of microstructures cannot be manufactured properly. In our method, connectivity is provided by adding elements to the neighbors of the unconnected cells in contrast to the other methods deleting the unconnected cell directly. The algorithm is employed on the configuration shown in Figure 2. The fourth cell is initially unconnected. The first cell is connected and it can further be connected to the fourth cell through the second and the third cells. If the density of the second cell is higher than the third cell, a new microstructure is added to the second cell. Using the same approach, the sixth cell is also filled with a microstructure. Thus, a fully connected topology is obtained.

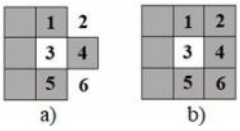

Figure 2. (a) Before the connectivity analysis; (b) After the connectivity analysis.

2.5. Fabrication

In this study, four parts shown in Figure 3 were fabricated using Arcam EBM machine with Ti6Al4V alloy powders. All the parts were fabricated with a thickness of 10 mm. Additionally, part (a) was extended by 7 mm, and parts (c) and (d) were extended by 6 mm in order to provide a surface large enough for the load application in the structural tests.

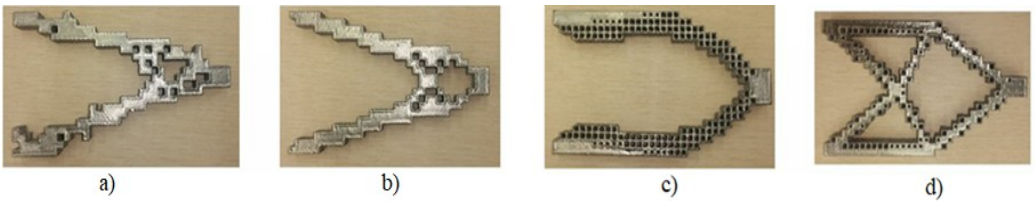

Figure 3. Parts optimized by (a) the genetic algorithm; (b) the homogenization method; (c) the proposed method with PF of 1; (d) the proposed method with PF of 3.

3. ANALYSIS and TESTS

FEA are applied on all the geometries in order to compare the performance of the proposed method with the genetic algorithm and the homogenization methods. The parts are fixed from the left side, and a load is applied to a 10mm x 10mm x 10mm area at the top surfaces of the rightmost microstructures. In order to validate the analysis results, all the specimens are also examined with a compression test by Instron 8872 Fatigue Testing Machine as shown in Figure 4. Each specimen is tested under the same loading conditions as FEA. The crosshead, which is the load interface of the machine, moves at a rate of 0.6 mm/min and the load is increased as the crosshead moves downwards. The tests were executed until the parts deformed plastically. The results are summarized in Table 2.

Figure 4. Test setup.

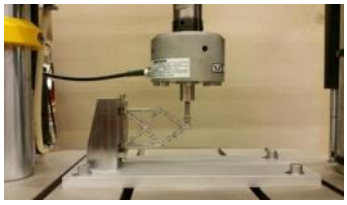

Table 2. FEA (A) and test (T) results of the optimized geometries.

Optimization Method	Weight (N), A/T	Load at Yielding (N), A/T	Load/Weight (N/N), A/T
Genetic Algorithm	0.66/0.628	3720/2902	5636.4/4621
Homogenization	0.62/0.60	2815/2414	4540.3/4023.3
SIMP with PF of 1	0.55/0.53	1910/811.2	3472.7/1530,6
SIMP with PF of 3	0.65/0.649	9000/3907	13846.2/6020

The geometries are compared according to the maximum load they can carry before yielding. Since the heavier parts are expected to withstand higher loads, the ratio of load carrying capacity to weight may give a better insight for comparison. It is seen that the performance of the proposed method with PF of 3 gives the best results. The genetic algorithm method follows right after it. Then, the homogenization and the proposed method with unity penalization come. Although the analysis and the test results are compatible in terms of the order of performances of the methods, it is seen that the magnitude of forces obtained at yielding differs. It is considered that these differences may arise from

the clearances in the fixtures used for the tests. As the load applies, the parts being tested may move up to some degree that clearances allow. However, the parts are assumed to be perfectly fixed in analysis. The part optimized with a PF of 3 shows greater difference between its analysis and the test results when compared to the other parts. It is squeezed between the walls of the fixture by screwing the bolts touching its topmost and bottommost surfaces at the left side as shown in Figure 4. The bolts started yielding before the part during the test. Due to the deformation in the fixture, no further measurements could be taken. Thus, this part is expected to start yielding at a higher load than its test result specified in Table 2. Another point to emphasize is that some amount of powder could not be removed from the smaller holes on the artifacts before tests. Therefore, the specimens obtained with the proposed method are probably lighter than they are.

5. CONCLUSIONS

The proposed method is applied to a cantilever geometry which was previously optimized by the SIMP with PFs of 1 and 3. Then, the outputs are compared with the genetic algorithm and the homogenization methods through the analysis and tests. It is seen that the method gives the best results among compared techniques when it is applied on the part optimized by the SIMP with a penalization of 3. However, when the SIMP is applied without penalization, the output of the proposed method (see Fig. 3, c) remains weak compared to the others. The performance of the part may be further improved by reducing the lower limit on the density, which is set to prevent formation of microstructures in the regions having densities lower than that limit. If the limit is reduced from 0.25 to 0.1, there would occur more microstructures in the design domain which may result in a stiffer topology.
This method is currently applicable for 2.5D parts having straight geometries. As a future work, it is planned to implement the method on 3D geometries having complex features. Additionally, analyses and tests will be performed on many parts optimized by the proposed and the other methods to further ensure the validity of the technique.

REFERENCES

Bendsøe, M. P., Kikuchi, N. (1988). Generating optimal topologies in structural design using a homogenization method. Computer Methods in Applied Mechanics and Engineering, 197-224.

Bendsøe, M. P. (1989). Optimal shape design as a material distribution problem. Structural optimization, 1, 193-202.

Chapman, C.D, Saitou, K., Jakiela, M.C. (1994). Genetic algorithms as an approach to configuration and topology design. Journal of Mechanical Design, 116, 1005-1012.

Gibson, I., Rosen, D., Stucker, B. (2014). Additive manufacturing technologies: 3d printing, rapid prototyping and direct digital manufacturing, Springer.

Jakiela, M.J., Chapman, C.C., Duda, J., Adewuya, A., Saitou, K. (2000). Continuum structural topology design with genetic algorithms. Computer Methods in Applied Mechanics and Engineering, 186, 339-356.

Kandemir, V., Dogan, O., Yaman, U. (2018). Topology optimization of 2.5D parts using the SIMP method with a variable thickness approach. Procedia Manufacturing, 17, 29-36.

Rozvany, G.I.N., Zhou, M., Birker, T. (1992). Generalized shape optimization without homogenization. Structural optimization, 4, 250-252.

Ti6Al4V Titanium Alloy. (2019). Retrieved from http://www.arcam.com/wp-content/uploads/Arcam-Ti6Al4V-Titanium-Alloy.pdf

TopOpt Plugin for Grasshopper3D. (2019). Retrieved from http://www.topopt.dtu.dk/?q=node/908, last accessed: August 24, 2019.

Zegard, T., Paulino, G.H. (2016). Bridging topology optimization and additive manufacturing. Structural and Multidisciplinary Optimization, 53, 175-192.

NUMERICAL STUDY OF HEAT DITURBUTION IN Ti-6Al-4V THIN WALLED CYLINDER DURING ELECTRON BEAM MELTING PROCESS

Roozbeh Saghatchi[a, b, c,1], Shaghayegh Saeidiharzand[a, b, c, 2], Mehmet Yildiz[a, b, c, 3], Bahattin Koç[a,b,c,4]

[a] *Integrated Manufacturing Technologies Research and Application Center, Sabanci University, Orhanli-Tuzla, 34956 Istanbul, Turkey*

[b] *Composite Technologies Center of Excellence, Sabanci University-Kordsa, Istanbul Technology Development Zone, Sanayi Mah. Teknopark Blvd. No: 1/1B, Pendik, 34906 Istanbul, Turkey*

[c] *Faculty of Engineering and Natural Sciences, Materials Science and Nano Engineering, Sabanci University, Orhanli-Tuzla, 34956 Istanbul, Turkey*

[1] *roozbeh@sabanciuniv.edu*

[2] *shaghayegh@sabanciuniv.edu*

[3] *meyildiz@sabanciuniv.edu*

[4] *bahattinkoc@sabanciuniv.edu*

Abstract. Heat distribution in a thin wall cylindrical component of Ti-6Al-4V caused by continuous and 5 step circular movements of electron beam melting (EBM) as an additive manufacturing (AM) process are numerically studied. Finite volume method (FVM) was employed in order to solve governing equations of this process. Effect of speed and power of EB on temperature distribution were investigated. Also, heat distribution in 5 step movement of electron beam was discussed. It was shown that in 5 step process, temperature gradient is smaller than the continues one, which can lead to more homogeneity in the microstructure and better mechanical properties.

Keywords: *Additive manufacturing, Electron Beam melting, Ti-6Al-4V, Finite volume method, circular movement.*

1. INTRODUCTION

Ti-6Al-4V is the most used titanium alloy. However, production of the components of this alloy usually accompanies with some difficulties. electron beam melting (EBM), one of the newly developed techniques of additive manufacturing (AM), has been extremely practical to produce semi-finished and finished products of Ti-6Al-4V (Carroll, Palmer, & Beese, 2015). However, there are still some issues that need further investigations. Directional solidification and the resulted nonhomogeneous microstructure during EBM process is one of the most concerned problems. This phenomenon leads to the production of the components that do not have highly desirable mechanical properties with a service life less than what is expected (Gockel, Beuth, & Taminger, 2014). Modeling of heat distribution through the components during the EBM can be extremely helpful to gain a better understanding into this phenomenon. Most researches have been only focused on the linear movement of the heat source (Jamshidinia, Kong, & Kovacevic, 2013) however, for some complex geometries, circular movement of EB can lead to the better results. In this study, two different types of circular movements of the EB during manufacturing a thin walled cylinder via AM process were offered: a) continuous and b) 5 step movements. Both approaches were modeled and compared to each other. 5 step movement processed was investigated thoroughly in order to find an optimized process with more uniform heat distribution.

2. MATERIALS AND METHODS

During the EBM process, molten fluid is assumed to be Newtonian and incompressible with flat surface. All physical properties are assumed to be constant during the simulation. Governing equations of the problem are full Navire-Stokes equation as well as energy equation (Jamshidinia et al., 2013)(Brent, Voller, Reid, Voller, & Enthalpy-porosity, 2017):

$$\frac{\partial(\rho u_i)}{\partial x_i} = 0 \quad (1)$$

$$\frac{\partial(\rho u_j)}{\partial t} + \frac{\partial(\rho u_i u_j)}{\partial x_i} = \frac{\partial}{\partial x_i}(\mu \frac{\partial u_j}{\partial x_i}) + \mathrm{S}_j \quad (2)$$

$$\frac{\partial(\rho h)}{\partial t} + \frac{\partial(\mathrm{u}_i \rho h)}{\partial x_i} = \frac{\partial}{\partial x_i}(\alpha \frac{\partial h}{\partial x_i}) + \mathrm{S}_h + q \quad (3)$$

where ρ is fluid density, u is velocity component, t is time, μ is viscosity, h is sensible enthalpy, k is thermal conductivity, T is temperature, and S_j, S_h and q are source terms which are defined as follow:

$$S_j = -\frac{\partial p}{\partial x_j} + \frac{\partial}{\partial x_i}(\mu \frac{\partial u_i}{\partial x_j}) - \mathrm{C}(\frac{(1-f_L)^2}{f_L^3 + B})\,\mathrm{u}_j + \rho g_j \beta(\mathrm{T} - \mathrm{T}_{ref}) - \rho U \frac{\partial(\rho u_j)}{\partial x_i} \quad (4)$$

$$S_h = \frac{\partial(\rho \Delta H)}{\partial t} + \frac{\partial(\rho u_i \Delta \mathrm{H})}{\partial x_i} \quad (5)$$

$$\dot{q} = \frac{8\eta P_B}{\pi d_b^2 l_B} \times \exp(\frac{-8(\mathrm{x}^2 + \mathrm{y}^2)}{d_b^2}) \times (-3(\frac{z}{l_B})^2 + 2(\frac{z}{l_B}) + 1) \quad (6)$$

in which p is pressure, U is the electron beam scanning speed, third and fourth terms at the right side of the Eq.4 account for enthalpy-porosity approach and Boussinesq approximation respectively in which C is a constant accounting for the mushy-region morphology, f_L is the element liquid fraction, B is merely a computational constant introduced to avoid division by zero, g is the gravitational acceleration, β is thermal expansion coefficient, and U is the electron beam velocity. $H = f(T)$ is the latent heat content, which is defined as a function of temperature. First term at the right side of the Eq.6 corresponds to electron beam power which is absorbed by surface, in which η is efficiency coefficient, P_B, d_b, and l_B are power, spot diameter and absolute penetration depth of the electron beam respectively. Second and third terms at the right side of the Eq.6 corresponds to electron beam distribution in radial and z directions respectively. Due to the turbulent nature of the weld pool, the contribution of the fluctuating velocities is taken into account by using turbulence model that provides a systematic framework for calculating effective viscosity and thermal conductivity. To do it, k-ϵ model is used (Balogh, Parente, & Benocci, 2012). In order to solve the governing equations, finite volume method was used and solved using OpenFOAM package. BouyantPimpleFOAM solver was used which uses PIMPLE algorithm to solve the pressure–velocity coupling. Temporal discretization was done based on Euler method.

3. RESULTS AND DISCUSSION

In order to verify the code accuracy, two different cases were simulated and compared with the previous studies. Figure 1 shows the temperature distribution during the EBM process in a cubic piece. As it can be observed in this figure, our results showed good accuracy in comparison with the results of Shen and Chou (Shen & Chou, 2016). In order to validate the code quantitatively, temperature variation on the beam path and axis parallel to it were extracted and shown in Figure 2. Our results are fairly close to the results of Rouquette et al. (Rouquette, Guo, & Masson, 2007).

Figure 2 shows the defined geometry and mesh used in this study in which only ¼ of the complete cylinder is shown to demonstrate the mesh detail. In all the simulation z assumed to be 3 mm. In order to reduce the heat gradient and improve the mechanical behavior of the finial result, laser beam applied in an alternative sequence as shown in Figure 3. The section of electron beam intersection with surface has the finer mesh and also the mesh size in z-direction varies to get the more accurate result at the upper surface of the cylinder. In order to decrease the simulation time, the physical domain decomposed into smaller part and solved using parallel architecture. Properties of the material were taken from the (Jamshidinia et al., 2013) and shown in Table 1.

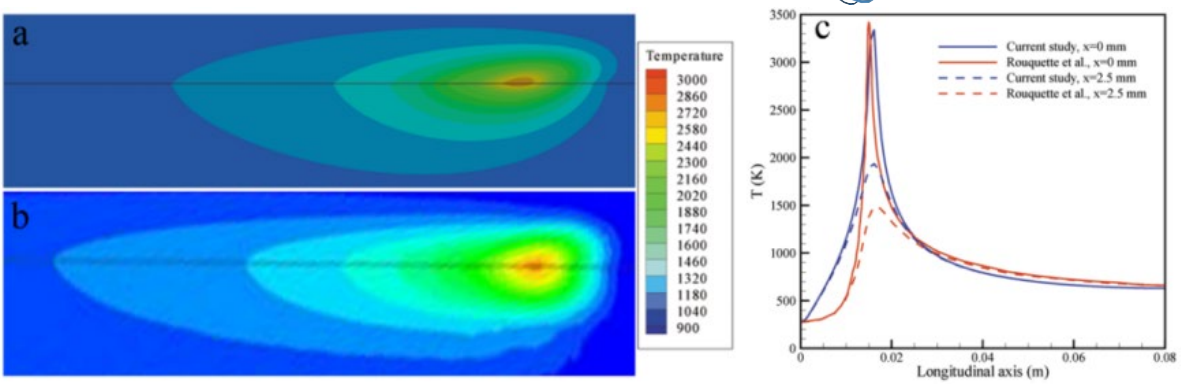

Figure 1. Temperature distribution during BMP for current study (a) and results of Shen and Chou (b) and comparison of temperature variation during BMP for current study and results of Rouquette et al. (c).

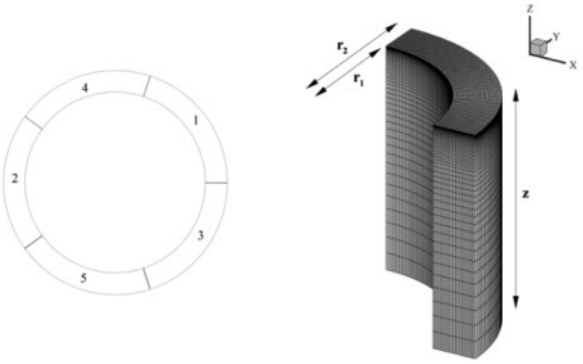

Figure 2. Laser path sequence from top view (left) and schematic geometry and mesh view for ¼ of a thin walled cylinder (right).

Temperature distribution of the thin- wall cylinder for different rotational speed, beam current and wall thickness are shown in first, second and third row of Figure 3 respectively. At higher speeds, laser beam applies the heat in shorter time which means the surface gets smaller portion of heat and the temperature rise will be small consequently. Laser power corresponds with its current, which means for higher current applied energy is high as well. Thus, as current increases, the temperature rise is high as well. Another important factor is wall thickness which has also influence on the temperature distribution. As the wall thickness increases, upper surface of the cylinder increases as well which leads to higher radiative heat transfer to the ambient, and the maximum temperature decreases as well.

Table 1. Parameters for EBM process of Ti-6Al-4V used in this simulation.

Parameters	Unit	Value
Wall thickness ($t=r_2-r_1$)	mm	0.6
Rotational speed (ω)	rad/sec	16π
Beam diameter	mm	0.18
Penetration depth	mm	0.02
Beam voltage	kV	60
beam current (I)	mA	14
Solidus and liquidus temperature	K	1877, 1923
Latent heat J/kg K	J/kg K	2.68×10^{5}
Volume expansion coefficient	1/K	8×10^{-6}

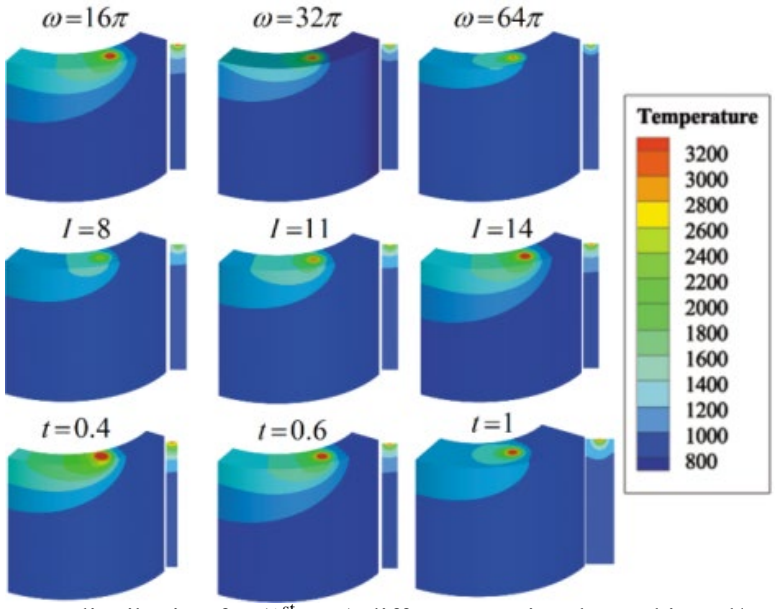

Figure 3. Temperature distribution for (1st row) different rotational speed in rad/s, (2nd row) different current in mA and (3rd row) different wall thickness in mm.

Temperature distribution during the process for the 5-step EBM is shown in Figure 4. In this figure, starting and ending instances of each step is shown. In order to show the effect of 5 step EBM on the final result, temperature distribution at the end of process for both 5 step and continues EBM are shown in Figure 5. As shown in this figure, final temperature distribution is uniform for 5 step EBM, while it is non-uniform for continues case. In order to show the advantages of 5 step EBM quantitatively, temperature and its gradient along the z direction at the points in which electron beam finished one cycle and θ direction at z=2.2 mm are shown in Figure 5 (c) and (d) respectively. As it can be observed in these figures, temperature gradient is larger for continues EBM in comparison with 5 step case. It should be noted that high peak of temperature gradient in θ direction in 5 step EBM which shown with dashed-line is correspond to current laser position.

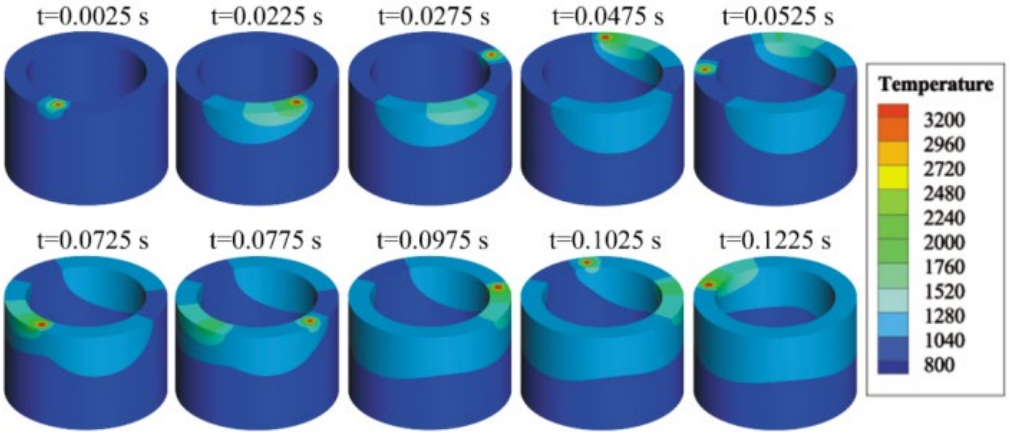

Figure 4. Temperature distribution during the 5 step EBM.

Effect of electron beam on temperature gradient can be justified considering that heating up and cooling down sequences. In continues case, first point of melted zone, has enough time to cooling down until electron beam moves 360° and reaches to this point again and makes a high temperature gradient consequently. On the other hand, for 5 step case, there is not enough time for this process and all sections were kept in relatively same temperature.

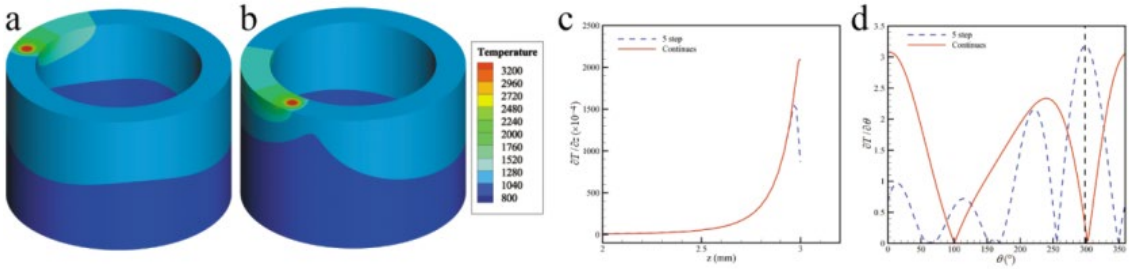

Figure 5. Temperature distribution at the end of the EBM for (a) 5 step process and (b) continues process and temperature gradient in (c) z- and (d) θ directions.

4. CONCLUSIONS

In this study, EBM process for thin wall cylinder was numerically modeled and temperature distribution was obtained. Two different configurations were implemented including continues and 5 step EBM. It was shown that 5 step EBM resulted in uniform final temperature distribution in comparison with continues one, which consequently led to smaller temperature gradient. Effect of EB speed and current, and wall thickness were also investigated and shown that speed and wall thickness have reverse effects on final temperature while increasing current leads to higher resultant temperature.

REFERENCES

Balogh, M., Parente, A., & Benocci, C. (2012). Journal of Wind Engineering RANS simulation of ABL flow over complex terrains applying an Enhanced k - e model and wall function formulation: Implementation and comparison for fluent and OpenFOAM. Jnl. of Wind Engineering and Industrial Aerodynamics, 104–106, 360–368. https://doi.org/10.1016/j.jweia.2012.02.023

Brent, A. D., Voller, V. R., Reid, K. J., Voller, V. R., & Enthalpy-porosity, K. J. R. (2017). Enthalpy-porosity technique for modeling convection-diffusion phase change: application to the melting of a pure metal change: application to the melting, 5720(August). https://doi.org/10.1080/10407788808913615

Carroll, B. E., Palmer, A., & Beese, A. M. (2015). ScienceDirect Anisotropic tensile behavior of Ti – 6Al – 4V components fabricated with directed energy deposition additive manufacturing. Acta Materialia, 87, 309–320. https://doi.org/10.1016/j.actamat.2014.12.054

Ding, R., Guo, Z. X., & Wilson, a. (2002). Microstructural evolution of a Ti – 6Al – 4V alloy during thermomechanical processing, 327, 233–245.

Gockel, J., Beuth, J., & Taminger, K. (2014). Integrated control of solidification microstructure and melt pool dimensions in electron beam wire feed additive manufacturing of ti-6al-4v. Additive Manufacturing, 1, 119–126. https://doi.org/10.1016/j.addma.2014.09.004

Jamshidinia, M., Kong, F., & Kovacevic, R. (2013). Numerical Modeling of Heat Distribution in the Electron Beam Melting ® of Ti-6Al-4V. Journal of Manufacturing Science and Engineering, 135(6), 061010. https://doi.org/10.1115/1.4025746

Rouquette, S., Guo, J., & Masson, P. Le. (2007). Estimation of the parameters of a Gaussian heat source by the Levenberg – Marquardt method: Application to the electron beam welding, 46, 128–138. https://doi.org/10.1016/j.ijthermalsci.2006.04.015

Shen, N., & Chou, K. (2016). MSEC2012-7253, 1–9.

THERMAL SIMULATION OF POWDER BED FUSION PROCESS USING FINITE ELEMENT METHOD

Can Bayraktar, Eralp Demir
Sabancı University Department of Manufacturing Engineering, canbayraktar@sabanciuniv.edu
Sabancı University Department of Manufacturing Engineering, edemir@sabanciuniv.edu

Abstract. Powder bed fusion process is an additive manufacturing method that is used to manufacture geometrically complex parts. Local very high temperature gradients have a negative effect on the mechanical properties of the final product due to residual stresses and geometric distortion. The temperature field is determined by using finite element method in conjunction with a moving heat source model. Developed model offers flexibility and adjustability with using user-subroutines feature of finite element software. Temperature dependency of properties such as conductivity, density and specific heat are taken into consideration as well as powder properties which is different than raw properties. Results such as temperature history and melt size are presented and discussed.

Keywords: Powder bed fusion process, finite element method, additive manufacturing, thermal modelling

1. INTRODUCTION

Additive manufacturing has received high attention of many industries and currently being implemented in high cost tolerant industries such as aerospace and medical because of its benefits over conventional manufacturing methods. (Megahed et al,2016). Laser powder bed fusion (LPBF) process is an additive manufacturing method that allows to manufacture complex geometries with a rapid design stage. LPBF uses laser as heat source to melt metal powder particles and make them solidify by cooling to manufacture layer by layer. After solidification of each layer, a new powder material is placed. Although process has great advantages, it has downsides in terms of the residual stress formation during deposition and distortions of the end product caused by high thermal gradients on process. These have a negative effect on the mechanical performance of the end product. In this manner effect of process parameters; laser speed, laser power, scan strategy on thermal history is significant for optimizing the parameters. Experimental ways to track temperature history during process is difficult and costly.
Zhao et al. developed a thermomechanical model for Direct Metal Laser Sintering process for titanium alloys. They used 3-D and 2-D models developed in COMSOL environment for single and multi-layer simulations respectively and TiAl6V4 as material. (Zhao et al, 2017). They compared and revealed their results as melt pool size, temperature history and residual stresses. Denlinger et. al. developed a thermoelastoplastic model for LPBF process with a mesh coursing strategy for the analysis of a relatively large part which has a volume of 91mm^3. They compared their model with in-situ measurements and achieved %5 error accuracy in their simulation. (Denlinger et. al,2017). Parry et al. studied on developing a model to compare laser scan strategies on the effect of residual stresses in the built part (Parry et al. 2016). Zhang et al. developed a 3D thermal model and focused on the effect of different heat source models on melt pool sizes. (Zhang et al. 2017)
The objective of this study is to develop a computational finite element model to track the thermal history of LPBF process and in order to better understand and model the effect of process parameters; laser speed, laser power and scan strategy. Inconel 718 is used as the material in this study.

2. MATERIALS AND METHODS

Thermal Analysis
Discretized form of energy balance is shown in Equation (1)

$$[\boldsymbol{C}]\{\dot{\boldsymbol{T}}\} + ([\boldsymbol{K}] + [\boldsymbol{H}])\{T\} = \{\boldsymbol{r_q}\} + \{\boldsymbol{r_s}\} + \{\boldsymbol{r_h}\} \quad (1)$$

Internal energy storage is defined with [**C**] matrix as shown in Equation (2). {**N**} is the shape functions.

$$[\boldsymbol{C}] = \iiint \rho c\{N\}^T\{N\}dV \quad (2)$$

Conductivity stiffness term is [**K**] matrix defined by gradient operator [**B**] in Equation (3)

$$[\boldsymbol{K}] = \iiint [B]^T k[B]dV \quad (3)$$

Convection stiffness term is [**H**] as shown in Equation (4)

$$[\boldsymbol{H}] = \iint \int \{N\}^T h\{N\}dS \quad (4)$$

Equations 5,6,7 shows volumetric heat input, surface heat flux and heat loss by convection respectively.

$$\{\boldsymbol{r_q}\} = \iiint \{N\}^T \dot{Q}dV \quad (5)$$

$$\{\boldsymbol{r_s}\} = \iint \{N\}^T q_s dS \quad (6)$$

$$\{\boldsymbol{r_h}\} = \iint \{N\}^T h T_{amb} dS \quad (7)$$

Powder Properties

Powder material properties differ from bulk properties. For the temperature dependent properties such as conductivity, emissivity and density equations below are used. Conductivity of powder is shown as k_p, φ is the porosity of powder, k_f is conductivity of gas, k_s is conductivity of solid and k_r is the radiation between powder spheres. Density of powder, ρ_p is related with density of solid, ρ_s similarly in Equation (9). (Denlinger et al. 2017) (Sih et al. 2014)

$$k_p = k_f[\left(1-\sqrt{1-\emptyset}\right)\left(1+\emptyset\frac{k_r}{k_f}\right)+\sqrt{1-\emptyset}\left(\frac{2}{1-k_f/k_s}\left(\frac{2}{1-\frac{k_f}{k_s}}ln\frac{k_s}{k_f}-1\right)+\frac{k_r}{k_f}\right)] \quad (8)$$

$$\rho_p = \rho_s(1-\varphi) \quad (9)$$

Emissivity of powder ε_p, is related with solid emissivity ε_s by using A_H, porous are fraction of powder and ε_H, emissivity of powder surface vacancies as shown in Equations (10), (11) and (12) (Denlinger et. Al 2017).

$$\varepsilon_p = A_H\varepsilon_H + (1-A_H)\varepsilon_s \quad (10)$$

$$A_H = \frac{0.908\varphi^2}{1.908\varphi^2-2\varphi+1} \quad (11)$$

$$\varepsilon_H = \frac{\varepsilon_s[2+3.082(\frac{1-\varphi}{\emptyset})^2]}{\varepsilon_s\left[1+3.082\left(\frac{1-\varphi}{\varphi}\right)^2\right]+1} \quad (12)$$

Tracking phase change is important to assign corresponding material properties. A state variable algorithm is used to decide the material phase. All elements initialized as powder and if temperature exceeds melting temperature material phase becomes liquid first and as it cools down solidifies.

$$f = \begin{cases} -1\ (powder) \\ 0\ (liquid) \\ 1(\ solid) \end{cases} \quad (13)$$

Heat Source Model

As most of the additive manufacturing process simulations heat input is modelled as Goldak double-ellipsoid as shown in Equation (14) r_x, ry and r_z represents laser spot size in directions x, y and z. P is the laser power and μ is the efficiency. (Karlsson and Goldak 2014).

$$q(x,y,z) = \frac{6\sqrt{3}P\mu}{r_x r_y r_z} e^{\left[\frac{3x^2}{r_x}+\frac{3y^2}{r_y}+\frac{3z^2}{r_z}\right]} \quad (14)$$

Temperature dependency of properties such as conductivity, specific heat and density are considered. A commercial FE software MSC Marc® is selected and user-subroutines are used. The input data for the manufacturing process parameters, finite element model, and heat source path are generated in MATLAB® environment. Simulation algorithm is shown in figure 1. Eight subroutines are used in Fortran® for the model and their purposes are explained below:

- UBGINC: is used to set up the initial values of common variables, to do initialization at the beginning of constants.
- UTIMESTEP: is used to set time step at each increment
- UFILM: is used to define thermal convection coefficient over the free surfaces (at each increment)
- UACTIVE: is used to active/deactive the deposited elements during analysis (at each int. pt. at each increment)
- INTCRDS: is used to locate integration point coordinates (once at the beginning)
- USPCHT: is used to calculate temperature dependent specific heat (at each int pt. at each increment)
- ANKOND: is used to calculate temperature dependent conductivity (at each int. pt. at each increment)
- FLUX: is used to define volumetric heat flux (at each int. pt. at each increment)

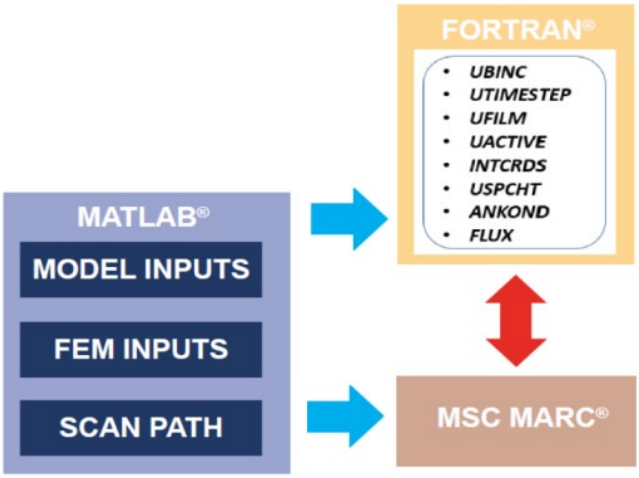

Figure 1. Thermal process simulation model algorithm.

3. RESULTS AND DISCUSSION

A preliminary study is done on a 1 mm x 1 mm geometry for one layer with a powder thickness of 50 µm. Powder is on a 1.5 mm x 1.5 mm x 0.1 mm base plate that has a fixed temperature of 298 K. Size of the geometry purposely selected very small to reduce computational time at the development stage. Element size is 50 µm cube in the built part. There is 3600 elements and 4556 nodes in the mesh. The time step is 0.05 milliseconds. Figure 2 below shows the temperature field at t=0.0055 seconds. The maximum limit of the plot is set to 1610 K to show melt pool clearly. Comparison is made for two laser power which is 200 W and 80 W as shown in figure 2. Melt pool is around 0.2 mm in length and 0.15 mm along width direction and 0.15 mm in length and 0.1mm along width direction at that particular time increment for 200 W and 80 W laser power respectively. As it is expected 200 W laser source creates approximately %50 larger melt pool area. The size of the melt pools are in agreement with literature findings that use similar process parameters. (Zhao et al, 2017) (Parry et al, 2016). In figure 3, deposited elements is shown at the end of simulation.

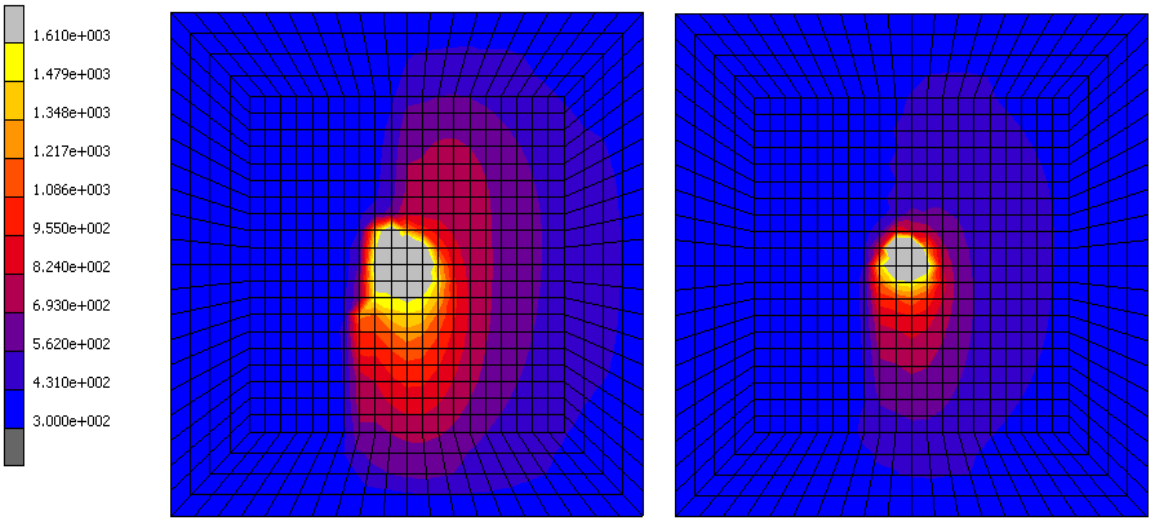

(a) (b)

Figure 2. Comparison of melt pool size of 200W(a) and 80W(b) heat source

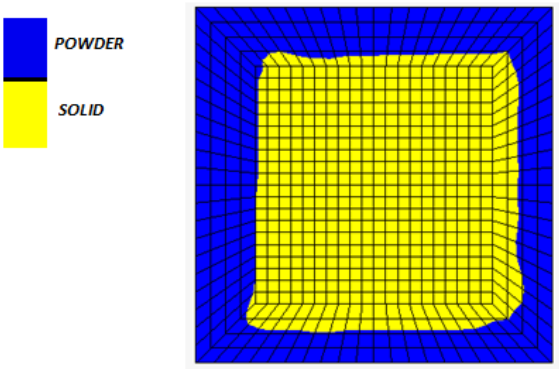

Figure 3. Deposited part at the end of simulation

4. CONCLUSIONS

A thermal computational model for LPBF process is developed to predict thermal history of the built part. Transient temperature field and melt pool size during process is in agreement with the literature findings. In the next stage of this preliminary work, the output of this study will be used for predicting residual stresses and distortions of final part.

REFERENCES

Chiumenti, M., Neiva, E., Salsi, E., Cervera, M., Badia, S., Moya, J.,Davies, C. (2017). Numerical modelling and experimental validation in Selective Laser Melting. Additive Manufacturing, 18, 171–185. https://doi.org/10.1016/j.addma.2017.09.002

Denlinger, E. R., Gouge, M., Irwin, J., & Michaleris, P. (2017). Thermomechanical model development and in situ experimental validation of the Laser Powder-Bed Fusion process. Additive Manufacturing, 16, 73–80. https://doi.org/10.1016/j.addma.2017.05.001

Hussein, Ahmed, Hao, Liang, Yan, Chunze, and Everson, Richard (2013). Finite element simulation of the temperature and stress fields in single layers built without-support in selective laser melting, Materials Design, volume 52, pp. 638–647, 2013

Karlsson, L. and Goldak, J., 2014. Computational Welding Mechanics. In Encyclopedia of Thermal Stresses (pp. 630-637). Springer Netherlands.

M. Megahed, H.-W. Mindt, N. N'Dri, H. Duan, O. Desmaison (2016). Metal additive manufacturingprocess and residual stress modeling. Integrating Mater. Manuf. Innov. 5 1–33. doi:10.1186/s40192-016-0047-2.

Mills, K. C., 2002, Recommended Values of Thermophysical Properties for Selected CommercialAlloys, Woodhead Publishing, Cambridge, UK, pp.211–216.

Parry, L., Ashcroft, I. A. and Wildman, R. D. (2016). Understanding the effect of laser scan strategy on residual stress in selective laser melting through thermo-mechanical simulation, Additive Manufacturing, 12, pp. 1–15. doi: 10.1016/j.addma.2016.05.014

S.S. Sih, J.W. Barlow, The prediction of the emissivity and thermal conductivity of powder beds, Particul. Sci. Technol. 22 (4) (2004) 427–440.

Zhang, Z. Yuze Huang, Adhitan Rani Kasinathan, Shahriar Imani Shahabad, Usman Ali,Yahya Mahmoodkhani, Ehsan Toyserkani (2019). 3-Dimensional heat transfer modeling for laser powder-bed fusion additive manufacturing with volumetric heat sources based on varied thermal conductivity and absorptivity, Optics and Laser Technology, 109, pp. 297–312. doi: 10.1016/j.optlastec.2018.08.012.

Zhao, Xinran & Iyer, Akshay & Promoppatum, Patcharapit & Yao, Shi-Chune. (2017). Numerical modeling of the thermal behavior and residual stress in the direct metal laser sintering process of titanium alloy products, Additive Manufacturing, 14, pp. 126–136. doi: 10.1016/j.addma.2016.10.005.

THE MICROSTRUCTURE AND MECHANICAL PROPERTIES OF POROUS STRUCTURES PRODUCED FROM AlSi10Mg BY DIRECT METAL LASER SINTERING

Mustafa Enes Bulduk[1,2], A. Tamer Ertürk[1], Mert Coşkun[2], Gürkan Tarakçı[2], Uğur Ergin[1]
[1]*Kocaeli University*
[2]*Fatıh Sultan Mehmet Vakif University*
mebulduk@fsm.edu.tr, tamer.erturk@kocaeli.edu.tr, mcoskun@fsm.edu.tr, gtarakci@fsm.edu.tr, ugure42@gmail.com

Abstract. Porous structures from aluminum alloys have used in several prominent applications such as bulletproof clothing, fuel cells, automotive, aerospace and heat exchanger products. The low cost and short production time make Direct Metal Laser Sintering (DMLS) as a natural choice over the existing traditional techniques in a production of customized parts. In this study, the mechanical durability of the porous structures made up of AlSi10Mg alloys produced by DMLS evaluated. SpaceClaim program was used to design the computer-aided design (CAD). The different models with porous profiles fabricated at different scan spacings, and their weights before and after the productions were measured. Besides, using weight reduction ratios, the models were improvised into a lattice structure by SpaceClaim. Microhardness and compressive strength of the porous structures were compared.

Keywords: Metal additive manufacturing, Direct metal laser sintering, Aluminium alloy, Lattice support structures

1. INTRODUCTION

Historically, the idea of producing cellular structures has been developed through porous materials such as pumice stone, coral, wood and bone found in nature (Ashby & Medalist, 1983; Gibson & Ashby, 1999). Metal cellular structures can offer high performance properties such as high strength, energy absorption properties and heat and sound insulation properties (Nakajima, 2007). It can be used in places where energy absorption is needed, such as cellular metals, bulletproof clothing, vehicle chassis, or lightening in aircraft technology, automotive technology and unmanned vehicles. Metal cellular structures usually are formed in two types. These are stochatic porous structures and regular cellular lattice structures. Metal stochastic porous structures have a random distribution of open or closed spaces, whereas periodic cellular structures consist of repetitive unit cells (Yan et al., 2015).

Today, there are many methods for producing open and closed porous foam structures. These; in general, they are formed by injecting gas bubbles into molten metals or metal powders, using space holder materials or using foaming agents and decomposing foaming agents used in these processes (Ertürk, 2013). However, the foams produced by these techniques are long and complex. It is therefore difficult to check for part defects and precision. Aluminum open cellular structures, for example, have been commercially available for several decades, but due to the limitations of conventional manufacturing methods, there are a few reports on the periodic cellular lattice structures of aluminum alloy. Duocel aluminum open cell foam belongs to the designed cellular structures. Open-celled cellular made from polymer foam is first molded and then filled with a slurry of heat-resistant material. After drying, the polymer is removed and a molten aluminum alloy is poured into the cavity. When the molding material is mechanically removed, an aluminum cellular structure remains (Körner & Singer, 2000). These manufacturing processes are complex, time-consuming and costly. Due to the long and complex nature of these processes, the prices of Duocel foams are high (Yan et al., 2015).

Additive manufacturing (AM) is the process of producing an object in layers by dividing it into specific intervals. Additive Manufacturing is able to produce complex shapes from computer aided design (CAD) models (Qiu, Adkins, & Attallah, 2013). There are several ways of layered manufacturing and model production. DMSL is a powder-bed fusion technology that does not laser-sinter the powdered metal layers in an inert atmosphere (Lengua, 2017). Produced by DMLS method, these lattice structures offer good and competitive mechanical properties and design flexibility (Crupi, Kara, Epasto, Guglielmino, & Aykul, 2017). With the DMLS method, large volume cellular lattice structures which are unit cell type diamonds

and flexible structures for light applications can be produced. The periodic lattice structures of aluminum alloy produced with DMLS increase with the compression modulus and strength with increasing volume fraction. In other words, it complies with the results calculated using Gibson-Ashby model (Yan et al., 2014). It obtains porous, cellular structure from different materials by using different layered manufacturing technology for many sectors and needs. For example, for bone implants, Peter et al. have produced macroporous cellular structures using the selective electron beam melting (EBM) method of titanium material (Heinl, Müller, Körner, Singer, & Müller, 2008). McKown et al. produced a series of 316L stainless steel lattice structures based on two types of unit cells with octahedral and column octahedral geometry by SLM process and examined the compression and burst loading behavior of these lattice structures (McKown et al., 2008). Yan et al. Have produced gyroid cage structures with circular supports and a spherical core with unit cell sizes of 2-8 mm from 316 L material with SLM technology. They have shown that SLM technology can be produced with traditional production methods that are difficult or impossible to produce (Yan, Hao, Hussein, & Raymont, 2012). Rehme et al. produced honeycomb structures with negative poisson's ratio with SLM technology. Titanium for implants and titanium alloys have produced lattice structures (Rehme & Emmelmann, 2009). Using the DMLS technology, Betrol et al. Examined the analysis of different sintering parameters and discussed the production of customized implants in titanium alloy (Ti - 6Al - 4V) with complex geometry and internal structures (Bertol, Júnior, da Silva, & Aumund-Kopp, 2010). Ameli et al. developed an aluminum / ammonia heat pipe with a sintered wick structure. Using SLM technology, they produced wick-structured aluminum heat pipes designed by repeating an octahedral unit cell (Ameli et al., 2013).
In this study, the behavior of the porosity structures with equal weight was investigated depending on the space design. In order to interpret the results correctly, the samples were produced by DMLS method. Samples were produced with EOS M290 machine by applying 2 mm hatch distance for porous sample. Later, it was produced by transforming into 2 different lattice structures with CAD SpaceClaim program. Porous structures were comparative in terms of microhardness and compression behavior. In addition, the microstructure of the samples was examined by SEM.

2. MATERIALS AND METHODS

A 20x20x40 mm rectangular prism chose for the sample geometry. In addition to standard parameters, a sample was first produced with 2 mm hatch distance in an EOS M290 DMLS machine. Moreover, a 3-dimensional lattice infill pattern type and double pyramid lattice with cross-type structures were designed in SpaceClaim program and produced with standard parameters. Microhardness of the porous and lattice structures were measured at 200 g load using Shimadzu G21D microhardness machine. Microstructures of the samples were examined by Hitachi SU3500 T2 scanning electron microscope (SEM) and Oxford XACT electron dispersion spectroscopy (EDS). ALŞA 100 kN electromechanical test device was also used to compression test of the samples.

3. RESULTS AND DISCUSSION

Scanning electron micrographs illustrating the structure of the porous structure and lattice structure are shown in Fig. 1. Figure 1a shows an SEM image of the porous structure produced at 2 mm hatch distance. Figures 1b shows the double pyramid lattice with cross-type lattice structure and Figures 1c show the 3-dimensional lattice infill pattern type lattice structure.

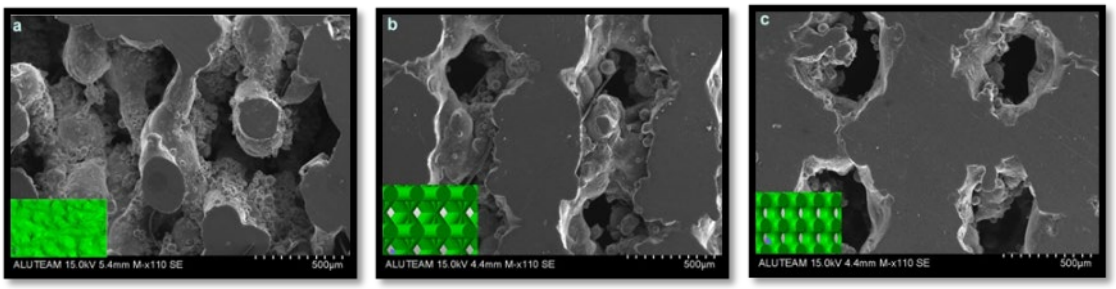

Figure 1. SEM images; a- structure manufactured by changing hatch distance parameter; b- double pyramid lattice with cross; c- 3-dimensional lattice infill pattern.

The comparison of microhardness and oxidation of the porous structure and different lattice types is given in table 1.

Table 1 Micro hardness and oxidation properties of porous structure and different lattice types

Sample Name	Average Microhardness (HV)	Average Weights (g)	Oxygen Content (%)	Al_2O_3 (%)	SiO_2 (%)
Porous structure	112.98	24.8	47.58	91.76	8.24
3-Dimensional Lattice Infill Pattern	123.5	24.9	47.51	92.96	7.04
Double Pyramid Lattice with Cross	125.83	25.4	47.56	92.06	7.94

Quasi-static compressive stress–strain curves for samples are shown in Fig. 2. In all three structures, it can be seen that under quasi-static loading, it exhibits a smooth transition from elastic to plastic zone. It can be seen that there is a regular follow-up on the curve up to the maximum tension in the elastic region. Figure 1a is the stress – strain graph of the compression test of the porous structure produced with the 2 mm hatch distance parameter. The yield strength of this sample is 45,126 MPa. Figures 1b is the stress – strain graph of the 3-dimensional lattice infill pattern type lattice compression behavior. The yield strength of this sample is 212,423 MPa. Figures 1c is a stress-strain graph of the compression test of a double pyramid lattice with cross type lattice structure. The yield strength of this sample was found to be 178,97 MPa.

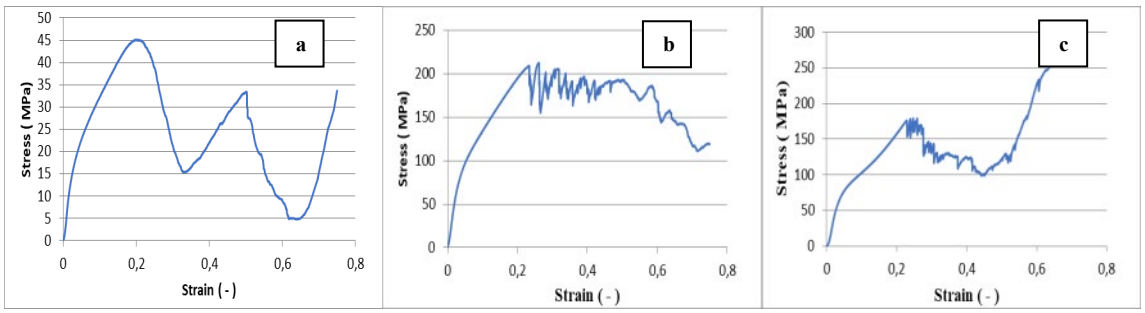

Figure 2. Compressive stress–strain curves of samples; a- structure manufactured by changing hatch distance parameter; b- 3-dimensional lattice infill pattern; c- double pyramid lattice with cross

4. CONCLUSIONS

The importance of space design was compared in three samples produced by DMLS method. As a result of microhardness tests, hardness of double pyramid lattice with cross type lattice structures were found to be better. It is seen that the oxygen content of the porous structure produced by changing the parameter is higher than the lattice structures. The yield strength was observed to be approximately 75% lower than the other samples in the sample produced with the changing hatch distance parameter. Two different lattice structures were used in the space design. Although these

structures were of the same weight, the strength behavior was different. The main reason for this change was the design of the spaces. In the continuation of our work, we aim to use different spaces in space design.

REFERENCES

Ameli, M., Agnew, B., Leung, P. S., Ng, B., Sutcliffe, C. J., Singh, J., & McGlen, R. (2013). A novel method for manufacturing sintered aluminium heat pipes (SAHP). *Applied Thermal Engineering*, *52*(2), 498–504.

Ashby, M. F., & Medalist, R. F. M. (1983). The mechanical properties of cellular solids. *Metallurgical Transactions A*, *14*(9), 1755–1769.

Bertol, L. S., Júnior, W. K., da Silva, F. P., & Aumund-Kopp, C. (2010). Medical design: direct metal laser sintering of Ti–6Al–4V. *Materials & Design*, *31*(8), 3982–3988.

Crupi, V., Kara, E., Epasto, G., Guglielmino, E., & Aykul, H. (2017). Static behavior of lattice structures produced via direct metal laser sintering technology. *Materials & Design*, *135*, 246–256.

Ertürk, A. (2013). Alüminyum köpük malzemelerin uygulamaya yönelik üretimi ve mekanik özelliklerinin incelenmesi alpay.

Gibson, L. J., & Ashby, M. F. (1999). *Cellular solids: structure and properties*. Cambridge university press.

Heinl, P., Müller, L., Körner, C., Singer, R. F., & Müller, F. A. (2008). Cellular Ti–6Al–4V structures with interconnected macro porosity for bone implants fabricated by selective electron beam melting. *Acta Biomaterialia*, *4*(5), 1536–1544.

Körner, C., & Singer, R. F. (2000). Processing of metal foams—challenges and opportunities. *Advanced Engineering Materials*, *2*(4), 159–165.

Lengua, C. A. G. (2017). History of Rapid Prototyping. In *Rapid Prototyping in Cardiac Disease* (pp. 3–7). Springer.

McKown, S., Shen, Y., Brookes, W. K., Sutcliffe, C. J., Cantwell, W. J., Langdon, G. S., … Theobald, M. D. (2008). The quasi-static and blast loading response of lattice structures. *International Journal of Impact Engineering*, *35*(8), 795–810.

Nakajima, H. (2007). Fabrication, properties and application of porous metals with directional pores. *Progress in Materials Science*, *52*(7), 1091–1173.

Qiu, C., Adkins, N. J. E., & Attallah, M. M. (2013). Microstructure and tensile properties of selectively laser-melted and of HIPed laser-melted Ti–6Al–4V. *Materials Science and Engineering: A*, *578*, 230–239.

Rehme, O., & Emmelmann, C. (2009). Selective laser melting of honeycombs with negative Poisson's ratio. *J. Laser Micro/Nanoeng*, *4*, 128–134.

Yan, C., Hao, L., Hussein, A., Bubb, S. L., Young, P., & Raymont, D. (2014). Evaluation of light-weight AlSi10Mg periodic cellular lattice structures fabricated via direct metal laser sintering. *Journal of Materials Processing Technology*, *214*(4), 856–864.

Yan, C., Hao, L., Hussein, A., & Raymont, D. (2012). International Journal of Machine Tools & Manufacture Evaluations of cellular lattice structures manufactured using selective laser melting. *International Journal of Machine Tools and Manufacture*, *62*, 32–38. https://doi.org/10.1016/j.ijmachtools.2012.06.002

Yan, C., Hao, L., Hussein, A., Young, P., Huang, J., & Zhu, W. (2015). Microstructure and mechanical properties of aluminium alloy cellular lattice structures manufactured by direct metal laser sintering. *Materials Science and Engineering: A*, *628*, 238–246.

ORIENTATION AND DYEING EFFECTS ON MECHANICAL STRENGTH OF THE MULTI JET FUSION PRINTED PARTS

Serif Gunenc[1,2], Emrecan Soylemez[2*]
[1]Tridi Co., Maslak, 34467, Sariyer, Istanbul, TURKEY, serif@tridi.co
[2]Department of Mechanical Engineering, Istanbul Technical University, Gumussuyu, Istanbul, TURKEY
esoylemez@itu.edu.tr, *Corresponding author.

Abstract. Additive manufacturing enables producing end-use functional parts with good mechanical properties. Multi Jet Fusion technology is one of the powder bed fusion processes. Printed parts usually are post-processed by the dyeing method to obtain end-use products. This paper aims to find the mechanical properties for different orientated specimens and investigates the possible effects of the dyeing method on the mechanical strength of the parts. To achieve this, ASTM D368-14 Type I specimens were prepared along three different axes and one orientation was selected to test the dyeing effects. Results of tensile testing demonstrate that dyeing the parts reduces percent elongation and tensile strength at break by an average of 6.4% and 2.12 MPa, respectively. Also, this work presents the variation of mechanical strength based on the printing orientation.

Keywords: Multi Jet Fusion, Polyamide 12, Mechanical properties, Part Orientation, Part Dyeing Effects

1. INTRODUCTION

Multi Jet Fusion technology (MJF™) is a powder bed fusion printing process where a carriage unit moves the inkjet heads over the building area. Inkjets deliver bonding agent droplets over polyamide 12 (PA12) powder layer, then infrared heating fuses the agents to increase the adhesion between the particles (HP Development Company L.P., 2014). There are two bonding agent types, the first one is called fusing agent and the other one is detailing agent. Fusing agent is jetted to a part area and helps to melt the powder, while the detailing agent is jetted around the part slice area to increase resolution and to improve the dimensional stability.
The MJF™ technology is widely used for prototyping and low volume production due to its high mechanical strength parts and smooth surface finish. Produced parts by MJF™ are believed to have isotropic mechanical strength properties contrary to the other polymer-based additive manufacturing (AM) processes (Domingo-Espin et al., 2015; Tas, 2018). In this study, we investigated three different orientation effects and dyeing effect on the mechanical strength of the parts.

2. MATERIALS AND METHODS

ASTM D638 Type I specimen was selected as a sample model. 12 pieces of the specimen were nested in the build chamber along with the other models as illustrated in Figure 1. HP Jet Fusion 3D (Model: 4200) was used to manufacture the 12 specimens. They were divided into 4 groups based on their orientation axes and whether they were post-processed. The balanced print profile selected to print the parts. Density value is 4.85% and that describes percent of total parts volume to build chamber volume for specified height. The first three groups oriented along x, y and z directions as shown in Figure 2 stand for without dyeing process. The last group represents painted parts printed in x orientation. All specimens were sandblasted right after printing to remove the unfused powder. Each specimen named with AB01 coding system (A: Orientation direction; x, y, z; B: Dyed or Undyed; Number: Same group at a different location in the build chamber).
Dyeing of plastic AM parts is analogous to coloring synthetic fabrics. The specimens were dyed with generic commercial nylon dye for 3D printed parts (Cameron & Boucher, 2014). A mixture of dye and water was heated up to 95˚C and parts were immersed for 10 to 30 minutes in a closed chamber (Cameron & Boucher, 2014).

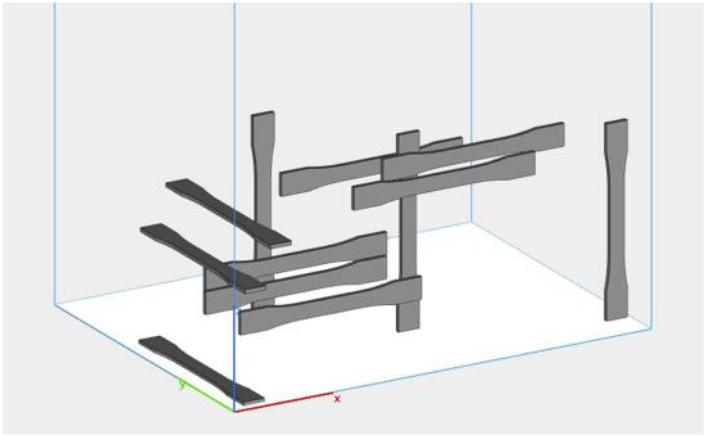

Figure 1. Part Orientation Inside the Build Chamber (Other Parts Are Hidden)

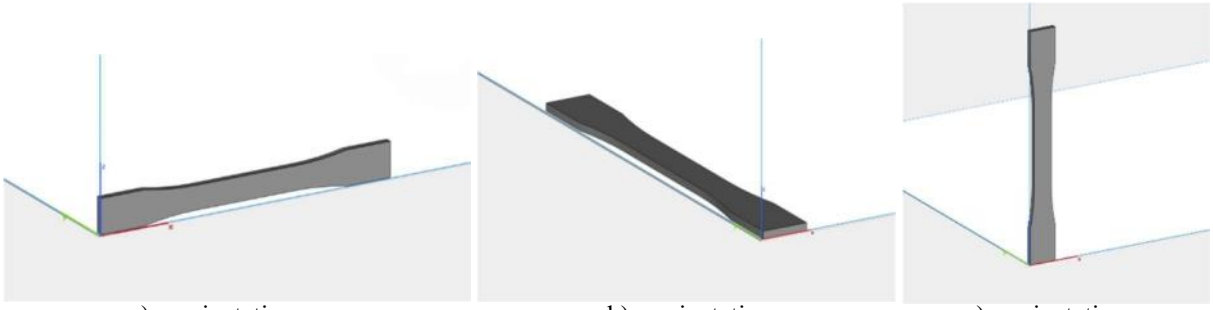

a) x orientation b) y orientation c) z orientation

Figure 2. Part Orientation Directions

Geometric dimensions of the specimens were measured from three different points in gauge area to get mean length and width values. Tensile tests were performed using Shimadzu AG-X Plus universal testing machine with a video extensometer apparatus. Speed of testing was selected 5mm/min as suggested in ASTM D638-14. The mean values of the calculation results of three specimens for each group were given in Table 1.

Table 1. Mechanical Testing Results Mean Values for Each Group

Specimen Code	Mean Value of Ultimate Tensile Strength (MPa)	Mean Value of Tensile Stress at Break (MPa)	Mean Value of Percent elongation at break (%)	Mean value of Modulus of Elasticity (MPa)
XU01, XU02, XU03	44.79 ±0.17	31.95 ±4.62	20.42 ±4.59	1466.90 ±68.0
YU01, YU02, YU03	42.35 ±0.62	29.90 ±5.24	19.98 ±1.32	1326.66 ± 4.8
ZU01, ZU02, ZU03	46.26 ±1.29	40.33 ±4.06	22.06 ±7.68	1717.35 ± 50.8
XD01, XD02, XD03	42.67 ±1.32	33.76 ±9.58	14.03 ±1.21	1486.16 ± 69.5

3. RESULTS AND DISCUSSION

All orientations have similar tensile strength results, yet anisotropic behavior is observable. z-axis believed to be weaker than other axes in other AM technologies. However, test results prove that orientation in the z-axis has the highest ultimate tensile strength with 46.26 MPa (Table 1). Besides, stress-strain curves of z-group specimens are superior to the others as represented in Figure 4. On the other hand, parts orientated in z-axis have high deviation values, especially on the percent elongation at break results. O'Connor, Dickson, & Dowling (2018) explained the higher strength in z-axis with the added weight of the layers generates dense and less porous print. Surface capillarity effect observed on the top surface of all the printed specimens (Figure 3). Polyamide powder acts like fluid when it is melted to be fused. The fused region tends to rise along its edges and sinks to the center. z-axis specimens have the maximum number of layers along z direction. All the layers apply pressure on the former one and make the part more solid. Considering y-axis specimens, parts have the minimum height compared

to the other axes and the mechanical testing results are the lowest. Layer height shows a correlation with mechanical performance by Z>X>Y due to the nature of the powder bed fusion process.

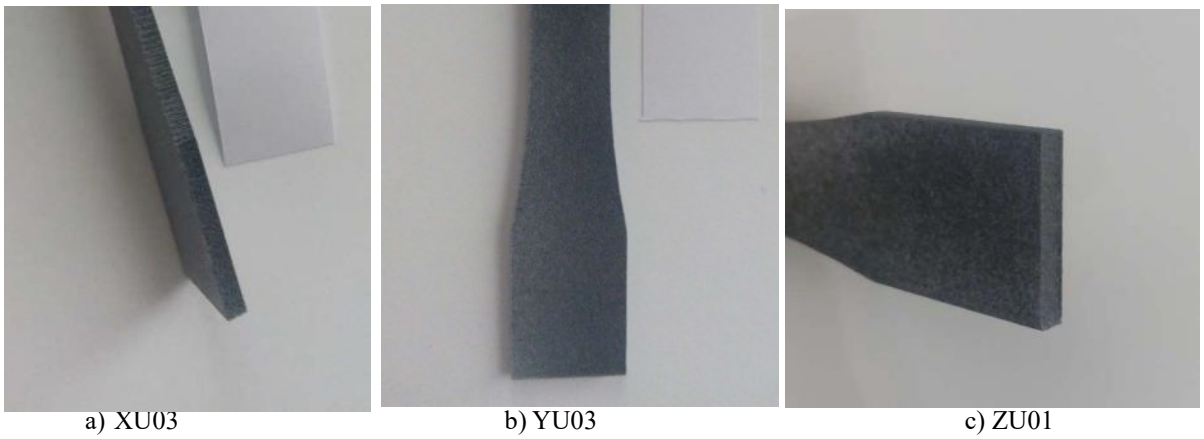

a) XU03 b) YU03 c) ZU01

Figure 3. Surface Capillarity on Specimens Top Surfaces

Mechanical test results done with produced parts with Multi Jet Fusion in other studies validate that the z-axis has the highest tensile strength trend (O'Connor et al., 2018). However, strength trend results of the other orientations that our work differentiates from other studies due to selecting different rotation in the same orientation (O'Connor et al., 2018; Sillani, Kleijnen, Vetterli, Schmid, & Wegener, 2019). O'Connor et al. (2018) selected the x specimen perpendicular to the ground, while the y specimen orientated vertical and the mechanical strength of y-axis is better in contrary to this study's results.
This paper expresses that the mechanical performance is not only related to the direction it is also correlated to layer stacking height. The mechanical properties of printed parts with MJF™ technology get better when the part gets denser because of layers mass. To obtain better mechanical properties, parts should be orientated with the highest number of layers.
The y-axis is the most stable building direction with 0.62 MPa deviation from the mean value of ultimate tensile strength and ±1.32% elongation at break. The carriage unit that carries the inkjets travels along y-axis (scan-axis). The inkjets, jet bonding agent droplets along the y-axis and fuses that area simultaneously; so, parts slice area solidifies uniformly that maintains homogeneous warm-up and cool down. Besides, the high deviation values possibly related to the part position in the build chamber (Figure 1). y-axis specimens located close to each other, while z-axis specimens dispersed in the build chamber; higher deviation values observed compared to y-axis group.
Dyeing process causes a significant decrease in percent elongation at break by an average of 6.39% and ultimate tensile strength by 2.12 MPa The dyeing mechanism can be explained as the floating dye particles inside the hot water-dye mixture fill the material pores. This mechanism causes decrease in ductility of the material. The dyeing process should be studied further in order to avoid these adverse effects.

4. CONCLUSIONS

This work reveals the tensile strength of three building directions and dyeing process. z-axis can be selected to get better ultimate tensile strength and y-axis for more stable results. The mechanical properties may vary from print job to other, engineers and designers should take that into account. Moreover, dyeing process has unfavorable effects on printed parts such as lowering the ultimate tensile strength and percent elongation values. Considering all, capabilities of Multi Jet Fusion technology meet necessities for producing end-use parts. Optimization of dyeing methods may be studied in the future work as well as the cause of the variation of mechanical properties.

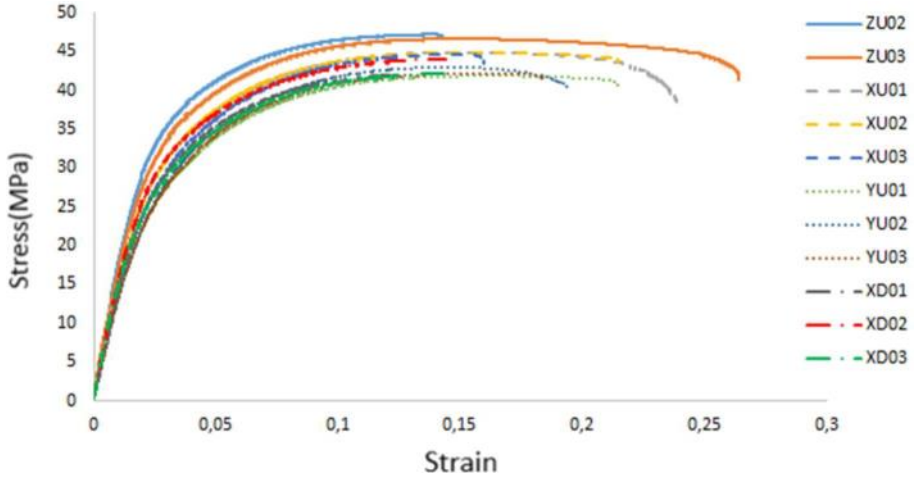

Figure 4. Tensile Stress-Strain Curves

ACKNOWLEDGMENT

Characterization part of the work was carried out at Istanbul Technical University EKAM laboratory supported by ISTKA under Grant TR10/18/YMP/0005 "Additive Manufacturing Education and Research Center".

REFERENCES

ASTM (D638-02a). (2003). American Society for Testing and Materials. Standard test method for tensile properties of plastics (D 638 - 02a) - SCAN VERSION. Astm, 08, 46–58. https://doi.org/10.1520/D0638-14.1

Cameron, D., & Boucher, A. (2014). Dyeing SLS Parts. 1–24. Retrieved from https://research.gold.ac.uk/11419/1/Dyeing SLS Parts - Interaction Research Studio.pdf

Domingo-Espin, M., Puigoriol-Forcada, J. M., Garcia-Granada, A. A., Llumà, J., Borros, S., & Reyes, G. (2015). Mechanical property characterization and simulation of fused deposition modeling Polycarbonate parts. Materials and Design, 83, 670–677. https://doi.org/10.1016/j.matdes.2015.06.074

HP Development Company L.P. (2014). HP Multi Jet Fusion technology. Technical White Paper, 8.

O'Connor, H. J., Dickson, A. N., & Dowling, D. P. (2018). Evaluation of the mechanical performance of polymer parts fabricated using a production scale multi jet fusion printing process. Additive Manufacturing, 22(April), 381–387. https://doi.org/10.1016/j.addma.2018.05.035

Sillani, F., Kleijnen, R. G., Vetterli, M., Schmid, M., & Wegener, K. (2019). Selective laser sintering and multi jet fusion: Process-induced modification of the raw materials and analyses of parts performance. Additive Manufacturing, 27(January), 32–41. https://doi.org/10.1016/j.addma.2019.02.004

Tas, A. (2018). Evaluation of SLS-made PA12 Under Uniaxial Tensile Test. Politecnico Milano.

EVALUATION OF GEOMETRICAL DEVIATIONS AND POROSITIES ON BOTH CFRP AND AISI 316L STEEL MATERIAL ON ADDITIVE MANUFACTURING

Aysu Hande YEŞİLOVA[1], Azmi TİMUR[2], Mustafa BAKKAL[3],
[1]*Department of Mechanical Engineering Istanbul Technical University, ayesilova@itu.edu.tr*
[2] *Department of Mechanical Engineering Istanbul Technical University, timura@itu.edu.tr*
[3] *Department of Mechanical Engineering Istanbul Technical University, bakkalmu@itu.edu.tr*

Abstract. Although additive manufacturing method has many advantages, the final product can face with problems like dimensional deviations, poor surface finish, porosity, distortion, anisotropy, composition differences and residual stress, which occurs during rapid heating and cooling cycles. In this study, 3D basic geometries (hollow cylinders, hemi-spheres, triangle prisms etc.) are designed for evaluation of different features of primitives. Then designed primitives manufactured with different parameters via FDM (Fused Deposition Modelling) and DMLS (Direct Metal Laser Sintering) methods with CFRP and 316L materials respectively. After manufacturing step, geometrical deviations on CFRP and 316L primitives determined with CMM measurements and surface roughness for 316L. Then, the porosity percentages of 316L material determined via XRD, basic level of micro-CT and Archimedes' method.

Keywords: *Additive Manufacturing, DMLS, FDM, micro-CT Scan, CMM, XRD Analysis*

1. INTRODUCTION

Additive manufacturing as an accepted technology of the future is a kind of manufacturing method that creates a product layer by layer from 3D model. Since additive manufacturing has become a mass production method, the importance of the method increases in recent years. In this technology, dimensional deviations, surface roughness, porosity are important parameters for physical and mechanical properties of the built specimens.

CT scan method is used to investigated particle size and morphology, porosity, dimensional accuracy, roughness of surface, mechanical and physical properties [1-4]. Richard and Thompson (2019) studied on CT number also known as the Hounsfield Unit in order to investigate physically properties of AM materials in different geometries. They analysed resultant images. Density of each sample was calculated and CT images of the specimens were inspected any porosity and sectional variation [1]. Villarraga-Gómez at all.(2015) compared printed parts with their CAD data dimensionally [2]. Hassen et all. (2016) also says that micro-CT can be used in quality control. In order to detect porosity and dimensional deviations, micro-CT is a common method for additive manufacturing [3].

CMM (Coordinate Measuring Machine) works on X, Y, Z coordinate axes and dimensions are compared with these coordinates. Thus, geometrical deviations of the built geometries is established [5-8]. Yakout, et all. (2018) investigated to characteristics of stainless steel 316L parts manufactured with SLS in terms of geometrical deviations, surface microstructure and residual stress [5]. Nahata et all. (2019) was used CMM for quantitative assessment of surgical instruments for hip and knee implants produced by SLS [6].

Porosity have an important role on mechanical and physical properties of the materials. Gu and Shen (2008) studied on porous metals [8].

This study aims to find the role of these parameters out for metal and polymeric materials.

2. MATERIALS AND METHODS

In this study, the specimens which are 316L stainless steel and carbon based fiber were manufactured with DMLS method (Figure 1). The simple geometric features in 1.5-2 mm thickness were produced with these manufacturing methods and they were characterized physically, mechanically.

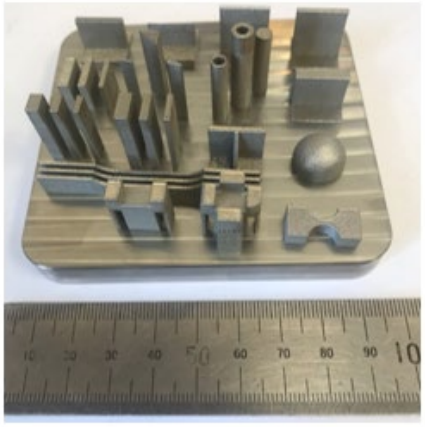

Figure 12: 316L SS geometries.

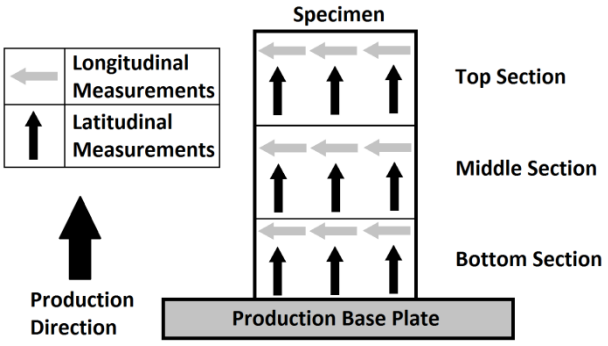

Figure 13: Schematic representation of surface roughness measurement.

In powder-bed based direct laser melting process, the 316L stainless steel powder that has 45±10 µm powder size distribution was used with a chemical composition complying to CL 20ES which is an austenitic stainless steel for the production of functional parts for pre-production moulds. Also, CL 20ES can be used for the parts which are sensitive to warpage and it has dense and homogeneous structure after manufactured with DMLS additive manufacturing method [9].

The 316L SS specimens were produced with Concept LASER Mlab cusing R machine. The specimens were produced with 25-µm layer height using YAG fiber laser that has maximum laser power 100 W and laser spot size of 50 microns. The printing parameters of two distinct plates for 316L SS are shown in Table 1. Although layer height is same for each, printing speed values are not similar.

Table 4: Printing parameters for 316L stainless steel specimens.

	Power (W)	***Speed (mm/s)***	
		#1	**#2**
Lattice Supports	60	300	1500
Surface Area	90	750	3000
Inner Contour	60	300	1500
Outer Contour	60	300	1500

In this study, 3D basic geometries are created for 316L SS materials in different height, thickness, angle, radius, wall thickness and manufactured by means of DMLS method.

2.1 Geometrical Deviations

First, in order to evaluate the dimensional accuracy of the specimens, 3D optical scanning (Solution X 500 C) in ± 0.007 microns tolerances was used for physically characterization after manufacturing. The angular, linear and radial dimensions, parallelism and perpendicularity of the each 316L SS specimens that are on distinct tables were analyzed separately.

The surface roughness of the SS 316L that printed according to #1 parameters was measured using Mitutoyo SJ 201P. The measurements were done for both side of the specimens three times for each section that bottom, middle, top and each directions to prevent the previous measurement effects on the surface. The roughness measurements were done in XZ and YZ planes latitudinal and longitudinally in order to evaluate the effects of orientation of the layer (Figure 2).

2.2 Microstructural Deviations

For printed specimens, densification is one of the most important parameters for industrial applications. To determine porosity percentage, three different techniques that are micro-CT scan, XRD analysis and Archimedes' method were preferred.

The 316L SS specimen (Figure 3) was scanned with both CT scan and micro-CT in order to evaluate porosity percentage. Firstly, SS 316L printed specimens were scanned with SkyScan 1147v2 scanner with step and shoot detector motion type with the parameters as given in Table 2.

Table 5: The scanning parameters of CT scan.

Parameters	*Scanning 1*	*Scanning 2*
Source Voltage (kV)	50	50
Source Current (µA)	800	800
Exposure (ms)	2000	2000
Rotation Step (deg)	1.000	1.500

Secondly, another scanning was also done with SkyScan 1172-marked micro-CT. Number of layers 567, which is equals to 0.3787 % object volume, was scanned with 25.9 µm pixel size. The scanning parameters are shown in Table 3. After the micro-CT scanning, porosity percentages and total volume of pores that belong to closed and open pores were obtained separately.

Table 6: *The scanning parameters of micro-CT scan*

Pixel size	*0.0259 x 0.0259 x 0.0259 mm^3/voxel*
Total grid size	999 x 999 x 567 pixels
Object volume	31.381mm^3
Total volume of interest (VOI)volume	9871.745 mm^3

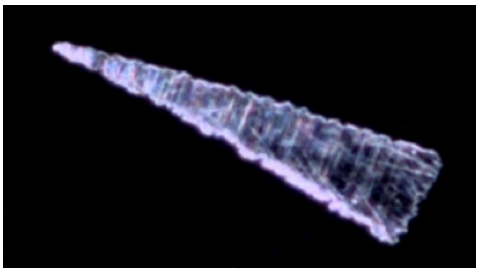

Figure 14: Scanned 316L SS specimen.

In XRD analysis method, firstly, cell volume and its mass were determined with Rigaku SmartLab X-Ray diffractometer. Next, XRD density was calculated with molecular weight (M_w), Avogadro's number (N_A), lattice constant (a) and number of the lattice points (n) of the each unit cell (Eqn. 1.a). Then, the porosity was obtained from the following equation (Eqn. 1.b) with bulk density (ρ_b)

$$\rho(x) = \frac{M_W.n}{N_A.a^3} \quad (1.a)$$

$$porosity = 1 - \frac{\rho_b}{\rho(x)} x100 \quad (1.b)$$

In Archimedes density measurement technique, porosity percentage depends on density measurement. The three specimens were weighed on a scale to find their mass. One of them is mentioned below #3 was grinded for a while to eliminate surface roughness. Then, the apparent density of the specimens were calculated from a theoretical density of 7.985 g/cm^3 to evaluate porosity percentage.

3. RESULTS AND DISCUSSION

3.1 Geometrical Deviations

In order to evaluate dimensional accuracy, as-built 316L SS geometries were scanned with 3D optical scanning.

In Figure 5, 316L specimens on the tables are given with colour scale in the specified tolerances. The geometries on two distinct tables were built in different parameters #1 (a) and #2 (b).

316L(a), 15, 30, 60 and 90-degree angles are not in angular tolerance ±0.1. Deviation is nearly 0.5 for them. In contrast, 45-degree angle is in the tolerance. The cylindiric and circular deviation is around 0.05 for hollow geometries. Hemi-sphere and other radial geometries are not in 0.05 tolerance for 316L(a). The radial deviation is not uniform for any radii.

Similarly, 316L(b) was evaluated in ±0.1 angular tolerance. However, triangular prisms are not in the range. Angular deviation is ranging from -0.5 to 2. The some triangular prisms had same degrees have not similar deviation values. Though circular deviation of the hollow cylinders are in tolerance ±0.05, cylindrical deviation is around 0.6 with 0.01 standard deviations. Radial deviations are not even in ±0.1 tolerances. Hemi-sphere has -0.3 deviation.

All in all, the angular deviation is bigger for 316L(a) when the triangular prisms examine individually.

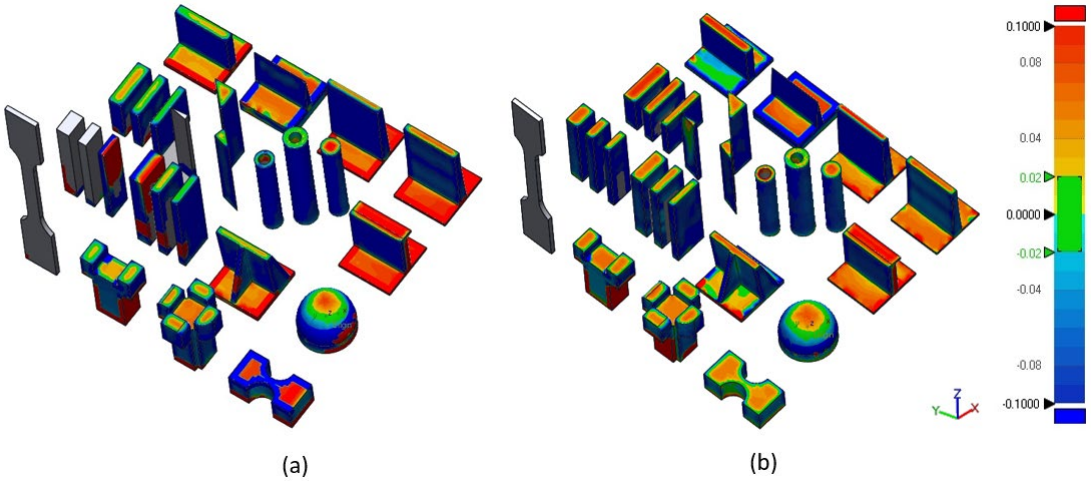

Figure 15:316L SS specimens built in different parameters #1 (a) and #2 (b).

Although circular deviation of the hollow cylinders for both parameters are in tolerance values, cylindrical deviation is shown higher for #2.

Surface roughness of the stainless steel built in parameter #1 was measured latitudinal (red) and longitudinal (blue) to realize importance of orientation of the layer. For the both orientations, many measurements were taken section by section, bottom, mid and top and average values are given in graph (Figure 6). There is an increase from bottom to top for each orientations.

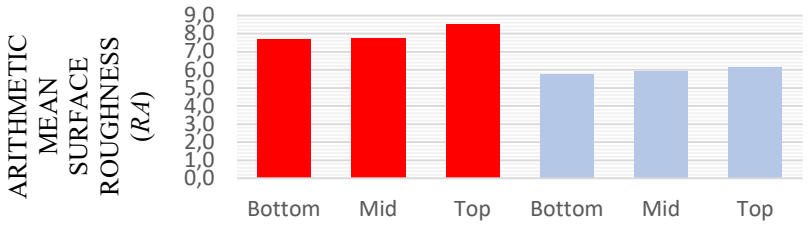

Figure 16: Surface roughness of the specimens in latitudinal (red) and longitudinal (blue) orientations.

After the micro-CT Scan, a non-uniformity was seen around the specimen tooth like shaped as shown in Figure 7. The tooth-shape may result from laser touch.

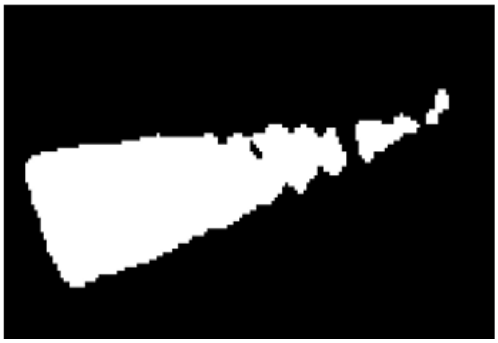

Figure 17: Image of 316L SS specimen after micro-CT scan.

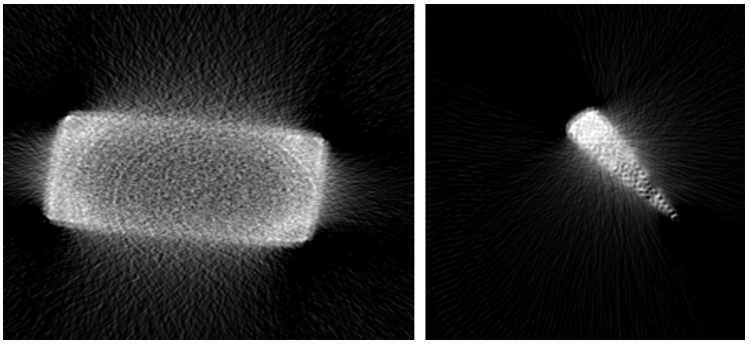

Figure 18: Scattering images of 316L SS after CT scan.

3.2 Porosity

In order to determine porosity percentage in 316L SS specimens, three different techniques were preferred that are XRD analysis, micro-CT scan and Archimedes' method.

In XRD method, XRD density (ρ(x)) was evaluated according to Equation 1.a. and then, porosity percentage was determined according to Equation 1.b. Molecular weight (M_w), Avogadro's number (N_A), lattice constant (a), number of lattice points of each unit cell (n), ρ(x) and ρ_b values are given in Table 4.

Table 7: The parameters for calculation porosity percentage with XRD analysis.

Molecular weight (M_w)	*56.2075*	*$\rho(x) = 8.068x10^6$*
Avogadro's number (N_A)	$6.02214199x10^{23}$	
lattice constant (a)	0.3596	
number of lattice points of each unit cell (n)	4	
ρ_b	7.985 g/cm^3	Porosity (%) = 0.099 %

The determined porosity percentages of the three specimens with Archimedes' method is given in Table 5. In order to specify porosity percentage, CT scan was preferred. However, there is no result about porosity because the applied low voltage that was 50 kV is not appropriate to obtain some interpretable results. Scattering exists because of the scanned material as seen Figure 8.

On the other hand, when the voltage and current reach 95 kV and 104 mA, porosity percentage was obtain after micro-CT scan of interested volume. The volume of interest was 9871.74 mm^3 for scanned specimen. The result of the micro-CT scan shows that roughly 0.099% porosity exists in interested section.

In micro-CT Scan method, number of closed pores, volume of closed pores, surface of closed pores and closed porosity percentage, volume of open pore space and open porosity percentage, total volume of pore space and total porosity percentage were evaluated (Table 6).

Table 8: Calculated porosity percentages for the three specimens with Archimedes' method.

	#1	***#2***	***#3***
Archimedes	0.206 %	0.234 %	0.175 %

Table 9: The porosity values of closed, open and total porosity.

number of closed pores	393
volume of closed pores	0.05128765 mm^3
surface of closed pores	5.46954107 mm^2
closed porosity	0.13701303 %
volume of open pore	9834.31615956
open porosity	0.37919 %
total volume of pore	9834.36744721
total porosity	0.37867

4. CONCLUSIONS

In this experiment, the specimens which are 316L stainless steel were manufactured with DMLS and FDM methods, respectively. The simple geometric models in 1.5-2 mm thickness were produced with these manufacturing methods and they were characterized in terms of physical, mechanical and microstructural. Dimensional accuracy, surface roughness, porosity percentage, mechanical properties and microstructure were studied.

Dimensional accuracy was evaluated with CMM for 316L SS specimens. The angular deviation of 316L(a) is bigger than 316L(b) when the prisms analysed individually. Circular deviation of the hollow

cylinders for both parameters are in specified tolerance values. However, cylindrical deviation is bigger for 316L(b).

In order to examine importance of orientation of the layer for surface roughness, the 316L specimens printed with the given parameter #1 were tested in both latitudinal and longitudinal directions section by section. There is an increase from bottom to top for each orientations.

According to literature, under 1% porosity is acceptable for DSLM method. The results of the preferred three methods, porosity percentage of the 316L SS is same with the literature [10].

5. REFERENCES

[1] Slotwinski, J. A., Garboczi, E. J., Stutzman, P. E., Ferraris, C. F., Watson, S. S., & Peltz, M. A. (2014). Characterization of Metal Powders Used for Additive Manufacturing. Journal of Research of the National Institute of Standards and Technology, 119(September), 460. https://doi.org/10.6028/jres.119.018

[2] Richard, J., & Thompson, D. (2019). Computed tomography characterisation of additive manufacturing materials.

[3] Villarraga-Gómez, H., Lee, C., Corbett, T., Tarbutton, J. A., & Smith, S. T. (2015). Assessing additive manufacturing processes with X-ray CT metrology. Proceedings - Aspe 2015 Spring Topical Meeting: Achieving Precision Tolerances in Additive Manufacturing, (April 2016), 116–121.

[4] Hassen, A. A., & Kirka, M. M. (2016). Additive Manufacturing : The Rise of a Technology and The Need for Quality Control and Inspection Techniques 2 . Forms of Additive Manufacturing Technology 2 . 1 Metal Additive Manufacturing.

[5] Cmm, C. İ. H., Zasyonu, M. İ., Brasyonu, K. A. L. İ., Kasyonu, V. E. R. İ. F. İ., Ve, D., & Zdek, Ü. İ. (2013). Koordinat ölçüm metrolojisi, üç boyutlu ölçüm cihazi (cmm) modernizasyonu, kalibrasyonu, verifikasyonu, dünyada ve ülkemizdeki durum. (Cmm), 26–28.

[6] Nahata, S., & Ozdoganlar O. B. (2019). Feasibility of Metal Additive Manufacturing for Fabricating Custom Surgical Instrumentation for Hip and Knee, Trade-off between used capacity and operational efficiency. Procedia Manufacturing, 34(July), 772–779. https://doi.org/10.1016/j.promfg.2019.06.207.

[7] Yakout, M., Elbestawi, M. A., & Veldhuis, S. C. (2018). On the characterization of stainless steel 316L parts produced by selective laser melting. (October). https://doi.org/10.1007/s00170-017-1303-0.

[8] Gu, D., & Shen, Y. (2008). Applied Surface Science Processing conditions and microstructural features of porous 316L stainless steel components by DMLS. 255, 1880–1887. https://doi.org/10.1016/j.apsusc.2008.06.118.

[9] Handbook of CL ES20.

[10] Marbury, F. (2017). Characterization of SLM Printed 316L Stainless Steel and Investigation of Micro Lattice.

.

UTILIZATION OF INDUSTRIAL ADDITIVE MANUFACTURING CHALLENGES AND SOLUTIONS

Aydın Yağmur[1]
[1]*EOS GmbH Electro Optical Systems, aydin.yagmur@eos.info*

Abstract. Having started as a rapid prototyping method, Additive Manufacturing (AM) is gaining continuously share in manufacturing of industrial products. Laser powder bed fusion method is one of the most used types of AM due to not only reliable and repeatable process conditions, but also wide range of applicable materials. Beside adding value to the final product, the driving forces of the application development with AM are the new design opportunities, which are not possible with conventional manufacturing methods, the flexibility-enabled customization potential, and functional integration. In this study we will show a structured methodology of implementing AM in to industrial serial production and demonstrate intelligent solutions of challenges during the different phases of implementation.

Keywords: Additive Manufacturing, Industrial production, Design optimization, Customization, Application Development

1. INTRODUCTION

Changing the conventional manufacturing process and implementing AM in to the organization is at the very beginning a long term project, which has not only opportunities, but also challenges for organizations. Changing the mindset, which has been formed during many years of education and work experience, is the first and most important part of this new situation. The new definition of limitations with introduction of AM, is much more promising for the design space of in the designer`s mind. For instance integrating several parts in to one which is topologically optimized with weight reduction does not happen in daily business. This study aims to enlarge the view of the audience to be capable of focusing the improvement potentials and motivate to start to imagine in a new way.

2. MATERIALS AND METHODS

The implementation of AM in to the production is divided in to 5 steps by EOS (See *Figure 1*.) The first step is to detect the parts that have potential improvements such as weight reduction via topology optimization. After that the part should be improved and optimized to add value and increase business-potential and the production with AM can start. The next step is the assure quality of the products which is essential for every industrial sector. The final step is establishing a digital factory in which smart machine communicate with each other and perform every single step of production.

Figure 1. 5 Step approach of Industrial AM [Source: EOS]

3. RESULTS AND DISCUSSION

Weight reduction and functional integration of a satellite antenna was performed by RUAG. They have developed a design which is a balance of strength and weight, which was enabled by additive manufacturing. The completion of certification of the part to be used in space missions show the reliability and integrity of parts fabricated by AM. This study will consist of such case studies.

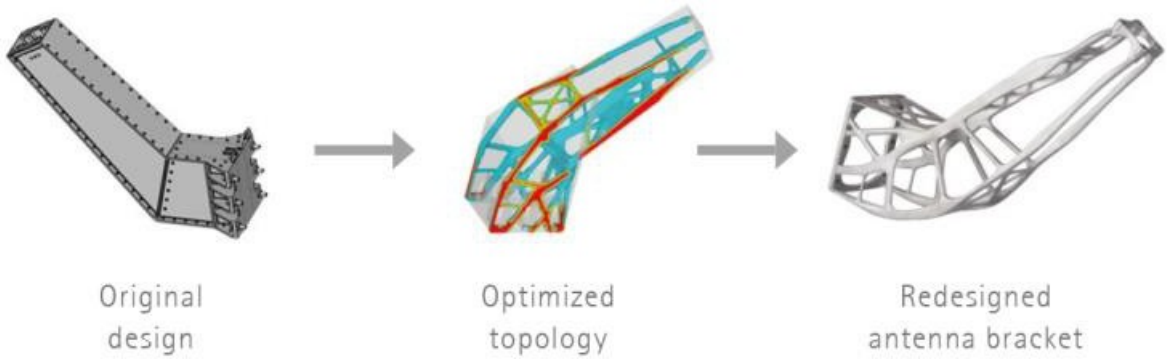

Figure 2. The improvement of design with functional integration and topology optimization (source: RUAG, Altair, EOS GmbH)

4. CONCLUSIONS

AM manufacturing is a reliable manufacturing method which enables the industry to add-value to parts via design and function optimization. Although there is no plug-and-play type solution, the implementation of AM with extended design freedom and secure structural integrity promise enables remarkable improvement in terms of cost and performance of the industrial products.

DE-ICING USING ADDITIVELY MANUFACTURED HEATING ELEMENT

Shaheryar Atta Khan, Ismail Lazoglu
[1] *Manufacturing and Automation Research Center, Mechanical Engineering Department, Koc University, Rumelifeneri Yolu, Sariyer, Istanbul, 34450, Turkey, skhan17@ku.edu.tr*

Abstract. The undesired accumulation of ice on aircraft wings, wind turbines, and evaporators results in aerodynamic and thermodynamic inefficiencies. This paper demonstrates the efficacy of heating elements additively manufactured from electrically conductive polymer composites. Virtuous to the flexibility and customizability offered by additive manufacturing, heating elements of application-specific customized geometries can be manufactured and implemented for deicing. An additively manufactured heating element with a mesh grid geometry was deposited on a carbon fiber-reinforced polymer (CFRP) composite sheet using the Direct Ink Writing (DIW) technique. Deposition of ice was simulated on the CFRP sheet and the heating performance was recorded. The performance of the additively manufactured heating element shows their potential in de-icing applications.

Keywords: Direct Ink Writing, Polymer Matrix Composite, Electrical Conductivity, De-icing

1. INTRODUCTION

The accumulation of ice on the aircraft wings, the blades of turbines, and the evaporators in refrigeration systems cause aerodynamic and thermodynamic inefficiencies which may lead to catastrophes (Bernabo, Cuccoli, & Baldini, 2015). Various de-icing techniques have been employed for de-icing such as heating elements, mechanical actuators and chemical de-icing (National Academies of Sciences, Engineering, and Medicine; Transportation Research Board; Airport Cooperative Research Program, 2010). Virtuous to the flexibility and customizability offered by additive manufacturing, heating elements of application-specific customized geometries can be manufactured and implemented for deicing.

Direct Ink Writing (DIW), which is variant of the material extrusion additive manufacturing, eliminates the need for a pre-formed filament by depositing viscous pastes called “inks”. DIW uses a pneumatic or motorized dispenser and a fine nozzle mounted on a manipulator to deposit inks. The inks have high viscosities and controlled shear thinning properties which makes it easier for the ink to flow through the nozzle. The ink regains its viscosity after it is deposited from the nozzle. The deposited ink is solidified either by the evaporation of solvents or by a curing reaction. Inks with functional properties (such as electrical, mechanical, chemical, and biological) can be deposited using this technique (Rueschhoff, Costakis, Michie, Youngblood, & Trice, 2016).

In this paper, we report the additive manufacturing of heating elements by DIW of electrically conductive polymer matrix composites. Furthermore, the performance of the heating elements for de-icing is also presented.

2. MATERIALS AND METHODS

A pneumatic DIW head mounted on a Mitsubishi Electric Melfa RV-2F robotic manipulator, as shown in Figure 1(a), was employed for additive manufacturing. Electrically functionalized polymer matrix composite with the electrical conductivity of 128 $S.m^{-1}$ was deposited by the DIW head to produce a heating element with a mesh grid geometry on a carbon fiber reinforced polymer sheet. The manufactured heating element is illustrated in Figure 1(b). To simulate icing, a block of ice was placed on the CFRP sheet and the heated was turned on. The temperature of the ice-CFRP interface was recorded by an NTC100k thermistor. The schematic of the de-icing experiment is illustrated in Figure 1(c).

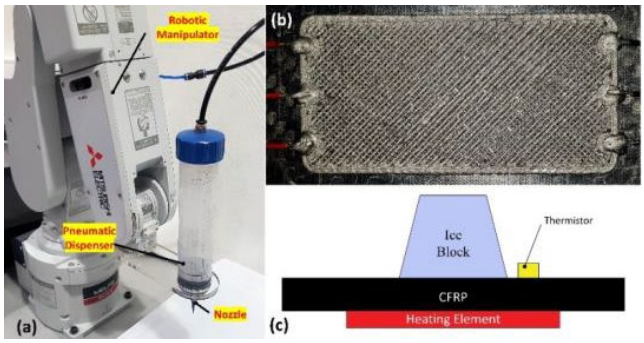

Figure 19. (a) Direct ink writing (DIW) head on a Mitsubishi Electric Melfa RV-2F robotic manipulator (b) Additively manufactured heating element (90 x 40 x 2 mm^3) with a resistance of 8.57 Ω (c) Schematic of the de-frosting experiment.

3. RESULTS AND DISCUSSION

The temperature of the CFRP-ice interface with and without heating is illustrated in Figure 2. The temperature of the CFRP-ice interface rises quickly which starts to melt the ice. The rise in temperature at the CFRP-ice interface demonstrates the resistive heating capability of parts additively manufactured with electrically conductive polymer matrix composites.

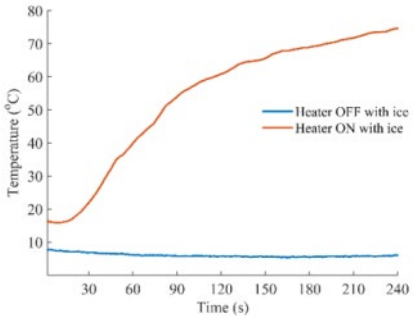

Figure 20. The temperature of the CFRP-ice interface during a de-icing experiment with and without heating.

4. CONCLUSIONS

The melting of ice demonstrates the suitability of additively manufactured parts as heating elements for de-icing. Customized heating elements of application-specific geometry can be conformally manufactured on free-formed surfaces, such as airfoils, using suitable manipulators and multi-axis AM tool path algorithms.

REFERENCES

Bernabo, P., Cuccoli, F., & Baldini, L. (2015). *Icing hazard for civil aviation*. In *2015 IEEE Metrology for Aerospace (MetroAeroSpace)* (pp. 295–300). IEEE. doi:10.1109/MetroAeroSpace.2015.7180671

National Academies of Sciences, Engineering, and Medicine; Transportation Research Board; Airport Cooperative Research Program. (2010). *Alternative Aircraft and Pavement Deicers and Anti-Icing Formulations with Improved Environmental Characteristics*. *Alternative Aircraft and Pavement Deicers and Anti-Icing Formulations with Improved Environmental Characteristics*. Washington, D.C.: Transportation Research Board. doi:10.17226/14370

Rueschhoff, L., Costakis, W., Michie, M., Youngblood, J., & Trice, R. (2016). Additive Manufacturing of Dense Ceramic Parts via Direct Ink Writing of Aqueous Alumina Suspensions. *International Journal of Applied Ceramic Technology*, *13*(5), 821–830. doi:10.1111/ijac.12557

OCTOBER 17 THURSDAY, MAIN SESSION	
8:00-8:30	REGISTRATION
8:30-9:15	OPENING/WELCOME CEREMONY
SESSION 1 - Chair : Prof. Bahattin Koç	
9:15-10:00	COMBINING ADDITIVE AND SUBTRACTIVE LASER MANUFACTURING: SELECTIVE LASER MELTING, EROSION AND REMELTING
	Keynote Speaker : PROF. JEAN-PIERRE KRUTH
10:00-10:30	WEIBULL DISTRIBUTION OF SELECTIVE LASER MELTED ALSI10MG PARTS FOR COMPRESSION TESTING.
	Authors : Khan H.M., Dirikolu M.H., Koç E.
	INFLUENCE OF BUILD ORIENTATION ON RESIDUAL STRESSES IN 3D PRINTED PARTS
	Authors : Pant P., Peng R., Moverare J., Simonsson K., Sjöström S.
10:30-11:00	MICROSTRUCTURE AND EFFECT OF HOLE ON MECHANICAL PROPERTIES OF INCONEL 718 BUILT VIA DIRECT METAL LASER SINTERING
	Authors : Işık M., Yıldız M., Koç B.,
	INFLUENCE OF HOT ISOSTATIC PRESSING AND SUBSEQUENT HEAT TREATMENT ON MECHANICAL PROPERTIES OF DIRECT METAL LASER SINTERED ALSI10MG ALLOY
	Authors : Ertuğrul O., Öter Z.Ç., Yılmaz M.S., Şahin E., Coşkun M., Tarakçı G., Koç E.
11:00-11:15	COFFEE BREAK
SESSION 2 - Chair : Omar Fergani	
11:15-11:45	4D PRINTING - AN OVERVIEW, CHALLENGES AND A TECHNOLOGY ROADMAP
	Invited Speaker : DR. EUJIN PEI
11:45-12:30	PRINTABLE DENSITY LIMITS OF ADDITIVELY-MANUFACTURED STRUCTURED FOAMS
	Authors : Tanlak N.
	NOVEL PHYSICS-BASED TECHNOLOGY TO PREDICT AND CORRECT VECTOR-LEVEL OVERHEATING
	Authors : Eissing K., Fergani O.
	EVALUATION OF ALTERNATIVE PARAMETERS TO DESCRIBE THE QUALITY OF ADDITIVELY MANUFACTURED ALUMINIUM ALLOY SURFACES
	Authors : Buchenau T., Amkreutz M., Brüning H., Norda M.
12:30-13:45	LUNCH
SESSION 3 - Chair : Assist. Prof. Evren Yasa	
13:45-14:15	EFFECT OF DIFFERENT PROCESSING PARAMETERS ON SURFACE PROPERTIES OF SELECTIVE LASER MELTING PARTS
	Authors : Gulenc I.T., Todd I., Inkson B.J.
	ON THE OPTIMIZATION OF METAL SPATTER SWEEPING IN SELECTIVE LASER MELTING
	Authors : Gürkan A.Y., Bursa M., Yasa E., Öğüt E.
14:15-15:00	MAGNETIC DIRECTED ENERGY DEPOSITION: ASSESSMENT FOR MICROGRAVITY
	Authors : Smith P., Clare A., Segal J.
	PROCESSING OF NDFEB BY SELECTIVE LASER MELTING
	Authors : Genç K., Mumtaz K., Todd I.
	VALIDATION OF DYNAMIC MODELS OF ADDITIVE MANUFACTURED PARTS USING SELECTIVE LASER MELTING METHOD
	Authors : Orhangül A., Şanlıtürk K.Y.
15:00-15:15	COFFEE BREAK
Session 4 - Chair : Assist. Prof. Emrecan Söylemez	
15:15-15:45	BALLOON EXPANDABLE AND SELF-EXPANDING STENTS PRODUCED BY LASER POWDER BED FUSION:FROM DESIGN TO TESTING
	Invited Speaker : DR. ALI GOKHAN DEMIR
15:45-16:30	HEAT TREATMENT TEMPERATURE-INDUCED MICROSTRUCTURE, MICROHARDNESS AND WEAR RESISTANCE OF INCONEL 718 PRODUCED BY SELECTIVE LASER MELTING
	Authors : Karabulut Y., İnce İ., Taşçıoğlu E., Kaynak Y.
	ON THE EFFECT OF UNFIXED PROCESS VARIABLES ON MECHANICAL PROPERTIES IN SELECTIVE LASER MELTING
	Authors : Yasa E., Ersoy K., Koç B.,
	EVALUATION OF GEOMETRICAL DEVIATIONS AND POROSITIES ON BOTH CFRP AND AISI 316L STEEL MATERIAL ON ADDITIVE MANUFACTURING
	Authors : Yeşilova A.H., Timur A., Bakkal M.
16.30-16:45	COFFEE BREAK
Session 5 - Chair : Assoc. Prof. Yusuf Kaynak	
16.45-17:30	NEXT GENERATION AGILE ON DEMAND PRODUCTION (WHY ADDITIVE MANUFACTURING AND TRADITIONAL WORKS WILL JOIN FORCES AND DO NOT SUBSITUTE EACH OTHER)
	Keynote Speaker : STEFAN RITT
17:30-18:00	THE EFFECT OF POST PROCESSING ON SURFACE PROPERTIES OF AS-PRINTED AND HEAT TREATED TI-6AL-4V ALLOY PRODUCED BY ELECTRON BEAM MELTING
	Authors : Sirin T.B., Kaynak Y., Tan E., Gümüş B.
	SELECTIVE LASER MELTING PROCESS DEVELOPMENT FOR ENHANCED PRODUCTIVITY WITH PH17-4 STAINLESS STEEL
	Authors : Yasa E., Atik İ., Bayrak İ.
GALA DINNER (17/10/2019)	

OCTOBER 18 FRIDAY, MAIN SESSION	
8:00-9:00	REGISTRATION
Session 6 - Chair : Prof. Oğuzhan Yılmaz	
9:00-9:30	THREE CHALLENGES FOR METAL ADDITIVE MANUFACTURING
	Invited Speaker : PROF. ADAM CLARE
9:30-10:00	IN SITU ELEMENTAL ANALYSIS AND FAILURES DETECTION DURING ADDITIVE MANUFACTURING PROCESS UTILIZING LASER INDUCED BREAKDOWN SPECTROSCOPY
	Authors : Lednev V.N., Sdvizhenskii P.A., Asyutin R.D., Grishin M.Y., Tretyakov R.S., Stavertiy A.Y., Fedorov A.N., Pershin S.M.
	A METALLURGICAL PHASE TRANSFORMATION MODEL APPLIED TO DIRECTED ENERGY DEPOSITION ADDITIVE MANUFACTURING OF TI-6AL-4V
	Authors : Baykasoğlu C., Akyıldız Ö., Tunay M.
10:00-10:30	TOPOLOGY OPTIMIZATION AND FINITE ELEMENTAL ANALYSIS FOR AN INCONEL 718 ENGINE MOUNTING BRACKET MANUFACTURED VIA ELECTRON BEAM MELTING
	Authors : Işık M., Kısa E., Koç B., Yıldız M., Pehlivanoğulları B., Orhangül A., Poyraz O., Akbulut G.
	A PROCESS PLANNING STUDY IN WIRE ARC ADDITIVE MANUFACTURING
	Authors : Yıldız A. S., Gebel E., Koç B., ŞEN A.A., Yılmaz O.
10:30-10:45	COFFEE BREAK
Session 7 - Chair : Prof. Cengiz Kayacan	
10:45-11:30	TITLE TO BE ANNOUNCED
	Keynote Speaker : PROF. PAULO JORGE DA SILVA BARTOLO
11:30-12:30	IMPROVEMENT MECHANICAL AND BIOLOGICAL PROPERTIES OF COCR SCAFFOLDS FABRICATED BY SELECTIVE LASER MELTING
	Authors : Özeren E., Altan M.
	DESIGN AND VALIDATION OF GRADED POROUS STRUCTURES PRODUCED BY POWDER BED FUSION PROCESS
	Authors : Kaş M., Yılmaz O.
	CERAMIC COMPOSITE COATING AND LASER SURFACE MELTING OF COCR ALLOY, AND ITS CHARACTERIZATIONCTERIZATION
	Authors : Işık M., Bandyopadhyay A., Shivaram A., Avila J.D., Dernell W.S., Bose S.
	LASER INDUCED BREAKDOWN SPECTROMETRY FOR ONLINE ANALYSIS OF METAL PARTICLES FEEDSTOCK DURING LASER METAL DEPOSITION PROCESS
	Authors : Sdvizhenskii P.A., Lednev V.N., Asytin R.D., Grishin M., Pershin S.M.
12:30-13:30	LUNCH
Session 8 - Chair : Assit. Prof. Ebubekir KOÇ	
13:30-14:00	OPPORTUNITIES AND CHALLENGES FOR HIGH-PERFORMANCE ADDITIVELY MANUFACTURED MATERIALS
	Invited Speaker :DR. BANDAR ALMANGOUR
14:00-14:45	NUMERICAL STUDY OF HEAT DITURBUTION IN TI-6AL-4V THIN WALLED CYLINDER DURING ELECTRON BEAM MELTING PROCESS
	Authors : Saghatchi R., Saeidiharzand S., Yıldız M., Koç B.
	THERMAL SIMULATION OF POWDER BED FUSION PROCESS USING FINITE ELEMENT METHOD
	Authors : Bayraktar C., Demir E.
	THE MICROSTRUCTURE AND MECHANICAL PROPERTIES OF POROUS STRUCTURES PRODUCED FROM ALSI10MG BY DIRECT METAL LASER SINTERING
	Authors : Bulduk M.E., Ertürk A.T., Coşkun M., Tarakçı G., Ergin U.
14:45-15:00	COFFEE BREAK
Session 9 - Chair : Prof. İbrahim Etem Saklakoğlu	
15:00-15:30	GENERATIVE TOPOLOGY OPTIMIZATION FOR METAL ADDITIVE MANUFACTURING
	Authors : Polat M.F., Koç B.
	INVESTIGATION OF ENERGY ABSORPTION BEHAVIOR OF STIFFNESS OPTIMIZED LATTICE STRUCTURES
	Authors : Görgülüarslan R.M., Göngör O.U., Erem E., Yıldız S.
15.30-16:00	TRANSIENT MELT POOL MODELING FOR THE ABRUPT PROCESS PARAMETER CHANGE IN SELECTIVE LASER MELTING PROCESS
	Authors : Söylemez E.
	A NEW DESIGN APPROACH FOR ADDITIVE MANUFACTURING OF SATELLITE COMPONENTS
	Authors : Badır M.E., Dagkolu A., Söğütkıran E., Yılmaz O.
16:00-16:15	COFFEE BREAK
Session 10 - Chair : Assist. Prof. Eralp Demir	
16:15-16:45	UTILIZATION OF INDUSTRIAL ADDITIVE MANUFACTURING CHALLENGES AND SOLUTIONS
	Yağmur A.
	THERMAL PROCESS SIMULATION FOR DIRECT ENERGY DEPOSITION ADDITIVE MANUFACTURING PROCESS
	Demir E., Dörtkaşlı K.
16:45-17:15	CHARACTERIZATIONCTERIZATION AND COMPRESSION TESTING OF DOUBLE GYROID LATTICE STRUCTURES PRODUCED BY DIRECT METAL LASER MELTING
	Kavas B., Yasa E., Sönmez Ş.
	FEASIBILITY OF CMT ADDITIVE MANUFACTURING TECHNIQUE FOR IN718
	Berme B.
17:15-17:30	EVALUATION OF TANTALUM ALLOY WITH TITANIUM IN UNIVERSAL POWDER BED SYSTEM (UPB) FOR ELECTRON BEAM MELTING PROCESS
	Çelebi A., Gulizia S., Doblin C., Fraser D., Prentice L.

OCTOBER 18 FRIDAY, PARALLEL SESSION	
Session 11 - Chair : Prof. İsmail Lazoğlu	
15:00-15:30	**ADDITIVE MANUFACTURING OF COMPOSITE MATERIALS**
	Karas B., Fairclough P., Mümtaz K.
	FAILURE ANALYSIS OF CARBON FIBER REINFORCED PA11 PRODUCED BY SLS
	Gümüş S., Bayram A., Lackner J.M., Çallı M., Ergin D., Kraschitzer W., Krenn R., Hanning H.
15.30-16:00	**MEASURING HAZE, TRANSMITTANCE AND COLOUR OF CLEAR 3D PRINTED STEREOLITHOGRAPHY RESINS**
	Fitpatrick D., Hajatpour O., Branagan D.
	MECHANICAL PROPERTIES OF 3D PRINTED PARTS MADE OF RECYCLED POLYMERS
	Bakır A.A., Atik R., Özerinç S.
16:00-16:15	**COFFEE BREAK**
Session 12 - Chair : Assist. Prof. Ulaş Yaman	
16:15-16:45	**PRODUCTION OF PRIMECAST® POLYSTYRENE BY SELECTIVE LASER SINTERING (SLS) METHOD AND DEVELOPMENT OF SURFACE ROUGHNESS OF SINTERED PARTS**
	Özbay B., Özer G., Bulduk M.E., Tarakçı G., Öter Z.Ç., Koç E.
	ORIENTATION AND DYEING EFFECTS ON MECHANICAL STRENGTH OF THE MULTI JET FUSION PRINTED PARTS
	Günenç S., Söylemez E.
16:45-17:15	**MODELLING TOPOLOGICALLY OPTIMIZED PARTS WITH MICROSTRUCTURES**
	Özkapıcı D., Yaman U.
	THE EFFECT OF PROCESSING PARAMETERS ON THE MICROSTRUCTURE AND MECHANICAL PROPERTIES OF SLS PEKK
	Gümüş S., Bayram A., Lackner J.M., Çallı M., Ergin D., Kraschitzer W., Krenn R., Hanning H.
17:15-17:30	**DE-ICING USING ADDITIVELY MANUFACTURED HEATING ELEMENT**
	Khan S.A., Lazoğlu İ.

2019@amcturkey.org

2019.amcturkey.org

TAMA
TURKISH ADDITIVE MANUFACTURING ASSOCIATION

origin
event marketing communications